The Investigation of Aspects of Chemical Looping Combustion in Fluidised Beds

Ruinan Mao
St Edmunds College
April 2018

This Dissertation is submitted for the degree of Doctor of Philosophy at the Department of Engineering, University of Cambridge

Preface

The work described in this dissertation was undertaken in the Department of Engineering, University of Cambridge, between November 2011 and April 2018. It is the original and independent work of the author except where specifically acknowledged in the text. Neither the present dissertation, nor any part thereof, has been previously submitted at any other university.

This dissertation contains 61712 words and 77 figures in total.

Ruinan Mao
Department of Engineering
University of Cambridge
April 2018

Acknowledgements

I would like to thank everyone who offered help during my PhD. I especially want to thank my supervisor, Dr Stuart Scott, for his support, continued guidance and encouragement. I also want to show my appreciation to my advisor, Dr John Dennis.

I would like to thank my laboratory mates, in particular: Wenting Hu, Felix Donat, Wen Liu, Mohammad Ismail, Yaoyao Zheng, Marco Saucedo and Ryan Harper. Also, I would like to thank the staff of the Department of Engineering, especially Peter Benie and Mick Underwood, who helped me with computer and equipment issues, respectively.

I would like to thank the Engineering and Physical Sciences Research Council (EPSRC) for funding my PhD.

I am grateful to my family for their love and support. I also want to thank my friends, who made my time in Cambridge such a memorable one.

I would like to thank St Edmunds College for offering me excellent accommodations and colorful social life.

Abstract

During the past 30 years, the surface temperature of the earth has increased because of the increased greenhouse effect. The stronger greenhouse effect is thought to be caused by industrial emissions of greenhouse gases. Thus, Carbon dioxide (CO_2) capture and storage (CCS) is necessary to reduce the greenhouse effect. Chemical looping combustion (CLC) is a promising fossil fuel combustion technology, which is able to separate CO_2 from the flue gases without a large consumption of energy. In this thesis, the study was extended to look at the use of chemical looping materials within traditional fluidised bed combustion and investigation of the interaction between the fuel, the supplied air and the chemical looping agent. Three topics of chemical looping combustion are discussed, including 1) the Sherwood number in the fluidised bed; 2) properties of different oxygen carriers, Fe_2O_3 and CuO (with supporting materials), were tested in the fluidised bed reactor; 3) the simulation of a steady state and a dynamic model of a coal-fired CLC power plant using Fe_2O_3 as oxygen carriers.

The Sherwood number, which represents the mass transfer rate, is important in the calculation of CLC process. With Sherwood number, the mass transfer rate kg around the acting particle can be calculated using correlation $Sh = kg \cdot d/D$, where d is the diameter of acting particle, and D is the diffusivity around the acting particle. Hayhurst and Parmar (Hayhurst and Parmar 2002) calculated the Sherwood number in the fluidised bed by using the CO/CO_2 ratio, which was measured by the

temperature difference between the carbon particle and the bulk phase (Hayhurst and Parmar 1998). However, the temperature of the particle could be overestimated, so the CO/CO_2 ratio could be underestimated. In this thesis, a universal exhaust gas oxygen (UEGO) sensor was employed, which could measure the actual carbon consumption rate in the fluidised bed by oxidizing CO in the sample gas into CO_2 and. Fe particles of the same size of the char particle is used to measure the O_2 consumption rate, and thus eliminate uncertainty in the Sherwood number. The CO/CO_2 ratio was calculated by using the carbon consumption rate and the O_2 consumption rate. In contrast to Hayhurst and Parmar (Hayhurst and Parmar 2002) who assumed CO_2 was the main product, for this char the actual ratio of CO/CO_2 was almost zero. The measurement here is in agreement with Arthur. This more accurate determination of CO/CO_2 allows a better estimate of the mass transfer coefficient and leads to a correction of the Hayhurst and Parmar's (Hayhurst and Parmar 2002) correlation by a factor of ½. Interestingly, very small fluidised beds have mass transfer coefficients which are about twice that expected in a large bed (owing to the very different flow and indeterminate flow pattern). This means the correlation of Hayhurst and Parmar (Hayhurst and Parmar 2002), by fortuitous coincidence works wells for beds with diameters < 30 mm., without the correction factor, should be ignored.

In the fluidised bed in a typical CLC process, different fluidising material could have different influence on the reactions. Thus, it is worth discussing different kinds of fluidising materials. The char combustion in the fluidised bed was simulated by using inert (sand) and active (Fe_2O_3 or CuO) fluidising materials, and air as fluidising

gas. The results indicated that 1) CO combustion in the boundary layer leads to smaller carbon consumption rate and larger oxygen consumption rate; 2) Using Fe_2O_3 particles as fluidising materials slows down the carbon consumption rate, since the diffusivity of CO_2 is smaller than CO; 3) CuO particles slow down the carbon consumption rate at large Sherwood number (Sh =2 or 2.5). The influence of using CuO as fluidising material is further discussed experimentally by using low O_2 fluidising gas. The results indicated that since the amount of CuO used in the experiment is small, when the O_2 concentration in the bulk phase is lower than the equilibrium concentration, the O_2 concentration in the bulk phase gradually decreases, and the O_2 concentration in the bulk phase has large influence on the char particle combustion.

A steady state model of a coal-fired CLC power plant was simulated. The aim of the model was to test the suitable operating conditions of the power plant, such as recycle rate of oxygen carriers, for the power plant design. In the steady state model, the power plant consists of a combustor and a steam cycle. Hambach lignite coal, Polish bituminous coal and natural gas were tested as fuels. The results indicated that: (1) The effect of the fuel is largely due to the amount of oxygen required per GJ released; (2) Preheating is important, but seems to have a minor effect since the most of the heat is released at temperatures well above the pinch point; (3) since the temperatures of heat source in this research is well above the pinch point, all heat are usable for the steam cycle. In this case, the steam cycle and the chemical looping plant could be optimised separately; (4) As long as the preheat temperature of the air

flow into the air reactor is higher than the temperature of turbines, in most of cases the power output is unaffected by the choice of variables, leaving the designer free to choose the most convenient.

With the conclusions above, a dynamic model of a coal-fired CLC power plant using Fe_2O_3 as oxygen carrier is then simulated. The aims of this simulation include: 1) explaining the kinetics of Fe_2O_3 oxygen carriers at high temperature (1223K) in a fluidised bed reactor using Brown's data (Brown 2010); 2) a 1GWth dynamic power plant was simulated to test different cases including changing power supply and power storage. In the dynamic model, a chemical looping power plant using Hambach lignite char is tested, and the parameters of the system are adjusted so as to simulate the operations of a real chemical looping power plant. The two-phase model is employed for the fluidised bed reactors. Experimental data from Brown (Brown 2010) was simulated using this model first to test its validity. Then the model is scaled up to simulate a 1GWth dynamic power plant. The ideal operation conditions are found, and a char stripper is found helpful for carbon capture. The response time of the system is about one hour and a half. Two methods of energy storage are discussed, and in both methods the energy stored in the system is about the energy of 90 seconds of inflow of fuel, meaning that using the chemical looping material as a transient store of energy for load balance is not likely to be of value.

CONTENTS

CHAPTER 1 INTRODUCTION

1.1 MOTIVATIONS

1.1.1 Green house effect and carbon dioxide emissions

The greenhouse effect is a natural process, in which the short wavelength visible light from the sun passes through the atmosphere, but longer, infrared wavelengths re-radiated from the earth's surface are trapped. Without it, the earth would be a much colder planet. However, if the greenhouse effect becomes stronger, it will make the earth less habitable and result in global temperature rises. ('Greenhouse Gas' 2016)

During the past 30 years, the surface temperature of the earth has increased because of the increased greenhouse effect. Using the global average temperature of 1961-1990 as the reference, the global average temperature lower in the 1880 - 1935 period; in contrast, since 1980, the global average temperature has been continuously higher. The lowest temperature recorded appears in 1917 (-0.47K relative to the reference period). Since then, the earth became warmer, and the most recent years show the highest temperature recorded of +0.6K (relative to the reference period) in the past 130 years. (ProcessTrends.com and globalissues.org 2015)

The stronger greenhouse effect is thought to be caused by industrial emissions of greenhouse gases (ProcessTrends.com and globalissues.org 2015). There are many kinds of greenhouse gases, which mainly include water vapour (H_2O), carbon dioxide

(CO_2), methane (CH_4), and nitrous oxide (N_2O), plus three fluorinated industrial gases: hydrofluorocarbons (HFCs), perfluorocarbons (PFCs) and sulphur hexafluoride (SF6).

Although carbon dioxide is not the most potent of greenhouse gases, it is still the most important one. In the period 1751 -1849, the CO_2 emissions were small. Since 1849, more factories were built because of the industrial revolution, and the amount of CO_2 emissions began to increase rapidly. In 1919, emissions reached 1000 Gt of carbon per year; at present, it is almost 9000 Gt of carbon per year, a nine-fold increase over the past 90 years. (‘Carbon Dioxide Information Analysis Center (CDIAC)’ 2010)

In 2011, world primary energy consumption grew by 2.5%, which is close to the historical average. Oil, coal and natural gas, three types of traditional fossil fuel, account for almost 90% of global energy consumption. Oil is still the world's leading transport fuel, accounting for 33.1% of global energy consumption. The market share of coal of 30.3% was the highest during the past 20 years. Renewable energy sources are growing, but account for just 10% of the total. (‘BP’s 2011 Statistical Review of World Energy’ 2011)

It is easy to conclude that the global energy consumption heavily relies on the fossil fuels. Therefore, there is a strong motivation to develop new technology to use fossil fuels without CO_2 emissions to atmosphere.

1.1.2 Carbon dioxide capture and storage

British Petroleum (BP) defined Carbon dioxide (CO_2) capture and storage (CCS) as 'a process consisting of the separation of CO_2 from industrial and energy-related sources, transport to a storage location and long-term isolation from the atmosphere'. (Intergovernmental Panel on Climate Change 2005)

There are different types of CO_2 capture systems: post-combustion, pre-combustion and oxyfuel combustion. The selection of a capture system depends on the fuel type (gas or solid), the concentration of CO_2 in the gas stream, and the pressure of the gas stream.

Post-combustion capture is a process, which separates CO_2 from flue gases. There are different kinds of post-combustion capture technologies being investigated, such as chemical absorption (Rochelle 2009), Ca-Looping technology (Martínez et al. 2016), adsorption (Harlick and Tezel 2003), membrane separation (Zhao et al. 2008), and cryogenic fractionation (Hart and Gnanendran 2009) etc. Most of the technologies are not commercially applied in industry, which is because of the reasons such as the low partial pressure of CO_2 in the flue gas of coal-fired power plants (Wang et al. 2017).

Nowadays, post-combustion capture is the most mature CCS technology, which has proven pilot projects and commercial scale plants (Theo et al. 2016), and uses a hydrogen-producing process. Firstly, the fossil fuel is gasified with pure oxygen to produce synthesis gas (a mixture of carbon monoxide and hydrogen). Then the synthesis gas goes to a water gas shift reactor. In the reactor, the carbon monoxide in

the synthesis gas reacts with steam to produce CO_2 and hydrogen. CO_2 is then separated by a physical or chemical absorption process. The hydrogen-rich gas can be used as a fuel in a standard power cycle (Herzog and Golomb 2004).

Oxyfuel combustion is a combustion process, which use pure oxygen rather than air as the oxidant. The main components of the flue gas are CO_2 and water vapour. A condensation step can easily remove the water vapour from the flue gas. The main energy consumption step is to separate oxygen from the air to obtain pure oxygen (Lewis and Gilliland 1954).

The capture efficiency in oxyfuel combustion is expected to be very close to 100%, which is higher than pre- and post-combustion (85-95%) (Herzog and Golomb 2004). Here, the capture efficiency is defined as the fraction of CO_2 separated from the gas stream.

1.2 CHEMICAL LOOPING COMBUSTION

Chemical-looping combustion is a promising fossil fuel combustion technology, which is able to separate CO_2 from the flue gases without a large consumption of energy. The basic ideas of chemical-looping combustion were from a patent in 1954 to produce of pure carbon dioxide from fossil fuels (Richter and Knoche 1983). In 1983, Richter and Knoche proposed a similar idea, which focus on the increasing the thermal efficiency for power production (Ishida and Jin 1994). In 1994, Ishida and Jin

suggested that it was possible to employ this technology to capture CO_2 from fossil fuels in order to control greenhouse effect (Ishida and Jin 1996).

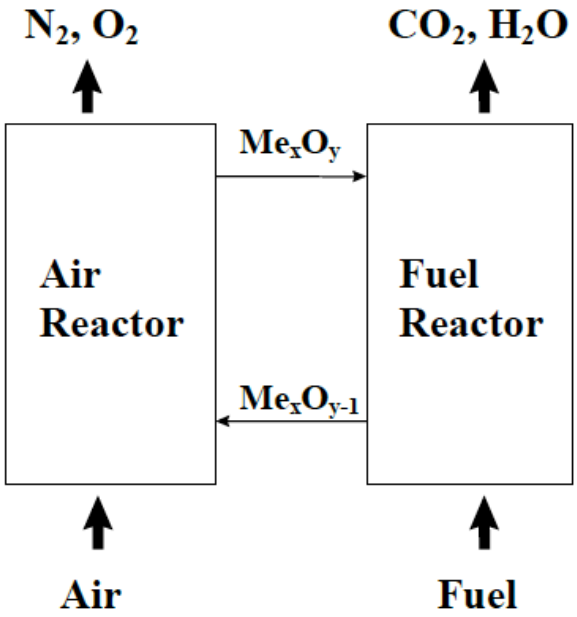

Figure 1.1 Schematic representation of the chemical-looping combustion process.

Figure 1.1 shows the basic concept of chemical looping combustion. There are two interconnected reactors. The inlet air continuously flows into the air reactor and the fuel continuously flows into the fuel reactor. Solids oxygen carriers are required to facilitate the reactions in the reactors. Generally, metal oxide particles are utilised to transfer oxygen from the combustion air to the fuel. Direct contact between fuel and air is avoided by a gas-solid reaction between the fuel and the metal oxide. After water vapour condensation, a high-purity CO_2 stream without N_2 is obtained from the fuel reactor. The oxygen carriers are used repeatedly between the two reactors, so the physical and chemical stability is as important as its oxygen carrying capacity.

In the air reactor, the reduced metal oxide, denoted Me_xO_{y-1}, is oxidized by air according to reaction (1.1) and in the fuel reactor it is reduced back to its initial state by a fuel, according to reaction (1.2).

$$O_2 + 2Me_xO_{y-1} \Leftrightarrow 2Me_xO_y \quad (1.1)$$

$$C_nH_{2m} + (2n+m)Me_xO_y \Leftrightarrow nCO_2 + mH_2O + (2n+m)Me_xO_{y-1} \quad (1.2)$$

The oxidation of metal oxide (reaction (1.1)) is strongly exothermic, but the oxidation of fuel (reaction (1.2)) could be either exothermic or endothermic depending on the characteristics of the oxygen carriers and the type of fuel. However, the oxygen carriers just facilitate the fuel combustion reactions, so the energy released in total is equal to the heat released in conventional combustion, where the air and the fuel contact directly. No extra energy is required for the CO_2 separation. Additionally, because there is no air in the fuel reactor, there is little formation of NO_x in the process (the nitrogen in the air would react with oxygen to produce thermal NO_x at high temperature). In the air reactor, the temperature is too low to generate any thermal NO_x. (Lewis and Gilliland 1954)

The development of oxygen carriers plays a key role in chemical-looping combustion. A successful oxygen carrier should be able to satisfy the following criteria: 1, High reactivity with oxygen and fuel; 2, High conversion of the fuel to CO_2 and H_2O; 3, High resistance to agglomeration, high crushing strength and low attrition; 4, Low cost; 5, Environmental compatibility and low toxicity; 6, High melting temperature, for both oxidized and reduced forms. (Chuang 2009)

The most studied transition state metal oxides, primarily based on Ni, Cu, Mn and Fe, are employed as oxygen carriers because they satisfy the criteria above. Their reactivity is in the descending order of NiO > CuO > Fe_2O_3 > Mn_2O_3, although this order depends on how the oxide is supported. (Chuang et al. 2008)

The supporting material is very important in the oxygen carrier. It is either active or inert, and can increase the performance of the oxygen carrier. This material acts as a porous support, thus, increases the surface area. It also helps to maintain the particle structure during the reactions.

As an oxygen carrier in chemical looping combustion, iron oxide has many advantages. First, it has high reactivity with oxygen and fuel; second, it has high resistance to agglomeration, high crushing strength and low attrition, which are important properties for application in industrial system. Finally, ore mines are inexpensive and environmental friendly. In contrast, nickel oxide and copper oxide are relatively expensive and toxic.

In a chemical looping combustion process using iron based oxygen carriers, the fuel can be either solid, such as coal, or gasified. The coal can be gasified by steam and produce syngas (CO and H_2), and this process is energy required. The syngas is then oxidized by iron oxide to produce water and CO_2.

$$3Fe_2O_3 + H_2 \leftrightarrow 2Fe_3O_4 + H_2O \qquad \Delta H^0_{1123K} = -5.9kJ/mol \qquad (1.3(a))$$

$$Fe_2O_3 + 3CO \leftrightarrow 2Fe + 3CO_2 \qquad \Delta H^0_{1123K} = -0.3kJ/mol \qquad (1.3(b))$$

$$0.947Fe_2O_3 + 0.841CO \leftrightarrow 2Fe_{.947}O + 0.841CO_2 \qquad \Delta H^0_{1123K} = -33.3kJ/mol \qquad (1.3(c))$$

Figure 1.2 shows the equilibrium constant $K_p = \frac{P_{CO_2}}{P_{CO}}$ versus Temperature (K) for iron oxides (Fe_2O_3, Fe_3O_4,$Fe_{.947}O$) reduction by CO. The equilibrium constant K_p is related to the standard free energy change of the reaction at temperature *T*, by

$$\Delta G^0(T) = -RTln(K_p) \tag{1.4}$$

From the K_p values in Figure 1.2, it is obvious that only reaction between Fe_2O_3 and Fe_3O_4 can be used to achieve near complete combustion.

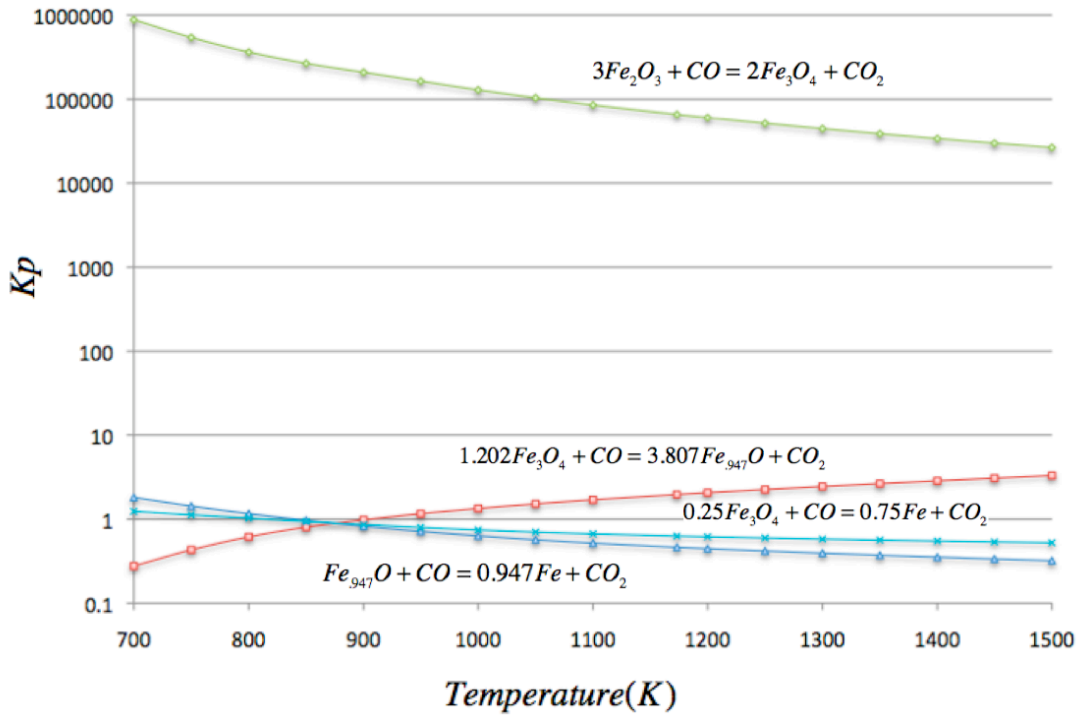

Figure 1.2 A plot of $K_p = \frac{P_{CO_2}}{P_{CO}}$ for various temperatures. The triple point of the iron system is 848.7K. (Data sources: NASA Database (McBride, Zehe, and Gordon 2002))

The magnetite can be oxidized by air

$$4Fe_3O_4 + O_2 \Leftrightarrow 6Fe_2O_3 \qquad \Delta H^0_{1123K} = -237.2kJ/mol \tag{1.5}$$

Previous research (Copeland et al. 2002) indicates that the particles of pure iron oxide can be deactivated in chemical looping combustion cycling. Particles of pure iron oxide were cycled at 993–1073 K and both the oxidation and reduction were fast, and no significant attrition was observed over 50 cycles. However, if the temperature was increased over 1173K, the pure iron oxide particles began to agglomerate and deactivate. Bohn *et al*. (C. D. Bohn et al. 2010) reported the results of the kinetics of the reduction of pure iron oxide by CO mixed with CO_2. It was found that the rate of reduction of Fe_2O_3 to Fe_3O_4 remained constant over 10 cycles; however, the rate of reduction of Fe_3O_4 to $Fe_{.947}O$ declined by 60–85% over cycles 2-10. Pre- exponential factors were found to decrease; In contrast, activation energies remained constant with cycling, which implied that deactivation was due to the loss of surface area in the oxygen carriers. Other research (Li et al. 2009) indicates that, if pure iron oxide oxygen carriers were reduced completely to Fe, it would deactivate within several cycles. However, it is more stable when reduced to $Fe_{.947}O$.

Adding supporting materials to particles is a way to avoid sintering and increase reactivity. Alumina (Al_2O_3) is one such supporting material, which was found to be able to increase the crushing strength and resistance to agglomeration (Cho, Mattisson, and Lyngfelt 2000). It was observed that Al_2O_3 is not inert. Using X-ray diffraction, Kierzkowska *et al*. (Kierzkowska et al. 2010) confirmed the formation of $FeAl_2O_4$. In their experiment, the particles were reduced in a mixture of CO and N_2, and were oxidized in a mixture of steam and N_2. Stable conversion over 40 cycles was observed. Ishida *et al*. (Ishida et al. 2005) also reported the formation

of solid solutions of hematite and corundum in Fe_2O_3 (25 wt%)/ Al_2O_3 (75 wt%) composite particles above 1000 °C. The mechanical strength was improved by increasing the content of corundum, which appeared to act as a binder. Fang *et al*. (F. He, Wang, and Dai 2007) used impregnation methods to prepare Fe_2O_3 (80 wt%) / Al_2O_3 (20 wt%) oxygen carriers. These particles showed good reactivity in 20-cycle redox tests in a TGA reactor. 85% of the CH_4 was converted to CO_2 and H_2O during most of the reduction periods with minor formation of CO and H_2. Mattisson *et al*. (Mattisson, Johansson, and Lyngfelt 2004) prepared particles composed of 40-80 wt % Fe_2O_3, together with Al_2O_3, ZrO_2, TiO_2, or $MgAl_2O_4$ by freeze granulation. The reactivity of the oxygen-carrier particles was evaluated in a laboratory fluidized bed, where the alternating atmosphere that an oxygen carrier encounters in a CLC system was simulated by exposing the sample to reducing (50% CH_4, 50% H_2O) and oxidizing (5% O_2) conditions at a temperature of 1223 K. Fe_2O_3 / Al_2O_3 was found to have good reactivity. Kidambi *et al*. (Kidambi et al. 2012) synthesized Fe_2O_3 / Al_2O_3 composite particles by the co-precipitation method. The particles were reduced to Fe with CO and oxidized by steam and air. Different weight ratio of Fe_2O_3 / Al_2O_3 were tested and the optimum loading of Al_2O_3 in the composite particles was found to be 25 wt % for the production of hydrogen over 50 cycles. Therefore, Fe_2O_3 / Al_2O_3 oxygen carrier is a promising oxygen carrier for chemical looping combustion.

Other supporting materials, such as ZrO_2, $MgAl_2O_4$, TiO_2, and SiO_2 (J. Adanez et al. 2004), have also been used as binder and support in iron-based oxygen carriers. Unlike alumina, supporting materials, such as $MgAl_2O_4$ and ZrO_2, are inert. Johansson

et al. (Johansson, Mattisson, and Lyngfelt 2004) suggested that the Fe_2O_3/ $MgAl_2O_4$ oxygen carrier showed best reactivity among the iron oxides supported on six different inert materials. Various sintering temperatures and ratios of metal oxide/inert were used to find the optimal particle properties. The particles consisting of Fe_2O_3 (60wt%) / $MgAl_2O_4$ sintered at 1373 K was found to be the most suitable oxygen carrier, and exhibited reasonable crushing strength and resistance toward agglomeration and fragmentation. Corbella and Palacios (Corbella and Palacios 2007) found that the available oxygen of Fe_2O_3 /TiO_2 particles for methane combustion in the reduction stage was lower than expected since the active phase interacts with the support forming $FeTiO_3$, ilmenite. Zafar *et al*. (Zafar, Mattisson, and Gevert 2005) reported similar results for Fe_2O_3/SiO_2 oxygen carrier; the formation of Fe_2SiO_2 reduced the reactivity of the Fe_2O_3/SiO_2 particles.

Copper oxides are often suggested because copper is cheap, relatively low toxicity, and relatively high reaction rate (Chuang et al. 2008). In addition, the large amount of heat produced from the reduction and oxidation of CuO is important for the endothermic gasification reactions. Although there are two disadvantages of copper oxides (Mattisson, Järdnäs, and Lyngfelt 2003): first is the agglomeration of CuO; second is that CuO decomposes when the temperature is high, which lowers its capacity of oxidizing fuel in the fuel reactor.

Here, the materials used in chemical looping, whilst important, are not the main focus of this thesis. Therefore, only iron and copper based materials are considered, for the reasons outlined above. This thesis instead focuses on more general aspects of

chemical looping, including investigating process scale models, and how oxygen carriers can interact with solid fuels within a fluidized bed. Combustion of char in a fluidized bed is also revisited, and compared with combustion of metal oxide particles. These aspects are not reviewed here, and the reader is instead referred to the introduction in each chapter.

1.3 COMBUSTION MODELS

1.3.1 Reaction of solid fuels

The burning of solid fuels, such as coal, is a multistate process: first losing volatiles, then the remaining char reacts with oxygen and sometimes CO_2 and water. The work here is mostly concerned with this latter stage, since devolatilization is fast and not rate limiting, and there is good interaction between the volatiles and the oxygen carrier.

1.3.2 Char combustion models

In a conventional combustion process, oxygen will diffuse to the surface of the particle and the char will burn by $C+O_2 \rightarrow CO_2 + CO$. If the particle is porous then three regimes often occur (Turnbull 1984). Regime 1 is kinetics control, in which oxygen can diffuse through the particle leading to a fall in density uniformly throughout; regime 2 in which particles burn only at their outer surface as oxygen is consumed before it can penetrate far into the particle, and regime 3 is external mass

transfer control. Here regime 2 and regime 3 are most relevant when gas phase oxygen is present. Similar classification also applies to particles of metal oxide being reoxidised, as discussed in Chapter 2 and Chapter 6. Regime 1 and regime 2 are most relevant to systems in which there is no oxygen, e.g. when trying to combust a solid fuel using an oxygen carrier, such as iron oxide, which does not produce gas phase oxygen. In this case, the active gas phase species is CO_2 or water, which being less reactive than O_2 tends give slower rates of reaction.

1.3.3 Mass transfer in the boundary layer

In regime 2 and regime 3, mass transfer in the boundary layer of the reacting particle is important. Thus, it is necessary to know the Sherwood number, so as to calculate the mass transfer coefficient via $Sh = kg \cdot d/D$, where kg is the mass transfer coefficient, d is the diameter of the reacting particle, and D is the diffusivity of the vapour in the gas flow. When dealing with non-equilmolar or dilute diffusion, the extra convective terms, which appear in e.g. the Stefan-Maxwell diffusion equation, mean the exact meaning of kg is unclear. Conventionally the kg is now interpreted to be a hypothetical kg that would be measured in for equimolar counter diffusion. Using this value of kg directly in a non-equimolar problem (e.g. the diffusion of oxygen to a surface against a flux of carbon monoxide) would be incorrect. Hayhurst and Parmar (Hayhurst and Parmar 2002) addressed this by translating the equimolar kg and Sh from into a boundary layer thickness, with this thickens then used as a boundary condition for a more correct description of diffusion.

1.4 AIMS AND OVERVIEW

This research investigates two important aspects of chemical looping, i.e. process level models, and the interaction of chemical looping agents with fuels in fluidised beds. This thesis investigates the following:

1) The combustion of char at elevated temperature is a very fast reaction, and attempts to measure the kinetics have often been confounded by the reaction being limited by the rate at which the oxygen can be transported to the char particle from the bulk. A large particle of char may either burn in the fully mass transfer controlled limit, or in a regime in which the external mass transfer resistance cannot be neglected. The Sherwood number is essential for the chemical looping combustion calculation. However, if the Sherwood number is measured by char combustion method, the ratio of CO/CO_2 must be known, and there are many uncertainties in the measurements of ratio of CO/CO_2. Thus, Fe particles and char particles at the same size are used at the same experimental conditions to measure the ratio of CO/CO_2 and the Sherwood number. This provides insights into mass transfer processes in fluidized bed combustion.
2) Models are used to predict the interaction between chemical looping agents in the fluidised bed and the hypotheses generated are tested experimentally.
3) In char combustion, when the reaction is mass transfer controlled, higher O_2 transport rate could increase the reaction rate. At high temperatures, when the local O_2 concentration is low, CuO decomposes and produces O_2. Thus, both CuO

and sand are used as fluidising materials at different O_2 concentrations of inlet gas to examine interactions between the active chemical looping agent in the mass transfer boundary layer and the fuel. Materials such as CuO could produce O_2 in the boundary layer and increase the combustion rates, beyond those allowed by mass transfer in conventional combustion systems.

4) A steady state model for a 1GJ CLC power plant is modeled with the focus on the steam cycle. The power plant model consists of the combustor of coal via chemical looping combustion and a steam cycle using the heat generated by the chemical looping combustor. The maximum efficiency is evaluated for different kinds of fuel, temperatures of reactors, with or without preheating. The results are compared with other technologies.

5) Brown (Brown 2010) used the two-phase theory of fluidization to model the chemical looping combustion process in a bubbling bed. At 1073K, Brown (Brown 2010) assumed the char gasification is kinetics controlled, and successfully modeled it; at 1223K, the shrinking core model is tested in this thesis. The dynamic model for a 1 GJ CLC power plant is modelled with the focus on the reactors. Several tests are made: 1, the response time of the system; 2, the importance of the char stripper; 3, using an 'energy storage mode' of chemical looping to meet transient demands.

CHAPTER 2 MASS TRANSTER TO BURNING PARTICLES IN A FLUIDISED SYSTEM AND THE EFFECT OF THE RATIO OF CO TO CO_2 PRODUCED BY THE REACTION

2.1 INTRODUCTION

The combustion of char at elevated temperature is a very fast reaction, and attempts to measure the kinetics have often been confounded by the reaction being limited by the rate at which the oxygen can be transported to the char particle from the bulk. A large particle of char may either burn in the fully mass transfer controlled limit, or in a regime in which the external mass transfer resistance cannot be neglected (Gavalas 1980) (Hayhurst and Parmar 2002). The importance of mass transfer processes surrounding the char particle has therefore been extensively studied (for example the review of Scala (Scala 2007)) , with the output of such work often being a correlation which links the properties of the fluidised bed to the effective mass transfer coefficient, via the Sherwood number. Usually, correlations applicable to the fluidised bed will have a form close to that for flow of fluid past a sphere, e.g. the expression given by Frossling (Frössling 1938). Frossling (Frössling 1938) correlated the rate of mass transfer from an evaporating droplet in a gas flow with the following expression derived from dimensional analysis,

$$Sh = 2.0 + 0.552Re^{1/2}Sc^{1/3} \qquad (2 \leq Re \leq 1300) \qquad (2.1)$$

Where the Sh is the Sherwood number ($Sh = d \cdot k_g/D$), d is the diameter of the

reacting droplet, kg is the mass transfer coefficient of the droplet and D is the diffusivity around the reacting particle; Re is the Reynolds number ($Re = \rho_g \cdot U \cdot d/\mu_g$), ρ_g is density of gas flow, U is the total superficial velocity of gas flow and μ_g is dynamic viscosity of gas flow; Sc is the Schmidt number ($Sc = \mu_g / D \cdot \rho_g$). The first term, 2, represents the situation when there is diffusion through a stagnant medium; the second term, $0.552Re^{1/2}Sc^{1/3}$, represents the contribution from convection. Expressions of this form also arise from theoretical considerations, e.g. surface renewal models (La Nauze, Jung, and Kastl 1984) or from consideration of the boundary layers (Hayhurst and Parmar 2002). Despite the difficulties with the theoretical justification, expressions of a similar form have been used with some success (though with different constants) (LaNauze and Jung 1982) to correlate the observed mass transfer coefficient in fluidised beds.

With the measured Sherwood number, the mass transfer coefficient of the droplet kg, can then be calculated with the correlation $Sh = d \cdot k_g/D$.

2.1.1 Measurements of the rate of mass transfer around freely moving active particles in the fluidised bed of inert particles

Measurements of the rate of mass transfer around freely moving active particles in the fluidised bed of inert particles have been made using various methods, as outlined below. It should be noted, that, whatever the method chosen, a mass transfer coefficient is implicitly a steady state quantity, so in the case of transient experiments, the experiment must be of sufficient duration for the processes external to the particle

to have time to establish a pseudo steady state.

2.1.1.1 Liquid evaporation from porous particles

In this method, porous particles (i.e. the active particle) are loaded with a volatile liquid and added to the fluidised bed and the rate of evaporation determined by measuring the concentration in the off-gas from the bed. Various liquids have been used, for instance, 1) Tsotsas (Tsotsas 1994) and Bradshaw and Myers (Bradshaw and Myers 1963) used water; 2) Riccetti and Thodos (Riccetti and Thodos 1961) used nitrobenzene and water; 3) Wilkins and Thodos (Wilkins and Thodos 1969) used n-decane.

Difficulties with this method include correctly accounting for the intra particle mass transfer, and for the latent heat of evaporation. An accurate determination of the particle temperature is needed, since the rate of mass transfer must be determined from difference between the saturated vapour pressure (a strong function of temperature) and the partial pressure in the bulk; to some extent this issue can be resolved by solving the heat balance alongside the mass transfer equations. Liquid on the surface of the particle could also influence the fluidisation. Finally, the inert bed material could absorb the evaporating liquid which could influence the mass transfer surrounding the particle (Scala 2007).

2.1.1.2 Sublimation of solid particles

This method uses a solid, which sublimes (typically naphthalene) to overcome

some of the issues with using a liquid impregnated into a particle. However, as noted by Prins (Prins et al. 1985), both mechanical attrition of spheres of naphthalene and the adsorption of naphthalene vapour by inert material could increase the apparent mass transfer rate.

Hsiung and Thodos (Hsiung and Thodos 1977) added spheres of naphthalene to a fluidised bed of styrene divinylbenzene copolymer particles (which are at the same size and density). They correlated their results with:

$$Sh = \left(0.04Re_{mf} + 2.12Re_{mf}^{0.41} + \frac{0.62}{Re_{mf}^{0.51}}\right)Sc^{\frac{1}{3}}$$

$$(0.3 < Re_{mf} < 2000) \quad (2.2)$$

where Re_{mf}, the Reynolds number at the minimum fluidization condition, is $Re_{mf} = \rho_g U_{mf} d/\mu_g$. U_{mf} is the minimum fluidising velocity. They found that the Sherwood number was independent of the total fluidization velocity, and only depended on the particle size and on the minimum fluidization velocity.

Prins (Prins et al. 1985) also added spheres of naphthalene to a fluidised bed, and investigated the effect of the relative sizes of the bed and naphthalene particles. Their correlation of Sherwood number is,

$$Sh = \frac{Sc^{\frac{1}{3}}(1-\varepsilon_{mf})}{\varepsilon_{mf}}\left\{\frac{\varepsilon_{mf}^3 Ar_p}{150(1-\varepsilon_{mf})^2}\right\}^{1-m}\left\{1.5 + 0.1\left(\frac{d}{d_p}\right)\right\}$$

$$(0.1 < Re_{mf} < 20 \text{ and } 1 \leq d_n/d_p < 200) \quad (2.3)$$

where $m = 0.35 + 0.29\left(\frac{d}{d_p}\right)^{-0.5}$, d is the diameter of reacting particle (m), d_p is the diameter of mean diameter of inert bed particles (m), ε_{mf} is the voidage at incipient fluidization and Ar_p is the Archimedes number for the fluidised inert

particles

$$Ar_p = (\rho_p - \rho_g)\,\rho_g g d_p^3/\mu_g^2 \tag{2.4}$$

where ρ_p is the density of inert particles.

Joulie et al. (R. Joulié and Rios 1993) (Joulie et al. 1986) (Régis Joulié, Barkat, and Rios 1997) used two kinds of inert particles, sand and zeolite, with different densities. Their correlation of Sherwood number is,

$$Sh = 0.165 Ar_p^{0.55} \left(\frac{d}{d_p}\right)^{0.81} \left(\frac{\rho_c}{\rho_p}\right)^{2.7} \left[\frac{U_{opt}-U_{mf}}{U_{mf}}\right]^{1.91} \tag{2.5}$$

where U_{opt} is the optimal gas velocity when maximum sublimation rate is reached; ρ_c is the density of reacting particles. Here, it should be noticed that in Equation (2.5), the Sherwood number is a function of the gas velocity in fluidised bed, which is different from Equation (2.3) in which the Sherwood number is just a function of U_{mf}.

2.1.1.3 Combustion of carbon particles

In this method, the rate of combustion of a particle is determined by measuring the mass change or rates of production of CO and CO_2. In most of cases, large carbon particles were used to ensure the reaction is fully mass transfer controlled (Hayhurst and Parmar 2002). Otherwise, kinetics and internal mass transfer must be carefully considered. This topic will be further discussed in *Section 6.1.2.2.4*.

Mass transfer is usually characterized with a Sherwood number (Sh) defined as $Sh = kg \cdot d/D$, where kg is the mass transfer coefficient, d is the diameter of

the reacting particle, and D is the diffusivity of the vapour in the gas flow. When dealing with non-equilmolar or dilute diffusion, the extra convective terms, which appear in e.g. the Stefan-Maxwell diffusion equation, mean the exact meaning of kg is unclear. Conventionally the kg is now interpreted to be a hypothetical kg that would be measured in for equimolar counter diffusion. Using this value of kg directly in a non-equimolar problem (e.g. the diffusion of oxygen to a surface against a flux of carbon monoxide) would be incorrect. Hayhurst and Parmar addressed this by translating the equimolar kg and Sh from into a boundary layer thickness, with this thickness then used as a boundary condition for a more correct description of diffusion.

It is now conventional to correct any non-equimolar measure of the rate of mass transfer, back to an equivalent equimolar value before it is reported (e.g. Hayhurst and Parmar (Hayhurst and Parmar 2002)). Fortunately in many cases this correction results in very little difference (Hayhurst and Parmar 2002). This topic will be further discussed in *Section 3.2*.

Other issues may arise when using the combustion of carbon to determine mass transfer rates include (1) accounting for the change in size of the particle as it combusts, depending on whether or not an ash layer forms. This can largely be overcome by using these initial rates, when very little of the carbon has combusted; (2) mechanical attrition or fragmentation of the carbon particles, which would reduce the size of the carbon particles, and the size change leads to the change of reaction rate; (3) the reaction between oxygen and char can produce CO and CO_2, with some

uncertainty in the product distribution (Hayhurst and Parmar 1998). To a first approximation, for a fixed Sherwood number, a particle producing entirely CO would appear to combustion twice as fast as one which was burning to CO_2 (Hayhurst 2000). Consequently, any attempt to measure the rate of mass transfer of oxygen in a combustion experiment must assume something about the ratio of CO to CO_2 produced. The CO/CO_2 ratio also has large influence on heat balance, since the enthalpy change of reaction of $C + \frac{1}{2}O_2 = CO$ and $C + O_2 = CO_2$ are $-110.6kJ/mol$ and $-395.5kJ/mol$ at 298.15K, respectively. Any combustion of CO within the boundary layer would influence the rate of oxygen transport, since it could change the temperature of the boundary layer, and influence the diffusivity of gases species in the boundary layer.

Avedesian and Davison (Avedesian and Davidson, 1973) used the carbon particle burn-out time to determine the Sherwood number and argued that, for Frossling's equation, the inert bed sand around the burning particle makes it harder for the particle to get O_2. They replaced the first term 2 for $Re_p = 0$ with $2\varepsilon_{mf}$. Where $Re_p = \rho_g U_p d_a/\mu_g$, and U_p is the gas velocity in the particulate phase. The expression of U_p given by Glicksman et al. (Glicksman et al. 1981).

$$U_p = U_{mf}(1-\varepsilon_b)\left\{1-\frac{\pi}{2}ln\left(1-\frac{6\varepsilon_b}{\pi}\right)\right\} \tag{2.6}$$

where ε_b is bubble fraction, and is given by Kunii et al. (Kunii and Levenspiel 1968).

La Nauze (LaNauze and Jung 1982) used single petroleum coke particles and the mass change of carbon was measured. La Nauze assumed that: 1) CO is oxidized

near the particle; 2) both the diffusive and convective terms in Frossling's equation should be modified by the mean voidage ε. For the diffusive term, gases can just diffuse in the void space in the fluidized bed, so diffusion becomes slower. For the convective term, the inert sand increases the relative velocity of gas around the burning carbon particle from U to U/ε. Here, the definition of ε is ambiguous: it is defined as the mean bed voidage, however, when U/U_{mf} = 2.8, it is equal to 0.46, and is numerically similar to the value of the voidage at incipient fluidisation ε_{mf}. Thus, no matter what the definition of mean voidage ε is, practically, the voidage at incipient fluidization (when the bed just becomes fluidised) ε_{mf} is used to modified the Frossling's style's expression of Sherwood number,

$$Sh = 2\varepsilon + 0.69\left(\frac{Re}{\varepsilon}\right)^{\frac{1}{2}} Sc^{\frac{1}{3}} \tag{2.7}$$

Where $Re = Ud/\nu$, which means Sherwood number should be a function of total superficial velocity U. However, La Nauze did not show any evidence for this.

La Nauze (La Nauze, Jung, and Kastl 1984) suggested another correlation derived from surface penetration theory,

$$Sh = 2\varepsilon_{mf} + \left[\frac{4\varepsilon_{mf} d\left(\frac{U_{mf}}{\varepsilon_{mf}} + U_b\right)}{\pi D}\right]^{\frac{1}{2}} \tag{2.8}$$

Here, ε_{mf} = 0.35 for metallic spheres, and ε_{mf} = 0.556 for fused alumina particles. In terms of structure, the appearance of mean rise velocity of the bubbles U_b in (2.8) means that the Sherwood number depends on, amongst other factors the overall fluidisation velocity and the bubble size.

Hayhurst (Hayhurst 2000) used single freely moving graphite spheres and coal char particles, and the concentration of CO and CO_2 in the outlet gas was measured. The results of CO/CO_2 ratio (Hayhurst 2000) were then used by Hayhurst and Parmar (Hayhurst and Parmar 2002) in the calculations of the Sherwood number. They (Hayhurst and Parmar 2002) used large spheres of graphite to ensure the combustion of the spheres is controlled by external mass transfer. They give,

$$Sh = 2\varepsilon_{mf} + 0.61 Re_p^{0.48} Sc^{1/3} \tag{2.9}$$

This expression of Sherwood number is valid only when the char particle is much larger than the inert sand in the fluidised bed. They do note however that for large enough reacting spheres,

$$Sh = 2\varepsilon_{mf} + 0.69 \left(\frac{Re_{mf}}{\varepsilon_{mf}}\right)^{1/2} Sc^{1/3} \tag{2.10}$$

Equation (2.10) is quite similar to Equation (2.7), only ε is changed into ε_{mf}, and is Re is changed into Re_{mf}, which means that Hayhurst and Parmar (Hayhurst 2000) believe that the Sherwood number is just a function of U_{mf}, rather than U.

Thus, for the most part correlations for the effective Sherwood number are largely empirical, though sometimes with some theoretical basis. The use of equations, which are based on the Frossling equation, (e.g. Equation (2.4), (2.9)) is attractive since under stagnant conditions the Sherwood number should be 2, but modified to account for the diffusion hindered by particles in the particulate phase. Since Sherwood number is based on molecular diffusivity, this correction factor is the ratio of the hindered to molecular diffusivity, hence the correction of ε_{mf} in e.g.

Equations (2.3), (2.8) (La Nauze, Jung, and Kastl 1984) (Prins et al. 1985). The use of ε_{mf} as the correction is itself somewhat uncertain since for diffusion through packing there should also be an effect of tortuosity, i.e. $D_{eff} = D\frac{\varepsilon}{\tau^2}$, thus there is an implicit assumption that $\frac{\varepsilon}{\tau^2} \sim \varepsilon_{mf}$. (Tortuosity, which is a property of curve being tortuous, will be fully discussed in *Section 3.2.1.3*). As noted by Hayhurst and Parmar (Hayhurst and Parmar 2002) and Scala (Scala 2007), there is experimental uncertainty in the Sherwood number at low Reynolds number and a value of ε_{mf} is not unreasonable. It also seems intuitively reasonable to use the modified convective term in Frossling equation to account for the velocity of the gas in the particulate phase surrounding the active particle (Hayhurst and Parmar 2002) (LaNauze and Jung 1982). The use of the particulate phase velocity here, which is not a function of the overall fluidising velocity, reflects the observation made by many authors (La Nauze, Jung, and Kastl 1984) (Hsiung and Thodos 1977) (Hayhurst and Parmar 1998) that the mass transfer rate seems only to depend on the U_{mf} and not U.

La Nauze et al.'s (La Nauze, Jung, and Kastl 1984) attempt to derive an expression based on surface renewal theory, which is also intellectually attractive, with diffusion through a stagnant medium, which is refreshed over a time scale related to bubble passage; however, mechanistically compelling, it is difficult to combine the rates at which gas and particles "refresh" the stagnant medium surrounding the particle. These use of potential flow theory to account for the motion of the gas and through the particulate phase by Coelho and Guedes de Carvalho (Coelho and Guedes De Carvalho 1988) also seems reasonable, but neglects the fact

that the particulate phase surrounding the particles will be periodically perturbed. Others (Hayhurst 2000) have tended to view the mass transfer process as being across a film of stagnant material, which also leads to expressions of the form suggested by Frossling. The actual picture of what is happening around a particle is likely to be complex and is probably a combination of these effects, with their relative importance governed by the time scales for diffusion through the medium surrounding the particle, the length scale over which the particulate phase can be considered relatively stagnant, and the frequency over which the material is perturbed by passing bubbles and other flow structures.

2.1.2 CO/CO_2 ratio from combustion of char

The ratio of CO/CO_2 in char combustion is a long studied topic. In addition to having an impact on the mass transfer, burning to CO_2 releases twice as much heat as burning to CO, meaning that a small change in CO/CO_2 can change the temperature at which a particle of char is combusting. It is also important to distinguish between the primary products of char combustion produced by,

$$C + O_2 = CO_2 \qquad (2.11(a))$$

$$2C + O_2 = 2CO \qquad (2.11(b))$$

at a carbon surface, with that measured some distance away from the carbon. This is because of intermediate reactions, which can oxidize CO into CO_2 once CO is in the gaseous phase. To complicate matters further (W. He et al. 2011), there may be changes in the ratio of CO to CO_2 from secondary reactions (e.g. the gasification of

carbon by the CO_2 produced from the primary reaction) as the gases diffuse through the pores. Once outside the particle, combustion of the CO in the gas phase usually proceeds via a free radical mechanism in which CO is attacked by an OH radical, which is then regenerated by other reaction. There are many mechanisms to explain the reactions: for instance, at high temperature (Hayhurst and Parmar 1998)

$$HO_2 + C_s = CO + OH \quad (2.12(a))$$

$$CO + OH = CO_2 + H \quad (2.12(b))$$

$$H + O_2 + M = HO_2 + M \quad (2.12(c))$$

where M is any gaseous molecule acting as a chaperon to remove the energy released when a molecule of HO_2 is formed.

In the context of combustion in a fluidised bed, this means that the rate of CO combustion depends on the amount of water vapour present (for example the kinetic expressions of (W. He et al. 2011) (Dryer and Glassman 1973)). In addition, the fluidised material around the char particle can quench radicals, suppressing the rate of combustion. The combustion of CO and other hydrocarbons has been observed in particulate phase of fluidised beds at temperatures higher than 1273 K; at lower temperatures the oxidation of these species is confined to bubbles and the freeboard regions. (Howard, Williams, and Fine 1973) (Hayhurst and Tucker 1990)

Hayhurst and Parmar (Hayhurst and Parmar 1998) took a pragmatic approach to measuring the CO/CO_2 ratio by assuming that any CO oxidised to CO_2 in the boundary layer was equivalent to that produced at the external surface of a particle, then measured the temperature of the combusting particle to infer the overall fraction

of carbon combusted to CO_2. This only relied on heat from CO being combusted within the mass transfer boundary layer being transmitted back to the combusting particle.

Attempts have been made to measure the primary CO/CO_2 ratio free from the influence of secondary reactions. Arthur (Arthur 1951) used the inhibitor $POCl_3$ to depress the oxidation of CO in a flow system. The carbon particles he used were artificial graphite and a kind of coal char. Arthur (Arthur 1951) noted that when the temperature is low, $POCl_3$ retards the combustion of the artificial graphite particles and assumed that the results would be similar for coal char particles. They found that when the temperature is between 753 K and 1173 K, the ratio of CO/CO_2 is just a function of temperature and increases exponentially with temperature. When the temperature was higher than 1173K, they found they ratio of CO to CO_2 increased with gas velocity, perhaps indicating some secondary combustion of the CO.

Tognotti et al (Tognotti, Longwell, and Sarofim 1991) used electrodynamic balance to obtain the CO/CO_2 ratio and found that it was related to partial pressure of oxygen; they explained this by suggesting that the reactions of oxidation of carbon into CO or CO_2 have different orders of reaction with respect to oxygen. In the context of mass transfer this might imply that the ratio of CO to CO_2 might be observed under mass transfer controlled combustion (where the oxygen concentration at the outer surface is zero) would be different to that under kinetic control. The low concentration of oxygen at the particle surface would lead to more CO, which as noted previously would lead to higher rates of combustion than would be expected if

the ratio of CO/CO_2 for kinetic controlled combustion applied.

Du et al. (Du et al. 1991) used soot particles. The found that the rate of CO formation is of fractional order with respect to the O_2 partial pressure, and is suggesting that CO and CO_2 could be produced at different active sites on the carbon. They also found that calcium and other impurities catalysed the rate of production of CO_2, resulting in a higher proportion of the carbon oxidising to CO_2 rather than CO.

Linjewile and Agarwal (Linjewile and Agarwal 1995) used petroleum coke spheres in (1) bubbling fluidised beds, (2) incipiently fluidised beds and (3) convective flow. The results showed that CO/CO_2 ratio in incipiently fluidized beds is higher than that in convective flow. In bubbling fluidized beds, the ratio of CO/CO_2 was not a function of the size of coke sphere within the range in the experiments and the average CO/CO_2 ratio was between 0.1 and 0.55, which is similar to the results from Prins (Prins 1987).

If it assumed that the rates of production of CO and CO_2 at the carbon surface have the same order with respect O_2, and then the expression for the ratio of CO/CO_2 would be expected to have the form,

$$[CO]/[CO_2] = A\, exp(-B/T_p) \qquad (2.13)$$

where A and B are constants, and T_p is the temperature of the burning carbon particle. Table 2.1 gives a summary of the various expressions given in the literature for $[CO]/[CO_2]$.

Table 2.1 Ratio of CO and CO_2 in products from carbon combustion as a function of temperature. The particle pressure is in atmosphere. (Adapted from Hayhurst (Hayhurst and Parmar 1998))

System	Reference	Material	Temperature (K)	Vol. % O_2	[CO]/[CO_2]
Flow system	Arthur (1951)	Coal char and graphite	730 - 1170	5-25	2510exp(-6240/T)
	Rossberg (1956)	Electrode carbon	790 - 1690	5-25	1860exp(-7200/T)
	Otterbein and Bonnetain (1968)	Vitreous carbon	770 - 920	3-15	25.7exp(-2000/ T)
Fluidised bed	Basu et al. (1976)	Anthracite coal	1123	21	0.38
	Prins (1987)	Graphite	985 - 1110	20	0.17 – 0.5
	Linjewile and Agarwal (1995)	Petroleum coke	890 - 1215	21	0.1 - 0.55
	Hayhurst et al. (1998)	Graphite	1080 - 1400	21	
Static system	Walker et al (1959)	Graphon	800 - 950	1-26	170exp(-2000/T)
Electrodynamic balance	Tognotti et al. (1990)	Spherocarb char	670 - 1670	5-100	50exp(-3040/T) $P_{O_2}^{0.21}$
Entrained flow reactor	Mitchell et al. (1990)	Coal char	1500 - 1800	6-12	8.5×10^{9}exp(-33200/T)
Thermo-gravimetric analyser	Du et al. (1991)	Soot	670 - 890	5-100	120exp(-3200/T)

From Table 2.1, it is clear that there is still some uncertainty in the primary

ratio of CO/CO_2 produced by a carbon particle, despite the best efforts of various authors to remove the effects of secondary reactions.

2.1.3 Theory of the calculation of ratio of CO/CO_2 at the outer surface of the char particles via Sherwood number

One way to infer the ratio of CO/CO_2 at the outer surface of char particles is *via* the Sherwood number (Hayhurst and Parmar 2002). For the combustion of a char particle under external mass transfer control, if CO were the only product of the char particle combustion, the rate of consumption of oxygen (R_{O_2}) would be half of the rate of carbon consumption (R_C),

$$R_C = 2R_{O_2} = 2\pi d^2 k_g C_{O_2} \tag{2.14}$$

where C_{O_2} is the molar concentration of oxygen in the particulate phase, d is the diameter of the carbon particle. If CO_2 were the only product of the char particle combustion, the rate of consumption of oxygen would be equal to the rate of consumption of carbon,

$$R_C = R_{O_2} \tag{2.15}$$

The rate of carbon consumption R_C is effectively measured directly by UEGO, and if the reacting char particle produces $(1-\eta)R_C$ mol/s of CO and ηR_C mol/s of CO_2,

$$\frac{R_{O_2}}{R_C} = \frac{1+\eta}{2} \tag{2.16}$$

The Sherwood number from experiments is calculated by,

$$Sh = \frac{k_g d}{D} = \frac{\frac{R_{O_2}^{Ini}}{A\Delta C} d}{D} \tag{2.17}$$

where $R_{O_2}^{Ini}$ is the initial reaction rate of the reaction, and here it is equal to the initial oxygen consumption rate; ΔC is the difference of oxygen concentration between the particulate phase and the outer surface of the particle at the start of the reaction. The definition of $R_{O_2}^{Ini}$ is discussed in Section 2.4.1. In addition, since it is assumed that the reactions are all mass transfer controlled, ΔC for both the char and Fe particles are equal to the oxygen concentration in the particulate phase ($C_{O_2}^{\infty}$). Given the same diameter of the char and Fe particles, it is assumed the Sherwood number of char particles Sh_C is equal to the Sherwood number of Fe particles Sh_{Fe}. This assumption allows calculating ratio of CO/CO_2 from the measurement of R_C^{Ini}. Since only R_C^{Ini}, rather than $R_{O_2}^{Ini}$ can be measured in the char experiments, so the measured Sherwood number Sh_C' is given as,

$$Sh_C' = \frac{\frac{R_C^{Ini}}{A\Delta C} d}{D} = Sh_C \frac{2}{1+\eta} \tag{2.18}$$

And the ratio of CO_2/(CO_2+CO) (η) is given as,

$$\eta = 2\frac{Sh_{Fe}}{Sh_C'} - 1 \tag{2.19}$$

There is a slight correction for cases of non-equimolar counter diffusion, including Fe oxidation and char combustion when CO_2 is not the only product. The Sherwood number measured in those cases is not equal to the Sherwood number for EMCD cases. However, the difference between effective Sherwood number and Sherwood number for EMCD cases is small (Hayhurst and Parmar 2002), so this difference is omitted.

It is also worth noting that the assumption of char and Fe particles having the same diameter may not be the real case in experiments, which could be due to the irregular shape or attrition of particles. If Fe particles were smaller than char particles, the outer surface area of Fe particles would be smaller than char particles, so $R_{Fe}^{Ini} < R_C^{Ini}$, and $Sh_{Fe} < Sh_C$. Since η is linear to Sh_{Fe}, so both Sh_{Fe} and η would be underestimated.

2.2 OBJECTIVE

To examine the interactions between chemical looping and mass transfer in the boundary layer, during char combustion an accurate picture is first needed for the mass transfer and effective CO/CO_2 ratio under non-looping conditions (inert) conditions. Here, measurements of the effective mass transfer coefficient and Sherwood number are made under combustion conditions, and are discussed in the context of other published work on mass transfer to burning particles. A measurement of the primary CO/CO_2 ratio is also made by comparing the rate of mass transfer during char combustion with that for oxidation of a metal oxide under comparable conditions (where there is no ambiguity about the reaction products).

2.3 EXPERIMENTAL

2.3.1 Fluidised bed reactors

Experiments to measure the rate of oxidation of both chars and of reduced

metal oxide particles were carried out in various fluidised bed systems: stainless steel reactor, alumina reactor, large quartz reactor and small quartz reactor. The inner diameters of those fluidised bed reactors are different, and the inner diameter could influence the flow patterns in a fluidised bed reactor, and make the reactor be a bubbling bed or a slugging bed. Thus, it is important to test the properties of different reactors, and then decide which one should be used.

2.3.1.1 Stainless steel reactor (i.d. 78 mm)

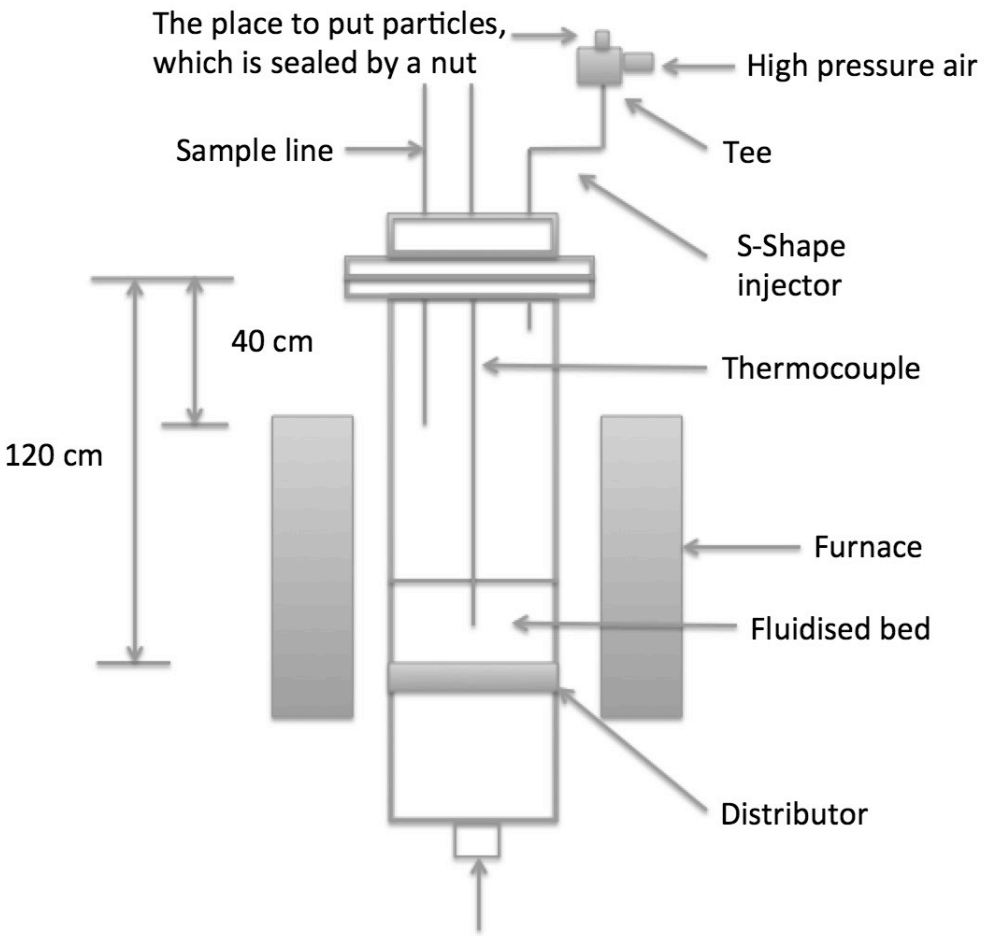

Figure 2.1 The diagram of the stainless steel reactor.

Figure 2.1 shows an externally heated fluidised bed reactor (i.d. 78 mm), which

is made from 316 stainless steel. The depth of the reactor, that is, the distance between the distributor and the lid, is 120 cm. The reactor had a perforated-plate distributor containing 37 holes, each 0.4 mm in diameter. The temperature of the bed was measured by a K-type thermocouple inserted from the top of the bed so that the tip was about 30 mm above the distributor, as shown in Figure 2.1. The reactor was set between 973 K and 1173 K and contained 1.2 L fluidising material (355 – 425 μm silica sand), fluidised with compressed air at a flow rate of 380-700 ml/s, as measured at 293 K and 1 bar. The superficial gas velocity, U, was ~0.3-0.5 m/s with U/U_{mf} ~4.5. A lid was added on the top of the reactor to avoid ambient air entering the reactor. Superwool® (Morgan Thermal Ceramics) was used as a gasket material. The off-gases left the top of the reactor *via* a 10 mm (i.d.) pipe, 300 mm long. The high flow rate in the effluent pipe made it difficult to add samples, especially when the diameter of char particle was smaller than 3 mm. So a sample injector was made (for 3mm or larger particles the materials could be added via the gas outlet). A stainless steel tube (i.d. 8 mm) was bend to S shape, and was put through a hole in the lid, which is shown in Figure 2.1. A Swagelok® tee was connected to the end of the stainless steel tube. One side of the tee was connected to compressed air at 3-bar gauge, via a solenoid valve. When adding the sample to the injector, the flow rate of the fluidised bed was lowered to 100-200 ml/s. Char particles were introduced into the injector via the remaining port on the T piece, which was then sealed by a nut. The fluidising gas flow was then returned to the flow rate required by the experiment, given previously. The char sample, stored in the S shape region of the injector, was

then blown into the reactor by opening solenoid valve. The solenoid valve was opened for less than 1 second. The compressed air through the injector had only minimal impact on the flows through the reactor, since pulse of the compressed air was short in comparison to the duration of the combustion experiments. If the diameter of the char particles was equal to or larger 3 mm, the injector was removed and the char particles were added directly through the hole in the lid. A sampling line was introduced into the reactor via the gas outlet. The sample line consisted of a 4 mm (i.d.) stainless steel tube, and was inserted 40 mm into the reactor. The sample gas passed through a stainless steel filter housing, which contained a piece of glass fibre filter paper, before entering the analyser. The filter paper was changed daily. The off-gas was extracted at a rate of ~ 4 L/min through the filter via a vacuum pump. The majority of the off-gas was vented to the extraction system (~3 L/min). The remainder of the off-gas was diverted to a fast responding oxygen analyser as described below in *Section 2.3.1.5*.

2.3.1.2 Alumina reactor (i.d. 18 mm)

Figure 2.2 shows an external-heated fluidised bed reactor (i.d. 18 mm), made from an alumina tube, and it was contained in a tubular furnace (Lenton). The distributor was made from irregular shaped recrystallised alumina (Boud Minerals and Polymers, 1.4 mm), held in place by Fortafix^{TM} cement. The thickness of the distributor is about 20 mm, and it was ~10 cm from the bottom of the tube. The distance between the bottom of the furnace and the bottom of the tube was ~ 5 cm.

The distance between sample line and distributor was ~50 cm. The temperature of the bed was measured by a K-type thermocouple, which was inserted from the top of the bed, so that the tip was about 10 mm above the distributor. The temperature of the reactor was set between 973 K and 1173 K. 9 ml silica sand (355-425 μm) was used as fluidising material, and was fluidised with compressed air at a flow rate of 34-60 ml/s, as measured at 293 K and 1 bar. The superficial gas velocity, U, was ~ 0.243 m/s with U/U_{mf} ~4.5.

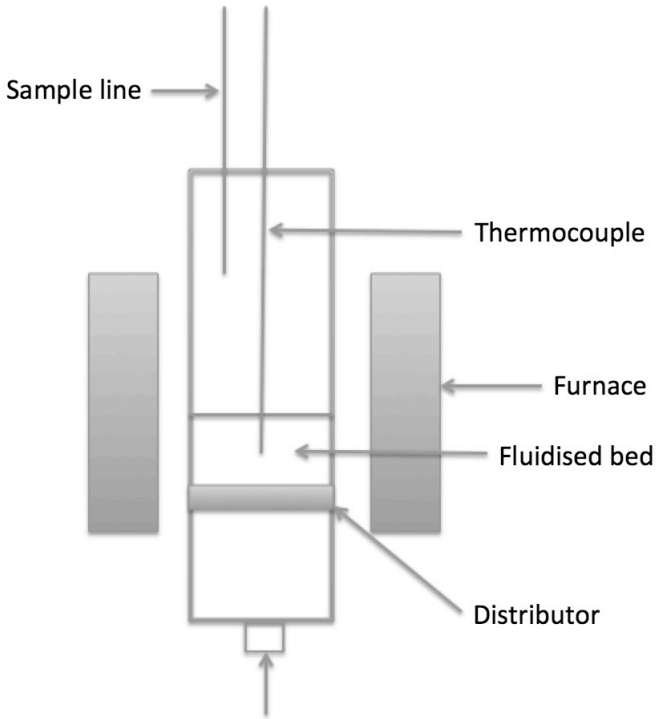

Figure 2.2 The diagram of the alumina reactor.

2.3.1.3 Large quartz reactor (i.d. 125 mm)

This fluidised bed reactor (i.d. 125 mm) was made of quartz, and was externally heated by an electric furnace. The reactor has two parts: the main body and a narrow

section on top of the main body. The function of the narrow section is to prevent the ingress of ambient air by increasing the velocity of gas leaving. A porous frit was used as the distributor and the pressure drop was about 0.3 bar. The height from the distributor to the top of the main body was 580 mm, and the height of the narrow section (i.d. 40 mm) was 190 mm. The distance between the distributor and the bottom of the reactor was 220 mm. The temperature of the bed was measured by a K-type thermocouple inserted from the top of the bed so that the tip was about 40 mm above the distributor. The temperature of the reactor was set between 973 K and 1173 K. 9 ml silica sand (355-425 μm) was used as fluidising material, and was fluidised with compressed air at a flow rate of ~3L/s, as measured at 293 K and 1 bar. The superficial gas velocity, U, was ~0.243 m/s with U/U_{mf}~4.5.

2.3.1.4 Small quartz reactor (i.d. 28 mm)

This fluidised bed reactor (i.d. 28 mm) is made of quartz, and is externally heated by an electric furnace. The height of the reactor is 350 mm from the distributor. A porous frit (4 mm thick, pore size +100, -160 μm) was used as the distributor. The length between the bottom of the reactor and the distributor was 110 mm. The temperature of the bed was measured by a K-type thermocouple inserted from the top of the bed so that the tip was about 30 mm above the distributor. The temperature of the reactor was set between 973 K and 1173 K and contained 13.4 ml sand. The sand (355-425 μm) is fluidised with compressed air at a flow rate of ~150 ml/s, as measured at 293 K and 1 bar. The superficial gas velocity, U, was ~0.243 m/s with

U/U_{mf} ~4.5. U_{mf} is calculated by the method of Wen and Yu (Wen and Yu 1966).

Table 2.2 made a comparison of set-ups of stainless steel reactor, alumina reactor, large quartz reactor and small quartz reactor.

Table 2.2. A comparison of set-ups of stainless steel reactor, alumina reactor, large quartz reactor and small quartz reactor.

	Stainless steel reactor	Alumina reactor	Small quartz reactor	Large quartz reactor
Reactor diameter	78 mm	18 mm	28 mm	125 mm
Fluidised bed height	62.8 mm	14.15mm	21.8mm	81.5 mm
Distance between distributor and the bottom of the reactor	80 mm	50 mm	110 mm	220 mm
Distributor	316 stainless steel pore size: 37 holes, 0.4 mm	Irregular shaped recrystallised alumina held in place by Fortafix™ cement.	A porous frit (4 mm thick, pore size +100, -160 μm)	A porous frit with pressure drop about 0.3 bar
Special features	A sealed lid with a pipe An S shape injector			A narrow section on top of the reactor

2.3.1.5 Fast Responding Gas Analysis system

The off-gas composition measured by a fast responding UEGO system (Granta Analytical, UK). Although nominally an oxygen analyser, the sensor is also sensitive to CO. As discussed by Saucedo (Saucedo-Martínez 2013) , the sensor effectively oxidizes any CO in the off-gas into CO_2 and measures the oxygen concentration if the gas sample was at chemical equilibrium. This makes the measurement of the carbon balance much easier, since from the point of view of calculating the rates of combustion, the off-gas oxygen concentration can be analysed as if all the carbon is combusted completely to CO_2. This eliminates the need to measure additionally either C_{CO} or C_{CO_2} to close the element balance and calculate the rate of carbon conversion.

2.3.2 Materials

The properties of the carbon and Fe_2O_3 particles are summarized below:

2.3.2.1 Char particles

Two kinds of carbon particles were used: (1) Lignite char particles, which are made of a low Hambach lignite coal (RWE Power AG, Germany). Since the new received Hambach lignite coal had a high content of moisture, it was put in an oven for 24 hours at 353 K to remove the moisture. After drying, the lignite coal lost 53 wt.% compared to the mass of coal before drying, which is consistent with the total content of moisture measured in the proximate analysis of 54.1 wt.%. The dried lignite coal was then put in a fluidised bed of sand at 1073 K in nitrogen to pyrolysis and to

produce lignite char. The char particles were sieved to three different size regimes: 600-850 μm, 1180-1400 μm and 1700-2000 μm. (2) Active carbon spheres. A kind of active carbon with commercial name of Matrix Carbon (Seachem Laboratories, Inc.) is used as well. It has the shape of a sphere. The carbon content of Matrix Carbon is around 93% - 95%, and it has a very low ash content about 5% - 7%. Its bulk density is about 980 kg/m^3. The char particles were measured by caliper and the particles with the diameter of 2.9 – 3.1 mm were chosen.

2.3.2.2 Fe_2O_3 particles

Fe_2O_3 particles were made by the mechanical mixing method. There are two recipes: 1) 50wt% Fe_2O_3 powder (supplier: VWR. UN Nr: 24189.468) and 50wt% Ciment Fondu (supplier: Kerneos Ltd); 2) pure Fe_2O_3 powder. The first proved to be better since pure Fe_2O_3 sintered, so some of Fe could not be oxidized. The first recipe was used in the stainless steel bed reactor experiments, and the second recipe was used in the alumina bed reactor experiments. The powder of each recipe was put in the bowl of kitchen mixer (supplier: kMix by Kenwood), and a small amount of DI water was sprayed on the powder. During each spray, the mixture was stirred in the kitchen mixer as the water was sprayed into the mixture. The kitchen mixer was used to remove lumps produced by the spray and make the mixing better (1 to 2 minutes for each time of stirring). The spraying – stirring process was repeated about ten times in total, and made the mass ratio of Fe_2O_3 powder to DI water around 100:12. Adding the correct amount of water was crucial, since too much water resulted in a mixture

with a consistency of a paste, rather than agglomerated particles as desired. After the DI water being well mixed with Fe_2O_3 powder, some agglomerated particles were put in a furnace at 1273 K for 6 hours. The sintered Fe_2O_3 particles were measured again by calliper and the particles with the diameter of 1.18-1.4 mm and 2.9 – 3.1 mm were chosen.

2.3.2.3 Fe particles

Fe particles were made using the calcined Fe_2O_3 particles in section 3.2.2. Calcined Fe_2O_3 particles were reduced by 1 L/min 5% H_2 in the 18 mm alumina tube reactor at 1173K for 6 hours. The mass loss of Fe particles were about 13% - 15% for 50wt% Fe_2O_3 and 50wt% Ciment Fondu, and 27% - 30% for pure Fe_2O_3, indicating that Fe_2O_3 in the particles was fully reduced to Fe. The Fe particles were preserved in a sealed container, full of N_2, to avoid oxidation.

2.3.2.4 Impregnated Fe and Cu particles

$Fe(NO_3)_3 \cdot 9H_2O$ and $Cu(NO_3)_2 \cdot 2.5H_2O$ were dissolved in DI water. The molar concentrations of both $Fe(NO_3)_3$ and $Cu(NO_3)_2$ solution are the same: 0.35 mol/100ml. The two kinds of solution were then dripped on 3 mm (diameter) Υ-Al_2O_3 particles, respectively, until the particles were fully impregnated. Each particle could absorb about 0.016 ml solution, which means a fully impregnated particle contains about 5.6×10^{-5} mol $Fe(NO_3)_3$ or $Cu(NO_3)_2$. The fully impregnated particles were then

calcinated in a furnace at 773K for 1 hour, and $Fe(NO_3)_3$ and $Cu(NO_3)_2$ transfer into Fe_2O_3 and CuO, respectively. The mass of a calcined particle is around 0.018 g, and each calcined particle contains about 0.00448 g Fe_2O_3 or CuO, respectively. Thus, the mass ratio of metal oxide in a calcinated particle is around 20%. Fe_2O_3 particles were then reduced in 5% H_2 at 1173K for 3 hours, and CuO particles were reduced to Cu in 5% H_2 at 773K for 3 hours. Fe particles and Cu particles were put in sealed containers. The reduction mass losses (including the moisture loss) of Fe_2O_3 and CuO particles were 10.5% and 11.9%, respectively.

2.4 RESULTS AND DISCUSSION

2.4.1 Definition of initial reaction rate

The definition of initial reaction rate is complicated because the heating up of the reacting particles in the reactor takes time, and during this process, materials are consumed by combustion. Figure 2.3 gives an example, the complete oxidation of the 3 mm Fe particles, to illustrate this issue.

In Figure 2.3, the vertical axis is the oxygen consumption rate. From 50s (the sample is introduced at 50 s) to 60s is the ‘heating up region’ in which the particle heats up, and the reaction rates increases. At 60s, the reaction rate reaches the maximum. However, about 10% Fe is consumed on average in each particle during this process. This means the Fe particles have already been partially consumed before the reaction region, 60s to 160s. The reaction rate gradually decreases in this region.

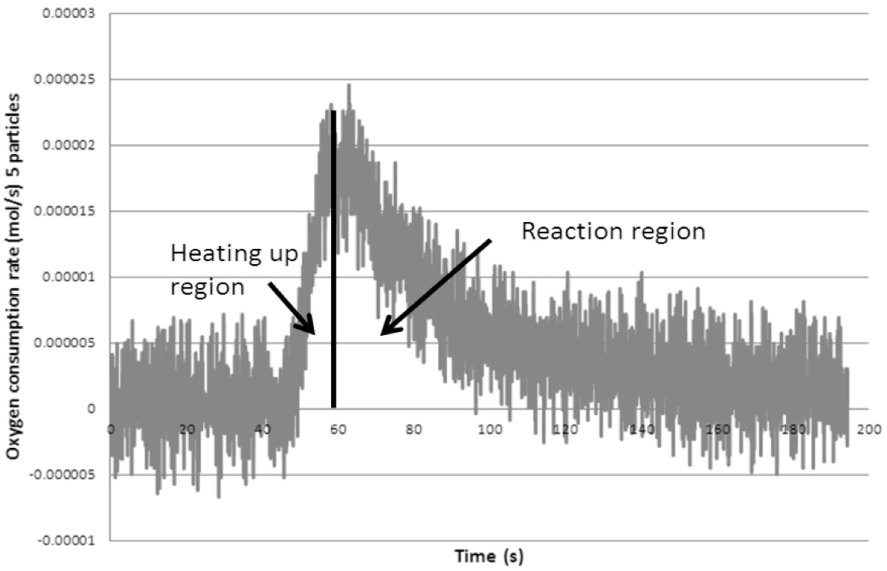

Figure 2.3 The oxidation of 5 Fe particles (3 mm) in the stainless steel reactor of 355-425 μm silica sand at 1173K with U/U_{mf} =4.5.

The consumptions of reacting particles in heating up region vary with type of particle, flow rates and temperatures in the reactor. In this research, the molar conversion was around 5%-10%, which is relatively small. Thus, the start of the reaction region is considered as the start of the reaction.

2.4.2 Effects of fluidised beds

The sizes of the fluidised bed could influence the rates of mass transfer, for example, because of the effects of walls and differing flow patterns. Table 2.3 shows the different reactor configurations used, with the corresponding rates of combustion shown in Figure 2.4. In all cases the ratio of unfluidised bed depth to diameter was fixed at ~0.8, except for the large quartz reactor where the ratio is 0.65, which is taken

from Saucedo (Saucedo-Martínez 2013) for comparison.

Table 2.3 A comparison of set ups of stainless steel reactor, alumina reactor, small quartz reactor, and large quartz reactor.

	Stainless steel reactor	Alumina reactor	Small quartz reactor	Large quartz reactor
Sand type	Silica sand	Silica sand	Silica sand	Silica sand
Sand size	355 - 425 μm	355 - 425 μm	355 - 425 μm	355 - 425 μm
Sand volume	300 ml	3.6 ml or 6 ml	13.4 ml	1000 ml
Reactor diameter	78 mm	18 mm	28 mm	125 mm
Bed height (unfluidised)	62.8 mm	14.15mm	21.8mm	81.5 mm
Bed height (unfluidised) /reactor diameter	0.8	0.78 or 1.3	0.79	0.65
U/U_{mf}	4.5	4.5	4.5	4.5
Char particle size	1180-1400 μm	1180-1400 μm	1180-1400 μm	1180-1400 μm
Mass of char particles in each batch (g)	~0.01 g	~0.0035 g	~0.05 g	~0.25 g

The initial rates of char combustion for the reactors in Table 2.3 are shown in Figure 2.4. The initial reaction rates in both the alumina reactor and the small quartz reactor are faster than the one in the stainless steel reactor. The rates in the 125 mm (i.d.) quartz reactor were almost the same as the stainless steel reactor. The rates from Saucedo (Saucedo-Martínez 2013) (large quartz reactor) are also shown in Figure 2.4 for comparison. In the small alumina reactor, for the 3.6 ml and 6 ml experiments, the reaction rates are almost same, which indicates that the volume of fluidising materials

has little influence on the reaction rate.

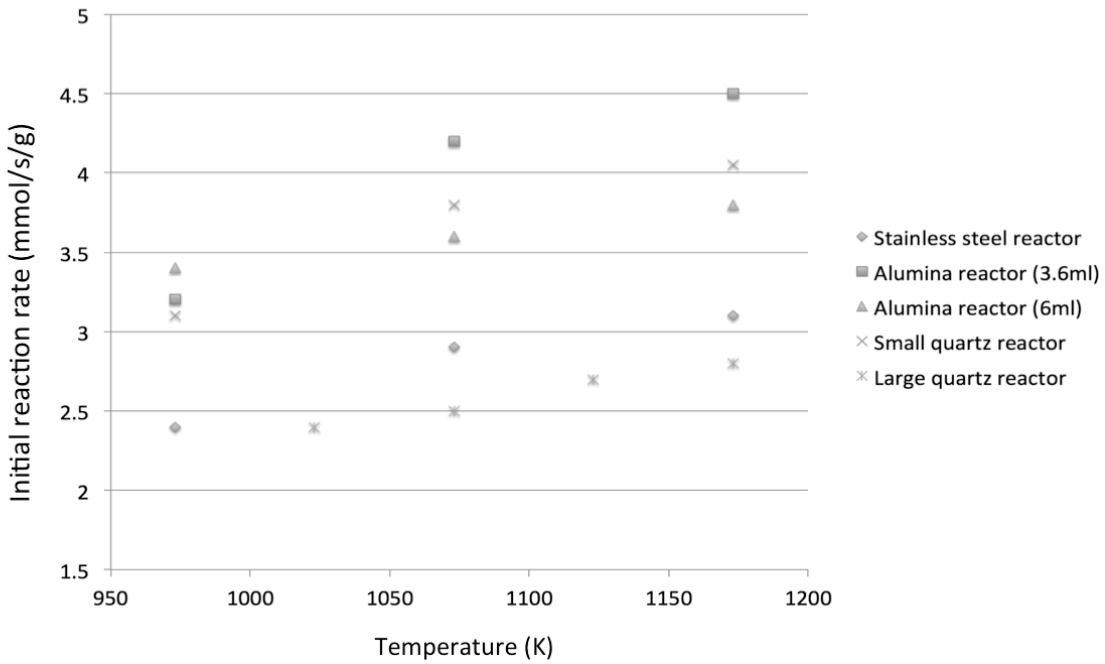

Figure 2.4 The comparison of initial reaction rate of 1180-1400 μm char combustion in stainless steel reactor, alumina reactor, large quartz reactor and small quartz reactor using 355-425 μm silicon sand at 973K, 1073K and 1173K

These results suggest that the rates of reaction increase as the diameter of the reactor decreases. The small reactors are more likely to be close to slugging bed reactors rather than bubbling bed reactors. (The factors determine whether a bed is slugging or bubbling will be discussed in *Section 2.4.5*) Since most of the fluidised beds employed in industries are bubbling beds, the small reactors are not representative. Thus, in the following sections, only the stainless steel reactor is used.

2.4.3 Effects of carbon particle size and temperature

Figure 2.5 shows that the carbon particle size also influences the reaction rate.

The smaller the carbon particle is, the larger the specific external surface area it has. Thus, at the same temperature, the larger specific external surface area leads to faster reaction rate per particle.

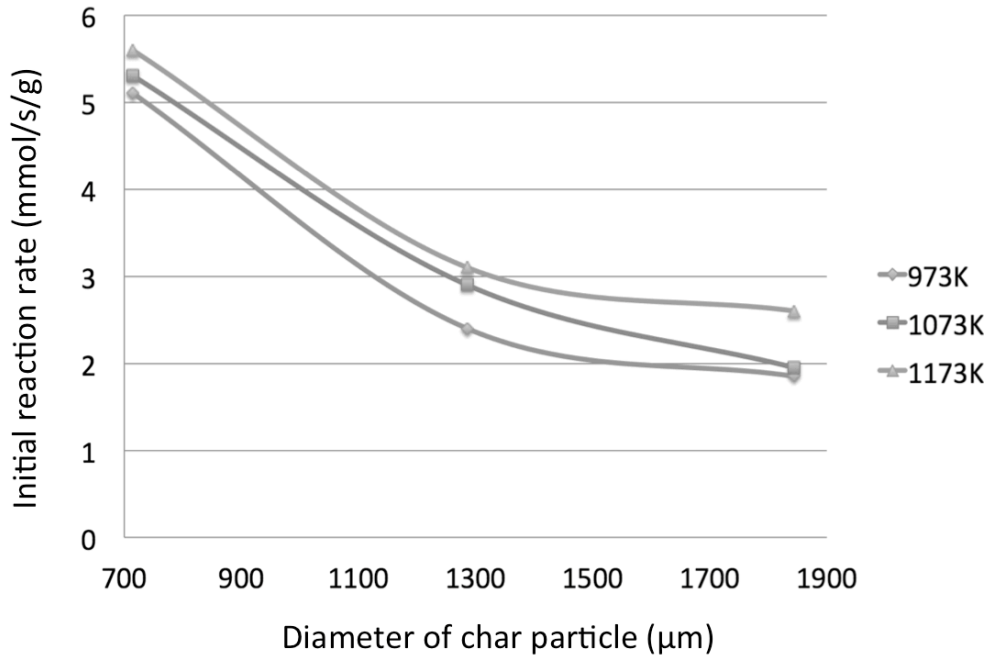

Figure 2.5 The initial reaction rate (mmol/s/g) versus the mean diameter of char particles (600 – 850 μm, 1180-1400 μm, 1700 – 2000 μm), at 973K, 1073K and 1173K in the stainless steel bed (355-425 μm silicon sand, U/U_{mf} = 4.5).

Figure 2.5 plots the initial reaction rate (mmol/s/g) versus the mean diameter of char particles (600 – 850 μm, 1180-1400 μm, 1700 – 2000 μm), at 973K, 1073K and 1173K in the stainless steel bed (355-425 μm silicon sand, U/U_{mf} = 4.5). It shows that the rate per gram of char particle goes down, but this still means the rate per particle could be going up. In addition, the higher the temperature is, the faster the reaction is for the particles of the same size, though the difference is not large.

2.4.4 Effects of superficial fluidising velocity

In principle both superficial fluidising velocity (U) and minimum fluidising velocity (U_{mf}) influence the rate of mass transfer, though most of studies in the literature suggest only U_{mf} is important (Salatino, Scala, and Chirone 1998). Thus, the importance of superficial fluidising velocity (U) was tested here.

In the experiment, U_{mf} was fixed, and U/U_{mf} is set to be 2.5, 4.5 and 6.5. The expression of U_{mf} is given by Wen and Yu (Wen and Yu 1966),

$$U_{mf} = \frac{(\rho_p - \rho_g) g d_p^2}{1650 \mu_g} \tag{2.20}$$

So fixing U_{mf} is equivalent to fixing the silica sand size, which is 355 – 425 μm. The reactions were run in the stainless steel reactor, the size of char particles was 2.9-3.1 mm, and the bed temperature was 1073K. All experiments have 5 repeats to ensure the accuracy. The results are shown in Table 2.4.

Table 2.4 The initial reaction rates (mmol/s/g) of 2.9-3.1 mm char particles when U/U_{mf}= 2.5, 4.5 and 6.5 at 1073K.

U/U_{mf}	2.5	4.5	6.5
Initial reaction rate (mmol/s/g)	0.64±0.1	0.80±0.12	0.96±0.17

Table 2.4 shows that the initial reaction rates increase with the increase of U, but the increase is small. Considering of errors in the measurements, it is hard to say that the superficial velocity U has a strong influence on the reaction rates.

2.4.5 Effect of reactor on mass transfer rates

The results in *Section 2.4.2* show that when the ratios of bed depth (unfluidised) / bed diameter are same, the reaction rates increase as: alumina reactor > small quartz reactor > stainless steel reactor > large quartz reactor, that is, the reaction rate increases when the reactor diameter decreases. This can be explained by the difference between the bubbling bed and the slugging bed.

In the bubbling fluidised bed, bubbles are first generated at the distributor, then grow and coalesce with each other as they rise, which makes the average diameter of the bubbles increase with height. When the diameter of bubbles is as large as the inner diameter of the fluidised bed, the diameter of bubbles stops growing, and the bubbling bed transitions to slugging bed. (Constantineau et al. 2007)

Three conditions can be used to judge if the fluidised bed is a slugging bed. In fact, just using one condition should be enough to make the judgment. However, different conditions could give different conclusions, so it is helpful to check all three conditions, and comprehensively consider with every conclusion.

1) Baeyens and Geldart (Baeyens and Geldart 1974) suggested that the height of fluidised sand H must be larger than a limiting bed height H_L, where coalescence complete and a stable slug spacing achieved H_L.

$$H_L = 1.3D_b^{0.175} \tag{2.21}$$

The height of fluidised sand H is important since only in deeper beds, can the bubbles fully grow and coalesce to produce slugging. In shallower beds, bubbles would leave the bed before their diameter reaching the inner diameter of the fluidised

bed reactor D_b.

2) Stewart and Davidson (Stewart and Davidson 1967) suggested that the total superficial velocity U must be larger than the slugging velocity U_{ms},

$$U_{ms} = U_{mf} + 0.07\sqrt{gD_b} \tag{2.22}$$

Baeyens and Geldart (Baeyens and Geldart 1974) suggested that the correlation above is valid for deep beds ($H_{mf} > H_L$). For shallower beds, the following correlation should be used,

$$U_{ms} = U_{mf} + 0.07\sqrt{gD_b} + 0.16\left(H_L - H_{mf}\right)^2 \tag{2.23}$$

3) The maximum stable bubble size should be no smaller than the order of the inner diameter of the fluidised bed reactor D_b.(Constantineau et al. 2007)

Thus, the above three conditions can be used to judge if the of stainless steel reactor, alumina reactor and small quartz reactor are bubbling or slugging fluidised bed under the condition of U/U_{mf} = 4.5 and the size of sand at 355 – 425 μm. The correlation of mean diameter of a bubble is given by Darton (Darton 1977)

$$d_b = \frac{0.3\left(U-U_{mf}\right)^{0.4}}{g^{0.2}H}\left\{\left(H + 4\sqrt{A_0}\right)^{1.8} - \left(4\sqrt{A_0}\right)^{1.8}\right\} \tag{2.24}$$

Where A_0 is the distributor area per orifice. The correlation of the velocity of bubbles U_b and the height of fluidised sand H are given by Davidson and Harrison (J. F. Davidson and Harrison 1963),

$$U_b = 0.711\sqrt{gd_b} \tag{2.25}$$

$$\frac{H-H_{mf}}{H} = \frac{U-U_{mf}}{U_b} \tag{2.26}$$

Where H_{mf} is the depth of fluidised bed at incipient fluidisation. The above three

equations should be solved simultaneously, and the results are shown in Table 2.5.

Table 2.5 Judgment of bubbling or slugging bed of stainless steel reactor, alumina reactor and small quartz reactor

	Stainless steel reactor	Alumina reactor	Small quartz reactor
A_0 (distributor area per orifice)	1.26×10^{-7} m^2	1.33×10^{-8} m^2	1.33×10^{-8} m^2
H (fluidised bed height, 1173K)	0.141 m	0.0665 m	0.075 m
H_{mf} (Unfluidisd bed height)	0.063 m	0.01415 m	0.0218
H_L (limiting bed height)	0.83 m	0.64 m	0.7 m
U/U_{mf}	4.5	4.5	4.5
U_{mf} (973K)	0.0557 m/s	0.0557 m/s	0.0557 m/s
U_{mf} (1073K)	0.0526 m/s	0.0526 m/s	0.0526 m/s
U_{mf} (1173K)	0.0498 m/s	0.0498 m/s	0.0498 m/s
U (1173K)	0.2241 m/s	0.2241 m/s	0.2241 m/s
U_{ms}(slugging velocity, 1173K)	0.205 m/s	0.142 m/s	0.16 m/s
d_b (mean diameter of bubbles)	0.02 m	0.01 m	0.012 m
Sand volume	300 ml	3.6 ml	13.4 ml
Sand type	Silica sand	Silica sand	Silica sand
Sand size	355 - 425 µm	355 - 425 µm	355 - 425 µm
Condition 1	No. $H < H_L$	No. $H < H_L$	No. $H < H_L$
Condition 2	In the transition regime. $U \approx U_{ms}$	Yes. $U > U_{ms}$	Yes. $U > U_{ms}$
Condition 3	D_b/d_b = 3.9	D_b/d_b =1.8	D_b/d_b = 2.3

Table 2.5 shows that: 1) for condition 1, the bed height of all three fluidised bed is much shorter than the limiting bed height; 2) for condition 2, the stainless steel reactor is in the transient regime, since its total superficial velocity U is similar to the slugging velocity U_{ms}. For alumina reactor and small quartz reactor, it is clear that the total superficial velocity is larger than the slugging velocity U_{ms}; 3) for condition 3, ratio of D_b/d_b: stainless steel reactor > small quartz reactor > alumina reactor, which shows the trend that alumina reactor is the closest to slugging and the stainless steel reactor the furthest from slugging.

Thus, the stainless steel reactor is a bubbling bed, and both small quartz and alumina reactor are slugging beds, which indicates that the more slugging the reactor is, the faster the initial reaction rate it is. This can be explained by the changes to the mass transfer coefficient caused by the different flow pattern experienced in the small reactor.

2.4.6 Apparent activation energy and shrinking core model prediction to support the mass transfer limited assumption

In this chapter, it is assumed that the combustion of Fe_2O_3 or char particles with diameter of 3 mm in the fluidised bed is mass transfer limited, which can greatly simplify calculations. Confirmation of this assumption is obtained here by: 1) apparent activation energy; 2) shrinking core model prediction.

2.4.6.1 Apparent activation energy

According to the Arrhenius equation, the reaction rate constant k is given as,

$$k = Ae^{-\frac{E}{RT}} \tag{2.27}$$

where A is the frequency factor of the reaction, E is the activation energy, and R is the universal gas constant. The reaction rate (R_{arb}) for an arbitrary reaction $A + B \rightarrow C$ always has the form,

$$R_{arb} = kC_A^m C_B^n \tag{2.28}$$

Where C_A and C_B are the molar concentrations of the substances A and B, respectively. So

$$\ln(R_{arb}) = -\frac{E}{RT} + \ln(AC_A^m C_B^n) \tag{2.29}$$

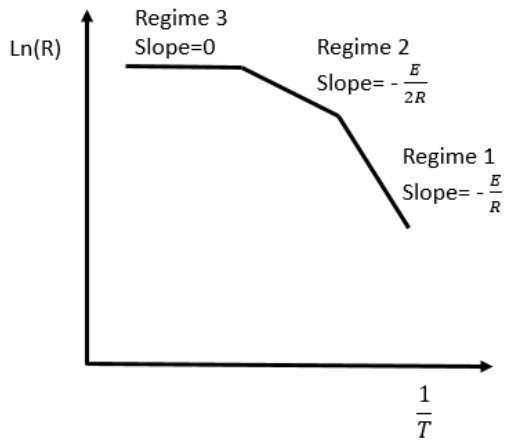

Figure 2.6 The summary of char combustion regimes.

The char combustion progress is summarized by Figure 2.6: regimes 1, 2 and 3 represent the kinetic control, transient regime, and mass transfer control, respectively. For a large char particle, initially it is in regime 3. As the reaction progresses, the reacting particle shrinks. When the particle becomes small enough, oxygen can penetrate through the particle and the reaction transfers from regime 3 to regime 1.

Thus, it is important to know the activation energy both at the start of the reaction and during the reaction to see if there is regime transfer.

Table 2.6 The apparent activation energy for both Fe and char particles (initial and 50% conversion) from 973K to 1173K (stainless steel reactor, 355 – 425 m silica sand, U/U_{mf} = 4.5).

	Fe particles	Char particles
Activation energy (Initial)	2.9kJ	10.5kJ
Activation energy (50% conversion)	5.18kJ	25kJ

Table 2.6 shows the apparent activation energy for both Fe and char particles (initial and 50% conversion) from 973K to 1173K (stainless steel reactor, 355 – 425 m silica sand, U/U_{mf} = 4.5). For each species, 5 data points (973K, 1023K, 1073K, 1123K, 1173K) were taken. Here, 'initial' is defined as at the start of 'reaction region', and 50% conversion is defined as 50% conversion since start of the 'reaction region'. The real conversions are 5% to 15% larger than 0 and 50% since the conversions in the heating up region should be considered. The activation energies (initial) of both Fe (2.9kJ) and char particles (10.5kJ) are very low, which supports the hypothesis of mass transfer control. As the reactions reaches 50% conversion, the activation energy of both Fe and char particles doubled, 5.18 kJ and 25 kJ, respectively, perhaps indicating a slight lessening of external mass transfer restrictions. However, the activation energy at 50% conversion is still relatively small, which means that the reaction is still mass transfer controlled.

2.4.6.2 The shrinking core model

Both char and Fe particles are porous. At lower temperatures, the reaction rate is low, so oxygen can diffuse throughout the particle and the particle burns uniformly. At higher temperatures, the reaction rate is high, and oxygen reacts near the surface of the particle, and cannot penetrate into the centre. In this case, the reaction occurs at a narrow front, giving rise to a shrinking core. For char ash is likely to be lost, giving rise to a shrinking particle. However, for Fe particles, iron oxide layer form during the oxidation process, and these layers hinder the transport of oxygen to the shrinking core.

2.4.6.3 The shrinking core model for Fe particles

There are several kinds of iron oxides: wustite ($Fe_{.947}O$), magnetite (Fe_3O_4) and hematite (Fe_2O_3), which makes the oxidation process quite complicated. Thus, it is assumed that the oxidation reaction is step-by-step and global from surface to core. That is, firstly, Fe changes into $Fe_{.947}O$ from surface to core, and then similar process happens in the oxidations of $Fe_{.947}O$ and Fe_3O_4. In the experiment, the 'oxidation status' is decided by measuring the total amounts of O_2 consumption.

Another two assumptions are made: 1) at high temperatures (1073K – 1173K), the reaction is mass transfer limited, which means that the oxygen concentration in at the unreacted core is zero; 2) the diffusion is pseudo-steady state. A diagram of a reacting Fe particle at high temperature is shown in Figure 2.7.

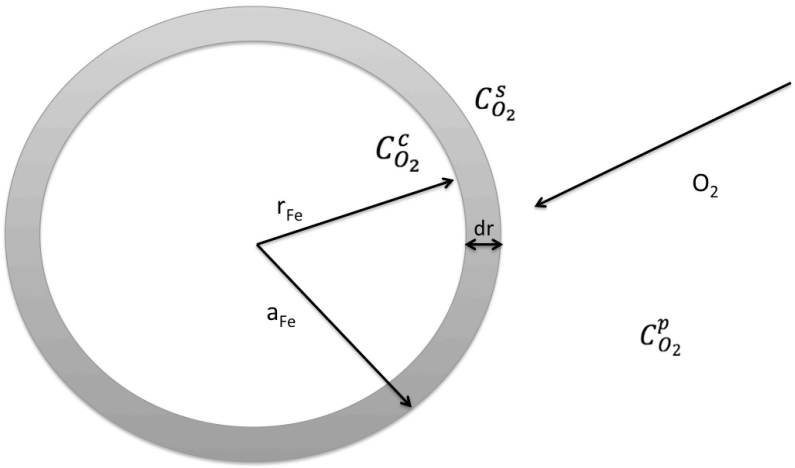

Figure 2.7 The diagram of a burning Fe particle at high temperatures (1073K – 1173K).

In Figure 2.7, a_{Fe} is the initial radius of the Fe particle, r_{Fe} is radius of unreacted core, and $dr_{Fe} = a_{Fe} - r_{Fe}$ is the thickness of the outer layer (Fe_2O_3); $C_{O_2}^p, C_{O_2}^s \; and \; C_{O_2}^c$ are the oxygen concentration (mol/m^3) in the particulate phase, on surface of the outer layer and in the unreacted Fe core, respectively.

Fick's law gives the rate of oxygen diffusion Q_{O_2} (mol/s) through the outer layer as

$$\frac{Q_{O_2}}{4\pi r^2} = -De_{Fe}\frac{dC_{O_2}}{dr_{Fe}} \tag{2.30}$$

where De^{Fe} is the diffusivity of O_2 in the outer layer, and C_{O_2} is the molar concentration of oxygen. Integrating from a_{Fe} to r_{Fe}, gives,

$$Q_{O_2} = \frac{4\pi De_{Fe}(C_{O_2}^s - C_{O_2}^c)}{\frac{1}{r_{Fe}} - \frac{1}{a_{Fe}}} = \alpha(C_{O_2}^s - C_{O_2}^c) \tag{2.31}$$

The rate of oxygen transport to the surface must be equal to the rate through the outer layer,

$$-4\pi a_{Fe}^2 kg\left(C_{O_2}^s - C_{O_2}^p\right) = \alpha(C_{O_2}^s - C_{O_2}^c) \tag{2.32}$$

Assuming oxidation is controlled by mass transfer, $C_{O_2}^c$=0, giving $C_{O_2}^s = \frac{4\pi a_{Fe}^2 kg C_{O_2}^p}{4\pi a_{Fe}^2 kg+\alpha}$. The rate of oxygen consumption is then

$$R_{Fe} = \frac{4\pi a_{Fe}^2 C_{O_2}^p}{\frac{1}{kg}+\frac{a_{Fe}}{De_{Fe}}\left(\frac{a_{Fe}}{r_{Fe}}-1\right)} = \frac{d\left(\frac{3}{4}\rho_{m,Fe}\frac{4}{3}\pi r_{Fe}^3\right)}{dt} \quad (2.33)$$

where $\rho_{m,Fe}$ is the molar density of unreacted Fe core. The fraction of the particle consumed during the initial transient (i.e. owing to heating etc.) is γ, so the radius of unreacted Fe particle at the start of the reaction region is taken as $r_{Fe}^0 = a_{Fe}(1-\gamma)^{\frac{1}{3}}$.

Integrating Equation (2.33) from r_{Fe} at a time t as

$$\frac{{r_{Fe}}^3}{3}\left(\frac{1}{kg}-\frac{a_{Fe}}{De_{Fe}}\right)+\frac{{r_{Fe}}^2 a_{Fe}^2}{2De_{Fe}}-\frac{{r_{Fe}^0}^3}{3kg}+\frac{{r_{Fe}^0}^3 a_{Fe}}{3De_{Fe}}-\frac{{r_{Fe}^0}^2 a_{Fe}^2}{2De_{Fe}} = -\frac{a_{Fe}^2 C_{O_2}^p}{\frac{3}{4}\rho_{m,Fe}}t \quad (2.34)$$

If the mass transfer limit control hypothesis holds, Equation (2.34) should fit experimental data in Figure 2.3. The average diameter of Fe particles is $a_{Fe} = 0.00142\ m$, and the average mass of each Fe particle is $m_{Fe} = 0.0211$ g. The mass ratio of Fe in the Fe particle is $\eta_{Fe} = 112/160 \times 0.5/(0.5 + 112/160 \times 0.5) = 41\%$. So the average molar density of Fe particle is $\rho_{m,Fe} = \frac{m_{Fe}\eta_{Fe}}{\frac{4}{3}\pi a_{Fe}^3 \times 56} = 12832\ mol/m^3$, $C_{O_2}^p$ is C_{O_2} in the particulate phase, which is taken from the experimental data. The problem is fully specified by fixing two parameter; here $C_{O_2}^s$ and De_{Fe} are fitted by least square method of Matlab. The fitting results are shown in Figure 2.8.

Figure 2.8 plots of reaction rate of the 3 mm Fe particle against time. The reaction rate of the model generally fits the experimental data well with $C_{O_2}^s$ is 0.39 mol/m^3, which means the O_2 percentage at the outer surface is 3.7%. The diffusivity of O_2 in the outer layer (De_{Fe}) is 4.93×10^{-5} m^2/s, which is about 0.275 of the

diffusivity of O_2 in air at 1123K, which can be explained by the porosity and tortuosity of the outer oxidised layer. The value of kg is 0.0775 giving a Sherwood number equal to 1.25.

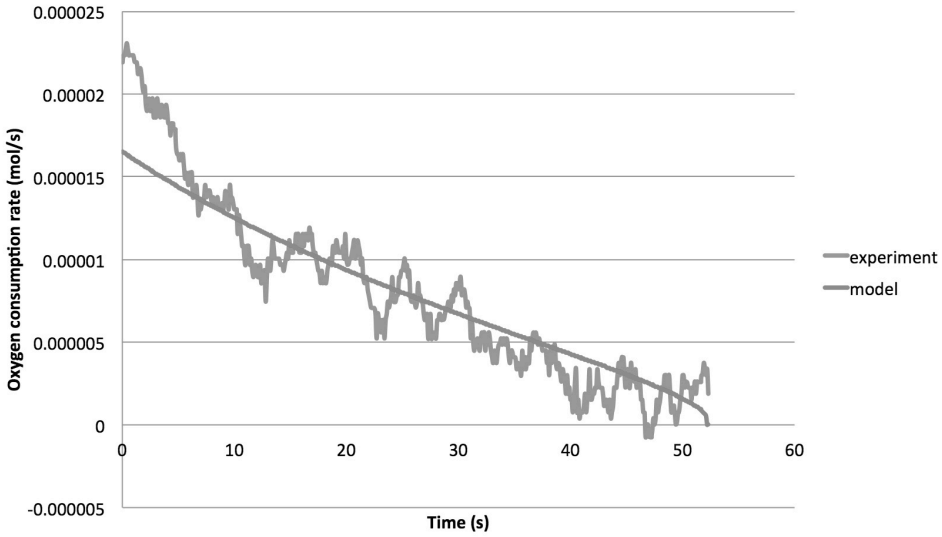

Figure 2.8 Fitted oxygen consumption rate for an Fe particle (3mm) in a fluidised bed of 355-425 μm silica sand at 1123K with U/U_{mf}=4.5 for experimental data and model

2.4.6.4 The shrinking core model for char particles

The combustion of char produces both CO and CO_2,

$$C + O_2 = CO_2 \qquad (2.11(a))$$

$$2C + O_2 = 2CO \qquad (2.11(b))$$

The fraction of carbon reacting to form CO_2 at the outer surface of char particle is set to be η. Assuming combustion is first order in oxygen and that Fick's law is approximately correct, the balance of oxygen in the shell of width dr is,

$$0 = -\frac{\partial}{\partial r}\left(-4\pi r_c^2 D_e \frac{\partial C_{O_2}}{\partial r}\right) dr - kC_{O_2} 4\pi r^2 dr \qquad (2.35)$$

Giving

$$C_{O_2} = \frac{a_c}{r}\frac{\sinh(mr)}{\sinh(ma_c)}C_{O_2}^s \tag{2.36}$$

where a_c is the initial radius of the char particle, $D_e = D\varepsilon/\tau^2$ is the effective diffusivity of oxygen, k is the reaction rate constant for the carbon combustion (the product is a mixture of CO and CO_2), and $m = \sqrt{\frac{k}{D_e}}$. Defining Thiele modulus ϕ as (Harper 2013),

$$\phi = ma_c = a_c\sqrt{\frac{k}{D_e}} \tag{2.37}$$

The rate of oxygen consumption per char particle (R_c) is,

$$R_c = 4\pi a_c^2 D_e m\left[\coth(\phi) - \frac{1}{\phi}\right]C_{O_2}^s \tag{2.38}$$

An effective volumetric rate constant Λk can be defined as $R_c = \Lambda k V C_{O_2}^s$, where V is the volume of the reacting particle and the effectiveness factor is (Harper 2013)

$$\Lambda = \frac{R_c}{\frac{4}{3}\pi a_c^3 k C_{O_2}^s} = \frac{3}{\phi}\left[\coth(\phi) - \frac{1}{\phi}\right] \tag{2.39}$$

The effectiveness factor versus Thiele modulus is plotted in Figure 2.10: when ϕ is low, $\Lambda = 1$, the rate is controlled by kinetics. When ϕ is high, $\Lambda \approx \frac{3}{\Phi}$, the reaction is mass transfer influenced and occurs at a sharp front (Harper 2013).

For high Λ the rate of oxygen consumption per char particle is,

$$R_c = \frac{VC_{O_2}}{\frac{V}{Ak_g} + \frac{\Phi}{3k}} \tag{2.40}$$

Since the product is a mixture of CO and CO_2, the expression for rate of carbon consumption also must take into account the ratio of CO_2/(CO+CO_2) (η),

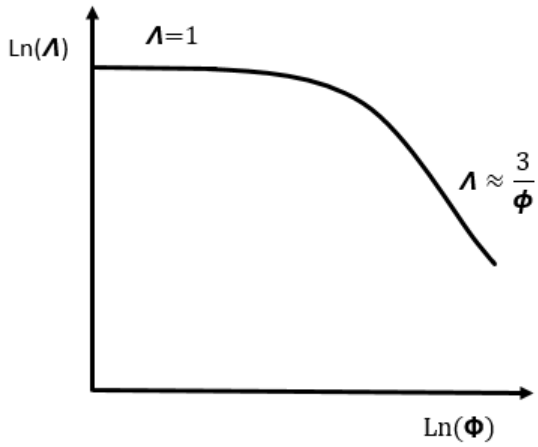

Figure 2.10 Effectiveness factor versus Thiele modulus.

$$\frac{R_c(1+\eta)}{2} = -\frac{d(\rho_{m,c}V)}{dt} \tag{2.41}$$

where $\rho_{m,c}$ is the molar density of the carbon particle. The rate of change of radius can then be found from

$$-\frac{C_{O_2}}{\frac{\rho_{m,c}}{2}(1+\eta)} = \left[\frac{1}{k_g} + \frac{\Phi}{a_c k}\right]\frac{dr_c}{dt} \tag{2.42}$$

Integrating from a_c to r_c, gives,

$$-\frac{C_{O_2}}{\frac{\rho_{m,c}}{2}(1+\eta)}\int_0^t dt = \int_{a_c}^{r_c}\left(\frac{1}{k_g} + \frac{\Phi}{a_c k}\right)dr_c \tag{2.43}$$

Substituting $k_g = \frac{ShD}{2a_c}$ into Equation (2.43) gives,

$$-\frac{C_{O_2}t}{\frac{\rho_{m,c}}{2}(1+\eta)} = \frac{r_c^2 - a_c^2}{ShD} + \frac{r_c - a_c}{\sqrt{kD_e}} \tag{2.44}$$

When the reaction is mass transfer limited, k is very large, and the term $\frac{r_c - a_c}{\sqrt{kD_e}} \approx 0$. So

$$r_c = \sqrt{-\frac{ShDC_{O_2}t}{\frac{\rho_{m,c}}{2}(1+\eta)} + a_c^2} \tag{2.45}$$

Here, the char combustion is assumed to be mass transfer controlled, so

Equation (2.45) is used to fit the experimental data (3 mm char particle, the stainless steel reactor, 355-425 μm silica sand, 1123K, U/U_{mf}=4.5). Sherwood number is 1.5 from the Fe experiment; $D = 1.794\times10^{-4} m^2/s$; C_{O_2} is from the experimental data; $\rho_{m,c} = 990\times10^3\times0.93/12 = 76725\, mol/m^3$; the heating up region in this experiment is about 8%, so $a_c = \frac{0.003}{2}\times(1-8\%)^{\frac{1}{3}} = 0.00146$ m; $\eta = 0.3$, which is fitted by least square method of Matlab. Plots of oxygen consumption rates (mol/s) against time (second) are shown in Figure 2.11.

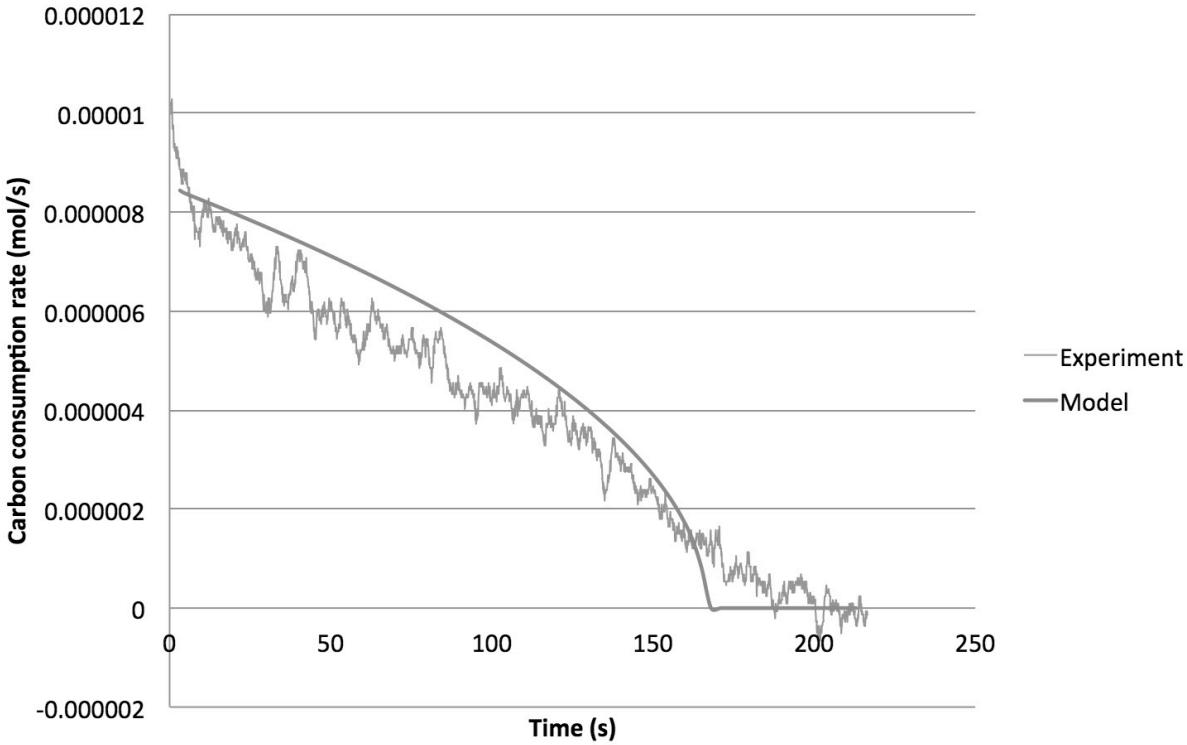

Figure 2.11 Plots of oxygen consumption rate of a 3 mm char particle against time in a fluidised bed of 355-425 μm silica sand at 1123K with U/U_{mf}=4.5.

In Figure 2.11, the shrinking core model generally fits the rate for the experiment shown. At 160s, the reaction rate of the model quickly drops to zero, 30 seconds earlier than the experimental data. In the shrinking core model, it is assumed

that the reaction is mass transfer controlled throughout. However, when the char particle becomes very small, the reaction transitions to kinetic control. Thus, Figure 2.11 offers evidence that the combustion of char particles in the experiments is generally mass transfer controlled until the particles become very small (from 160s to the end).

Figure 2.11 shows the shape of oxygen consumption rate curve in the reaction region at 1123K, and the complete reaction rate curve at 1173 is shown in Figure 2.12 (a). When the temperature drops to 973K, the shape of reaction rate curve does not change. However, when the temperature drops further to 873K, the shape changes, as shown in Figure 2.12 (b).

In Figure 2.12 (a) and (b), it is easy to see the difference between the shape of curves at 1123K and 973K. When the temperature is at 1123K, the transient, heating up region is very small, and the reaction rate increases quickly, and it takes 20s to reach the peak. In contrast, the reaction rate curve at 873K is more complex: from 45s (when the experiment starts) to 55s, the rate first increases quickly, and forms a 'shoulder' at 55s; from 48s to 270s, it then increases with a slower speed. It takes much longer, 230s, for the curve at 873K to reach the peak. The differences imply two different reaction mechanisms: (1) when the temperature is at 1123K, the combustion of char particles can be described by the shrinking core model; (2) when the temperature is 873K, the char particles is first heated up, then the morphology of the char particle gradually evolves. Pores in the char particle initially grow and the total surface area inside the char particle increases. After the peak, the surface areas

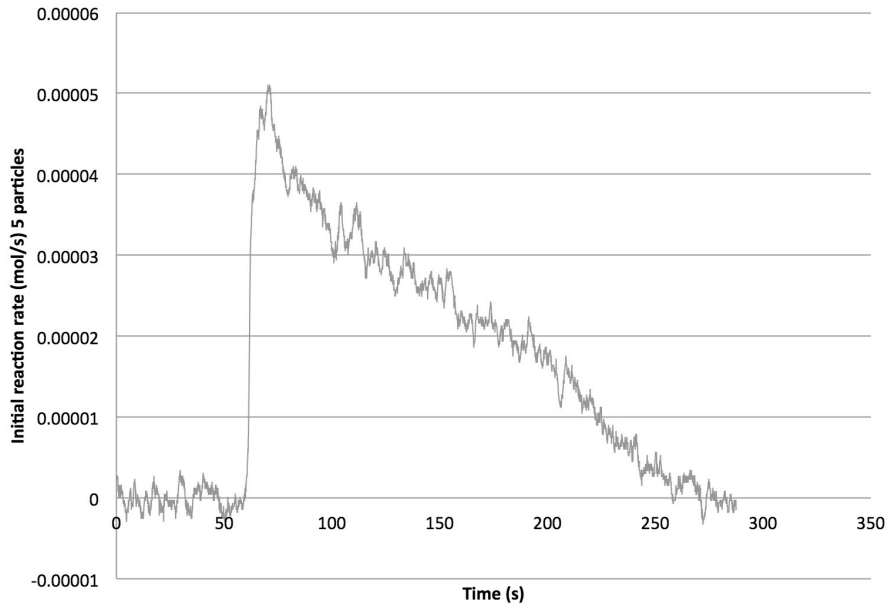

Figure 2.12 (a)

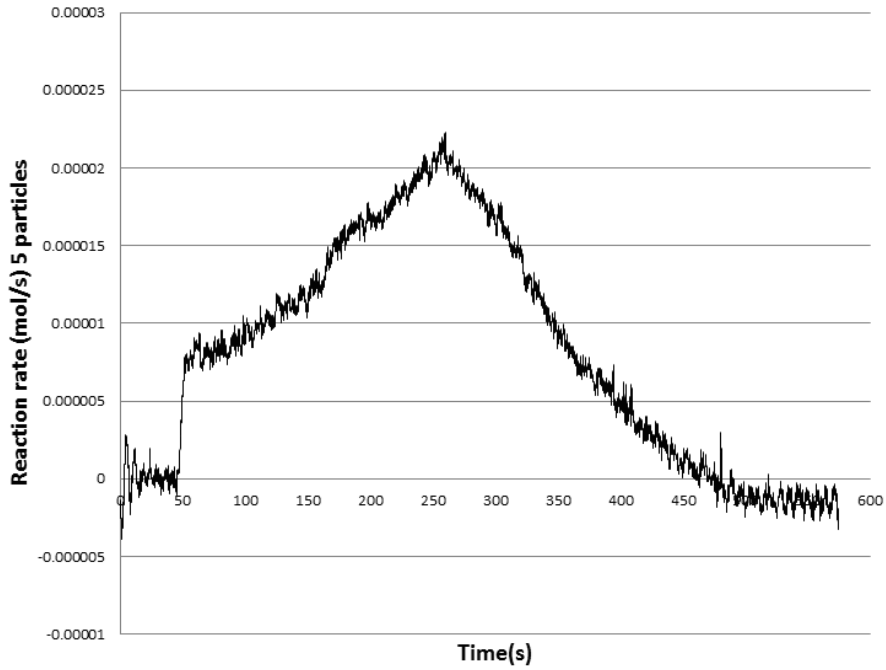

Figure 2.12 (b)

Figure 2.12 Plots of oxygen consumption rate of five 3mm char particles against time(s) in a fluidised bed of 355-425 μm silica sand at 1123K (a) and 873K (b) with U/U_{mf}=4.5.

inside the char particle start to decrease when pores grow too large and overlap (Saucedo-Martínez 2013). This effect can be described by the function of the rate of reaction at conversion X, $R(X)$

$$R(X) = R_0 \times f(X) \tag{2.46}$$

where $f(X)$ is the relative change of the surface area as a function of conversion X of the char particle, and R_0 is the initial reaction rate, which is the reaction rate at the 'shoulder'. Here, the conversion is the average conversion of the whole particle, rather than the local conversion. This difference should be noticed since the conversion is a function of radius, which is due to the resistance to intraparticle mass transfer.

The discussions above indicate that from 973K to 1173K, the reaction is mass transfer controlled; when the temperature drops to 873K, the reaction becomes controlled by chemical kinetics.

2.4.7 The comparison of Sherwood numbers and CO/CO_2 ratio from the experiments and literatures

The comparison of Sherwood number of Fe particles (2.9-3.1 mm), char particles (2.9-3.1 mm) from 973K to 1173K from the experiments in the stainless steel reactor (Table 2.5), and from the correlation suggested by Hayhurst (Hayhurst 2000) is shown in Figure 2.13.

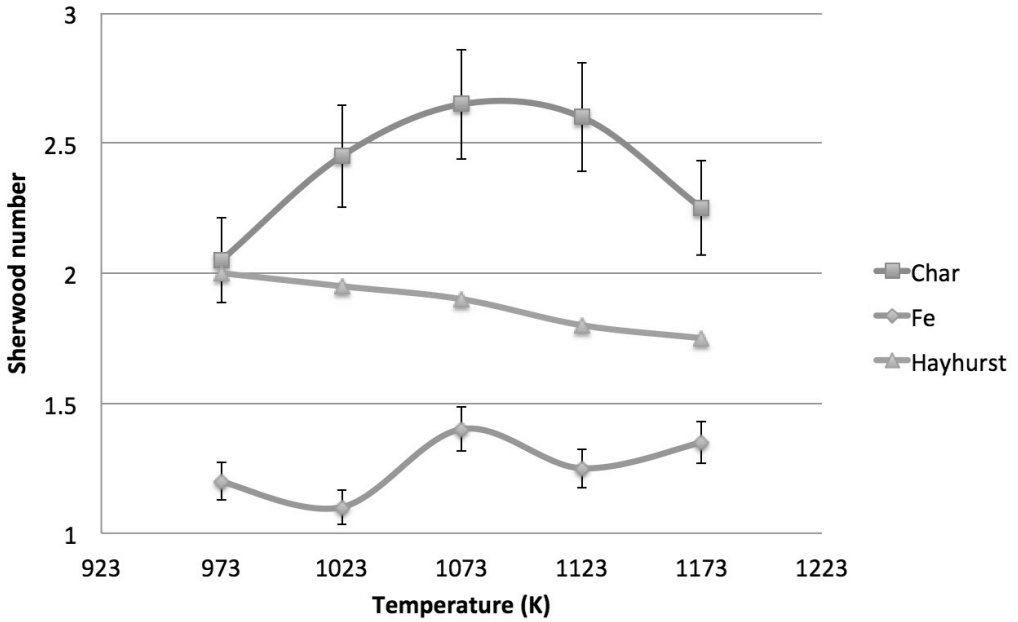

Figure 2.13 The comparison of Sherwood number of Fe particles (2.9-3.1 mm), char particles (2.9-3.1 mm) in stainless steel reactor and the correlation from Hayhurst (Hayhurst 2000).

In Figure 2.13, the measured Sherwood numbers of Fe particles are between 1.1 and 1.4, and the measured Sherwood numbers of char particles are between 2.05 and 2.6, which are about twice of the Sherwood numbers of Fe. The values of Sherwood numbers from Hayhurst and Parmar's (Hayhurst and Parmar 2002) correlations are between 1.77 and 1.98, which are much larger than the measured Sherwood numbers of Fe particles. Hayhurst seems to be over predicting the Sherwood number and having biased his results by assuming a certain ratio of $CO_2/(CO+CO_2)$ (Hayhurst and Parmar 1998). In his work (Hayhurst and Parmar 1998), most of the products are CO_2, rather than CO. However, applying $\eta = 2\frac{Sh_{Fe}}{Sh_{C'}} - 1$ to the measured Sherwood number of Fe and char particles, the ratios of $CO_2/(CO+CO_2)$ in this research are

given as,

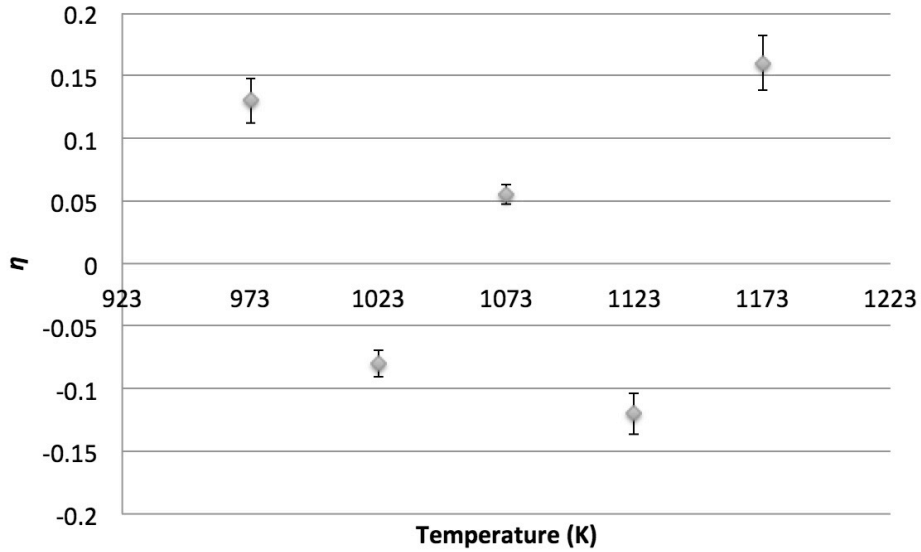

Figure 2.14 The fraction of 3 mm active carbon reacting to form CO_2 at the carbon particle's outer surface (η) in stainless reactor versus temperature (K).

Figure 2.14 shows the results of the fraction of carbon reacting to form CO_2 at the char particle's outer surface in stainless reactor versus temperature. The value is between 16% and -13%. The negative value data points could be due to different reasons, which are within the reasonable measurement errors, so they should not be discarded: 1) the noise in the char and Fe particles measurements is about $\pm$20% of the total signal; 2) the char particles are perfect spheres, but the Fe particles are slightly irregular. The diameter of the Fe particle measured is the largest diameter of the Fe particle, and in other directions, the diameter are much smaller. For instance, the widest direction of a Fe particle may be 3 mm, but its narrowest direction may be just 2.3 mm, and the average diameter is around 2.7 mm. If the diameter of Fe particle becomes smaller, its Sherwood number becomes larger. Thus, the negative values could indicate that the Sherwood numbers of Fe particles are underestimated. Given

the error in the measurements, it appears that approximately all of the carbon is converted to CO.

All of CO/CO_2 ratios from the correlations in Table 2.1 from 973K to 1173K are around 3 to 10, that is, η is between 25% and 9%, which agrees with the results in Figure 2.14 that most of products are CO.

Since the highest temperature of the stainless steel reactor is 1173K, similar experiments at higher temperatures were run at 1173K and 1323K in the alumina tube reactor (18 mm). The experimental conditions are shown in Table 2.5 (3.6 ml sand), and the sizes of char and Fe particles are both 1180 – 1400 μm. Here, it is worth noting that the small and large reactors appear to have very different Sherwood numbers: the small reactor has larger Sherwood number, which is discussed in detail in section of this chapter. In addition, the char used here (1180 -1400 μm) is Hambach lignite char, which is different from the 3 mm active carbon particles.

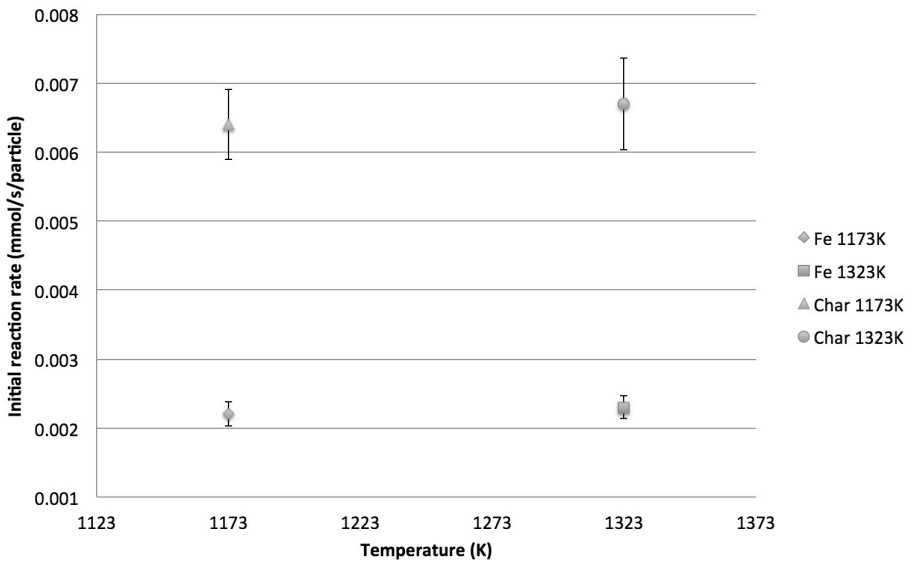

Figure 2.15 The initial reaction rate of char and Fe particles (1180 – 1400 μm) at 1173K and 1323K in alumina reactor

In Figure 2.15, the increase of initial reaction rate when temperature increases is small (5% for char particles and 1% for Fe particles), which indicates that the reactions are mass transfer controlled. The ratio Sherwood number of Fe over the Sherwood number of char is about 3, which is higher than 2. This could be due to that the char particles (1180 – 1400 μm) are sieved and not spheres. The sieved sizes are a bit strange and depend on shape, so the real ratio could be 2, and most of the products at higher temperatures are still CO rather than CO_2.

The difference between values of Sherwood number from Hayhurst and Parmar's correlation and from this research can be explained as follows. In Hayhurst and Parmar's work (Hayhurst and Parmar 2002), he deduced that

$$\frac{d(d^2)}{dt} = -\frac{8ShDC_{O_2}^{p}}{\rho_m(1+\eta)} \tag{2.47}$$

So $Sh/(1+\eta)$ can be measured by the equation above. η is given by Hayhurst and Parmar's previous results (Hayhurst and Parmar 2002), in which he calculated η by the heat balance of the burning particle. The values of η in Hayhurst and Parmar's work (Hayhurst and Parmar 2002) is in Figure 2.16.

In Figure 2.16, when the temperature of bed (T_b) is at 973K, η is around 0.25~0.5; when the temperature of bed is at 1173K, η is around 0.6~1. η in Figure 2.16 is always much higher than η in Figure 2.14, which is around 0. The high η in Hayhurst and Parmar's work (Hayhurst and Parmar 2002) can be explained by his method of calculation:

(1) He used a heat balance equation, which is shown in the following section;

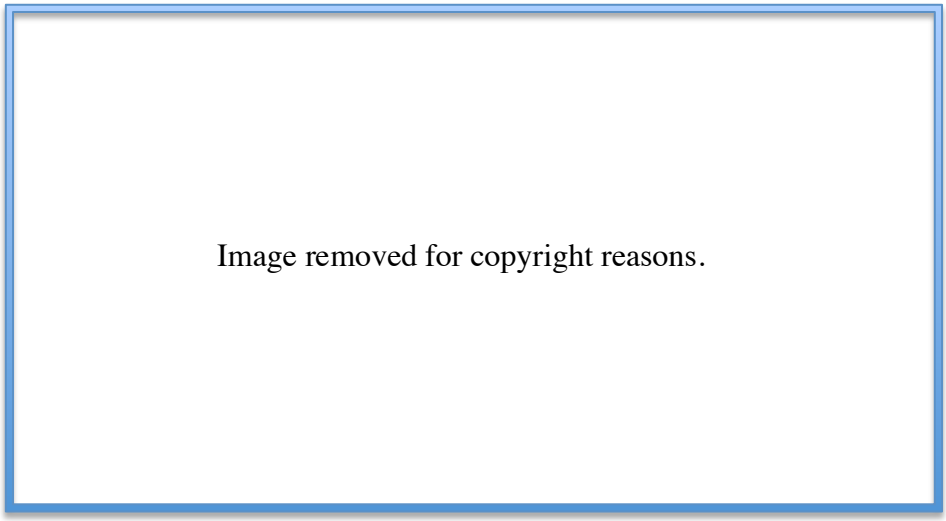

Figure 2.16 η versus temperatures of carbon particles in a fluidised bed using silica sand (417-571 μm) with U/U_{mf} = 3.5. (Reproduced from Hayhurst (Hayhurst and Parmar 1998) Fig.5)

(2) This assumed heat from conversion to CO_2 "in the vicinity" would heat up the particle. Heat release in the vicinity doesn't mean it happened in the mass transfer boundary layer or at the outer surface of particle, e.g. complexities of CO burning away from particle mass transfer boundary layer and heat being fed back by particle motion.

Thus, by using his method, he overestimated the temperature of carbon particles, and then overestimated η.

2.4.8 The temperature of reacting particles

In the combustion of char particles, the temperature of burning particles is higher than the temperature of the fluidised bed. The heat balance of the burning particle is expressed as (Hayhurst and Parmar 1998),

$$-r\{\Delta H_1 + \eta(\Delta H_2 - \Delta H_1)\} = \pi d^2 \left\{\frac{\rho C_p d}{6M_w}\frac{dT_p}{dt} + h\left(T_p - T_b\right) + \varepsilon'\sigma(T_p^4 - T_b^4)\right\} \quad (2.48)$$

where C_p is the molar heat capacity of the char particle, ε' is its emissivity, σ is the Stefan-Boltzmann constant, h is the coefficient for heat transfer from the fluidised bed to the reacting particle, M_w is the molar density of carbon, which is 12 g/mol. $\Delta H_1 = -110.6kJ/mol$ and $\Delta H_2 = -395.5kJ/mol$ are the enthalpy change of reaction of $C + \frac{1}{2}O_2 = CO$ and $C + O_2 = CO_2$. If it is assumed that the burning particle is pseudo steady state, the term $\frac{\rho C_p d}{6M_w}\frac{dT_p}{dt}$ could be omitted. The equation above becomes,

$$-r\{\Delta H_1 + \eta(\Delta H_2 - \Delta H_1)\} = \pi d^2\left\{h\left(T_p - T_b\right) + \varepsilon'\sigma(T_p^4 - T_b^4)\right\} \quad (2.49)$$

The particle temperatures are shown in Table 2.7 by solving the equation above (the value of CO/CO_2 ratio is taken from Figure 2.4, and the value of h is taken from Hayhurst and Parmar (Hayhurst and Parmar 1998). Table 2.7 shows that the difference between the temperature of the burning char particle and the fluidised bed is around 50 K.

There are two points need to be checked: 1) if η is a function of temperature. According to Figure 2.15 and Figure 2.16, η is always around zero in the temperature ranges of the figures; 2) if reaction rate is a function of temperature. If so, at worst it would change rate by factor of 2 if it caused the carbon to burn to CO_2. However, in this research, all reactions are mass transfer controlled, and the rates are insensitive to temperatures. Thus, 50 K difference has no substantial influence on the results above.

Table 2.7 The particle temperatures of burning char particles when the temperature of fluidised bed at 973 K, 1073 K and 1173 K.

Fluidised bed temperature	Particle temperature (T_p)	Heat transfer coefficient (from Hayhurst and Parmar (Hayhurst and Parmar 1998))
973K	1010K	270
1073 K	1128 K	340
1173K	1218 K	330

2.4.9 The fate of carbon monoxide and the potential effect its subsequent combustion has on overall combustion rates

If carbon particles burn without any surrounding inert sand, previous researchers note that CO could combust into CO_2 in the boundary layer (Hayhurst and Parmar 1998). Since the inert sand could inhibit the combustion of CO, the oxidation of CO in the combustion of carbon particles in the fluidised bed is complicated. Generally, it is agreed that CO would be eventually oxidized into CO_2 in the freeboard (Hayhurst 1991) (J. S. Dennis, Hayhurst, and Mackley 1982). Some argue that CO would just be oxidized in either bubble phase or freeboard. Hayhurst (Hayhurst 1991) pointed out that when the temperature is lower than 1023K, the silica sand would inhibit the combustion of CO, and CO would neither burn in the particulate phase nor the bubble phase, i.e. CO should only burn in the free board. When temperature is higher than 1073K (J. S. Dennis, Hayhurst, and Mackley 1982) oxidation of CO would take place in the bubble phase rather than the particulate phase. Linjewile and Agarwal (Linjewile and Agarwal 1995) argued that the inert bed

materials would quench the homogeneous oxidation of CO close to a burning sphere. Hayhurst and Parmar (Hayhurst and Parmar 1998) argued when the temperature is higher than 1400 K, CO would rapidly be oxidized into CO_2 close to the outer surface of carbon particles.

2.4.10 Comments on Hayhurst and Parmar's correlations of CO/CO_2 ratio

Hayhurst and Parmar (Hayhurst and Parmar 2002) used rates of char combustion to estimate Sherwood number, but has to use CO/CO_2 ratio from other experiments (Hayhurst and Parmar 1998). Thus, CO/CO_2 ratio is important in using his correlations to predict rate of combustions. If CO/CO_2 is different, there is inconsistency.

The experimental results in this chapter indicate that char all burning to CO, which is different to Hayhurst and Parmar (Hayhurst and Parmar 1998) assumed. The experimental results in this chapter agree with literatures (Arthur 1951)(Rossberg 1956), which also assume that the main gaseous product of char combustion is CO, rather than CO_2.

Hayhurst and Parmar's correlation (Hayhurst and Parmar 2002) actually overestimates the rate of mass transfer. Saucedo (Saucedo-Martínez 2013) used Hayhurst and Parmar's correlation and made a mistake that by dividing Hayhurst and Parmar's correlation results over 1.75 to make his rates of combustion agree with Hayhurst and Parmar's. By coincidence, Hayhurst and Parmar's results turn out to be correct for smaller bed. In that, it is observed in small bed, the mass transfer rate is

about twice than the larger bed, where wall effect is less significant. Previous work in small beds assumed that Hayhurst and Parmar's correlation was correct, fortuitously giving a reasonable rate of mass transfer.

2.4.11 The comparison of film model and surface renewal model

In the previous sections, the film model was discussed, which assumes that there is a film around the reacting carbon particle and all mass transfer and CO oxidation take place in the film. However, an alternative view is the renewal model, which is suggested by La Nauze et al. (La Nauze, Jung, and Kastl 1984). This assumes that there are two routes to transfer mass, which is illustrated in Figure 2.17:

(1) Via, the "packet", i.e. a fraction of the particulate phase. The packet gets fresh gas from the bulk and comes close to carbon particles then renews the oxygen concentration on the outer surface of the carbon particles;

(2) The gas convective component (the gas in the particulate phase has a velocity of U_{mf}/ε_{mf})

It is obvious that compared to the film model, the bubbles could increase the mass transfer rate by moving packets. The expression of Sherwood number from La Nauze's theory (La Nauze, Jung, and Kastl 1984) is,

$$Sh = 2\varepsilon_{mf} + \left[\frac{4\varepsilon_{mf} d\left(\frac{U_{mf}}{\varepsilon_{mf}} + U_b\right)}{\pi D}\right]^{\frac{1}{2}} \tag{2.50}$$

where ε_{mf}=0.44, d = 0.003 m, U_{mf} = 0.0498 m/s when the temperature is at 1173K, and the correlation of the velocity of bubbles U_b is given by David and

Harrison (J. F. Davidson and Harrison 1963),

$$U_b = U - U_{mf} + 0.71(gd_b)^{0.5} \tag{2.51}$$

where $U = 4.5 \times U_{mf} = 0.2241$ m/s when the temperature is at 1173K, and the correlation of the mean diameter of bubbles in the fluidised bed d_b is given by Darton (Darton 1977),

$$d_b = \frac{0.3(U-U_{mf})^{0.4}}{g^{0.2}H}\left\{\left(H + 4\sqrt{A_0}\right)^{1.8} - \left(4\sqrt{A_0}\right)^{1.8}\right\} \tag{2.52}$$

where A_0 is the distributor area per orifice, which is $\pi \times \left(\frac{0.0004}{2}\right)^2 = 1.26 \times 10^{-7}$ m^2. The correlation of the height of fluidised sand H is given by Davidson and Harrison (J. F. Davidson and Harrison 1963),

$$\frac{H-H_{mf}}{H} = \frac{U-U_{mf}}{U_b} \tag{2.53}$$

where H_{mf} is the depth of fluidised bed at incipient fluidisation, which is $300/1000000/3.14/(0.078/2)^2 = 0.063$ m.

The result of Sherwood number from La Nauze's model is around 1.25, which is similar to the results of this chapter. In term of mechanism, La Nause's results appears to be better for larger beds, though it is hard to justify the mechanisms surface renew versus film model.

2.5 CONCLUSIONS

Previous work (e.g. (Hayhurst and Parmar 2002)) has assumed a ratio of CO/CO_2 or used an indirect measurement to all allow mass transfer coefficients to be

determined. Here the problem was inverted to allow the ratio of CO/CO_2 to be calculated directly, by direct determination of the mass transfer coefficient using metal oxide particles. In contrast to Hayhurst and Parmar (Hayhurst and Parmar 2002) who assumed CO_2 was the main product, for this char the actual ratio of CO/CO_2 was almost zero. The measurement here is in agreement with Arthur. This more accurate determination of CO/CO_2 allows a better estimate of the mass transfer coefficient and leads to a correction of the Hayhurst and Parmar's (Hayhurst and Parmar 2002) correlation by a factor of ½. Interestingly, very small fluidised beds have mass transfer coefficients which are about twice that expected in a large bed (owing to the very different flow and indeterminate flow pattern). This means the correlation of Hayhurst and Parmar (Hayhurst and Parmar 2002), by fortuitous coincidence works wells for beds with diameters < 30 mm., without the correction factor, should be ignored.

CHAPTER 3 THE SIMULATION OF A BURNING CHAR PARTICLE IN THE FLUIDISED BED UNDER EXTERNAL MASS TRANSFER CONTROL

3.1 INTRODUCTION

The combustion of char at elevated temperature is a very fast reaction, and attempts to measure the kinetics have often been confounded by the reaction being limited by the rate at which the oxygen can be transported to the char particle from the bulk. To examine the interactions between chemical reactions and external mass transfer, an accurate picture is first needed when inert sand or active metal oxide particles are used as fluidizing materials. Here, parameters such as the effective mass transfer coefficient and Sherwood number are taken from literature (Hayhurst 2000) (Young and Todd 2005) (Hayhurst and Tucker 1990) or assumptions, and are discussed in the context of other published work on mass transfer to burning particles.

3.2 THEORY

The combustion of a char particle in the fluidised bed is simulated in this chapter. The full Stefan-Maxwell solution is compared to the more analytically tractable simplified forms, i.e. Fick's law (which is only valid for equimolar counter diffusion) and the simplified binary form of Stefan-Maxwell for non-EMCD diffusion. Three questions are examined here,

1) If CO is produced on the surface of char particle, the effect of CO combusting in the boundary layer on mass transfer.
2) The effects of active fluidising material. For the inert (sand) fluidising material, the oxygen supplied comes only from the oxygen diffusion; for the active (Fe_2O_3 or CuO) fluidising materials, the oxygen for CO oxidation could also from the fluidising materials. One difference between CuO to Fe_2O_3 is that when the O_2 concentration is very low, CuO could decompose and release O_2. If CuO decomposition is fast enough, the char combustion would no longer be mass transfer controlled;
3) The difference between mass transfer to a combusting char particle and metal particle. The complexity of char particle combustion arises from it produces both CO and CO_2. For the metal particle combustion, it has no gaseous product, which makes it easier to determine the Sherwood number.

3.2.1 Modelling the mass transfer to a combusting char particle

3.2.1.1 Mass transfer in the boundary layer.

Figure 3.1 shows the schematic diagram of the combustion of char in air. Region I (R-I) is the internal region inside the char particle, and Region II (R-II) is the external region in the boundary layer.

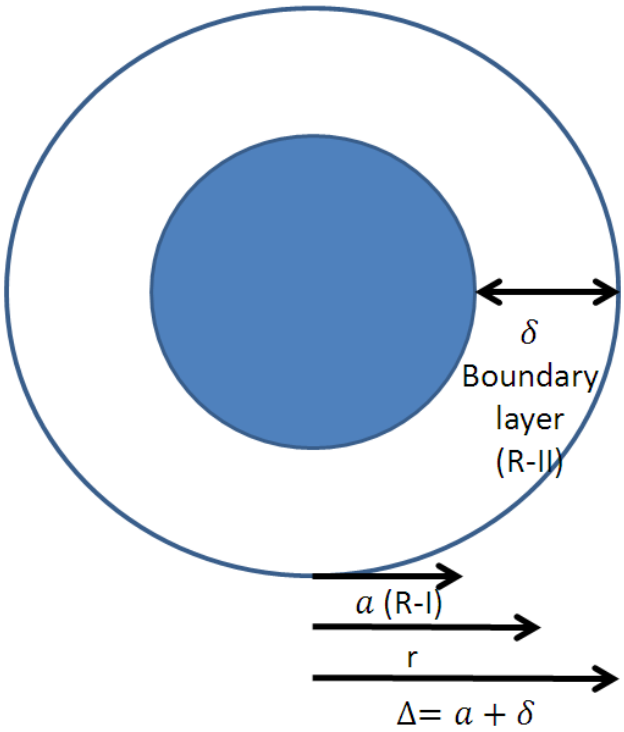

Figure 3.1 Schematic diagram of the combustion of char in air. Region I (R-I) is the internal region inside the char particle, and Region II (R-II) is the external region in the boundary layer. Here, a is the radius of the char particle, and δ is the thickness of the boundary layer.

Three reactions take place on the outer and inner porous surfaces in Region I of the char particle:

$$C + O_2 = CO_2 \qquad (3.1(a))$$

$$2C + O_2 = 2CO \qquad (3.1(b))$$

$$C + CO_2 = 2CO \qquad (3.1(c))$$

There are three aspects controlling the reactions: 1) the intrinsic kinetics of the char, that is, reaction (3.1(a)), (3.1(b)) and (3.1(c)); 2) the intra-particle mass transport; 3) the external mass transport in the boundary layer.

The simulation shows the situation when the char particle combustion is under external mass transfer control, which means the concentration at the outer surface is approximately zero.

In Region II in Figure 3, mass conservation for the boundary layer around the particle of char, *i.e.* from $r = a$ to $r = a + \delta$, under pseudo-steady state conditions for the species i $(i = O_2, N_2, CO, CO_2)$ leads to,

$$\frac{1}{r^2}\frac{d(r^2 J_i)}{dr} - \xi_i = 0 \tag{3.2}$$

where $J_i$is the molar flux of species i and ξ_i is the molar production rate of species i per volume. Here, it is assumed that the boundary layer is full of reactant.

In the fluidised bed, ξ_i has to be modified by two factors, ε_{mf} and ε_p, which are the voidage in the particulate phase (taken to be equal to that when the bed is just fluidised) and the voidage of metal oxide particle (p =Fe_2O_3 or CuO), respectively. For heterogeneous reactions, ξ_i has to be multiplied by a factor $m = (1 - \varepsilon_{mf})(1 - \varepsilon_p)$; for homogeneous reactions, ξ_i has to multiplied by $m = \varepsilon_{mf}$. So in the fluidised bed, Equation (3.2) becomes,

$$\frac{dJ_{CO}}{dr} = m\xi_{CO} - \frac{2}{r}J_{CO} \tag{3.3}$$

$$\frac{dJ_{CO_2}}{dr} = m\xi_{CO_2} - \frac{2}{r}J_{CO_2} \tag{3.4}$$

$$\frac{dJ_{N_2}}{dr} = m\xi_{N_2} - \frac{2}{r}J_{N_2} \tag{3.5}$$

$$\frac{dJ_{O_2}}{dr} = m\xi_{O_2} - \frac{2}{r}J_{O_2} \tag{3.6}$$

3.2.1.1 Calculation of the boundary layer thickness by using EMCD assumption

If there is no CO combustion in the boundary layer, ξ_i is zero for all species. Thus, Equations (3.3) - (3.6) become,

$$\frac{dJ_{CO}}{dr} = -\frac{2}{r}J_{CO} \tag{3.7}$$

$$\frac{dJ_{CO_2}}{dr} = -\frac{2}{r}J_{CO_2} \tag{3.8}$$

$$\frac{dJ_{N_2}}{dr} = -\frac{2}{r}J_{N_2} \tag{3.9}$$

$$\frac{dJ_{O_2}}{dr} = -\frac{2}{r}J_{O_2} \tag{3.10}$$

To calculate the thickness of boundary layer, it is assumed that the diffusion in the boundary layer is equimolar counter-diffusion (EMCD). If O_2 diffuses towards a burning char particle and only CO_2 diffuses away, this assumption brings no error. However, if only CO were produced, this process would not be equimolar counter-diffusion. The Sherwood number correlations are reported for equimolar counter diffusion, so they are real correlations for boundary layer thickness in disguise. In that case, $Sh = Sh_{EMCD}/1.102$ for the char combustion in the air (Hayhurst 2000). If the product were a mixture of CO and CO_2, the difference between Sh and Sh_{EMCD} is less than 10.2%. Considering the errors of the experimental measurements are ±20%, the difference between Sh and Sh_{EMCD} can be ignored (Hayhurst 2000).

Under the EMCD assumption, the continuity equation with no reaction in spherical coordinates is given as,

$$\frac{\partial}{\partial r}\left(r^2 \frac{dC_i}{dr}\right) = 0 \tag{3.11}$$

where C_i is the molar concentration of species i. The solution of Equation (3.11) is,

$$C_i = -\frac{\alpha_i}{r} + \beta_i \tag{3.12}$$

where α_i and β_i are constants. The boundary conditions of equation (3.12) are,

$$C_i = C_i^s \quad at \;\; r = a \tag{3.13}$$

$$C_i = C_i^p \quad at \;\; r = a + \delta \tag{3.14}$$

where δ is the thickness of boundary layer. With the boundary conditions (3.13) and (3.14), α_i in Equation (3.12) is solved as,

$$\alpha_i = \frac{C_i^p - C_i^s}{\frac{1}{a} - \frac{1}{a+\delta}} \tag{3.15}$$

The molar flux J_i is given by Fick's law,

$$J_i = -D^{eff}\frac{dC_i}{dr}\Big|_{r=a} = \frac{D^{eff}}{a^2}\frac{C_i^p - C_i^s}{\frac{1}{\Delta} - \frac{1}{a}} = -\frac{D^{eff}}{a}\left(1 + \frac{a}{\delta}\right)\left(C_i^p - C_i^s\right) \tag{3.16}$$

where D^{eff} is a pseudo-binary effective diffusivity. The mass transfer coefficient k_g is,

$$k_g = \frac{-J_i}{C_i^p - C_i^s} = \frac{D^{eff}}{a}\left(1 + \frac{a}{\delta}\right) \tag{3.17}$$

The Sherwood number is based on molecular diffusivity D^{mol}, rather than effective diffusivity D^{eff},

$$Sh = \frac{k_g d}{D^{mol}} = \frac{\frac{D^{eff}}{a}\left(1+\frac{a}{\delta}\right)2a}{D^{mol}} = \frac{D^{eff}}{D^{mol}} 2\left(1 + \frac{a}{\delta}\right) \tag{3.18}$$

In the fluidised bed, the effective diffusivity D^{eff} is given by,

$$D^{eff} = \frac{\varepsilon_{mf}}{\tau^2} D^{mol} \tag{3.19}$$

where ε_{mf} is the minimum voidage in the particulate phase; τ^2 is the tortuosity,

which characterizes the lengthened diffusion pathways of gas through porous media. In the fluidised bed, the porous media refers to the fluidised particles, which gas has to go around.

Substituting the effective diffusivity into the expression of the Sherwood number,

$$Sh = \frac{2\varepsilon_{mf}}{\tau^2}\left(1 + \frac{a}{\delta}\right) \tag{3.20}$$

When $\delta \to \infty$, that is, the stagnant case, then,

$$Sh_0 = \frac{2\varepsilon_{mf}}{\tau^2} \tag{3.21}$$

where Sh_0 is the Sherwood number for the stagnant case. So, the thickness of boundary layer δ becomes,

$$\delta = \frac{a}{\frac{Sh}{Sh_0} - 1} \tag{3.22}$$

Since both ε_{mf} and τ^2 are hard to measure, by using Equation (3.21), the term of $\frac{\varepsilon_{mf}}{\tau^2}$ is replaced by $\frac{Sh_0}{2}$. The value of Sherwood number can be easily calculated from correlations (Hayhurst 2000).

For non-equimolar counter diffusion (i.e. using something other than a purely Fickian diffusion term), Hayhurst (Hayhurst 2000) argued that mass transfer rate calculated for an infinite boundary layer thickness should be scaled by a factor of $Sh_{EMCD}/2$, where Sh_{EMCD} is the Sherwood number which would occur for equimolar counter diffusion at the same Reynolds number. For the flux model

$$J_1 = (J_1 + J_2)C - \frac{DdC}{dr} \tag{3.23}$$

They found that this was equivalent to setting the boundary layer thickness to be

equal to the one that calculated from the EMCD model.

It is possible to show that (Hayhurst 2000)

$$\frac{Q_i(\delta)}{Q_i(\infty)} = \frac{Q_{i,emcd}(\delta)}{Q_{i,emcd}(\infty)} = \frac{Sh_{emcd}}{Sh_o} = \left(1 + \frac{a}{\delta}\right) \tag{3.24}$$

where $Q_i(x)$ is the mass transport rate for a boundary layer of thickness of x, and δ is a particular boundary layer thickness; $Q_{i,emcd}(\delta)$ is the mass transport rate of a species undergoing equimolar counter diffusion. Thus, mass transfer correlations, which give the Sherwood number, are usually reporting the equivalent EMCD Sherwood number, and can be regarded as correlations for the presumed boundary layer thickness.

3.2.1.3 Effective diffusivity in the fluidised bed

Care must be taken about the definition used for the effective diffusivity, as different authors attach different meanings to the correction to the molecular diffusivity (Kim and Chen 2006), defining effective diffusivity in different ways, e.g.

$$D_{eff} = D\frac{\varepsilon}{\tau^2} = D\frac{\varepsilon}{\tau'} = DA_d \tag{3.25}$$

where τ is the tortuousity (Kim et al. (Kim and Chen 2006), N. Epstein (Epstein 1989)), τ' is the tortuosity factor (Kim et al. (Kim and Chen 2006),Friedman et al. (Friedman and Seaton 1995)) and A_d is a correction factor to account for the fact that diffusion is hindered by the porous media (Kim et al. (Kim and Chen 2006) , Neale et al. (Neale and Nader 1973)).

It is conventional to assume that in the stagnant case ($\delta = \infty$), Sh_{EMCD} in a

fluidised bed approaches a value of $2\varepsilon_{mf}$ (Hayhurst and Parmar 2002). This implies that $A_d = \varepsilon_{mf}$, and if the porosity in the particulate phase is assumed to be ε_{mf}, and $\tau \sim 1$. Scala (Scala 2007) also suggests τ ~1. Friedman et al. (Friedman and Seaton 1995) has a model for the tortuosity factor and also reports some data for the tortuosity factor in packed spheres. They suggest that an apparent tortuosity of unity. Kim et al. (Kim and Chen 2006) carried out simulations of diffusion through various packing of spheres; for a solids volume fraction of about 0.6 (i.e. void fraction close to ε_{mf}) they give values of A_d around 0.3-0.4. They also quote the Maxwell model for spherical particles

$$\tau' = 1 + \frac{1}{2}(1 - \varepsilon) \tag{3.26}$$

Which implies,

$$A_d = \frac{\varepsilon}{1+\frac{1}{2}(1-\varepsilon)} = \frac{2\varepsilon}{3-\varepsilon} \tag{3.27}$$

This result is derived by Neale et al. (Neale and Nader 1973) for a random swarm of spheres and is independent of the size distribution of the spheres. For $\varepsilon = \varepsilon_{mf} \sim 0.4$, this gives $A_d = 0.31$, which is not far off ε_{mf}, given the errors associated in measuring the Sherwood numbers in a fluidised bed.

3.2.1.4 The calculation of fluxes in the boundary layer using full Stefan-Maxwell equations

The fluxes in the boundary layer are given by the full Stefan-Maxwell equations (Young and Todd 2005),

$$\frac{dx_i}{dr} = \frac{RT}{P}\sum_k \frac{x_i J_k - x_k J_i}{D_{ik}^{eff}} \tag{3.28}$$

where x_i is molar fraction of species i and Equation (3.28) becomes for different species i,

$$\frac{dx_{CO}}{dr} = \frac{RT}{P}\left\{\frac{x_{CO}J_{N_2} - x_{N_2}J_{CO}}{D_{CO,N_2}^{eff}} + \frac{x_{CO}J_{CO_2} - x_{CO_2}J_{CO}}{D_{CO,CO_2}^{eff}} + \frac{x_{CO}J_{O_2} - x_{O_2}J_{CO}}{D_{CO,O_2}^{eff}}\right\} \tag{3.29}$$

$$\frac{dx_{CO_2}}{dr} = \frac{RT}{P}\left\{\frac{x_{CO}J_{N_2} - x_{N_2}J_{CO}}{D_{CO,N_2}^{eff}} + \frac{x_{CO}J_{CO_2} - x_{CO_2}J_{CO}}{D_{CO,CO_2}^{eff}} + \frac{x_{CO}J_{O_2} - x_{O_2}J_{CO}}{D_{CO,O_2}^{eff}}\right\} \tag{3.30}$$

$$\frac{dx_{N_2}}{dr} = \frac{RT}{P}\left\{\frac{x_{N_2}J_{CO_2} - x_{CO_2}J_{N_2}}{D_{N_2,CO_2}^{eff}} + \frac{x_{N_2}J_{CO} - x_{CO}J_{N_2}}{D_{N_2,CO}^{eff}} + \frac{x_{N_2}J_{O_2} - x_{O_2}J_{N_2}}{D_{N_2,O_2}^{eff}}\right\} \tag{3.31}$$

$$\frac{dx_{O_2}}{dr} = \frac{RT}{P}\left\{\frac{x_{O_2}J_{CO_2} - x_{CO_2}J_{O_2}}{D_{O_2,CO_2}^{eff}} + \frac{x_{O_2}J_{CO} - x_{CO}J_{O_2}}{D_{O_2,CO}^{eff}} + \frac{x_{O_2}J_{N_2} - x_{N_2}J_{O_2}}{D_{O_2,N_2}^{eff}}\right\} \tag{3.32}$$

The boundary conditions for the solution of equations above are,

$$r = a \qquad x_{O_2,s} = 0 \tag{3.33}$$

$$r = a + \delta \qquad x_i = x_{i,B} \tag{3.34}$$

where $x_{O_2,s}$ is the molar fraction of O_2 on the surface of the char particle, and $x_{i,bulk}$ is the molar fraction of species i in the particulate phase.

In addition, when $r = a$,

$$2J_{O_2} + J_{CO} + 2J_{CO_2} = 0 \tag{3.35}$$

$$J_{CO} = \gamma J_{CO_2} \tag{3.36}$$

$$J_{N_2} = 0 \tag{3.37}$$

where γ is the production ratio of CO/CO_2 on the surface of the char particle, which is given by Arthur (Arthur 1951),

$$\gamma = 2500 \exp\left(-\frac{6240}{T}\right) \tag{3.38}$$

Similar to the previous section, to eliminate $\frac{\varepsilon_{mf}}{\tau^2}$, Equation (3.19) is first

substituted into Equation (3.29) – Equation (3.32), and $\frac{\varepsilon_{mf}}{\tau^2}$ is then replaced by $\frac{Sh_0}{2}$.

3.2.1.5 Accounting for CO combustion in the boundary layer

Hayhurst (Hayhurst and Tucker 1990) suggested that CO is the major product of the combustion of carbon. However, some of the CO could be burnt into CO_2 in the boundary layer around the carbon particle. In that case, CO_2 would be the major product of oxidation of carbon in practice. However, in the fluidised bed, the fluidising material, that is, sand would inhibit the oxidation of CO by heterogeneously removing radicals such as OH and HO_2 (Hayhurst and Tucker 1990). Thus, the hypothesis that CO could combust into CO_2 in the boundary layer is tested here. CO combustion is a homogeneous reaction. So in Equation (3.3) - Equation (3.6), $m = \varepsilon_{mf}$. Since the reaction takes place in the boundary layer is:

$$2CO + O_2 = 2CO_2 \tag{3.39}$$

and the ξ_i terms in Equation (3.3)- Equation (3.6) are given as,

$$\xi_{CO} = 2\xi_{O_2} = -\xi_{CO_2} \tag{3.40}$$

The rate expression used here is from Howard (Howard, Williams, and Fine 1973) (valid between 1113K and 2633K),

$$\varepsilon_{mf}\xi_{CO} = -\frac{dc_{CO}}{dt} = 1.3\times10^8 C_{CO} C_{O_2}^{0.5} C_{H_2O}^{0.5} exp\left(\frac{-125520}{RT}\right) \tag{3.41}$$

where C_{CO}, C_{CO_2} and C_{H_2O} are the molar concentrations of CO, CO_2 and H_2O, respectively. This rate expression would tend to over estimate the rate of combustion since it does not account for any effect of radical quenching.

3.2.2 The combustion of char particles using metal oxides as fluidising material

The fluidised particles in previous sections can be changed from inert sand to active metal oxide particles, for instance, Fe_2O_3 or CuO. Unlike sand, metal oxide particles could improve the combustion of CO in the boundary layer: these metal oxide particles come to Region II, which is defined in Figure 3.1, and are reduced by CO. In this section, Fe_2O_3 and CuO are used as metal oxide particles with the hypothesis that CO could combust in the boundary layer.

3.2.2.1 The combustion of char particles using Fe_2O_3 particles as fluidising material

There are three kinds of iron oxides: wustite ($Fe_{0.947}O$), magnetite (Fe_3O_4) and hematite (Fe_2O_3). Since the amount of CO produced in char particles combustion is very small, it is assumed that Fe_3O_4 is the only product of Fe_2O_3 reduction. Thus, for Fe_2O_3, the reaction taking place in the boundary layer is:

$$3Fe_2O_3 + CO = 2Fe_3O_4 + CO_2 \tag{3.42}$$

Since the reaction (3.42) is heterogeneous, so $m = (1-\varepsilon_{mf})(1-\varepsilon_{Fe_2O_3})$ for Equation (3.3) - Equation (3.6). And when the reaction (3.42) is under kinetics control, $m\xi_{CO}$ in Equation (3.3) becomes,

$$(1-\varepsilon_{mf})(1-\varepsilon_{Fe_2O_3})\xi_{CO} = (1-\varepsilon_{mf})(1-\varepsilon_{Fe_2O_3})k_{Fe_2O_3}\,C_{CO} \tag{3.43}$$

where $k_{Fe_2O_3}$ is the first order reaction rate constant of the reaction (s^{-1}) from C.D. Bohn et al. (C. D. Bohn et al. 2010), which is given by,

$$k_{Fe_2O_3} = 2.4\times10^7 \exp\left(-\frac{75000}{RT}\right)\left(1-\frac{P_{CO_2}}{P_{CO}}\frac{1}{K_p^{Fe_2O_3}}\right)\left(1-\frac{X_{Fe_2O_3}}{0.8}\right)^{0.4} \quad (3.44)$$

where P_{CO_2} is the partial pressure of CO_2; K_{p,Fe_2O_3} is the dimensionless equilibrium constant for reaction (3.42). Since K_{p,Fe_2O_3} is always larger than 10^4 between 298 K to 1400 K , which means that Fe_2O_3 can oxidise all CO to CO_2, so the term $\left(1-\frac{P_{CO_2}}{P_{CO}}\frac{1}{K_p^{Fe_2O_3}}\right) \approx 1$; $X_{Fe_2O_3}$ is the dimensionless conversion of Fe_2O_3 to Fe_3O_4. Since only a small amount CO is produced by char particles, and the Fe_2O_3 particles exchange between boundary layer and particulate phase is assumed to be fast. In this case, the conversion of Fe_2O_3 particles is assumed zero. Thus, the term $\left(1-\frac{X_{Fe_2O_3}}{0.8}\right)^{0.4} \approx 1$. Equation (3.44) becomes,

$$k_{Fe_2O_3} = 2.4\times10^7 \exp\left(-\frac{75000}{RT}\right) \quad (3.45)$$

However, the above rate expressions are only valid when the reactions are kinetically controlled. Since the reaction of iron oxide reduction is fast, it is worth testing if the reaction is kinetically or external mass transfer controlled.

At 1173 K, the reaction rate of a Fe_2O_3 particle under kinetics control is: $(1-\varepsilon_{Fe_2O_3})\xi_{CO}V_{Fe_2O_3} = 1.64\times10^{-7} mol\ s^{-1}$, where $V_{Fe_2O_3} = \frac{4}{3}\pi\left(\frac{d_{Fe_2O_3}}{2}\right)^3$ is the volume of the Fe_2O_3 particle.

The boundary region in which the metal oxide particle resides (i.e. the boundary layer surrounding the char particle) is similar to a packed bed, packed with metal oxide particles. The Sherwood number of the "packed bed" Sh_p is given by Wakao (Wakao and Funazkri 1978),

$$Sh_p = 2 + 1.1Sc^{\frac{1}{3}}Re^{0.6} \quad (3.46)$$

where $Sc = \frac{\upsilon}{D^{mol}}$ is the Schmidt number (υ is fluid kinematic viscosity), and $Re = Ud/\upsilon$ is the Reynolds number (d is the diameter of the particle, and U is the superficial velocity through packed bed). The kinematic viscosity of air at 1173K is $1.413\times10^{-4}\ m^2/s$, and the superficial velocity of the 'packed bed' is assumed as 0.4 m/s, which is the superficial velocity of the fluidised bed when $\frac{U}{U_{mf}} = 4.5$. At 1173 K, the molecular diffusivity is $D^{mol}_{CO,CO_2} = 1.75\times10^{-4} m^2\ s^{-1}$, the average diameter of the Fe_2O_3 particles is $d_{Fe_2O_3} = 380\ \mu m$. So $Sc = 0.807$, $Re = 1.075$, and $Sh_p = 3.07$.

Thus, the mass transfer coefficient $k_g^{Fe_2O_3} = Sh_p D^{mol}_{CO,CO_2}/d_{Fe_2O_3} = 1.69\ m\ s^{-1}$. C_{CO} is the molar concentration of CO in the bulk phase, and the molar concentration of CO on the surface of the Fe_2O_3 particle is assumed to be zero. So the reaction rate of a Fe_2O_3 particle under external mass transfer control is $k_g^{Fe_2O_3} A_{Fe_2O_3} C_{CO}$, where $A_{Fe_2O_3} = 4\pi\left(\frac{d_{Fe_2O_3}}{2}\right)^2$ is the surface area of the Fe_2O_3 particle. The ratio of the kinetic rate to the mass transfer rate is $k_{Fe_2O_3}/k_g^{Fe_2O_3} A_{Fe_2O_3}$. Here, the ratio is equal to 0.82, so both kinetics and external mass transfer should be considered. The reaction rate is then given as,

$$(1-\varepsilon_{mf})(1-\varepsilon_{Fe_2O_3})\xi_{CO} = \left(\left(1-\varepsilon_{mf}\right)\left(1-\varepsilon_{Fe_2O_3}\right)+1\right)\frac{C_{CO}}{\frac{V_{Fe_2O_3}}{A_{Fe_2O_3}k_g^{Fe_2O_3}}+\frac{1}{k_{Fe_2O_3}}} \quad (A.6)$$

The deviation of the equation above is shown in the Appendix A.

According to the stoichiometry,

$$\xi_{CO} = -\xi_{CO_2} \quad (3.47)$$

3.2.2.2 *The combustion of char particles using CuO particles as fluidising material*

The main difference between CuO and Fe_2O_3 is that CuO decomposes at high temperature when C_{O_2}, the O_2 concentration, is lower than $C_{O_2}^{eq}$, the equilibrium O_2 concentration of the reaction, and produces O_2 and Cu_2O,

$$4CuO = 2Cu_2O + O_2 \tag{3.48}$$

In the boundary layer, the O_2 concentration increases from the surface of the char particle to the outer layer, so there is a layer around the char particle where the O_2 concentration is lower than the equilibrium O_2 concentration of the reaction, as shown in Figure 3.2.

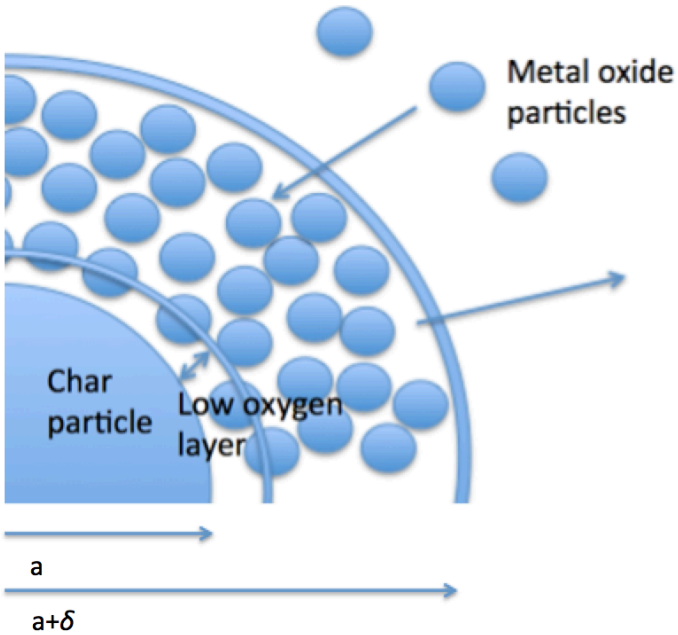

Figure 3.2 The low oxygen layer around the char particle. In the layer, C_{O_2} is lower than $C_{O_2}^{eq}$, and CuO particles decompose in the layer.

In this layer, oxygen is supplied both from diffusion and CuO decomposition. If the CuO decomposition is fast enough, C_{O_2} on the surface of the char particle is no

longer zero, and the char particle combustion is not external mass transfer controlled. If the CuO decomposition is not fast enough, C_{O_2} on the surface of the char particle is still zero, and the char particle combustion is external mass transfer control. Thus, it is important to compare the rate of CuO decomposition and external mass transfer.

The external mass transfer rate here is a lower bound estimate of rate, since it is assumed that the O_2 concentration on the surface of char particle is zero.

The kinetics of reaction (3.48) are given by Hu et al. (Hu et al. 2016),

$$R_{CuO} = 632exp\left(-\frac{59700}{RT}\right)\left(C_{O_2}^{eq} - C_{O_2}^{s}\right)(1 - X_{CuO}) \tag{3.49}$$

where R_{CuO} is the rate of conversion change of CuO, $C_{O_2}^{eq}$ is the equilibrium molar concentration of O_2 for the reaction. When reaction (3.48) is under kinetic control, the expression of $m\xi_{O_2}$ is given as,

$$(1 - \varepsilon_{mf})(1 - \varepsilon_{CuO})\xi_{O_2} = (1 - \varepsilon_{mf})(1 - \varepsilon_{CuO})\frac{dX_{CuO}}{dt} \times \frac{\frac{\rho_{CuO}}{m_{CuO}}}{4}$$

$$= \left(1 - \varepsilon_{mf}\right)(1 - \varepsilon_{CuO}) \times 1.25 \times 10^7 exp\left(-\frac{59700}{RT}\right)\left(C_{O_2}^{eq} - C_{CuO,O_2}^{s}\right)(1 - X_{CuO}) \tag{3.50}$$

where $\rho_{CuO} = 6.315\ \mathrm{g/cm^3}$ is the density of CuO, and $\varepsilon_{CuO} = 0.6$; $m_{CuO} = 80 g/mol$ is the formula weight of CuO; 4 is the stoichiometric coefficient for O_2. X_{CuO} is assumed to be small, so $1 - X_{CuO} \approx 1$. Thus, $m\xi_{O_2}$ becomes,

$$(1 - \varepsilon_{mf})(1 - \varepsilon_{CuO})\xi_{O_2} = 3 \times 10^6 exp\left(-\frac{59700}{RT}\right)\left(C_{O_2}^{eq} - c_{O_2}\right) \tag{3.51}$$

where C_{O_2} is the molar O_2 concentration, and CuO only produces O_2 when $C_{O_2}^{eq}$ is higher than C_{O_2}.

External mass transfer also has to be considered. Equation (3.51) reaches

maximum when $C^{S}_{CuO,O_2} = 0$. The equilibrium oxygen mole fraction at 1173 K is 1%, and $C^{eq}_{O_2} = 0.1\, mol\, m^{-3}$. The average diameter of the CuO particles is $d_{CuO} = d_{Fe_2O_3}$ =380 μm. So the maximum kinetic reaction rate for a CuO particle is $(1-\varepsilon_{CuO})\xi_{O_2} V_{CuO} = 3.15\times10^{-8} mol\, s^{-1}$

For reaction (3.48) at 1173K, $D^{mol}_{O_2,N_2} = 2.25\times10^{-4} m^2\, s^{-1}$, $Sh_p = 3.07$, and the mass transfer coefficient of CuO particle for reaction (3.48) is $k_g^{CuO,O_2} = Sh_p D^{mol}_{O_2,N_2}/d_{CuO} = 1.82$. When $C_{O_2} = 0$, and the O_2 concentration on the surface of the CuO particle $C^{S}_{O_2} = 0.1\, mol\, s^{-1}$, the external mass transfer rate for a CuO particle is $k_g^{CuO,O_2}(C^{S}_{O_2} - C_{O_2})\, A_{CuO} = 8.25\times10^{-8}\, mol\, s^{-1}$, which is about 2.6 times that for kinetic control. Thus, both kinetics and external mass transfer rates are considered, and the reaction rate expression of reaction (3.48) is given as,

$$\left(1-\varepsilon_{mf}\right)(1-\varepsilon_{CuO})\xi_{O_2} = \left(\left(1-\varepsilon_{mf}\right)(1-\varepsilon_{CuO})+1\right)\frac{C_{O_2}}{\frac{V_{CuO}}{A_{CuO}k_g^{CuO,O_2}}+\frac{1}{k_{CuO,O_2}}} \qquad \text{(A.7)}$$

where $k_{CuO,O_2} = 3\times10^{6} exp\left(-\frac{59700}{RT}\right)$ is the effective reaction rate constant for reaction (3.48).

Using Equation (A.7), the oxygen production rate from CuO decomposition for a char particle is $3.24\times10^{-7}\ mol\, s^{-1}$; the external O_2 transfer rate for a char particle is $\frac{ShD^{mol}_{O_2,N_2}}{d} C^{p}_{O_2} \pi d^2 = 8.9\times10^{-6} mol\, s^{-1}$, where $C^{p}_{O_2} = 2.1\, mol\, m^{-3} s^{-1}$ is the molar concentration of oxygen in the particulate phase. Here, the oxygen production rate from CuO decomposition is just about 4% of the external O_2 transfer rate, which means that the oxygen flux on the surface of the char particle just increases 4% with CuO decomposition, which is not enough to make the char combustion reaction

kinetics controlled. Thus, when CuO particles are used as the fluidising material, the char particle combustion is still external mass transfer controlled.

Similar to Fe_2O_3, CuO can be reduced to Cu_2O by CO in the boundary layer, and the reaction is,

$$CuO + CO = Cu + CO_2 \tag{3.52}$$

The kinetics of reaction (3.52) is given by many researchers, such as Garcı´a-Labiano et al. (Juan Adanez et al. 2012). However, most of the measurements were taking place in thermogravimetry, and Plewa (Plewa and Skrzypek 1989) pointed out that when the temperature is between 398 and 473 K, the apparent activation energy is 44 kJ/mol; when the temperature is above 473 K, the apparent activation energy is almost 0 and the reaction becomes external mass transfer control. Thus, the reaction rate of reaction (3.52) under external mass transfer control is given as,

$$(1-\varepsilon_{mf})(1-\varepsilon_{CuO})\xi_{CO} = \frac{A_{CuO}(1-\varepsilon_{mf})}{V_{CuO}} k_g^{CuO,CO}(C_{CO} - C_{CO}^s) \tag{3.53}$$

where ε_{CuO} is the voidage of the CuO particle; $A_{CuO} = 4\pi\left(\frac{d_{CuO}}{2}\right)^2$ and $V_{CuO} = \frac{4}{3}\pi\left(\frac{d_{CuO}}{2}\right)^3$ are the outer surface area and the volume of the CuO particle, respectively; d_{CuO} is the diameter of the CuO particle; $k_g^{CuO,CO} = Sh_p D_{CO,CO_2}^{mol}/d_{CuO}$ is the mass transfer coefficient of CuO particle for reaction (3.52), C_{CO}^s is the molar concentration of CO on the surface of the CuO particle, which is assumed to be zero under external mass transfer control. This reaction is assumed to run in parallel with the oxygen decomposition reaction.

3.2.3 The assumptions for the fluidised bed

There are two assumptions for the fluidised bed: 1) very small amount of char or metal is added to the fluidised bed, so the concentration of bulk gas in the particulate phase can be considered as same as in the inlet gas; 2) there is no cross flow limitation.

3.2.4 The solution of model equations

The Matlab ODE solver, ode45, is employed to solve Equation (3.3) – Equation (3.6) and Equation (3.29) – Equation (3.32). The unknown variables of those equations are put into one state vector ϕ,

$$\phi = [J_{CO}, J_{CO_2}, J_{N_2}, J_{O_2}, x_{CO}, x_{CO_2}, x_{N_2}, x_{O_2}] \tag{3.54}$$

And the derivative of vector ϕ, $d\phi/dr$, is given as,

$$\frac{d\boldsymbol{\phi}}{dr} = \left[\frac{J_{CO}}{dr}, \frac{J_{CO_2}}{dr}, \frac{J_{N_2}}{dr}, \frac{J_{O_2}}{dr}, \frac{x_{CO}}{dr}, \frac{x_{CO_2}}{dr}, \frac{x_{N_2}}{dr}, \frac{x_{O_2}}{dr}\right] \tag{3.55}$$

The boundary conditions on the surface of char particle are given by guessing three variables: J_{CO_2}, x_{CO} and x_{CO_2}. Then ODE45 steps forwards to the outer edge of the boundary layer. If the initial guesses are wrong, that is, the values at the edge of the boundary layer are incorrect, the initial guesses are changed iteratively until reasonable the outer values match the required boundary conditions. This was accomplished here using the Matlab function Fsolve to alter the three variables on the surface so that the correct values on the boundary were achieved.

3.3 RESULTS AND DISCUSSION

The reference conditions in the simulations are: Sh_0 is 0.88 (Hayhurst and Parmar 2002); pressure is 101325 Pa and temperature is 1173K; Sherwood number (Sh) is 2, the diameter of char particle is 3 mm, the ratio of CO/CO_2 is given by Arthur (Arthur 1951), 10.5, and the percentage of water $[H_2O]$ is 1.3%. All Sherwood numbers here are the EMCD equivalent Sherwood number.

The influences of different parameters are tested individually, by changing only one parameter. For instance, $Sh = 2.5$ means that only Sherwood number Sh is changed into 2.5, and other conditions are still the same as the reference conditions.

Cases 1 to 4 are defined as: (case 1) a char particle using sand as fluidising material with no CO combustion in the boundary layer; (case 2) a char particle using sand as fluidising material with CO combustion in the boundary layer; (case 3) a char particle using Fe_2O_3 particles as fluidising material; (case 4) a char particle using CuO particles as fluidising material. It is worth mentioning that for case 3 and case 4, CO could be oxidized into CO_2 in the boundary layer by Fe_2O_3 or CuO. The diagrams of cases 1 to 4 are shown in Figure 3.3.

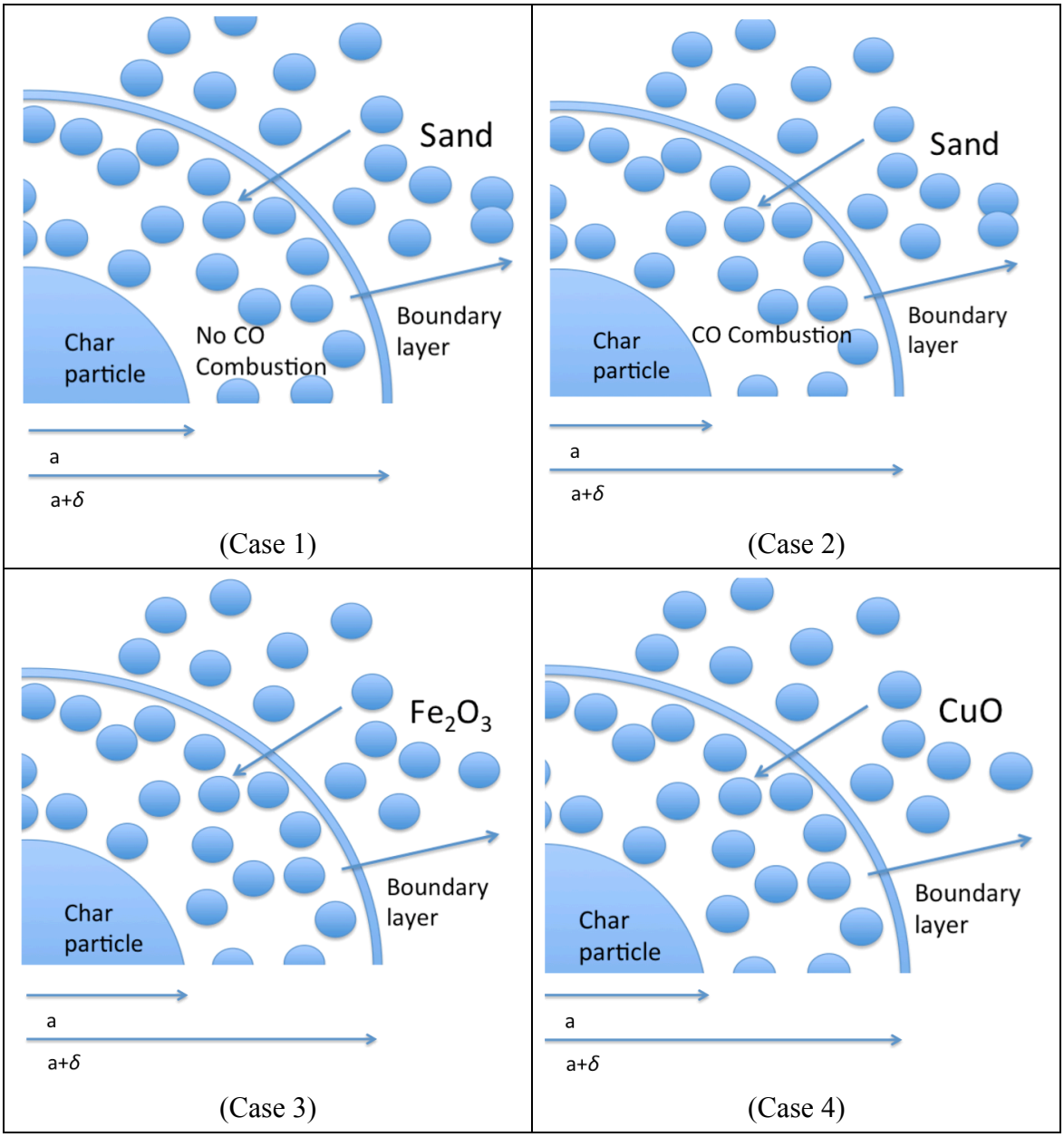

Figure 3.3 The diagrams of cases 1 to 4.

In Figure 3.4, the rates of carbon consumption for different cases are compared, and the rates of oxygen consumption decreases in the order: case 1 > case 2 ≥ case 3. Case 4 is special, and has to be discussed separately. The carbon consumption rate in case 1 is about 16% - 18% higher than in both case 2 and case 3; case 2 is a little bit faster than case 3. There are two reasons to explain why case 2 and 3 are slower than case 1,

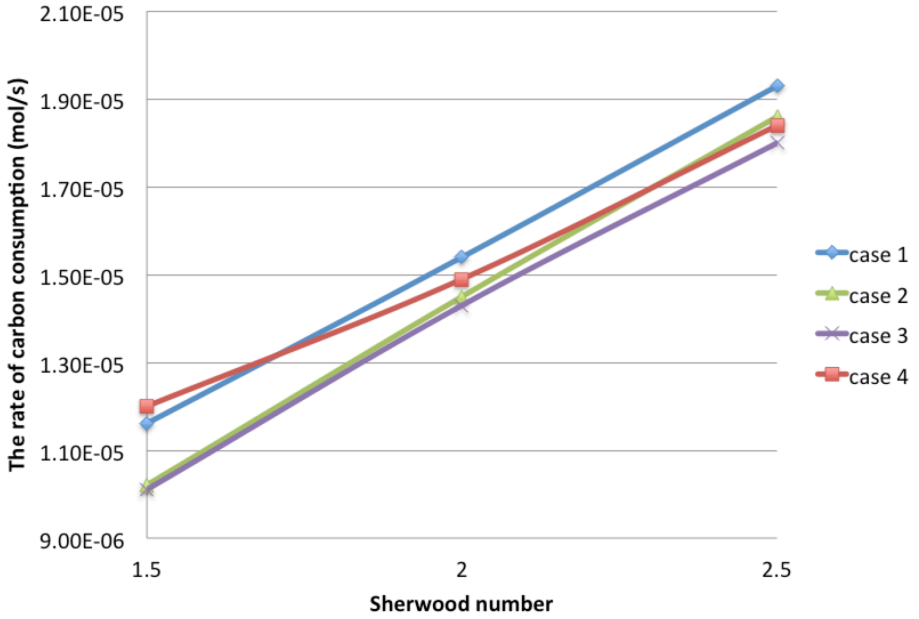

Figure 3.4 A comparison of Sherwood number versus the rate of carbon consumption at 1173K for cases 1 to 4.

1) For both case 2 and case 3, CO is oxidized into CO_2 in the boundary layer, and the diffusivity of CO_2 is smaller than CO. In the case 2 from oxygen diffusing in from the bulk and in case 3 by from the iron oxide. CO combustion decreases x_{CO} and increases x_{CO_2} in the boundary layer, compared to case 1, as shown in figure 5. For case 2, x_{CO}^{s} decreases from 30% to 26.2%, and $x_{CO_2}^{s}$ increases from 4% to 6.2%. For case 3, the changes are much bigger; x_{CO} decreased from 30% to 4.5% and $x_{CO_2}^{s}$ increases from 4% to 32.2%; when $r = 1.15a_c$, all CO from the char surface is oxidized to CO_2. At 1173K, $D_{CO_2,O_2}^{mol} = 1.75\times10^{-4}\ m^2/s$ is lower than $D_{CO,O_2}^{mol} = 2.21\times10^{-4}\ m^2/s$. Thus, if CO becomes CO_2, the diffusivity would decrease.

2) For case 2 (but note case 3), oxygen is consumed in the boundary layer i.e. oxygen diffused into the boundary layer is consumed on the way to the char

particle, and the O_2 flux on the char particle surface becomes smaller, so there is less O_2 for the char combustion. Thus most of the change in rate arises from more a larger amount of O_2 needing to be diffused into the boundary layer to produce the same carbon flux. In the limiting case of very fast combustion, this would result in all of the carbon leaving the surface as CO_2, which leads to half the rate of combustion compared to just producing CO. This is further discussed in Chapter 4.

Case 4, in which copper oxide is in the boundary layer, has two characters: 1) its carbon consumption rate is generally in between: case 1 $>\approx$ case 4 $>\approx$ case 2 $\geq$ case 3; 2) when the value of Sherwood number increases, the slope of carbon consumption rate is smaller than other three cases. These two characters can be explained by two reasons,

1) CuO decomposition near the surface of char particle. CuO particles decomposes and produce oxygen when $C_{O_2} < C_{O_2}^{eq}$, that is, near the surface of the char particle. The oxygen production from CuO decomposition increases the oxygen flux to the surface of char particle, and the carbon consumption rate;
2) CO oxidation in the boundary layer. Similar to Fe_2O_3, CuO oxidizes CO into CO_2 in the boundary layer. As discussed above, CO oxidation decreases the diffusivity, which would tend to decrease diffusivity.

CuO decomposition rate is not a function of Sherwood number. However, the CO flux in the boundary layer is a function of the O_2 supplied to the boundary layer, which is a function of Sherwood number. When the Sherwood number is small (e.g.

$Sh = 1.5$), CuO decomposition is more important, so the carbon consumption rate of case 4 at $Sh = 1.5$ is the faster than the other cases. When the Sherwood number becomes larger, O_2 flux into the boundary layer is more important, so the carbon consumption rate of case 4 becomes more similar to case 2 and case 3

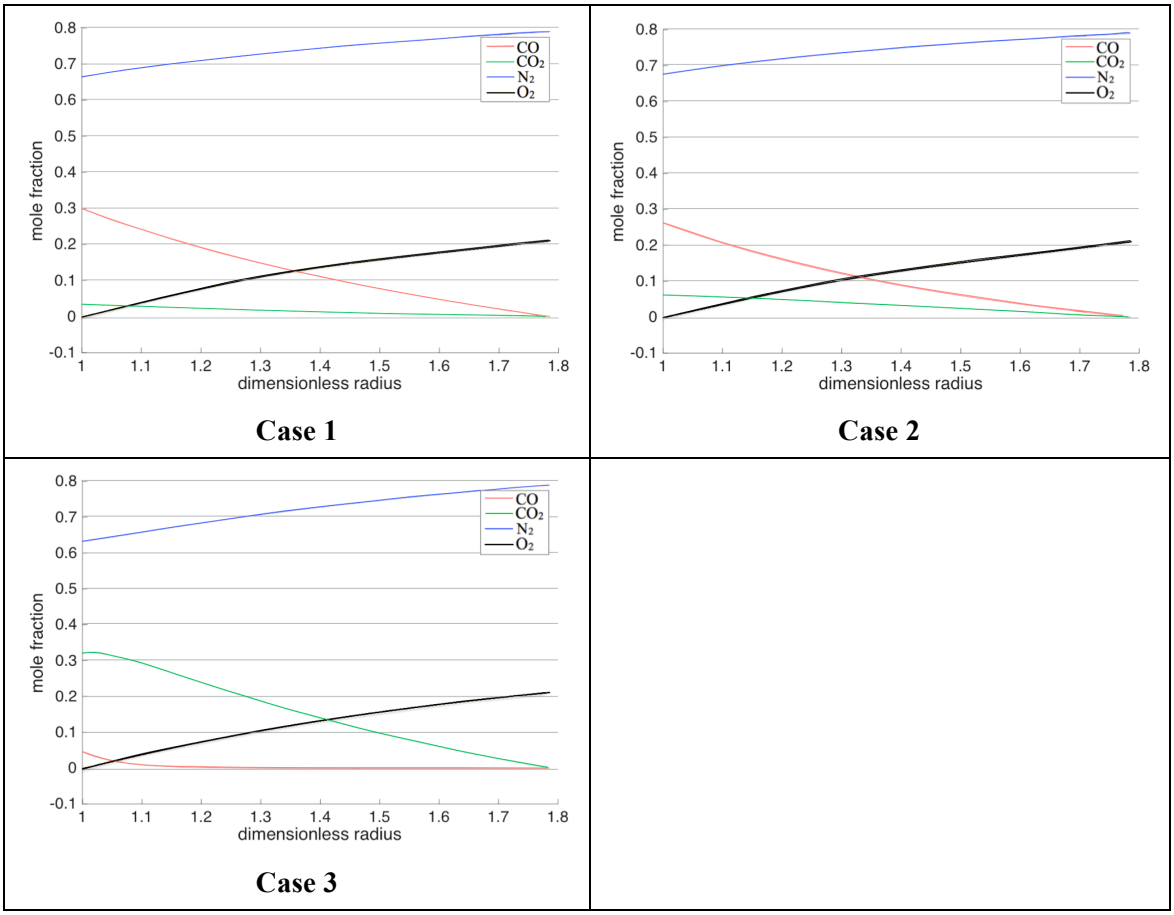

Figure 3.5 The molar fractions of CO, CO_2, N_2 and O_2 for case 1, case 2 and case 3 when $Sh = 2$.

Figure 3.6 compares the rate of oxygen consumption versus Sherwood number at 1173K for different cases. In case 2, oxygen is consumed at the surface of the char particle and in the boundary layer, so it has the largest oxygen consumption rate; in case 3 and case 4, metal oxide particles oxidize CO in the boundary layer, so there is no oxygen consumption in the boundary layer. In addition, the carbon consumption

rates for case 3 and case 4 are lower than case 1, which leads to lower oxygen consumption on the char particle surface. Thus, the total oxygen consumption rates for case 3 and case 4 are lower than case 1. The oxygen consumption rate for case 4 is a little lower than case 3, which is because, in case 4, CuO particles produce oxygen, so there is less need for oxygen from the particulate phase.

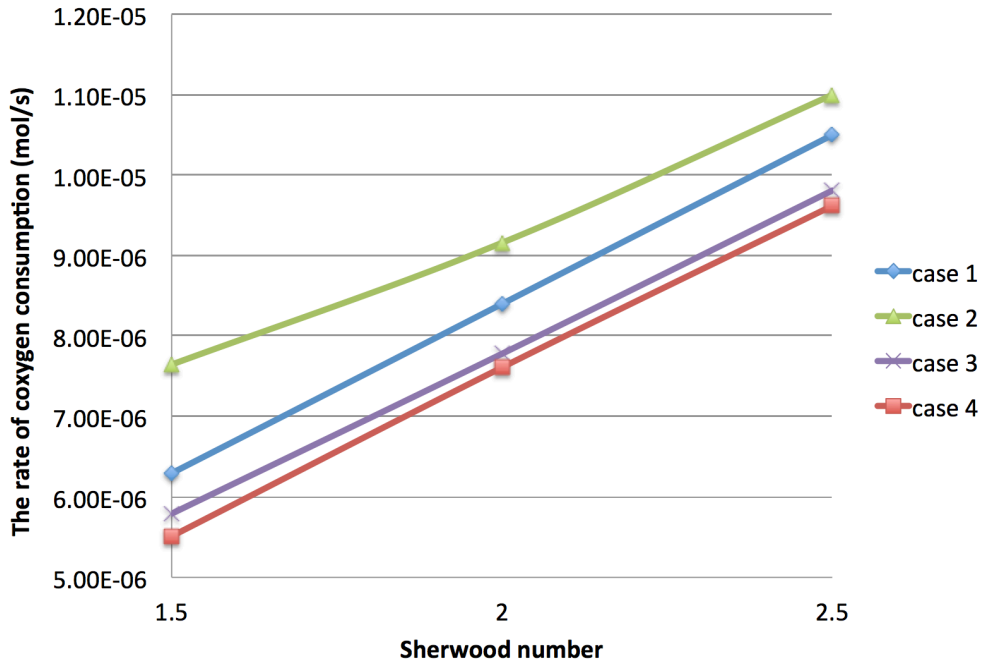

Figure 3.6 The rate of oxygen consumption versus Sherwood number at 1173K for cases 1 to 4.

In the previous results, the ratio of CO to CO_2 produced at surface of the char correlation was fixed to be 12, based on the correlation of Arthur (Arthur 1951). Figure 3.7 shows the effect of different primary ratios of CO to CO_2 on the rate of carbon consumption at 1173K for different cases. The rates of carbon consumption for all cases increase with the increase of the ratio of CO/CO_2. This is because 1 mol oxygen can produce 2 mol CO, but just 1 mol CO_2. So if the ratio of CO/CO_2 increases, the same amount of oxygen can oxidize more carbon. When CO/CO_2 =

0.001, that is, almost all product is CO_2, the rates of carbon consumption for all cases the same. The exception is case 4, which is higher than others by about 6%, because CuO particles produce oxygen, which increases the rate of carbon consumption. As the ratio of CO/CO_2 increases, there is more CO in the boundary layer, and the decrease of carbon consumption rate due to CO oxidation in the boundary layer becomes more important, so the char consumption rate is case 1 > case 4 > case 2 > case 3, which is due to the same reasons of Figure 3.4.

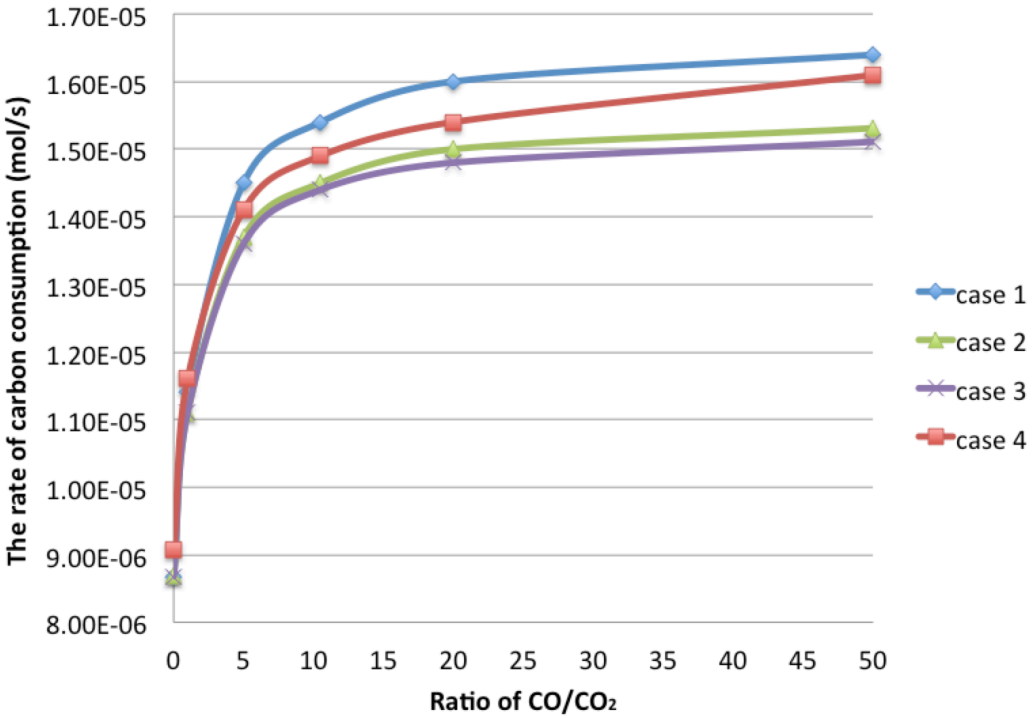

Figure 3.7 The ratio of CO/CO_2 leaving the surface of the char particle at 1173K for cases 1 to 4, when $Sh = 2$.

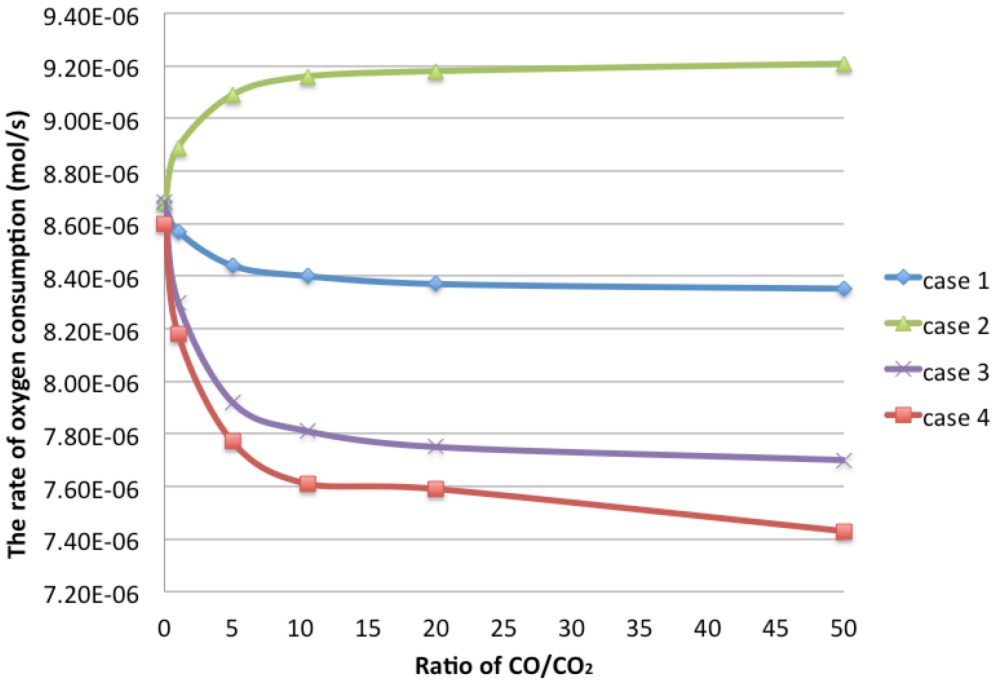

Figure 3.8 The ratio of CO/CO_2 versus the rate of oxygen consumption at 1173K for cases 1 to 4.

Figure 3.8 compares the ratio of CO/CO_2 versus the rate of oxygen consumption at 1173K for cases 1 to 4. The sequence of oxygen consumption rate is case 2 > case 1 > case 3 > case 4, which is same as in Figure 3.6 for the same reasons. When $CO/CO_2 = 0.001$, oxygen consumption rates are same except for case 4 (1.5% lower than others), which is because of oxygen production from CuO decomposition (same as in Figure 3.7). When the ratio of CO/CO_2 increases, oxygen consumption rates decreases for all cases except for case 2. This is because that for case 2, higher CO/CO_2 ratio leads to less oxygen consumption on the char particle surface and more CO combustion in the boundary layer, and the latter one is more important. Thus, the net effect is the increase of oxygen consumption.

3.4 CONCLUSIONS

1) CO combustion in the boundary layer leads to a smaller carbon consumption rate, because the diffusivity of CO_2 is smaller than CO. It also leads to a larger oxygen consumption rate, because CO combustion in the boundary layer needs more oxygen. However, the effect of CO combustion in the boundary layer is not large, and its effect is likely to be an overestimate owing to radical quenching.
2) Using Fe_2O_3 particles as fluidising materials slows down the carbon consumption rate, since the diffusivity of CO_2 is smaller than CO. Using CuO particles as fluidising materials at small Sherwood number ($Sh = 1.5$) makes the carbon consumption rate faster, since CuO decomposition produces O_2 near the surface of char particle; at large Sherwood number ($Sh = 2$ or 2.5), the rate of CO combustion in the boundary layer becomes larger and partly compensates for the oxygen produced by CuO decomposition, so the net effect is that CuO particles slow down the carbon consumption rate at large Sherwood number ($Sh = 2$ or 2.5). Both Fe_2O_3 and CuO particles decrease the oxygen consumption rate, since a part of oxygen required for the carbon consumption or CO combustion is from the active particles.

CHAPTER 4 THE COMBUSTION OF A CHAR PARTICLE AT LOW OXYGEN CONCENTRATION IN A FLUIDISED BED UNDER EXTERNAL MASS TRANSFER CONTROL

4.1 INTRODUCTION

The combustion of char is quite complex due to different factors, such as the oxidation of CO in the boundary layer, and the active fluidising materials. However, using CuO as fluidising material could make this process more complex, since it could produce O_2 in the boundary layer. Exploring the combustion process using CuO as fluidising material could help people have a deeper understanding of the char combustion.

4.2 OBJECTIVES

In the previous chapter, the char particle combustion using inert (sand) or active (Fe_2O_3 or CuO) fluidising materials in fluidised bed in air was discussed. The main difference between Fe_2O_3 and CuO as the fluidising material is that CuO produces O_2 when O_2 concentration is low. However, in Chapter 3, air is used as the fluidising gas, which has much higher O_2 concentration (21%) than the O_2 concentration for CuO to produced O_2, and the effect of CuO decomposition may not be apparent due to this reason. Thus, in this chapter, the situation when the fluidising gas is low O_2 concentration gas, rather than air, is studied. In addition, for the active fluidising

material, only CuO is used since it can both oxidize CO in the boundary layer and produce O_2 when the O_2 concentration is lower than the equilibrium value for reaction

$$4CuO \leftrightarrow 2Cu_2O + O_2 \quad (4.1)$$

The experimental temperature is set at 1223K, since at this temperature, CuO decomposition is fast, and the effects from CuO decomposition are clearer. The equilibrium O_2 concentration for CuO decomposition is about 4% at 1223K, so three O_2 concentrations were chosen for the experiments: 5% O_2 + 95% N_2, 1% O_2 + 99% N_2 and pure N_2 (in the following paragraphs, 5% O_2 + 95% N_2 and 1% O_2 + 99% N_2 will be referred to as 5% O_2 and 1% O_2 for the sake of simplicity). 5% O_2 is used because compared to air, its overall reaction time is longer. The response time for the CO/CO_2 analyser is around 5 seconds, so using 5% O_2 concentration gas means the analyser response does not influence the measurements. 1% and zero (pure N_2) O_2 concentration are chosen since their O_2 concentrations are lower than the equilibrium O_2 concentration. In addition, the results from the sand experiments are used as a control experiment for comparison.

4.3 EXPERIMENTAL

4.3.1 Fluidised bed reactor

Figure 4.1 shows an externally heated fluidising bed reactor (i.d. 21 mm), made from an alumina tube, and it was contained in a tubular furnace (Lenton). The distributor was made from irregular shaped recrystallised alumina (Boud Minerals

and Polymers, 1.4 mm), held in place by Fortafix^{TM} cement. The thickness of the distributor is about 20 mm, and it was 10 cm from the bottom of the tube and 5 cm from the base of the furnace. The temperature of the bed was measured by a K-type thermocouple, which was inserted from the top of the bed, so that the tip was about 10 mm above the distributor. The temperature of the reactor was set at 1223K. 5.8 ml silica sand or CuO particles (355-425 μm) were used as fluidising material, and was fluidised with pure N_2 or compressed air at different O_2 concentrations with U/U_{mf} ~7. The bed height before fluidization is 1.7 cm. The superficial velocity, which is defined as volume flow rate of inlet gas / cross section area of the fluidised bed, is 0.078 m/s for sand experiments, and 0.0514 m/s for CuO experiments. The high flow rate of fluidising gas is sufficient to ensure there is no air sucked into the sample line; the flow rate of the fluidised bed was at least twice the sample line gas flow rate (0.5L/min).

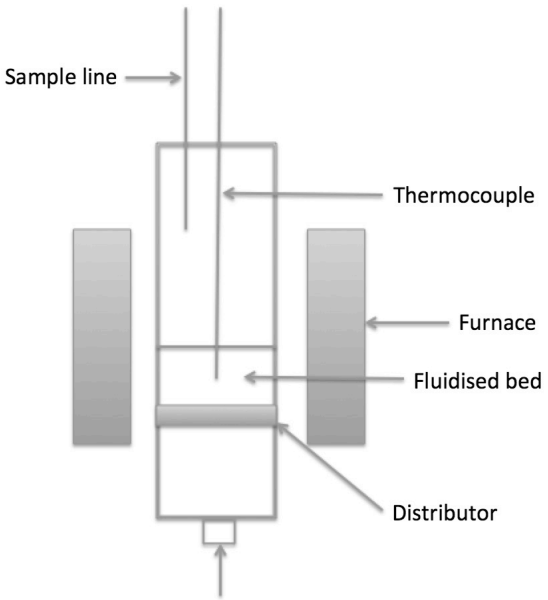

Figure 4.1 The schematic diagram of the alumina reactor.

4.3.2 Material

5.8 ml 355-425 μm silica sand was used, which were described in detail in Chapter 2. 5.8 ml 355-425 μm CuO particles were used. The recipe of CuO particles is adapted from Donat (Donat et al. 2015): 19.7g $Al(OH)_3$ and 9.38g $Ca(OH)_2$ were mixed together with de-ionised water, and the mixture was stirred on a magnetic hot plate at 313K for 2 hours. The dissolution of atmospheric CO_2, rather than CO_2 from a cylinder is used for the formation of Ca-Al layered double hydroxides. It is because that using the atmospheric CO_2 could produce CO_3^{2-}ions, which is helpful for the formation; but using CO_2 from a cylinder could produce HCO_3^- ions, which could reduce the repeatability of the synthesis process. Then 30g CuO powder was added to the mixture, and the mixture was stirred at 353K for 24 hours, so most of water had evaporated, forming a paste. The paste was then put in an oven at 373K for 24 hours, and the dried mixture was crashed and sieved to 355-425 μm. The sieved particles were fired in a furnace at 1273K for 6 hours. The calcined particles were sieved again to give 355-425 μm particles, and 5.8 ml CuO particles were measured for experiments. The material was characterised by powder X-ray diffraction (XRD) analysis (Donat et al. 2015), and the results indicate that calcium aluminate phase consists of $Ca_{12}Al_{14}O_{33}$ and $CaAl_2O_4$, and copper phase consists of CuO.

Spherical active carbon particles at the diameter size of 3 mm with commercial name "Matrix Carbon^{TM} (Seachem Laboratories, Inc.)" were used as fuel. The content of Matrix Carbon was measured to be 85% carbon, 10% moisture and 5% ash. Its density is 0.49 g/cm^3, and pore volume is 0.55-0.65 ml/cm^3. The char particles' sizes

were measured by caliper and the particles with the diameter of 2.9 – 3.1 mm were chosen. All these properties of active carbon particles are from the product description.

4.3.3 Gas analysis

For CuO experiments, CuO could act as an O_2 reservoir, meaning that the measured O_2 consumption rate might not be proportional to the rate of carbon conversion (and hence combustion). Thus, it is important to know the CO and CO_2 production rates. The off gases from the bed were anlaysed by NDIR analyzers for CO and CO_2, and a paramagnetic sensor for O_2. The gases were first passed through a $CaCl_2$ trap to remove moisture. The response time of the system when U/U_{mf}=7 at 1223K was ~10 s for all species (O_2, CO_2 and CO), as shown in the appendix. The deconvolution of the measurements is shown in the Appendix B.

ABB analyser, rather than UEGO, which is more accurate, is used in the experiments. It is because that: 1) in this chapter, CO, CO_2 and O_2 are measured. UEGO can only measure O_2, but ABB can measure all gaseous species; 2) there are difficulties in using both ABB analyser and UEGO. The inner diameter of the fluidised bed reactor is small, and it is hard to put sample lines of both ABB analyser and UEGO into the fluidised bed reactor at the same time; in addition, using two gas analyzers means higher sample line gas flow rate. The superficial velocities in *Section 4.2.1* have been quite large, so it is unwise to increase them. To ensure there is no air sucking into the fluidised bed reactor, there should only be one gas analyser used.

4.3.4 Experimental method for char particle combustion using CuO particles as fluidising material for oxygen concentrations below equilibrium

In the ideal experimental situation, the amount of CuO particles would be abundant, and produce enough O_2 to maintain the O_2 concentration at the equilibrium concentration. However, in the experiment performed here, the amount of CuO is limited and so the O_2 concentration initially reaches the equilibrium concentration, then gradually drops. In this case, when the char particle is dropped into the fluidised bed will influence the result. Here, the CuO particles are heated up in the fluidised bed to 1223K using air as the fluidizing gas. During the heating up period, the O_2 concentration of fluidised gas is higher than the equilibrium O_2 concentration of CuO decomposition, so no CuO will decompose. When the temperature of fluidised bed has reached 1223K, the fluidised gas is suddenly switched to 1% O_2 or pure N_2 by a solenoid valve. When the O_2 concentration in the fluidised bed drops to the equilibrium concentration, the fluidised bed is assumed to be completely purged and the char particle could be dropped into the fluidised bed.

Figure 4.2 shows how the concentration of O_2 changes during a switch from air to 1% O_2. Figure 4.2 suggests that the equilibrium O_2 concentration for CuO decomposition is about 2.7% at 110s, that is, the turning point. For the equilibrium O_2 concentration of CuO decomposition,

$$4CuO \leftrightarrow 2Cu_2O + O_2 \tag{4.1}$$

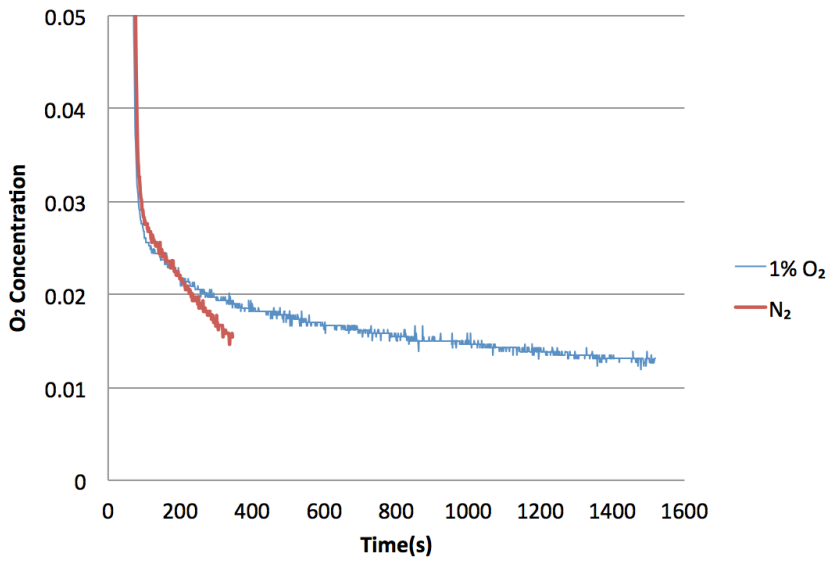

Figure 4.2 The measurement of O_2 concentration during CuO decomposition at 1223K in the fluidized bed with U/U_{mf} =7. CuO particles were first exposed to air, and then at about 100 s, fluidizing gas was switched to 1% O_2 gas flow or pure N_2.

Different databases give different results. For instance, the result from NASA database is 2.1%, and the result from NIST database is 4.3%. 2.7% is between the results from two databases. After the turning point, the O_2 concentration gradually decreases, and it takes about 1000s for the O_2 concentration to become zero for pure N_2; 2000s for the O_2 concentration to become 1% for 1% O_2 in the inlet.

Figure 4.2 also shows that it takes 25s (from 65s to 90s) for the reactor to reach equilibrium. Thus, the char particle should be dropped into the reactor after 90s, that is, the turning point. In this way, the oxygen consumed by the char combustion was from CuO decomposition rather than residual air in the reactor.

4.4 RESULTS AND DISCUSSION

4.4.1 Char particle combustion in 5% O_2

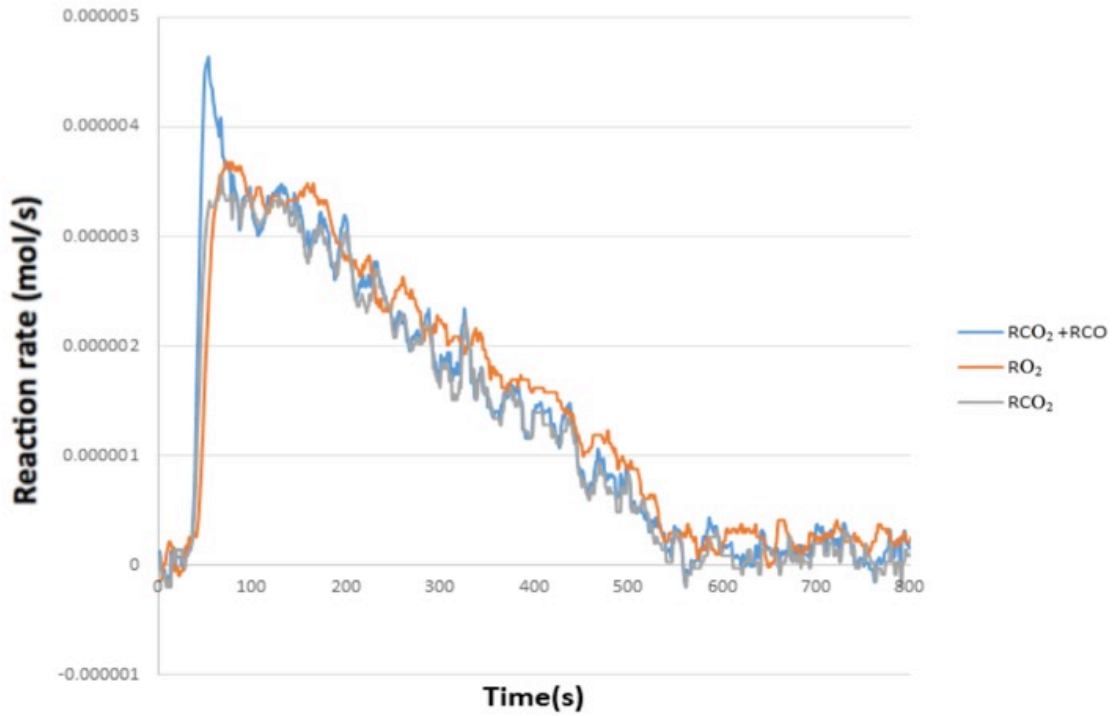

Figure 4.3 The CO_2 production rate (mol/s), CO+CO_2 production rate (mol/s) and O_2 consumption rate (mol/s) for the combustion of a 3 mm char particle at 1223 K, U/U_{mf} = 7, using sand (355-425 μm) as fluidizing material.

Figure 4.3 shows the CO_2 production rate, CO+CO_2 production rate and O_2 consumption rate for the combustion of a 3 mm char particle at 1223K, U/U_{mf} = 7, using sand (355-425 μm) as the fluidizing material. The O_2 consumption rate is defined as the difference between $(0.05 - y_{O_2}) \times total\ molar\ flow$. At the start of the combustion, there is a spike of CO, which is shown in CO+CO_2 production rate, and then CO disappears. Thereafter, the CO_2 production rate is a little lower than the O_2 consumption rate. If the total the oxygen required to produce the total amount of CO + CO_2 is considered, it is generally equal to the total amount of O_2 consumed,

within the measurement error ±5%. The fraction of CO produced is about 8%. There were three repeats for the measurement, and the results were very repeatable with a carbon balance in the range 96.5%-101%.

Figure 4.4 shows the production rate of CO_2 and consumption rate of O_2 for the combustion of a 3 mm char particle at 1223 K, using CuO particles as fluidizing the material. For the CuO experiment at 5% O_2, CuO could decompose in the boundary layer, but because 5% O_2 is higher than the equilibrium concentration measured in Figure 4.3, any Cu_2O in the boundary layer could potentially move back to the bulk particulate phase and be reoxidized into CuO. Thus, CuO could act as a kind of catalyst. There was no CO detected in the experiment, but the shape of CO_2 production rate is quite similar to the shape of CO + CO_2 production rate in Figure 4.3: a spike at the start of the combustion, and a profile similar to that of the O_2 consumption rate after the spike. The total amount of CO_2 produced is equal to the total amount of O_2 consumed, and the spike part is about 7% of the total amount CO_2 produced. Thus, it suggests that when CuO particles are used as fluidizing materials, all CO is oxidized by CuO into CO_2. In addition, the time for the complete reaction for the sand experiment is 550 s, and for the CuO experiment is about 430 s; the initial reaction rate of O_2 for the sand experiment is 3.6×10^{-6} mol/s, and for the CuO experiments is 4.6×10^{-6} mol/s, which means that the combustion becomes faster when CuO particles are used as fluidizing material. There were three repeats for each experiment, and the results were very repeatable: the carbon balance was between 83% and 87%; the conversion time was around 400 s; the initial rates of CO+CO_2

production were between 6.8×10^{-6} and 7.3×10^{-6} mol/s; the initial rates of O_2 consumption are between 4.3×10^{-6} and 4.7×10^{-6} mol/s.

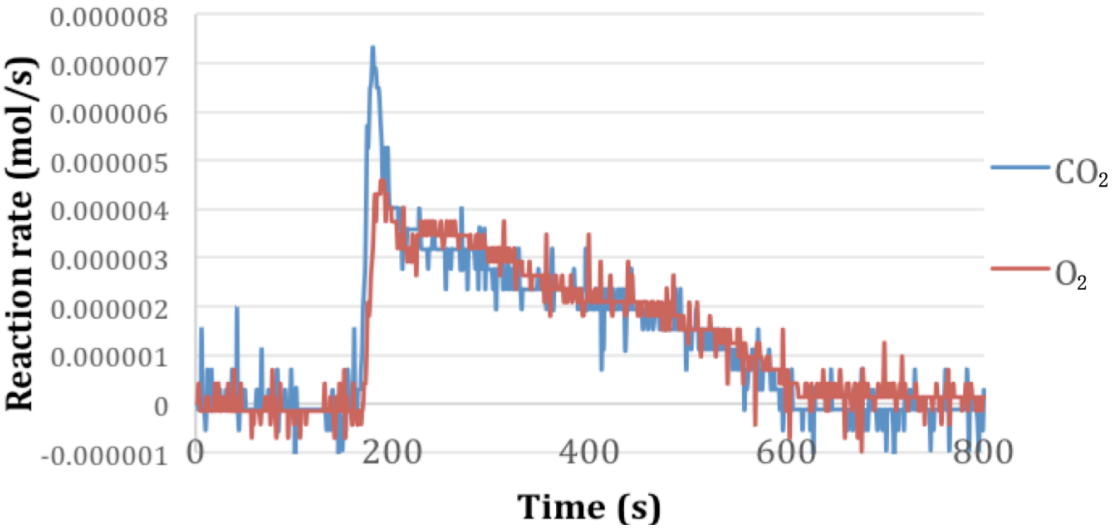

Figure 4.4 The production rate of CO_2 and consumption rate of O_2 for the combustion of a 3 mm char particle at 1223K, U/U_{mf} = 7, using CuO particles (355-425 μm) as fluidizing material.

4.4.2 Char particle combustion at 1% O_2

Figure 4.5 shows the rate of production of CO_2 and CO + CO_2 using sand as fluidizing material and the production rate of CO_2 using CuO particles as the fluidizing material at 1223 K using 1% O_2. There are several similarities between 5% and 1% O_2: 1) there is a CO spike at the start of combustion for the sand experiment; 2) there is no CO produced for the CuO experiment; 3) the combustion rate of the CuO experiment is faster than that of the sand experiment. Combustion in CuO experiments takes 1200 s, and in sand experiments, it takes 1750 s.

In addition, for both sand and CuO 1% O_2 concentration experiments, the

carbon balance reduces to 70% - 75%. There were three repeats for each experiment, and the results were very repeatable: for CuO experiments, the carbon balance was between 75% and 78%; the conversion time was between 1700s and 1750s; the initial rates of $CO+CO_2$ production are between 3.1×10^{-6} and 3.4×10^{-6} mol/s (here, all CO is oxidized by CuO into CO_2, so there is no CO measured); for sand experiments, the carbon balance was between 70% and 75%; the conversion time was between 2000s and 2100s; the initial rates of $CO+CO_2$ production are between 2.1×10^{-6} and 2.3×10^{-6} mol/s.

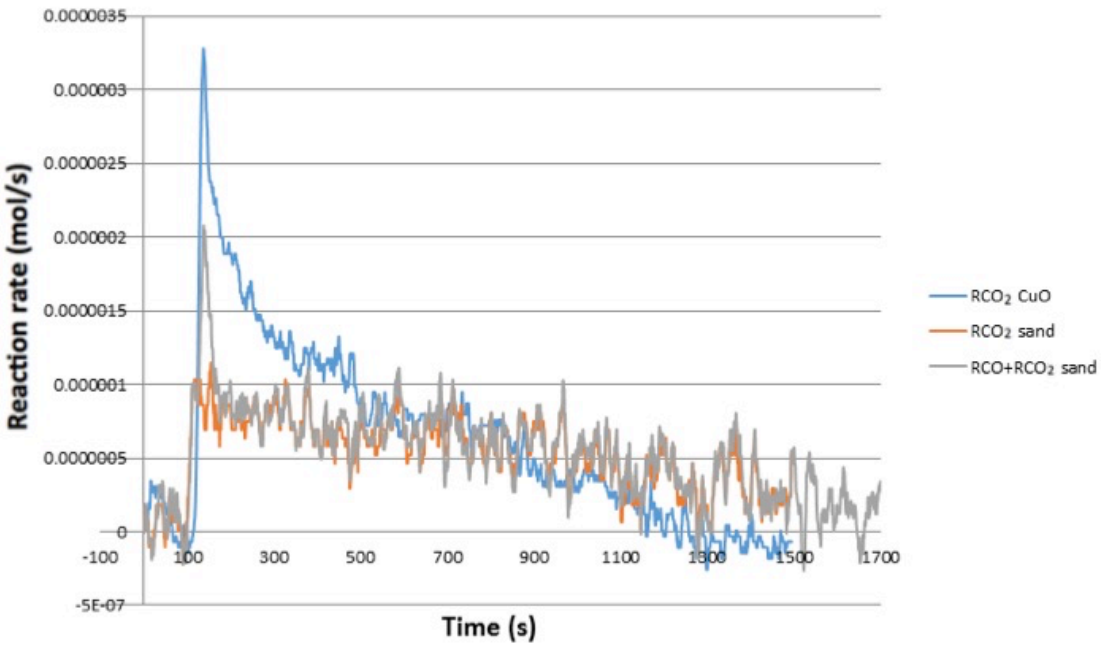

Figure 4.5 The reaction rates of CO_2, and $CO+CO_2$ for the combustion of a 3 mm char particle at 1223K, U/U_{mf} = 7, 1% O_2 concentration, using sand or CuO (355-425 μm) as fluidizing material. All CO is oxidized by CuO into CO_2, so there is no CO measured in CuO experiments.

As discussed above, here, O_2 consumption rate is not calculated when $[O_2]$ is lower than the equilibrium $[O_2]$ for CuO decomposition. According to Figure 4.1, the

average O_2 content of the CuO experiment for the first 200 s is about 2.3%, which is much higher than the sand experiment, (i.e. 1%), which may explain the increase in rate seen initially.

4.4.3 Char particle combustion in pure N_2

Figure 4.6 shows the CO_2 production rate and CO production rate for the sand and CuO experiments in pure N_2. Even in pure N_2, there were still a CO_2 spike and a CO spike, both very small, when the char particle was dropped into the fluidised bed. This is because, before the particle was dropped into the reactor, the porous char particle has absorbed oxygen. The total amounts of CO_2 and CO production were about 0.5% and 1.5% of total carbon, respectively. Since the scale of the noise is similar to production rate scale, there could be some errors in the production rate. The curves here look much worse than the previous ones are because that the pure N_2 environment made the analyser noisier.

For the CuO experiment, comparing to 1% O_2 CuO experiment, the initial reaction dropped by about 20% (from 3.3×10^{-6} mol/s to 2.8×10^{-6} mol/s), and there was no CO detected. There were three repeats for the CuO experiments: the carbon balance was between 75% and 85%; the conversion time was between 1000s and 1100s; the initial rates of $CO+CO_2$ production are between 2.7×10^{-6} mol/s and 3.0×10^{-6} mol/s. Both the carbon balance and conversion time gradually decrease when the O_2 concentration decreases from 5% to zero. The poorer carbon balance may be because signals become smaller, and influence from the noise obscures the

end of the reaction.

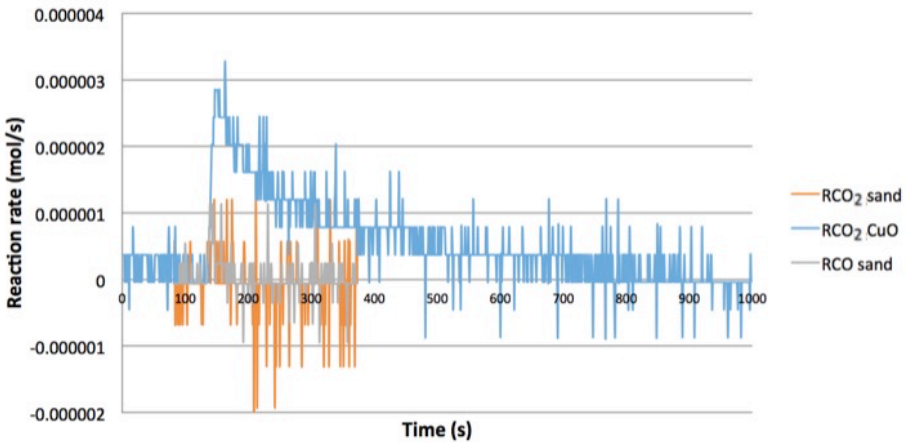

Figure 4.6 The production rates of CO_2 and CO for the combustion of a 3 mm char particle at 1223K, U/U_{mf} = 7, pure N_2, using sand or CuO (355-425 μm) as fluidizing material. All CO is oxidized by CuO into CO_2, so there is no CO measured in CuO experiments.

4.4.4 Validity of mass transfer assumption

In the previous chapter, the char combustion was assumed to be external mass transfer controlled. Thus, before comparison of results between simulations and experiments can be made, it is important to confirm that whether the experiments in this chapter are external mass transfer controlled or not.

The direct way is to compare the simulation results with experimental results. However, a key parameter, the ratio of CO/CO_2, hard to determine from the experiments. For instance, in the sand experiments in 5% O_2, 1223K, the measured ratio of CO/CO_2 is about 0.087, which is not the real CO/CO_2 ratio since CO could be oxidized in the freeboard. Thus, one indirect way to check whether the char

combustion is external mass transfer controlled is to see whether the production rate of CO+CO_2 from experimental results is between two extremes: i.e. only CO or only CO_2 produced on the surface of char particle. The 'reference conditions' of the simulation at 1223K are: the Sherwood number in the stagnant ($Re = 0$) gas is given as $Sh_0 = 2\varepsilon_0$ (Hayhurst 2000), and ε_0 is the voidage of the particulate phase, which is assumed to be 0.44 (Prins et al. 1985). So $Sh_0 = 2\times0.44 = 0.88$; pressure is 101325 Pa; in *Section 2.4.7*, the measured Sherwood number of char particle is around 2.7 - 3, so here the Sherwood number is set to be 3; diameter of char is 3 mm, and the ratio CO/CO_2 is 13.1 from Arthur (Arthur 1951). The comparison of results is shown in Table 4.1.

Table 4.1 A comparison of the production rates of CO+CO_2 from the sand experiments and simulations in 5% and 1% O_2 when CO or CO_2 is the only product on the char particle surface at 1223K.

	Production rate of CO+CO_2 (mol/s) (5% O_2)	Production rate of CO+CO_2 (mol/s) (1% O_2)
Sand experiment	4.7×10^{-6}	1.0×10^{-6}
Only CO (sand simulation, no CO combustion in the boundary layer)	6.5×10^{-6}	1.3×10^{-6}
Only CO_2 (sand simulation, no CO combustion in the boundary layer)	3.3×10^{-6}	6.5×10^{-6}
Only CO (sand simulation, CO combustion in the boundary layer)	6.5×10^{-6}	1.3×10^{-6}
Only CO_2 (sand simulation, CO combustion in the boundary layer)	3.3×10^{-6}	6.5×10^{-6}

In Table 4.1, it is noticeable that CO combustion in the boundary layer has no influence on the production rate of $CO+CO_2$. This is because the reaction rate for CO combustion in the boundary layer is sensitive to O_2 concentration, and when O_2 concentration drops to 5% or 1%, the oxidation rate is slow and has little influence on the production rate of $CO+CO_2$. The production rates of $CO+CO_2$ from sand experiment in 5% and 1% O_2 are both between their corresponding extremes (only CO or CO_2) in the simulation, which suggests that the experiments in this chapter are mass transfer controlled.

The experimental results at other temperatures further support the mass transfer control assumption. In *Section 2.4.2*, Figure 2.4 shows initial reaction rate of 1180-1400 μm char combustion in the alumina reactor using 355-425 μm silicon sand at 973K, 1073K and 1173K. The change of initial reaction rate due to temperature increase is small, so the activation energy is small, indicating that char combustion is mass transfer controlled.

4.4.5 Comparison of experimental results from ABB analyser and UEGO (Universal Exhaust Gas Oxygen)

As mentioned in Chapter 2, there are two advantages of the UEGO sensor: 1) fast response time, which means that, there is no need to deconvolute the results; 2) high sensitivity, which means that it has better carbon balance, especially when the O_2 consumption rate is low. In Figure 4.7, the char particle mass in UEGO and ABB analyser experiments are similar, and the consumption rate of O_2 from ABB analyser

generally overlaps with the consumption rate of O_2 from UEGO, which supports the validity of the measured results. The scale of noise of ABB analyser ($\pm 7\times10^{-7}$mol/s) is much larger than the scale of noise of UEGO ($\pm 1\times10^{-7}$mol/s).

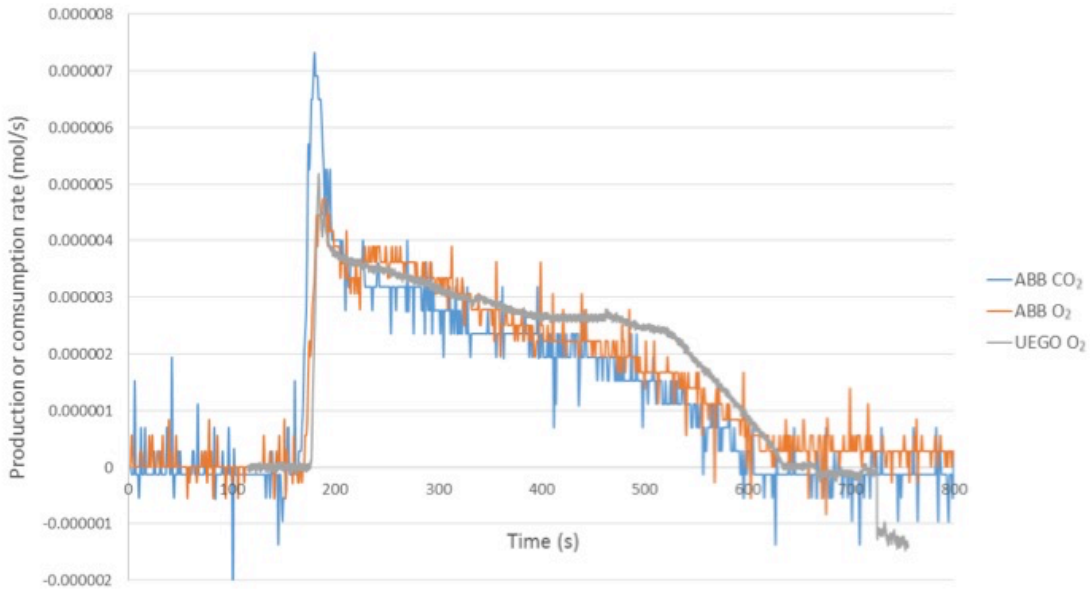

Figure 4.7 A comparison of 1) consumption rate of O_2 from UEGO; 2) production rate of CO_2 from ABB analyser; 3) consumption rate of O_2 from ABB analyser. The experimental conditions are: 21 mm alumina reactor; 1223K, 5% O_2 concentration, U/U_{mf} = 7, using CuO particles as fluidizing material, 1 char particle (3 mm). The char particle mass in UEGO experiment is 0.0169g, and mass balance is 90%; the char particle mass in ABB analyser experiment is 0.0163g, and mass balance is 85%.

For the experimental results from ABB analyser, when oxygen molar percentage is 5%, the carbon balance is between 85% and 90%; when O_2 is 1% or pure N_2, the carbon balance drops to 60%-70%. One possible reason for the drop of mass balance could be that the later part of production or consumption rate is too slow and it is masked by the noise of the ABB analyser. In this case, the initial rate is still

accurate and can be directly used. Figure 4.7 shows the combustion of the char in two different experiments using either the ABB analyser or the UEGO sensor. The char particle mass in UEGO and ABB analyser experiments are almost the same, and the consumption rate of O_2 from ABB analyser generally overlaps with the consumption rate of O_2 from UEGO. The fact that the fast UEGO sensor gives similar rates to the deconvoluted ABB signal also shows that in these experiments the ABB analyzer's slow response time is not a problem.

4.4.6 The spike of CO in the sand experiments

In the sand experiments (5% and 1% O_2), there are obvious CO spikes at the start of reactions, and then the CO spike quickly disappears. This can be explained by the absorbed O_2 in the char particle. As measured in pure N_2 sand experiment, which is shown in Figure 4.6, absorbed O_2 in the char particle could oxidize 0.5% char particle into CO_2 and 1.5% char particle into CO. Thus, if all absorbed O_2 in the char particle becomes CO, it could oxidize 2.5% carbon. This means the CO spike in other experiments can at least partly be explained by the absorbed oxygen.

Thus, it the CO spike should be ignored when determining the initial rates. For the sand experiment, the CO spike can be directly removed, and the shape of CO_2 production rate curve is similar to O_2 consumption rate curve. For the CuO experiment, the CO spike in the sand experiment is oxidized by CuO into a spike of CO_2. Thus, O_2 consumption can be generally used to represent CO_2 production rate without the CO spike.

4.4.7 The effect of CuO particles on the rate of combustion under mass transfer limitation

4.4.7.1 The simulation of char combustion using CuO particles as fluidizing material

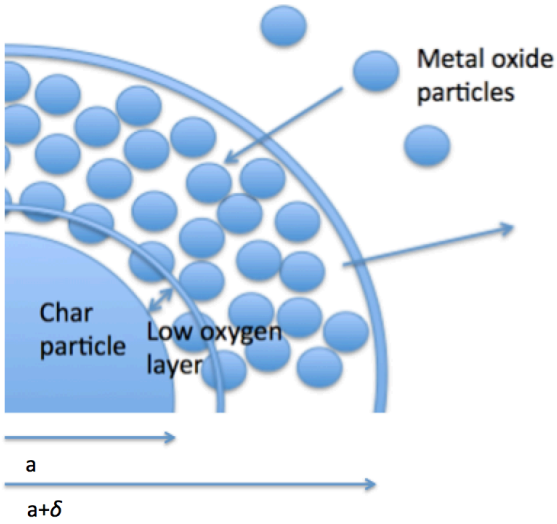

Figure 4.8 The low oxygen layer around the char particle when the O_2 concentration in the fluidizing gas (C_{O_2}) is higher than the equilibrium O_2 concentration of CuO decomposition ($C_{O_2}^{eq}$). In the low concentration layer, C_{O_2} is lower than $C_{O_2}^{eq}$, and CuO particles decompose in the layer.

For the char particle combustion using CuO particles as the fluidizing material, when the O_2 concentration in the fluidizing gas is higher than the equilibrium O_2 concentration for CuO decomposition (for instance, experiments with 5% O_2 at 1223K), there is a low oxygen region formed near the char particle in the boundary layer. In fact, under mass transfer control, the concentration of O_2 at the surface of the particle would be zero. The O_2 concentration in the low oxygen region is lower than the equilibrium O_2 concentration leading to CuO decomposition and the production of

O_2, as illustrated in Figure 4.8.

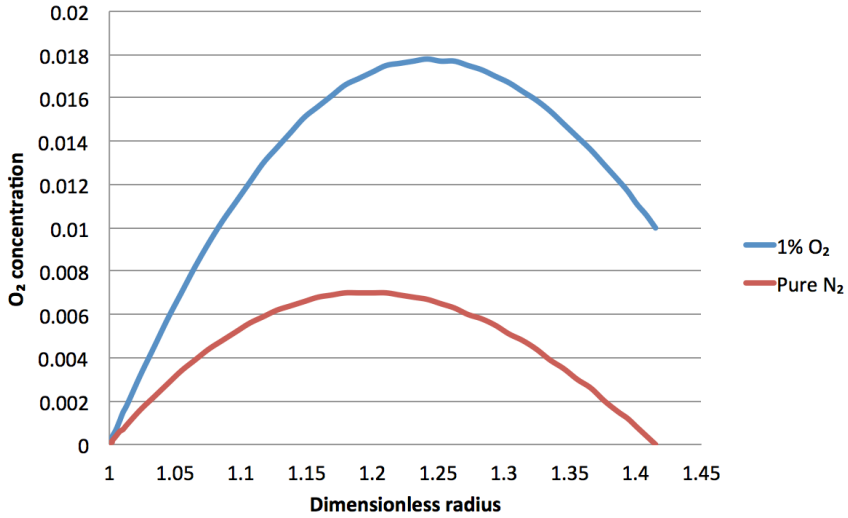

Figure 4.9 The O_2 concentration in the boundary layer of 1% O_2 case and pure N_2 case when their O_2 concentrations at the outer boundary layer are set to be 1% and 0, respectively.

When the O_2 concentration in the fluidising gas is lower than the equilibrium O_2 concentration of CuO decomposition, there is no 'low oxygen region' near the char particle, since O_2 concentration in the whole fluidised bed is lower than the equilibrium O_2 concentration. Thus, all CuO in the fluidised bed, rather than that in the 'low concentration layer', produces O_2. When there is insufficient CuO in the fluidised bed, the O_2 concentrations in the bulk phase for the 1% O_2 and pure N_2 cases gradually decrease during the char combustion, which means the O_2 concentration condition at the outer boundary layer is not a constant. It is a function of gas flow rate, the amount of CuO particles, temperature and the mass of char particle. Thus, it is not feasible to simulate the O_2 concentration in the bulk phase when CuO is not in excess. One solution is to straightforwardly set O_2 concentrations at the outer boundary layer

to be 1% and 0, respectively, so the O_2 concentrations in the boundary layer becomes the U-shape curves shown in Figure 4.9. The simulation model used in this chapter is from Chapter 3 with the assumption that CO could combust in the boundary layer.

Figure 4.9 shows that, by setting the bulk phase O_2 concentrations to be 1% and 0, there is a peak of O_2 concentration in the boundary layer. This is because in the model from Chapter 3, CuO decomposes to make the O_2 concentration reach the equilibrium concentration. However, the O_2 concentration in the boundary layer should be no higher than the O_2 concentration in the bulk phase, where CuO is also decomposing. There is a bulk flow through the fluidised particles that takes extra O_2 away when the O_2 concentration in the boundary layer tends to be higher than the one in the bulk phase, and this process is shown in Figure 4.10.

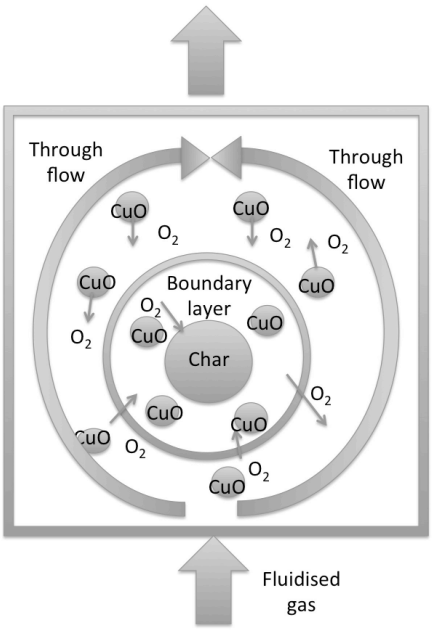

Figure 4.10 Illustration of the model from Chapter 3 with through flow using CuO as fluidising material when O_2 concentration in the fluidizing gas is lower than the equilibrium O_2 concentration. Not to scale.

Another option is to simulate the case when CuO is in excess, and the O_2 concentrations in the bulk phase for both 1% O_2 case and pure N_2 case are the same, i.e. the equilibrium, 2.7%. In the simulation, CO and CO_2 in the bulk phase produced by the char combustion are ignored, which is feasible since in the experiments, only small amount of char particles are dropped into the fluidised bed, and the concentrations of CO and CO_2 are small. The simulation results are shown in Figure 4.11, which shows the computed concentration profiles in the boundary layer under these assumptions.

In Figure 4.11, O_2 concentration increases from zero (the surface of char particle) to 2.7% (the outer boundary layer), and there is no peak as in Figure 4.9. The value of O_2 flux is negative from 1 to 1.25 dimensionless radiuses, means that in this region, O_2 flux is towards the surface of char particle; from 1.25 to 1.41 dimensionless radiuses, the value of O_2 flux is positive, means that in this region, O_2 flux is towards the outer boundary layer. It indicates that the amount of O_2 produced by CuO particles in the boundary layer is more than O_2 required for char combustion under the simulation conditions.

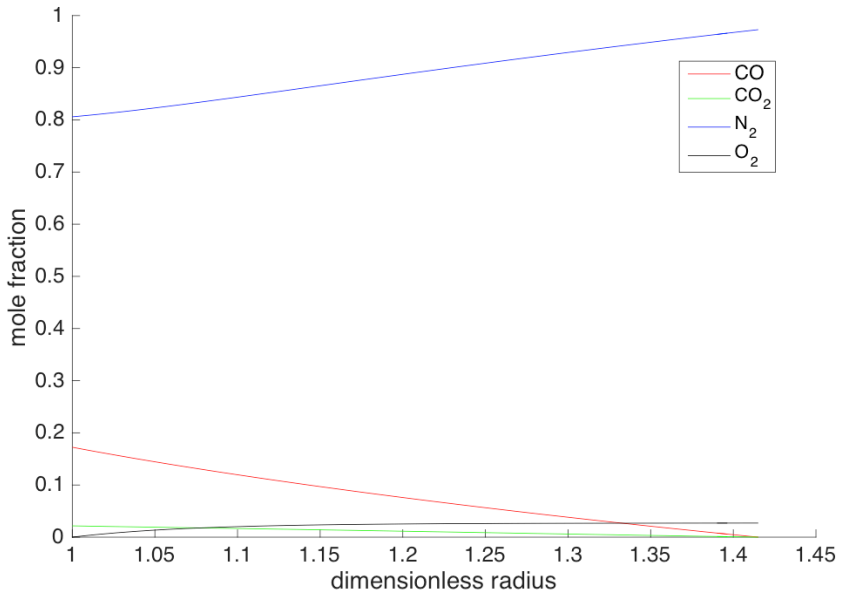

4.11(a)

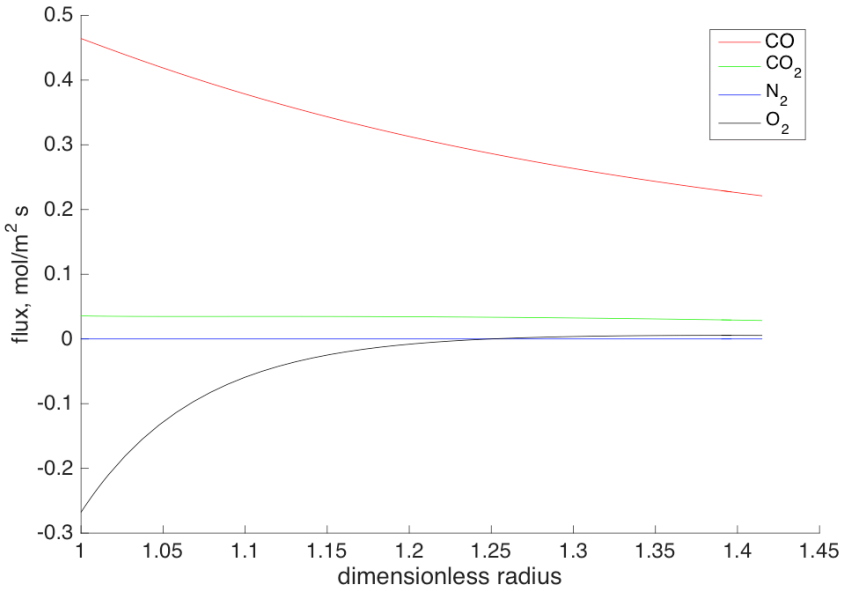

4.11(b)

Figure 4.11 The simulation results of (a) Molar fractions of CO, CO_2 and O_2; (b) Fluxes of CO, CO_2, N_2 and O_2. Simulation conditions: 1223K, Sh =3, Sh_0 = 0.88, pure N_2, 3 mm char particle; ratio of CO/CO_2 given by Arthur (Arthur 1951); using CuO as fluidising material. In Figure 4.11(b), negative value means the flux is towards the char particle.

4.4.7.2 The comparisons of experimental and simulation results using sand or CuO as fluidising material at low O_2 concentrations

In the previous section, it is assumed that the amount of CuO particles is large, so the O_2 concentration of the bulk phase is higher than the ones of experimental 1% O_2 and pure N_2 cases. Thus, it is worth comparing the experimental and simulation results, which is shown in Table 4.2.

Table 4.2 A comparison of the initial production rates of CO+CO_2 and the initial consumption rates of O_2 from 1) CuO experiments and simulations in 5% O_2, 1% O_2 and pure N_2; 2) sand simulations in 2.7% O_2. The simulation conditions: 1223K, Sh =3, Sh_0 = 0.88, 3 mm char particle. For the simulation, two extremes of CO/CO_2 are considered: only CO or CO_2 is the product on the surface of the char particle.

	Initial production rate of CO + CO_2 (mol/s) (Experiment)	Initial consumption rate of O_2 (mol/s) (Experiment)	Initial production rate of CO + CO_2 (mol/s) (Simulation)	
			CO is the only product	CO_2 is the only product
Pure N_2 (CuO)	2.6×10^{-6}	---	7.6×10^{-6}	3.77×10^{-6}
1% O_2 (CuO)	3.5×10^{-6}	---		
2.7% O_2 (Sand)	---	---	3.53×10^{-6}	1.77×10^{-6}
5% O_2 (CuO)	7.5×10^{-6}	5×10^{-6}	9×10^{-6}	4.64×10^{-6}
5% O_2 (Sand)	4.6×10^{-6}	3.5×10^{-6}	6.5×10^{-6}	3.5×10^{-6}

(Continue on next page)

	Initial consumption rate of O_2 (O_2 flux towards the char particle) (mol/s) (Simulation)			
	CO is the only product		CO_2 is the only product	
	Char particle surface	Outer boundary layer	Char particle surface	Outer boundary layer
Pure N_2 (CuO)	3.77×10^{-6}	-1.64×10^{-7}	3.77×10^{-6}	-8.49×10^{-8}
1% O_2 (CuO)				
2.7% O_2 (Sand)	1.77×10^{-6}	1.77×10^{-6}	1.79×10^{-6}	1.79×10^{-6}
5% O_2 (CuO)	4.54×10^{-6}	2.45×10^{-6}	4.62×10^{-6}	2.65×10^{-6}
5% O_2 (Sand)	3.3×10^{-6}	3.3×10^{-6}	3.3×10^{-6}	3.3×10^{-6}

For experiments with a bed of CuO results at 5% O_2 in Table 4.2, the production rates of $CO+CO_2$ are between the corresponding simulation results of two CO/CO_2 ratio extremes, and the same for experiments with sand. As noted previously this suggests that the experiments are mass transfer limited. The results also indicate that for CuO experiments, most of products are CO; for experiments with sand, the ratio of CO/CO_2 is around 1. Any discrepancy like this could be because of the assumptions of the model: for example, the underestimation of the rate of CuO decomposition. According to the models for CO/CO_2 ratios in Chapter 2, at 1223K, the products should be all CO.

In Table 4.2, the experimental consumption rates of O_2 for pure N_2 (CuO) and 1% O_2 (CuO) cases are not shown because in those two cases, a part or all of O_2

consumed is from CuO decomposition, and the rate of CuO decomposition is hard to determine. For 5% (CuO) case, it is assumed that all CuO decomposed could be quickly re-oxidized by the fluidising gas, so the O_2 consumed from CuO decomposition can be considered as indirectly from the fluidising gas. Thus, the O_2 consumption rate is equal to the O_2 loss rate from the fluidising gas.

As mentioned above, in the experiment, the O_2 concentration cannot be maintained at the equilibrium O_2 concentration since the amount of CuO is small, and the O_2 concentration in the fluidised bed continuously decreases, which is shown in Figure 4.2. In addition, the O_2 concentration in pure N_2 case decreases much faster than in 1% O_2 case. In the experiment, to ensure the fluidised bed is fully purged, the char particle was put in the fluidised bed at 20 seconds after the turning point in Figure 4.2. Thus, when the char particle is put in fluidised bed, the O_2 concentration of the fluidised bed for 1% O_2 case is higher than the pure N_2 case, and higher O_2 concentration leads to higher O_2 flux towards the char particle surface. So the faster $CO+CO_2$ production rate for 1% O_2 is because of its higher O_2 concentration in the fluidised bed. The CO/CO_2 ratio for the 1% O_2 case and the pure N_2 case are closer to the case CO_2 is the only product, which seem to contradict the results at 5% O_2 cases. However, as mentioned above, there are so many assumptions in the simulation it isn't surprising that this is a disagreement. The equilibrium O_2 concentration at the boundary used in simulations is 2.7%, yet through flow, which is not considered in the model, would change the apparent steady state oxygen concentration. In addition, during the combustion, the equilibrium O_2 concentration could be different from 2.7%

(e.g. local temperature differences owing the reaction).

The simulated O_2 concentration in the bulk phase of 1% O_2 and pure N_2 cases is same as in the 2.7% sand case, and initial $CO+CO_2$ production rate of the 1% O_2 case is more than twice of the pure N_2 case. Similarly, 5% O_2 (CuO) case and 5% O_2 sand case has the same O_2 concentration in the bulk phase, and the initial $CO+CO_2$ production rate of the 5% O_2 (CuO) case is about 1.3 time of the 5% O_2 sand case. This indicates that: 1) CuO is always helpful in char combustion, no matter whether the O_2 concentration in the bulk phase is higher or lower than the equilibrium concentration; 2) when O_2 concentration in the bulk phase is lower, the effect of CuO particles more significant, since for 5% O_2 (CuO) case, the 'low oxygen layer' is very thin, and for 1% O_2 and pure N_2 cases, the 'low oxygen layer' is the whole boundary layer.

The reaction rate of CuO decomposition is important. In the simulation of 1% O_2 and pure N_2 cases, the value of O_2 flux reaches zero at 1.25 dimensionless radius. If the reaction of CuO decomposition becomes faster, the zero point would shift to left, that is, closer to the surface of char particle; otherwise, it would shift to the right, closer to the outer boundary layer, until O_2 should be 'export' from the bulk phase.

In Figure 4.12, a comparison is made between simulated O_2 concentrations in the boundary layer for 5% O_2 concentration using sand and CuO as fluidising material. It is noticeable that the O_2 concentration for the CuO case is higher than the one for the sand case in the whole boundary layer. Since CuO decomposition only takes place when the O_2 concentration in the boundary layer is lower than the equilibrium O_2

concentration (2.7%), so there should be no O_2 produced when the O_2 concentration is between 2.7% and 5%. The explanation can be found in Figure 4.13.

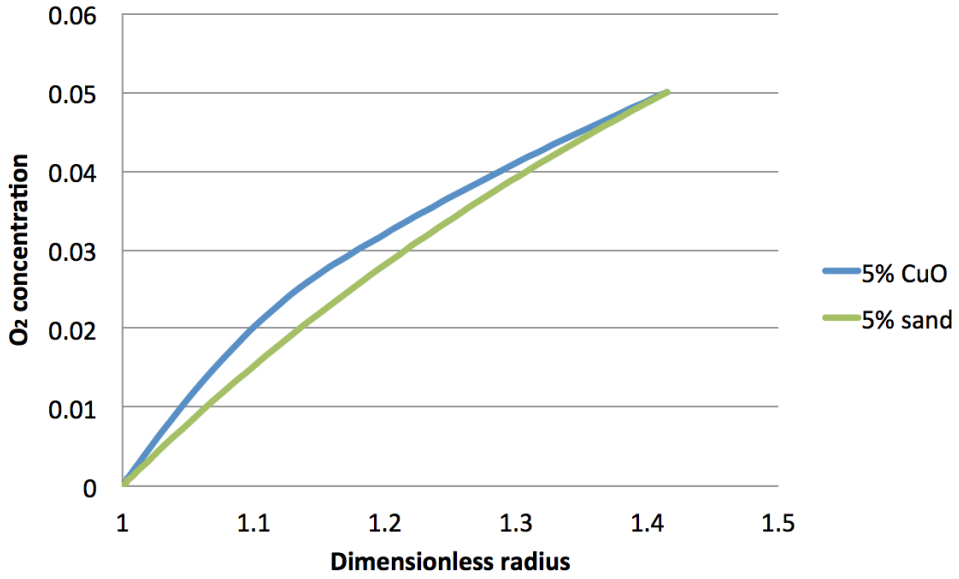

Figure 4.12 The comparison of O_2 concentrations simulation results in the boundary layer for 5% O_2 concentration using sand or CuO as fluidising material. Simulation condition: 1223K, Sh =3, Sh_0 = 0.88, 3 mm char particle; CO is the only product on the char particle surface.

In Figure 4.13, a comparison is made between O_2 fluxes simulation results in the boundary layer for 5% O_2 concentration using sand and CuO as fluidising material. At the outer boundary layer, the O_2 flux for the CuO case, -0.043 mol/(m^2 s), is much slower than the one for the sand case, -0.06 mol/(m^2 s). This is because that there is O_2 produced in the boundary layer for the CuO case, so there is less O_2 required from the bulk phase. There is a turning point for the O_2 flux curve in CuO case. At the turning point, the O_2 concentration is the equilibrium O_2 concentration, 2.7%. Between the turning point and the outer boundary layer, that is, the O_2 concentration

in the boundary layer is between 2.7% and 5%, the gradient in O_2 flux for both CuO and sand cases are similar since there is no CuO decomposition. Thus, in this region, the O_2 flux for CuO case is always smaller than the one for sand case, which explains why the O_2 concentration in this region for CuO case is always higher than the one for sand case.

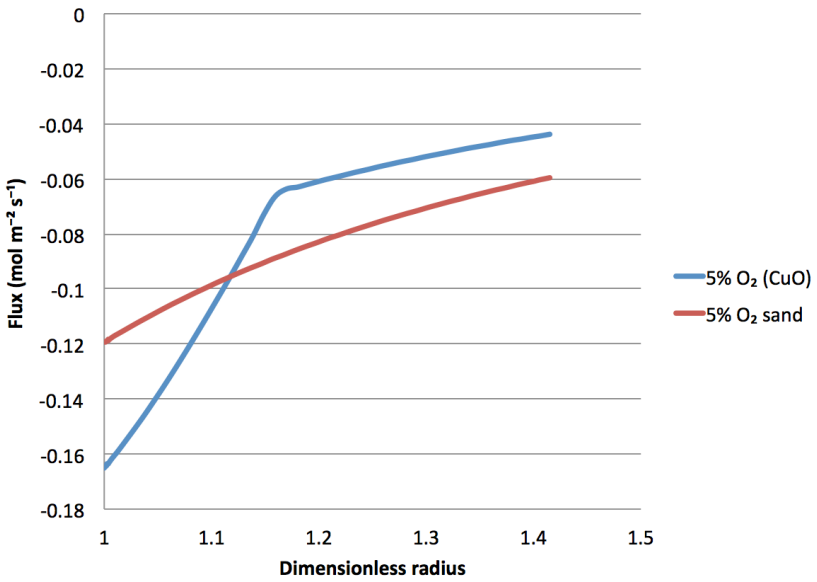

Figure 4.13 The comparison of O_2 fluxes simulation results in the boundary layer for 5% O_2 concentration using sand or CuO as fluidising material. Simulation condition: 1223K, Sh =3, Sh_0 = 0.88, 3 mm char particle; CO is the only product on the char particle surface. Negative O_2 flux in the boundary layer means the O_2 flux is from the outer layer of boundary layer to the reacting particle.

Between the turning point and the char particle surface, that is, the O_2 concentration in the boundary layer is between 2.7% and 0, there is CuO decomposition taking place and producing O_2. Thus, the O_2 flux slope for CuO case in this region suddenly increases, and the one for sand case generally keeps the same.

The O_2 concentration for CuO case decreases much quicker than the one for sand case, and they both become zero on the char particle surface.

4.4.8 Two possible cases of the char combustion in the fluidised bed using CuO as fluidising material

Since both the amount of CuO in the fluidised bed and the apparent CuO decomposition rate are important factors, experimentally there are two possible cases:

Case 1: The amount of CuO is large

In this case, the O_2 concentration in the bulk phase keeps at the equilibrium O_2 concentration for a long time, and the char particle combustion is mass transfer controlled. The O_2 concentration in the inlet fluidising gas has no influence on the char particle combustion. This case is close to the experiment when the amount of CuO in the fluidised bed is large.

Case 2: The amount of CuO is small

In this case, the O_2 concentration in the bulk phase cannot keep at the equilibrium O_2 concentration, and gradually decreases. The char particle combustion is mass transfer controlled. The O_2 concentration in the inlet fluidising gas has large influence on the char particle combustion. This case is close to the experiment in this chapter.

4.5 CONCLUSIONS

The roles of CuO particles as fluidising material in the char particle combustion in the fluidised bed can be concluded as:

1) When the O_2 concentration in the fluidised gas is higher than the equilibrium O_2 concentration of CuO decomposition, CuO particles act as a kind of catalysis for char particle combustion, and the reactions are given as,

$$4CuO \leftrightarrow 2Cu_2O + O_2 \quad (a1)$$

$$C + O_2 \rightarrow CO_2 \quad (a2)$$

$$2C + O_2 \rightarrow 2CO \quad (a3)$$

Reaction (a1) takes place in the low oxygen layer near the char particle, and the decomposed CuO particle in (a1) leaves the boundary layer to the bulk phase, where it is re-oxidized, that is, reversed reaction (a1).

2) When the O_2 concentration in the fluidised gas in lower than the equilibrium O_2 concentration of CuO decomposition, the O_2 concentration in the fluidised bed is equal to or less than the equilibrium O_2 concentration of CuO decomposition, so the decomposed CuO can not be re-oxidized, and CuO can no longer act as a kind of catalyst, but a source of O_2. However, the CO+CO_2 production rate for CuO case is still faster than the one for sand case at same bulk phase O_2 concentration, because CuO could produce O_2 in the boundary layer and increase the O_2 mass transfer rate to the char particle surface.

CHAPTER 5 STEADY-STATE MODEL OF COAL-FIRED CHEMICAL LOOPING POWER PLANT

5.1 STEADY-STATE MODEL

5.1.1 Introduction

Carbon capture and storage (CCS) technology can combine with different conversion technology. For instance, Integrated Gasification Combined Cycle (IGCC) (Cormos 2012), Natural Gas Combined Cycle (NGCC) (Chiesa et al. 2008), pulverized coal (PC) (Fan et al. 2012) and coal direct chemical looping (CDCL) (Fan et al. 2012). The average efficiencies are: 32% - 40% for IGCC, 43% - 50% for NGCC, and 30% - 35% for PC. (Mukherjee et al. 2014) Here a steady-state model is used to identify operating envelopes for possible chemical looping power plants, which use iron oxide as an oxygen carrier. Similar work was carried out by Cleeton (Cleeton 2011), Mukherjee (Mukherjee et al. 2014), Peltola (Peltola 2014), Kolbitsch (Kolbitsch, Pröll, and Hofbauer 2009), Abad (Alberto Abad, 2010) Jung (Jung and Gamwo 2008) and Deng (Deng et al. 2008). Cleeton (Cleeton 2011) examined the envelope for hydrogen production: iron oxide is used as oxygen carrier, and it is first reduced by a fuel gas steam. Then the reduced iron oxide is partially oxidized by steam to produce high-purity H_2, and eventually fully oxidized by air to release heat. Mukherjee (Mukherjee et al. 2014) compared flow sheet models of different technologies: pressure swing adsorption (PSA), physical adsorption (Selexol) and chemical looping combustion (CLC) based processes. In the latter case, the oxygen

carrier used was iron oxide. They also considered cases producing hydrogen, with or without the carbon dioxide being captured. They concluded that for production, the efficiency decreased in as PSA > CLC > Selexol. However, only an analysis of a single flow sheet for each technology is presented, and it is not clear how well optimised the flow sheet was for each technology, or how if the conditions assumed for the chemical looping system has been optimised.

Peltola (Peltola 2014) constructs a one dimensional fluidized bed model, that is, each reactor is divided into cells along vertical axis, and applied for simulations of CLC systems consisting of interconnected fluidized bed reactors. Even though the study is for steady state only, the fluidised bed model uses a dynamic modeling approach and equations are time dependent for future studies, and have conservation equations for solid, gas species and energy. Semi-empirical correlations are employed for the calculation of reaction kinetics, heat transfer and hydrodynamics. Kolbitsch (Kolbitsch, Pröll, and Hofbauer 2009) models a 120 kWth chemical looping with a one dimensional fluidised reactor model. The study is for steady state. Both the air and fuel reactors are assumed to be isothermal and ideally mixed for solids. The gas species are assumed to be plug flow. Abad (Alberto Abad, 2010) models a 120 kWth chemical looping plant by employing a macroscopic model for circulating fluidised beds. This semi-empirical model, developed by Pallares and Johnsson (Pallarès and Johnsson 2006), can be used to calculate solids concentration in the bed and gas species among bubbling phase and emulsion phase. The study is for steady state. Jung (Jung and Gamwo 2008) and Deng (Deng et al. 2008) employed multiphase

computational fluid dynamic (CFD) model to model the fuel reactor. Thus, various levels of detail can be used to model individual reactors within a flowsheet, however given the complexity of the flow sheet models, simplified models are usually employed for the individual units, e.g. the macroscopic model (Alberto Abad, 2010) or simple equilibrium or mass and energy based models (e.g. (Mukherjee et al. 2014), (Cleeton 2011)).

In the chemical looping power station, achieving a sensible energy balance is crucial, in that the fuel reactor could end up consuming heat, making the heat integration impossible (Fennell and Anthony 2015). The temperature of reactors, recycle flows and flows of air and fuel need to be set to both maximise power output, but also ensure that all reactors are a net producer of heat. These calculations allow the energy penalty associated with chemical looping to be compared with energy penalties associated with other carbon capture technologies.

In this chapter, simplified equilibrium models are used (similar to (Mukherjee et al. 2014), (Cleeton 2011)) to explore the optimisation of the chemical looping flow sheet, when integrated with a power cycle.

5.1.2 The steady-state model

The overall steady-state model consists of two systems: 1) the combustor of coal via chemical looping combustion; 2) a steam cycle, which uses the heat generated by the chemical looping combustor. These two systems interact with each other by heat exchange.

5.1.2.1 Chemical looping combustion

The flow sheet for chemical looping combustion, analysed here, is shown in Figure 5.1. Where T_F is the temperature of the fuel reactor (K), and T_A is the temperature of the air reactor (K). The thermodynamic calculations here (i.e. minimisation of free energy to compute the equilibrium composition leaving a reactor, and the enthalpy changes across a reactor) make use of the NASA database (McBride, Zehe, and Gordon 2002); this database does not contain thermodynamic data for complex fuels such as coal. Here three kinds of fuel, the characteristics which are shown in Table 5.1, are used: 1) low-rank Hambach lignite coal (Supplied by RWE Power AG, Germany); 2) Polish bituminous coal (#1286, characteristics from ECN laboratories ('ECN. Phyllis, Database for Biomass and Waste, Http://www.ecn.nl/phyllis, Energy Research Centre of the Netherlands', 2004)); 3) Methane. For the sake of simplicity, the minor components of coal (i.e. nitrogen and sulphur) are treated as inert and included within the ash component, which itself is modelled as silica.

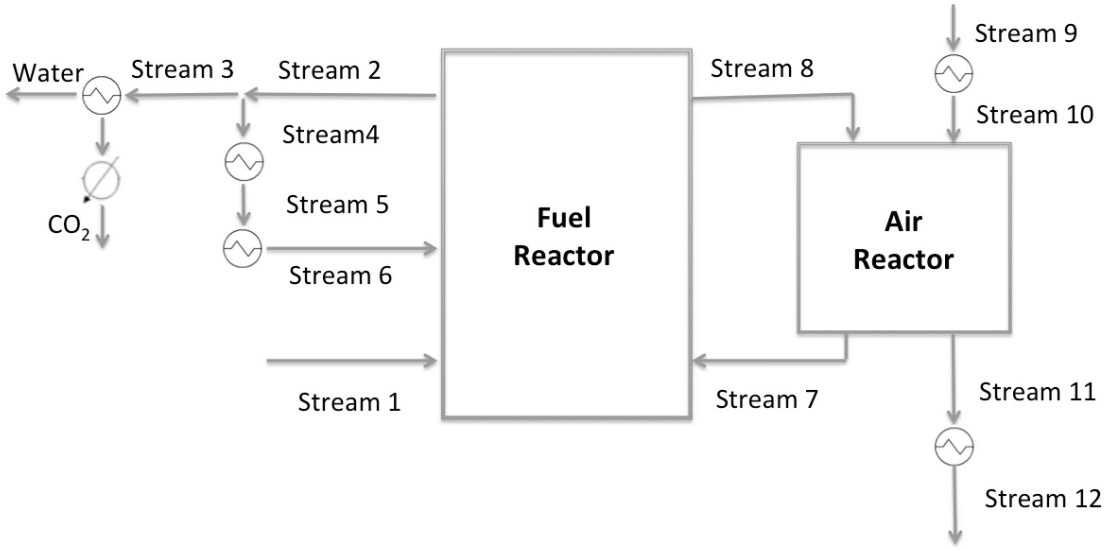

Figure 5.1 The chemical looping reactors within the flow sheet.

Table 5.1 The temperature and molar flow computed for the chemical looping reactors in Figure 5.1.

Stream	Temperature (K)	Flow rate and Components
1	298.15	1 kg/s Coal = 45.8 mol/s (C) + 27.4 mol/s (H_2) + 5.7 mol/s (O_2)
2	T_F	68.6 mol/s (CO_2), 41 mol/s (H_2O)
3	T_F	45.8 mol/s (CO_2), 27.4 mol/s (H_2O)
4	T_F	22.9 mol/s (CO_2), 13.7 mol/s (H_2O)
5	498	22.9 mol/s (CO_2), 13.7 mol/s (H_2O)
6	$T_F - 10$	22.9 mol/s (CO_2), 13.7 mol/s (H_2O)
7	T_A	$N_{recycle}$ (Fe_2O_3)
8	T_F	$N_{recycle} - x$ (Fe_2O_3), $\frac{2}{3}x$ (Fe_3O_4), 0.46 mol/s (C), 0.27 mol/s (H_2), 0.06 mol/s (O_2)
9	298.15	511.4 mol/s Air = 107.4 mol/s (O_2) + 404 mol/s (N_2)
10	$T_A - 10$	511.4 mol/s Air = 107.4 mol/s (O_2) + 404 mol/s (N_2)
11	T_A	Deplete air
12	298.15	Deplete air

The air reactor is modelled as an equilibrium reactor, with output found by minimising the free energy of the outputs at a specified T and P. The output flows of the fuel reactor were found by minimising the Gibbs free energy of the output (i.e. at thermodynamic equilibrium) subject to the constraint that 1% of the input carbon atoms leave as solid carbon (to model incomplete char conversion). Here, the fmincon (in Matlab) function is employed to minimize Gibbs free energy; in this case, varying the proportion of each output species whilst ensuring atoms are conserved.

Since the fuel is not contained within the thermodynamic database used, the heat balance of the fuel reactor, which converts the coal, is calculated by defining coal elementally and directly using elements of the coal in the reaction of fuel reactor.

Stream 4, the gas feed to the fuel reactor, is diverted from the outlet gas of the fuel reactor (Stream 2). The rest of Stream 2, that is, Stream 3, is then cooled down to 347.4 K and condensed. Stream 4 then flows back to the fuel reactor, pushed by a fan. However, the initial temperature T_F is too high for an industrial fan, so it has to be cooled down first, passed through the fan, then is preheated to T_F -10K. From a purely thermodynamic point of view, Stream 4 is not required since thermodynamics allows the metal oxide to react directly with the coal. However, in practice solid-solid reactions are very slow. Stream 4 therefore has two functions: 1) fluidising the coal and Fe_2O_3 in the fuel reactor; 2) gasification of carbon in the coal, and the product CO can then be oxidized by the fuel reactor. Thus, the flow rate (shown in Figure 5.1) of CO_2 and water in Stream 4 is chosen as the minimum flow rate of CO_2 and water for the gasification, i.e. calculated using a free energy minimisation as the flow needed to

avoid solid carbon, of 1 kg coal at 1073 K. The ratio of CO_2/H_2O in Stream 4 is the same as that in the Steam 2, which at steady state must be equal to ratio of CO_2/H_2O that is produced by combusting the coal. Since the gasification of carbon is thermodynamically favoured by increasing the temperature of the fuel reactor increases from 1073 K to 1273 K, the minimum flow rate at 1073 K would be large enough when the temperature increases.

In Stream 3, the partial pressure of water is 37.9 kPa, so its dew point is 347.4 K. Thus, it is cooled down to 347.4K, and the water in Stream 3 is separated. Cooling water from elsewhere is needed to meet this demand. A condenser then condenses the rest part of Stream 3, that is, pure CO_2. The condensation process is not shown in the heat integration, since the steam cycle pinches at the boiler feed water temperature (393K), and the condensation temperature is much lower than the boiler feed water temperature. Too low a temperature is of no use in the heat integration, and later it will be shown that this heat will have no effect on the power produced.

The calculations of material and heat balances for each reactor in the flow sheet and the various equilibrium calculations were performed in Matlab. The equilibrium compositions were calculated by minimising the free energy of the output streams of a reactor, subject to constraints imposed by element balances and any other constraints, using the fmincon function in Matlab.

Table 5.2 Lower heating value (LHV) and ultimate analysis for the Hambach lignite (John S. Dennis, Müller, and Scott 2010), Polish bituminous coal ('ECN. Phyllis, Database for Biomass and Waste, Http://www.ecn.nl/phyllis, Energy Research Centre of the Netherlands', 2004) and natural gas.

Ultimate analysis (wt%)	Hambach lignite (dried)	Polish bituminous coal (#1286) (dried)	Natural Gas
C	54.91	73.50	75
H	5.47	4.60	25
O	18.33	10.03	0
N	0.93	1.34	0
S	0	0	0
Other (ash)	5.83	3.98	0
Lower heating value (kJ/kg)	26003	29100	47141

5.1.2.2 The search for suitable conditions for the chemical looping system

In order for the chemical looping section of the flowsheet to be feasible, four criteria must be met:

1) There should be no CO in the outlet gas flow from the fuel reactor, which means the recycle rate of Fe_2O_3 should satisfy the minimum oxygen request to oxidize all carbon into CO_2. It should be noted that in this case the output would be constrained by the Fe_2O_3 to Fe_3O_4 equilibrium, which ensures that [CO] is very low.

2) The total heat balance of both air reactor and fuel reactor should be positive, which means there is no need to heat the reactors. At these temperatures, and at power scale, it is difficult to supply heat from external sources. As such it would not be

practical to, for example, transfer heat into either the air or the fuel reactor from elsewhere.

3) No hot utility should be required overall. A power station should be able to self-sufficient.

4) The temperature of air reactor cannot be too high: a high temperature of air reactor makes the cost of air reactor higher, since the more expensive materials are required. In addition, the melting point of FeO is 1650K, and the melting point of Fe_3O_4 is 1870K. In this research, Fe_2O_3 is only reduced to Fe_3O_4, rather than FeO. Taking all these factors into account, the maximum temperature of the air reactor is set to be 1573K, which is 300K lower than the melting point of Fe_3O_4.

The main variables, which determine whether the chemical looping section of the flowsheet is feasible, are the temperature of air reactor (T_A), fuel reactor (T_F), and the recycle rate of oxygen carrier ($N_{recycle}$). Other parameters in the chemical looping combustion flow sheet have only a minor effect and were thus fixed at reasonable values as shown in Table 5.2. For the steam cycle, all temperatures and pressures are fixed, so the only variable is the flow rate of water (kg/s). Since the rate of feed of fuel is fixed, the efficiency of the whole system then depends on the flow rate of water around the steam cycle.

In Table 5.3, a comparison of parameters for chemical looping combustion system is made with Kolbitsch (Kolbitsch, Pröll, and Hofbauer 2009) and Peltola (Peltola 2014). It shows that the temperature of the air and the fuel reactors are in the same range for all three pieces of work, which is within 1073 K and 1273 K.

Table 5.3 A comparison of parameters for chemical looping combustion system (base case) with Kolbitsch (Kolbitsch, Pröll, and Hofbauer 2009) and Peltola (Peltola 2014). (a. Calculated from the energy balance of the reactor system)

Parameters	Unit	Base case/ range	Base case/ range (Kolbitsch, Pröll, and Hofbauer 2009)	Base case/ range (Peltola 2014)
Flow rate of air into the air reactor (N_{air})	mol/s	19668	---	---
Flow rate of fluidising gas into the fuel reactor (N_F)	mol/s	1687	---	---
Fuel supply	kW	1000000	120	60-140
Recycle rate of metal oxide ($N_{recycle}$)	mol/s of Fe_2O_3	12423 to 49690	---	---
Temperature of the air reactor (T_A)	K	1093-1573	a	1140-1200
Temperature of the fuel reactor (T_F)	K	1073-1273	1123	1073-1223

5.1.2.3 Heat integration

A feasible plant requires that no single reactor is a net heat consumer, and that overall a net heat output is available for transfer to the steam cycle. To determine the feasibility of a given set of conditions, composite curves were generated for all the heat sources (the hot composite), the heat sinks (the cold composite) and the net heat availability, as a function of temperature (Grand Composite), for the chemical looping system alone. The reactors were modeled as well mixed systems, whose entire heat load was available at the outlet temperature of the reactor. Adding gases to the reactors at room temperature to a very hot reactor results in a massive loss of exergy, and can result in a negative heat output; preheating to the reactor temperature may not be feasible but would result in the least irreversibility. Therefore, the assumed temperature at which gases enter the reactors will have a large impact on the results. Table 5.4 below shows the base case in which the gases are assumed to be heated to within 10 K of the reactor temperature. Here, ΔT_{min} is defined to be the minimum temperature difference of the hot and the cold composite curves, and ΔT_{min}=10K. Stream 2, 4, 6 and 7 are defined and their components are shown in Figure 5.2.

Table 5.4 Inlet and outlet temperatures of hot and cold streams in chemical looping combustion part.

Stream	Inlet temperature	Outlet temperature	Hot or cold composite curve
Stream 9&10	298.15K	T_F	Cold
Stream 7	T_F	372.4 K	Hot
Stream 13&14	298.15K	T_A-10K	Cold
Stream 15&16	T_A	298.15K	Hot

If the hot and cold composite curves directly pinch with zero temperature difference at the pinch point, the area required for heat exchange would be infinite. Thus, a realistic solution is set a minimum temperature difference at the pinch point, which can be considered as a compromise between recovering the most energy, and an economical amount of heat transfer area. Here, the minimum temperature difference is set to be 10 K.

To plot the composite curves, heat capacity of the stream $C_p = \Delta H / \Delta T$ is needed, where ΔH is the enthalpy change of the stream and ΔT is the temperature difference. However, over the large temperature changes, heat capacity of the gas and solids streams cannot be assumed to be constant. Thus, the temperature difference can be divided into many small intervals, and the heat capacity of each temperature interval can be assumed to be constant with ignorable error. The plotting of the composite curves follows the same process: the temperature range of the composite curves is divided into finite intervals, and the enthalpy of each species at a given temperature T is found in NASA database. The total enthalpy (H_T) of a stream at temperature T is then calculated by summing all species in the stream up. The total enthalpy ($H_{T+\Delta T}$) of the stream at temperature $T + \Delta T$ is calculated in the same way, and then, the enthalpy change of the total enthalpy between T and $T + \Delta T$ can be calculated as $\Delta H = H_{T+\Delta T} - H_T$. The heat capacity is $C_p = (H_{T+\Delta T} - H_T)/\Delta T$.

5.1.2.4 Steam cycle

In Figure 5.2, a simplified steady-state steam cycle model is shown, with the corresponding thermodynamic data shown in Table 5.4. There are three turbines in this system. All temperatures and pressures used here are from Mukherjee (Mukherjee et al. 2014). Other steam cycle schemes are discussed in Section 5.2.4. The operating pressures of three turbines are set to be 124 bar (high pressure), 30 bar (intermediate pressure) and 6.5 bar (low pressure). The temperature of three turbines are 550 °C (high pressure), 550 °C (intermediate pressure) and 600 °C (low pressure). There are two stages of the low-pressure turbine. After the first stage, the stream is divided into two streams: one stream (mass ratio 89.4%) goes into the second stage and its pressure drops to the saturation pressure of steam at 40 °C (the temperature of the cooling water in a power plant) to maximise the work output; the second stream (mass ratio 10.6%) is used to preheat the boiler feed water. The temperature of boiler feed water is set as a variable. The isentropic efficiency of the turbines is assumed to be 88%, and the pumps are assumed to be isentropic (pump work is so small, and assuming the pumps are isentropic would have little influence on the chemical looping plant efficiency).

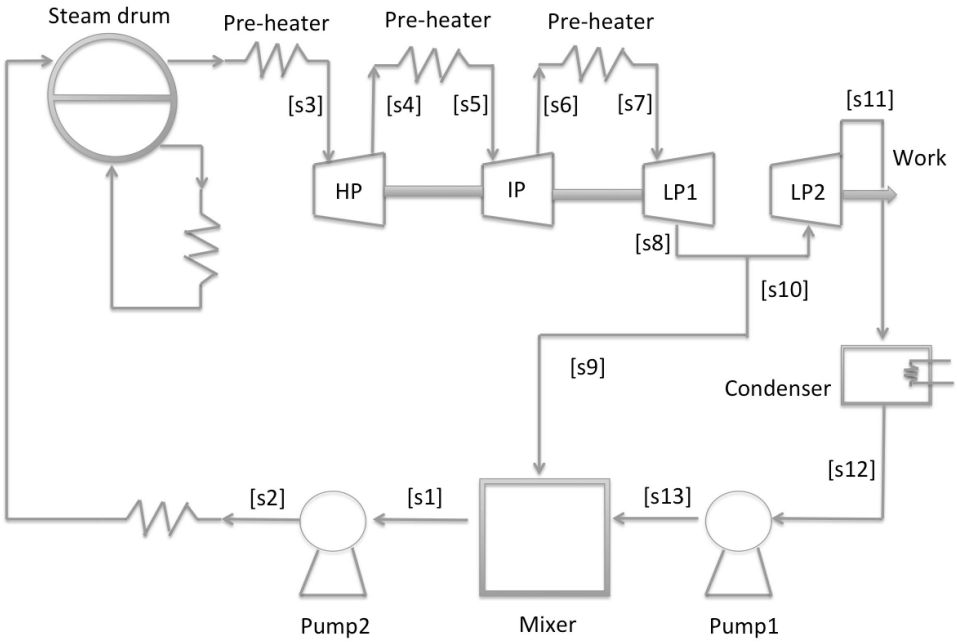

Figure 5.2 Schematic diagram of the steam cycle for power generation. Adapted from Mukherjee et al. (Mukherjee et al. 2014)

Table 5.5 Operation conditions for the steam cycle. m_{steam} is the flow rate of the steam cycle (kg/s).

Stream	Temperature	Pressure	Mass flow	Enthalpy	Entropy	Dryness
Unit	(℃)	(bar)	(kg s^{-1})	(kJ kg^{-1})	(kJ kg^{-1} K^{-1})	(-)
s1	T_{BFW}-273.15	1.987	m_{steam}	503.8	1.528	0
s2	T_{BFW}-272.15	124	m_{steam}	516.7	1.528	0
s3	550	124	m_{steam}	3477.6	6.636	1
s4	343.7	30	m_{steam}	3101.2	6.721	1
s5	550	30	m_{steam}	3569.6	7.377	1
s6	339.3	6.5	m_{steam}	3142.9	7.474	1
s7	600	6.5	m_{steam}	3701.3	8.232	1
s8	426.9	2	m_{steam}	3333.1	8.305	1
s9	426.9	2	0.106 $\times m_{steam}$	3333.1	8.305	1
s10	426.9	2	0.894 $\times m_{steam}$	3333.1	8.305	1
s11	95.1	0.074	0.894 $\times m_{steam}$	2678.5	8.564	0.988
s12	40	0.074	0.894 $\times m_{steam}$	167.5	0.572	0
s13	40	1.987	0.894 $\times m_{steam}$	167.7	0.572	0

For the steam cycle, all temperatures and pressures are fixed, so the only variable is the flow rate of water (kg/s). Since the rate of feed of fuel is fixed, the efficiency of the whole system then depends on the flow rate of water around the steam cycle.

5.1.2.5 Optimising the heat integration between the steam cycle and the chemical looping plant

There are two methods to optimise the heat integration between the steam cycle and the chemical looping plant,

1. Partial integration. The heat integration in the chemical looping plant is done first to get the grand composite curve for this subsystem, and then the waste heat is taken from grand composite curve into steam cycle.
2. Full integration. In this method, the cold composite curve includes both cold streams from the chemical looping plant and the heat absorbing streams from the steam cycle.

Method 2 might be expected to be optimal since this method minimised the exergy loss of the whole system. This can be explained by the fact that in the cold composite curve, the temperature of the stream in steam cycle can be higher than the temperature of the stream in the chemical looping plant reactor, so in method 2, the stream in higher temperature can be chosen. However given the reactors all operate at high temperature and there would be little difference. Most of the high temperature heats are usable for the steam cycle. Thus, there is no influence either the sequence of

the heat transfer is changed or not. In this chapter, method 2 is employed.

For the steam cycle, all temperatures and pressures are fixed, so the only variable is the flow rate of water (kg/s). Since the rate of feed of fuel is fixed, the efficiency of the whole system then depends on the flow rate of water around the steam cycle. The maximum flow rate of water is calculated as follows: the chemical looping flow sheet is fixed (flow sand temperature etc.), and the flow rate of water around the steam cycle is tested manually, step by step, increasing from zero until the flow rate of water reaches a critical value and the hot and cold composite curves are pinched. At this flow rates, the maximum amount of heat has been recovered into the steam cycle.

5.1.2.6 Exergy analysis

The exergy of a system (T, P) is defined as the work that can be extracted when it is brought to equilibrium with a reference environment (T_0, P_0). The reference environment used is from Kotas (1995), which is shown in Table 5.6 and Table 5.7.

The reference substances in Table 5.6 and Table 5.7 can be divided into two groups:

(1) Gaseous substances are from the atmosphere (water is consider as gaseous);

(2) Solid substances are from the Earth's crust.

Table 5.6 Chemical elements with gaseous reference substances. Noble gases and heavy water (D_2O) in the atmosphere are omitted. (T_0 = 298.15K, and P_0 = 101325Pa)

Chemical element	Chemical symbol	Mole fraction in dry air	Standard partial pressure in the environment P_i^{00}/bar	$\frac{-RT_0 \ln P_i^{00}/P^0}{\text{kJ/kmol}}$	Reference reaction
C	CO_2	0.0003	0.000294	20170	$C + O_2 \rightarrow CO_2$
H	H_2O (g)	---	0.0088	11760	$H + \frac{1}{4}O_2 \rightarrow \frac{1}{2}H_2O$
N	N_2	0.7803	0.7583	720	$N \rightarrow \frac{1}{2}N_2$
O	O_2	0.2099	0.2040	3970	$O \rightarrow \frac{1}{2}O_2$

Table 5.7 The reference environmental standard chemical exergy of pure substances. (T_0 = 298.15K, and P_0 = 101325Pa)

Substance	State	Standard chemical exergy ε^0 [kJ/kmol]
CO_2	g	20140
Fe_2O_3	s	20370
H_2O	g	11710
N_2	g	720
O_2	g	3970

The total exergy is often divided into two components: 1) the physical exergy, E_{phys}, 2) the chemical exergy, E_{chem}.

1) Physical exergy (E_{phys}). It is defined as difference between the "availability" of the stream and the reference environment. The expression of the availability of a material stream is,

$$B_{sys} = H - T_0 S \tag{5.1}$$

Where H and S are enthalpy and entropy of the stream, respectively. The expression for the availability same stream in the reference environment is:

$$B_{env} = H_0 - T_0 S_0 \tag{5.2}$$

Where H_0 and S_0 are enthalpy and entropy of the stream at environmental conditions, respectively. The physical exergy of a system with m species is,

$$E_{phys} = \sum_{i=1}^{m} \{n_i (h_i - h_{i,0}) - T_0 (s_i - s_{i,0})\} \tag{5.3}$$

Where n_i is the mole number of species i; h_i and s_i are enthalpy and entropy of species of the system; $h_{i,0}$ and $s_{i,0}$ are enthalpy and entropy the same species, at the same composition, but at the temperature and the pressure of the reference environment.

2) Chemical exergy (E_{chem}). It is defined as the work can be extracted when a system reaches chemical equilibrium (at constant T_0 and P_0) with a reference environment. For instance, if species A does not exist in the environment, but can be brought to equilibrium by reacting it with B in the environment to produce C in the environment,

$$A + 2B = C \tag{5.4}$$

The chemical exergy for reaction of one mole of A is,

$$E_{chem,A} = b_{chem,A} + 2b_{chem,B} - b_{chem,C} \tag{5.5}$$

The molar chemical exergy of species i, $b_{chem,i}$, is defined as,

$$b_{chem,i} = h_i - T_0 (s_i - R ln x_i) \tag{5.6}$$

Where h_i is the enthalpy of species i at temperature T; the term $R ln x_i$ only

applies to gases, and it corrects the entropy for the effect of mixing if the species is within a mixture of ideal gases at a mole fraction x_i, and R is the universal gas constant.

For complex compounds, such as coal, their chemical exergy can be calculated by a correlation provided by Kotas (1995) when the oxygen/carbon mass ratio is lower than 0.667,

$$E_{fuel,ex} = \left(LCV_{fuel} + 2442f_w\right)\varphi + 9417x_s \tag{5.7}$$

where

$$\varphi = 1.0437 + 0.1882\chi_H + 0.061\chi_O + 0.0404\chi_N \tag{5.8}$$

φ is only valid for dry and organic substances in coal. And where f_w is the mass fraction of the moisture in the coal; x_s is the mass fraction of sulphur in the coal; χ_H, χ_O and χ_N are the mass ratios of oxygen/carbon, hydrogen/carbon and nitrogen/carbon in the coal, respectively. Thus, for dried Hambach lignite coal, φ is 1.0835, which is within the range of values suggested by Kotas of 1.06-1.10. The value of $E_{fuel,ex}$ is calculated to be 28174.1 kJ/kg.

5.1.2.7 Figures of merit

The whole system is defined as the chemical looping plant and the steam cycle. The efficiency of the whole system is defined as

$$\eta = \frac{E_{steamcycle}}{E_{fuel}} \tag{5.9}$$

where E_{fuel} is the enthalpy of coal, -4981 kJ/kg, and $E_{steamcycle}$ is the net work of

the steam cycle,

$$E_{steamcycle} = \sum W_{Turbine} - \sum W_{Pump} \tag{5.10}$$

where $\sum W_{Turbine}$ and $\sum W_{Pump}$ are the sum of work of turbines and pumps in the steam cycle in respective.

The exergetic efficiency of a system is the ratio of the useful exergy output to the total exergy in the system. Here, the exergy output is the work output of the steam cycle.

$$\eta_{ex} = \frac{E_{steamcycle}}{E_{fuel,ex}} \tag{5.11}$$

5.2 RESULTS AND DISCUSSION

5.2.1 Operating regimes for the chemical looping plant alone

5.2.1.1 Base case with Hambach lignite fuel

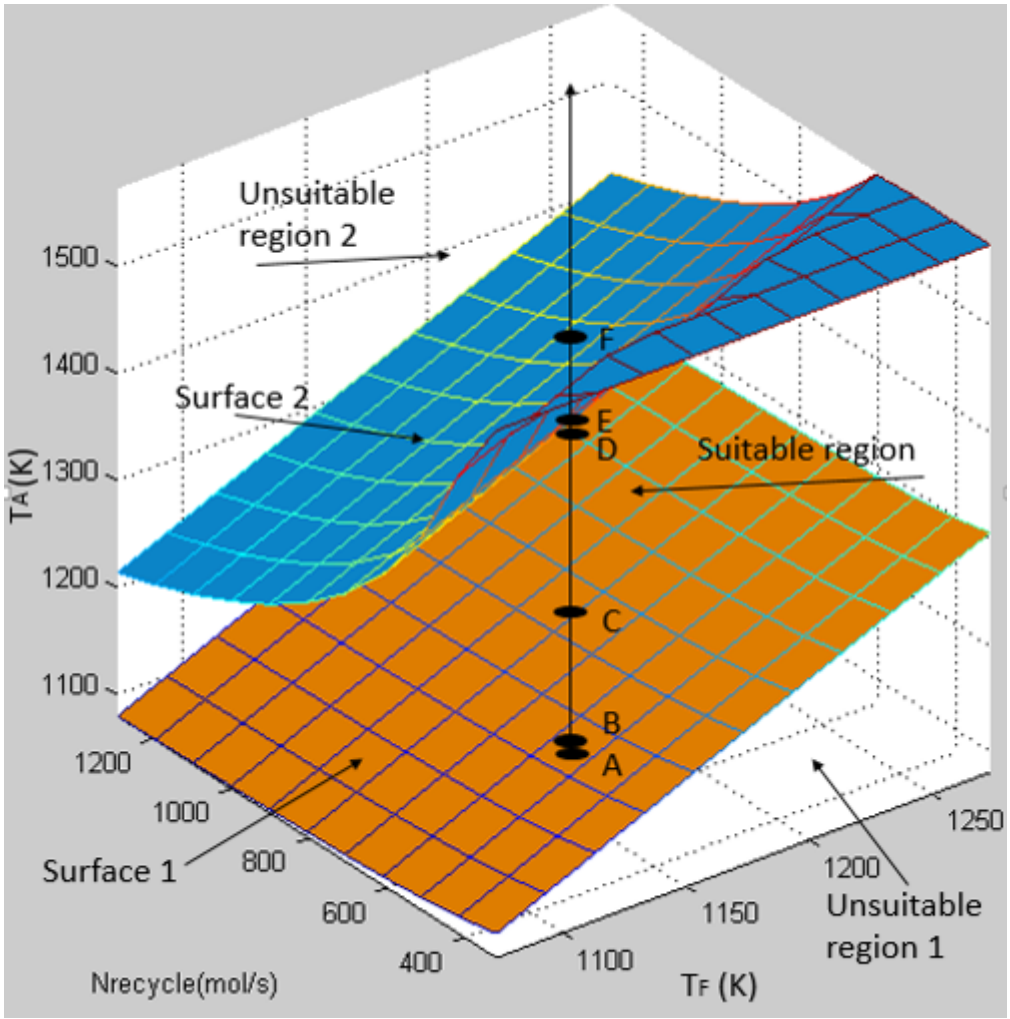

Figure 5.3 Plot of operating regimes as function of the temperature of the air reactor, temperature of the fuel reactor and the recycle rate of Fe_2O_3. The suitable region is indicated between surfaces 1 and 2 (including surface 1 and 2). Below surface 1 the fuel reactor is a net consumer of heat, above surface 2 heat integration is not possible. This is the base case and the fuel is Hambach lignite coal.

Figure 5.3 shows the conditions considered, and an envelope in which the

chemical looping plant would be "suitable" as defined in the previous section. To ensure there is no CO in the outlet gas, the minimum recycle rate of Fe_2O_3 required is 323 mol/s for a feed rate of coal 1kg/s; thus only recycle rates higher than this are shown in Figure 5.3. A higher recycle rate of Fe_2O_3 is possible and results in more rapid heat transfer between air reactor to fuel reactor, in fact, too low a recycle rate means insufficient heat is transported into the fuel reactor, and the fuel reactor becomes a net consumer of heat. In addition, a small recycle rate of Fe_2O_3 is preferred, since smaller recycle rates requires less energy to transport the material between the reactors. The temperature of fuel reactor was set between 1073K and 1273K. Gasification of even a reactive coal like lignite would be impractical at the lower temperature (John S. Dennis and Scott 2010).

In the space below surface 1 (region 1), the heat balance of fuel reactor is negative i.e. heat is required; the conditions under which the fuel reactor is adiabatic is shown by surface 1. Surface 2 shows the limiting case in which no heating from an external source is needed. At high T_F and low $N_{recycle}$, surface 2 is flat, which represents the situation when the calculated temperature of air reactor is limited to 1573K. Although in theory the air reactor could become a consumer of heat, this happens above surface 2 and does not need to be considered. The space between surface 1 and surface 2 is the suitable region, in which the heat balance of both air and fuel reactor is positive, and there is no hot utility needed.

The various cases can more easily be seen by taking a slice through Figure 5.3 at fixed fuel reactor temperature, as shown in Figure 5.4. Points A to F on Figure 5.3

and Figure 5.4, in which the temperature of the air reactor is increased, whilst keeping a constant recycle rate of 808.5 mol/s, show the different possible cases and are considered in more detail below.

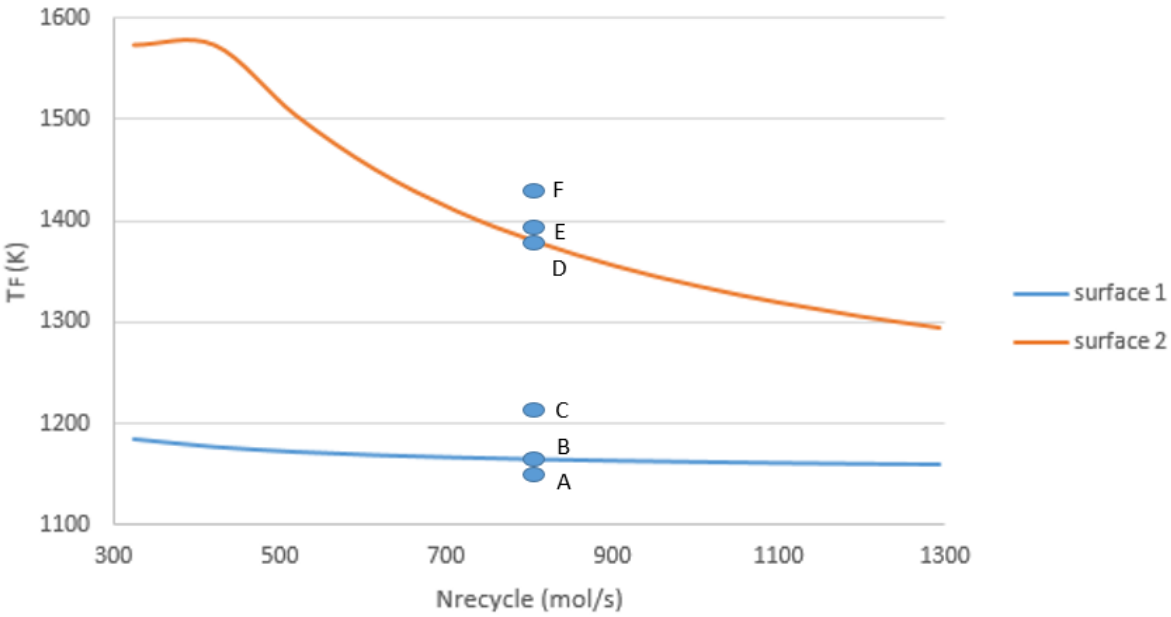

Figure 5.4 A cross section from Figure 5.3 (with T_A = 1153 K). Points A to F are shown.

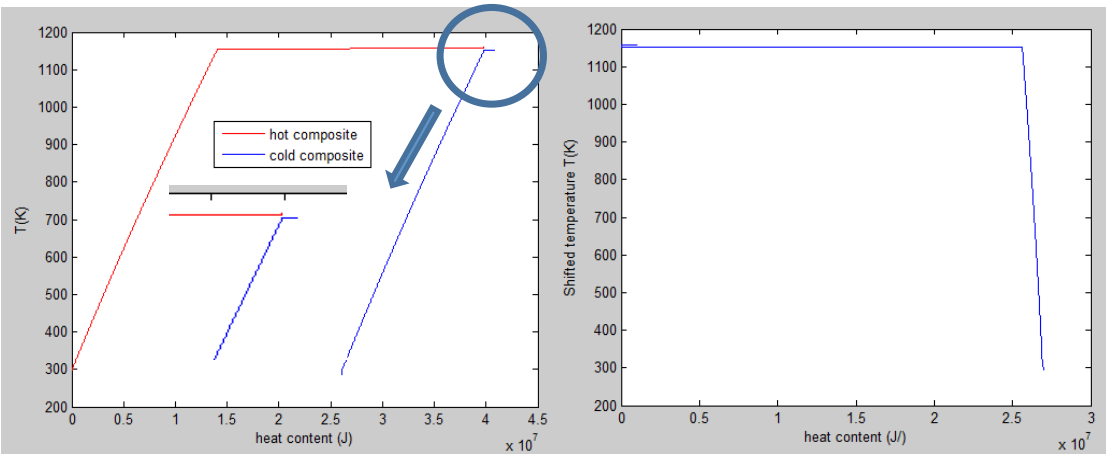

(a) (b)

Figure 5.5 (a) Composite curves at point A (T_F = 1153 K, T_A = 1156 K, $N_{recycle}$ = 808.5 mol/s). The tip part in the circle is enlarged. (b) Grand composite curve.

Figure 5.5 (a) shows the composite curves for Point A, i.e. a point below surface 1. The air reactor releases heat (and is hotter than the fuel reactor), so appears in the hot composite curve as the large horizontal section. The fuel reactor, being a consumer of heat is in the cold composite curve. Whilst, overall there is sufficient heat available, heat would have to be transferred between the air and fuel reactors, which are likely to be impractical in a large system. However, in Figure 5.5 (a), the temperature difference between the air reactor and the fuel reactor is 3K (i.e. less than the minimum temperature difference of the hot composite curve and the cold composite curve ΔT_{min} allowed), leading to pinch and meaning that hot utility is required. In addition, the difference of heat content between hot and cold composite curves is 26003 kJ, which as expected, is the heat of combustion of one kg of Hambach lignite coal.

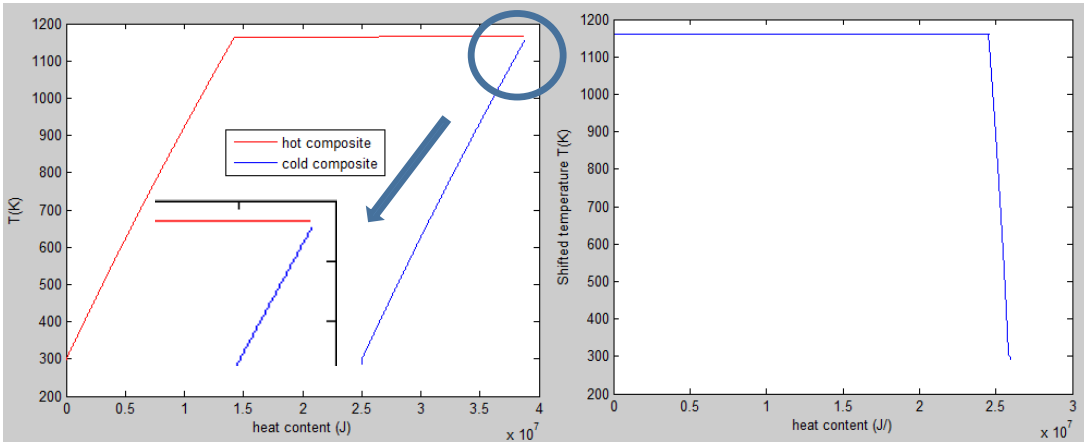

(a) (b)

Figure 5.6 (a) Composite curves at point B (T_F = 1153 K, T_A = 1165 K, $N_{recycle}$ = 808.5 mol/s). The tip part in the circle is enlarged. (b) Grand composite curve.

In Figure 5.5 (b), there is an extra part above the main body of the grand

composite curve, which represents the external heating for the cold composite curve.

Figure 5.6 shows the composite curves for point (B), i.e. on surface 1, when heat output of the fuel reactor is zero. Thus, there is no fuel reactor in the composite curves. Hot and cold composite curves pinch at the air reactor, and no hot utility needed.

In Figure 5.6 (b), most of heat available in the grand composite curve comes from the air reactor at a high temperature T_A. There are massive heat loads associating with heating and cooling gases, but these are hidden in the grand composite curves as the hot gases are used to preheat the cold feed streams. Practically, whilst being thermodynamically a good idea, it might not practical - lots of very large heat exchangers and pressure drops.

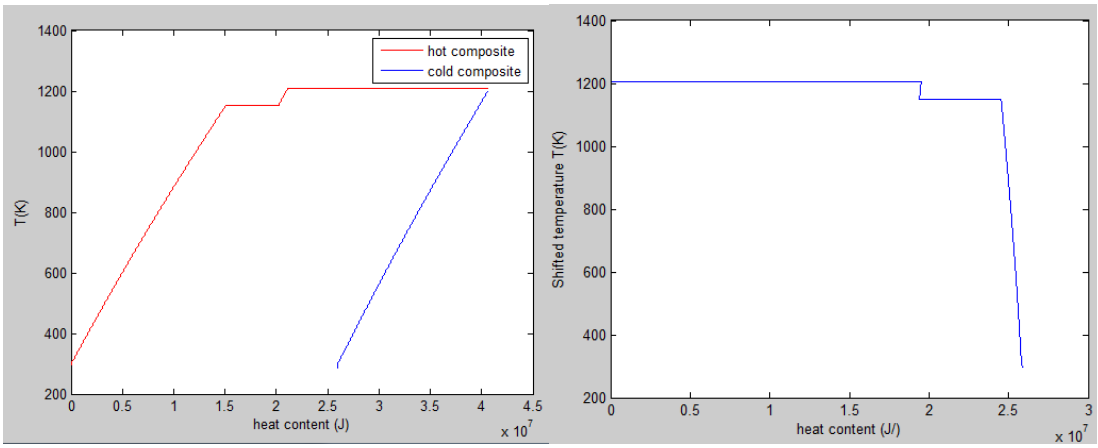

(a) (b)

Figure 5.7 (a) Composite curves at point C (T_F = 1153 K, T_A = 1210 K, $N_{recycle}$ = 808.5 mol/s). (b) Grand composite curve.

Figure 5.7 is for point C, in the suitable region, where both the fuel reactor and the air reactor are in the hot composite curve. In Figure 5.7 (a), the section of the cold

composite curve between T_F and T_A consists only of stream 14 (the air fed to the air reactor). The only heat sources available for this are the air reactor and the hot gases leaving the air reactor, since the fuel reactor is always colder. If the heat output of the air reactor is zero, there will be no heat source for available for stream 14 that able to heat it fully to the target temperature of 10 K below the air reactor temperature. If this happens, the cold composite curve has to move right, which means hot utility is required. Thus, the heat output of air reactor being zero cannot be used as the upper limit of the suitable region; instead, no hot utility required should be used as the upper limit.

In Figure 5.7 (b), the plats at T_A and T_F are shown in the grand composite curves. In addition, the grand composite curve decreases from T_A to T_F, which means the slope from T_A to T_F of the cold composite curve is larger than the hot composite curve.

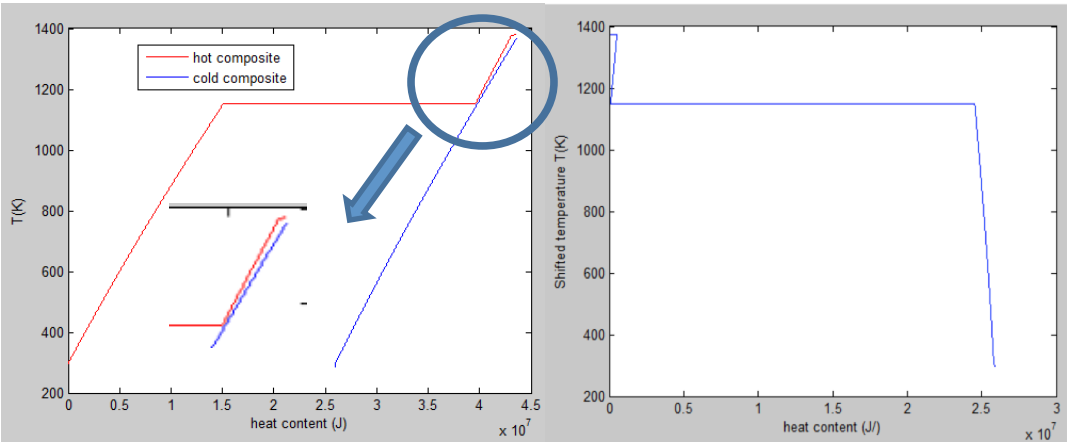

(a) (b)

Figure 5.8 (a) Composite curves at point D (T_F = 1153 K, T_A = 1378 K, $N_{recycle}$ = 808.5 mol/s). The tip part in the circle is enlarged. (b) Grand composite curve.

Figure 5.8 (i.e. point D) shows the limiting case (i.e. on surface 2) where the heat load for the air reactor is just sufficient to provide the heat required for preheating stream 14. In Figure 5.8 (a), the hot and cold composite curves pinch at both T_A and T_F. In Figure 5.8 (b), the grand composite curve reaches zero at both T_A and T_F.

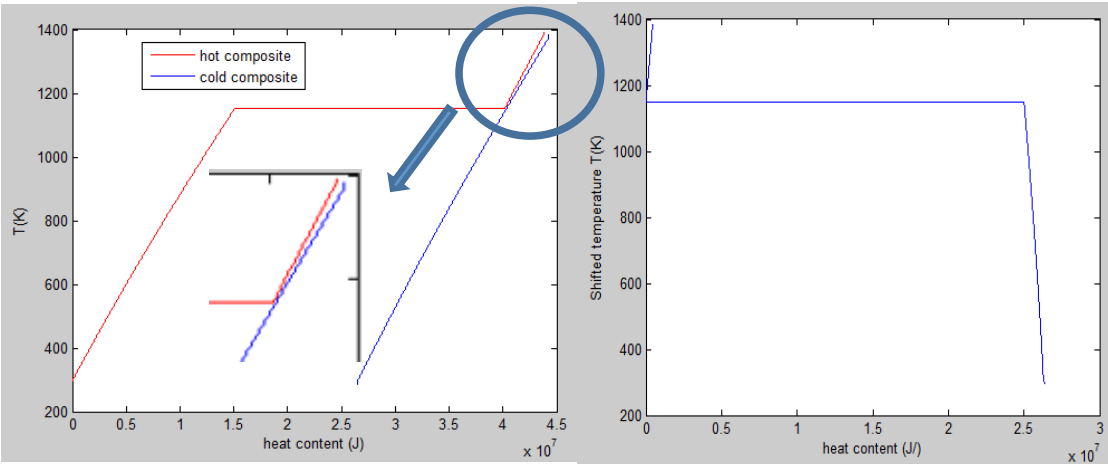

(a) (b)

Figure 5.9 (a) Composite curves at point E (T_F = 1153 K, T_A = 1383 K, $N_{recycle}$ = 808.5 mol/s). The tip part in the circle is enlarged. (b) Grand composite curve.

Figure 5.9, shows the point E, which is above surface 2, where the air reactor has become adiabatic. In Figure 5.9 (a), the hot and cold composite curves pinches at the fuel reactor. In this case, hot utility is needed for the preheating. In Figure 5.9 (b), the slope of the part of grand composite curve between T_A and T_F is negative since external heat is required.

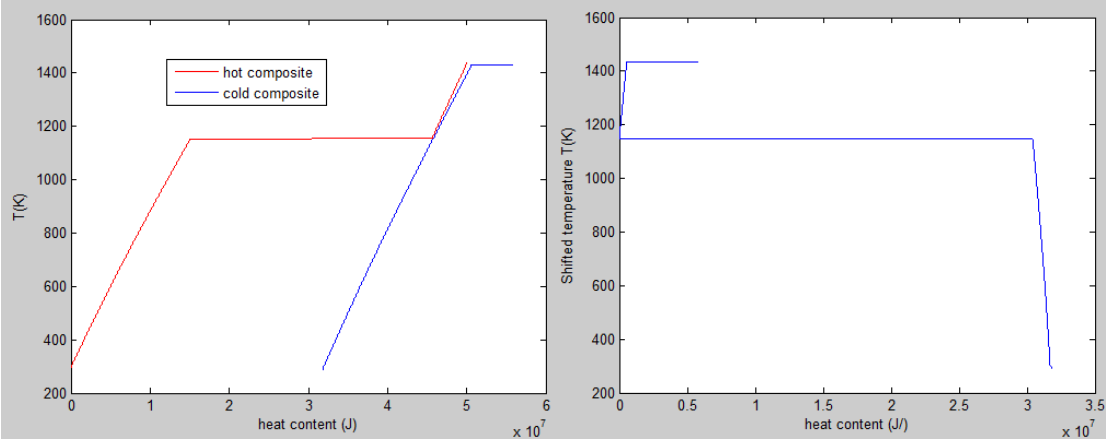

(a) (b)

Figure 5.10 (a) Composite curves at point F (T_F = 1153 K, T_A = 1430 K, $N_{recycle}$ = 808.5 mol/s). (b) Grand composite curve.

In Figure 5.10 (a), when the heat output of the air reactor is negative, the air reactor is in the cold composite curve, and the hot utility is needed. In Figure 5.10 (b), the top part of the grand composite curve is a combination of Figure 5.5 (b) and Figure 5.10 (b): the horizontal tip is similar to Figure 5.5 (b), which represents the external heating supply for the air reactor; the slope of the part between two horizontal parts is negative, which is similar to Figure 5.9 (b), representing even though there is heat supply from the hot composite curve, external heating is still required in this temperature region.

5.2.1.2 The search of efficiency of the whole system

The efficiency of the whole system, which is defined in *Section 5.1.1.6*, depends on both the energy content of the coal and the work produced by the steam cycle. For a fixed coal, and a fixed configuration of steam cycle (all temperatures and

pressures fixed), the only variable is the flow rate of steam cycle. The work produced by the steam cycle is proportional to the flow rate of the steam cycle, so searching for maximum efficiency of the whole system is equivalent to finding the largest flow rate of steam. For a given chemical looping system, the maximum flow rate of steam cycle is found by increasing the flow rate of steam, until the overall system (chemical looping system + steam cycle) becomes a net consumer of heat.

The search for the conditions in the chemical looping flow sheet, which maximise the steam flow rate (and hence work output) should consider the entire suitable region bounded by surface 1 and 2 in Figure 5.3. However, an analysis of the composite curve shows that this process can be simplified.

Figure 5.11 (a) shows the composite curves of the whole system in the suitable region. All conditions are the same as Figure 5.7, except for the flow rate of the steam cycle is 6.45 kg/s. Comparing to Figure 5.7, the part of cold composite curve at lower temperature expands to the left, and will pinch with the hot composite curve at 393K. 393 K is the temperature of preheating of the boiler, pinching at this temperature means the heat at temperature lower than 393K cannot be used, which supports the neglect of condensation of CO_2 in Stream 3 in heat integration.

In Figure 5.11, the part of cold composite curve between point a and point b consists of; the part between point b and point c consists of preheating; the part between point c and point d consists of the part between point c and point d

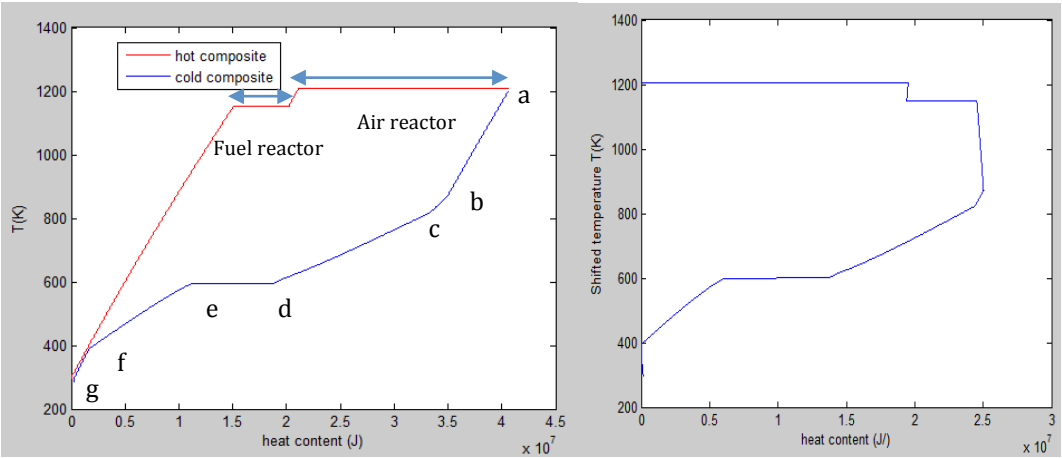

(a) (b)

Figure 5.11 (a) Composite curves at point C (T_F = 1153 K, T_A = 1210 K, $N_{recycle}$ = 808.5 mol/s) with the flow rate of steam cycle at 6.45 kg/s. (b) Grand composite curve.

Table 5.8 The analysis of cold composite curve

The part of cold composite curve	Preheating stream
Point a and Point b	Stream 5 and Stream 9
Point b and Point c	Stream 5, Stream 9 and s6
Point c and Point d	Stream 5, Stream 9, s4, s6 and the steam from steam drum
Point d and Point e	Evaporation in the steam drum
Point e and Point f	Stream 5, Stream 9 and boiler feed water
Point f and Point g	Stream 9

Now consider the effect of changing the heat output of the fuel reactor output by changing the recycle rate, keeping T_F and T_A Fixed. The optimum steam flow in the suitable region is determined by positioning the upper most point of the cold composite curve (Point a in Figure 5.11) directly beneath the upper most point of the

hot composite curve; and increasing steam flow until the cold composite curve pinches at the low temperature end (Point e). Changing the recycle rate simply changes the lengths of the segments representing the fuel and air reactors, whilst keeping the sum of the lengths equal. These lengths are able to change freely, without having any effect on the cold composite curve, and without requiring any change to the steam flow. The rebalancing of the heat load between reactors is all happening at temperatures well above the pinch point temperatures, and has no effect on the position of pinch point, requiring no change in steam flow to achieve that pinch point. Thus, providing the only pinch is the low temperature pinch, the optimum steam flow does not depend on the recycle rate of solids (i.e. starting on surface 1 and moving upwards in Figure 5.3 to surface 2). Surface 2 represents the limiting case, in which a second pinch appears in the system (as shown in Figure 5.12), however the region beyond surface 2 is of no interest since after this point some hot utility is then required. The optimisation of the system can then be simplified since only the points on surface 1 need to be examined. The analysis here would suggest that all the points between surface 1 and 2 are equally as good, however, in practice it would not be sensible to design the system to have two reactors releasing heat. In this case, capital cost would be increased as two heat exchange systems would be needed, and the system would be operating at a recycle rate greater than required (which results in an additional energy penalty not included in this analysis). In addition, T_A on surface 1 is lower than on suitable region or on surface 2. Lower T_A is preferred since the air reactor does not have to endure high temperature, and the cost of the air reactor can be

reduced. Thus, the searching for maximum steam flow is only needed to focus on surface 1.

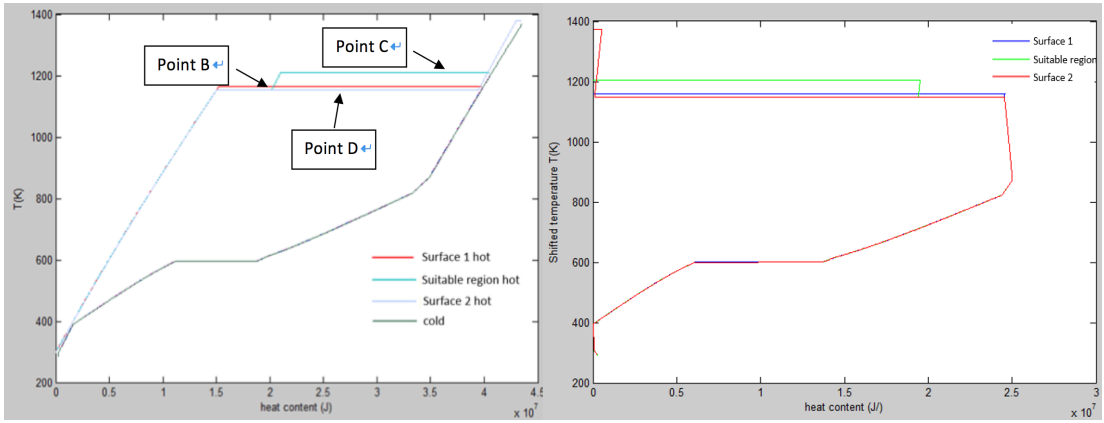

(a) (b)

Figure 5.12 A comparison of (a) composite curves, (b) grand composite curves in surface 1 (point B, T_F = 1153 K, T_A= 1165 K, $N_{recycle}$ = 808.5 mol/s), suitable region (point C, T_F = 1153 K, T_A = 1210 K, $N_{recycle}$ = 808.5 mol/s) and surface 2 (point D, T_F = 1153 K, T_A = 1378 K, $N_{recycle}$ = 808.5 mol/s). In (a), the cold composite curves are same and pinches with hot composite curves at low temperature (steam flow is at maximum 6.45 kg/s). Since cold composite overlap with each other, so their colours are same.

Figure 5.12 shows the how the composite curves change going from surface 1 (point B), through the suitable region (point C) to surface 2 (point D) at a constant recycle rate and a constant temperature of the fuel reactor, but this time increasing the temperature of the air reactor. Apart from conclusions from Figure 5.6, Figure 5.7 and Figure 5.8, which are still valid for Figure 5.12, there are some other conclusions can be reached from Figure 5.12: 1) The cold composite curves are fixed for points B, C

and D; 2) The parts of hot composite curves before the fuel reactor overlap with each other for points B, C and D; 3) Hot and cold composite curves for point B, C and D pinch at the same place: the temperature of preheating (the boiler feed water input temperature). 4) The maximum of flow rate of steam cycle is found to keep the same, that is, 6.45 kg/s.

Figure 5.13 (a) shows the comparison of composite curves at three random chosen points on surface 1: 1) point B, T_F = 1153 K, T_A = 1165 K, $N_{recycle}$ = 808.5 mol/s; 2) T_F =1073 K, T_A = 1103 K, $N_{recycle}$ =323 mol/s; 3) T_F =1273 K, T_A = 1281 K, $N_{recycle}$ = 1292 mol/s. The results of the maximum steam flow on surface 1 show that the maximum value keeps the same in all 3 points on surface 1: 6.45 kg/s. This can be explained that the slope of the part of hot composite curve before fuel reactor is fixed, and the change of conditions on surface 1 does not influence that part of composite curves. Combining with the conclusion from Figure 5.12, the maximum flow rates of suitable conditions are same at any point of surface 1, the suitable region and surface 2. This can also be explained by using the grand composite curve in Figure 5.13 (b). Basically, the heat left over is at such a high temperature it doesn't matter what recycle rates and T_F and T_A the chemical looping plant runs at. The steam cycle is at such a low temperature it makes no difference. **Thus, the operating condition can be chosen within the space (surface 1, the suitable region and surface 2) as the real situation requires.**

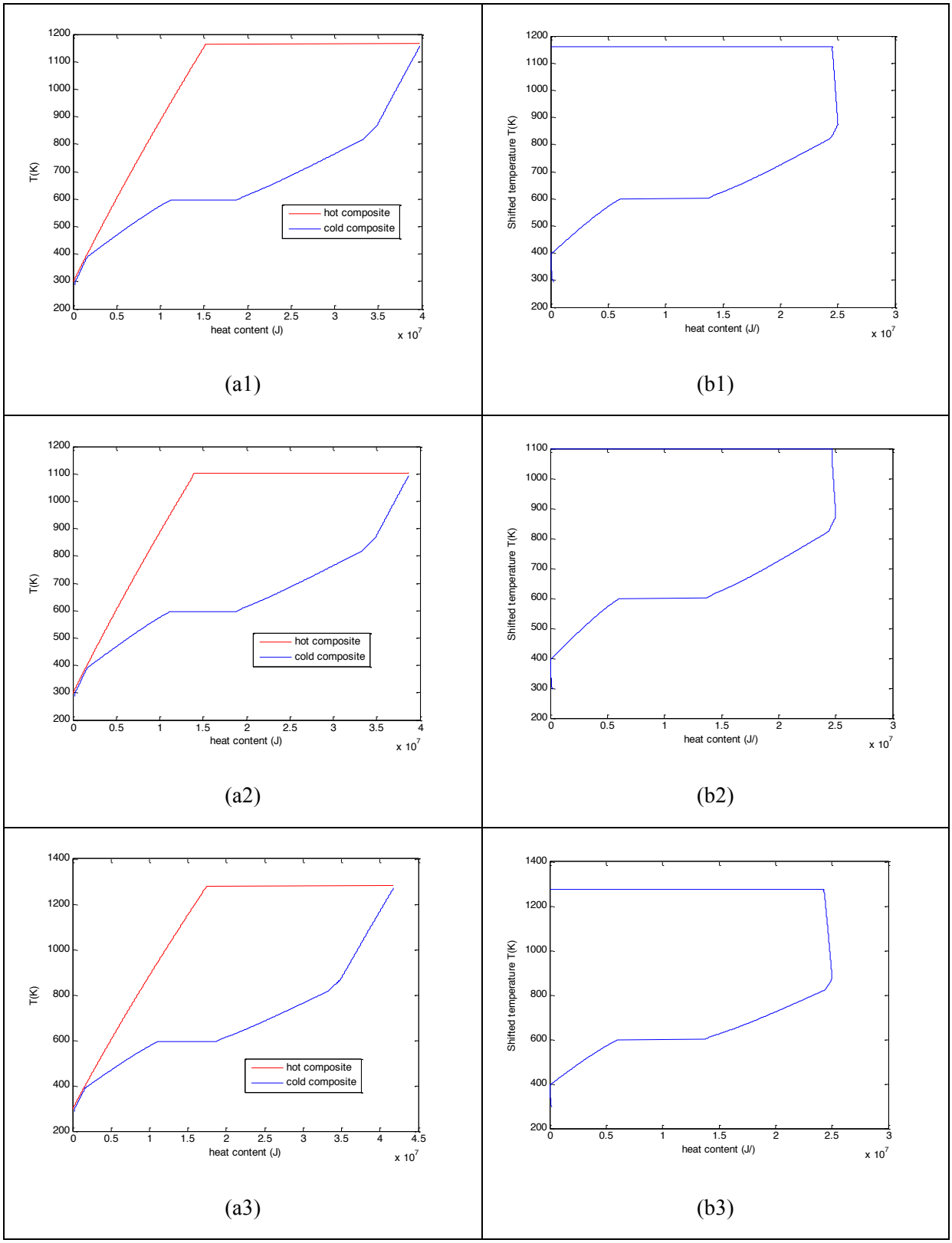

Figure 5.13 The composite curves and grand composite curves in three different points on surface 1: (a1, b1) point B, T_F = 1153 K, T_A = 1165.3 K, $N_{recycle}$ = 808.5 mol/s; (a2, b2) T_F =1073 K, T_A = 1103 K, $N_{recycle}$ =323 mol/s; (a3, b3) T_F

=1273 K, T_A = 1281 K, $N_{recycle}$ = 1292 mol/s. The cold composite curves are same and pinches with hot composite curves at low temperature (steam flow is at maximum 6.45 kg/s).

5.2.1.3 The exergy map of the whole system

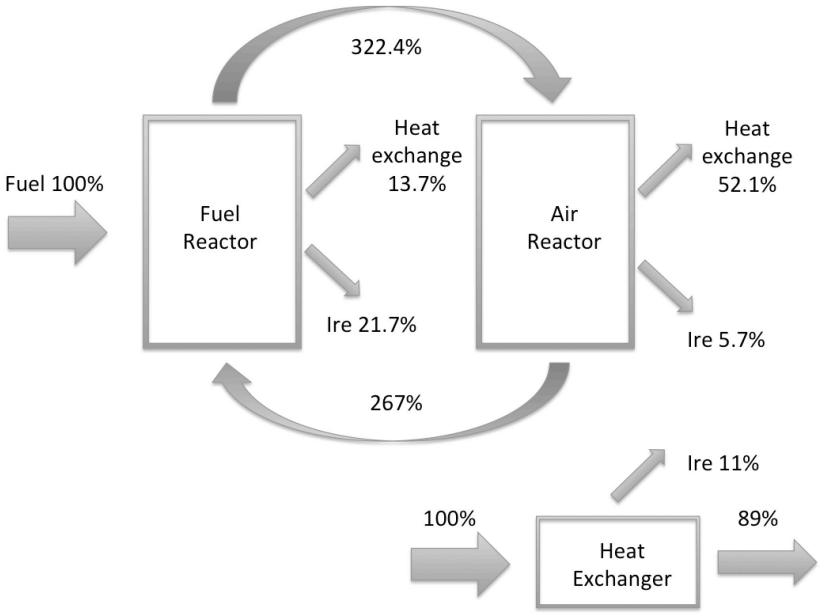

Figure 5.14 The exergy map of the chemical looping plant and the heat exchangers (T_F = 1153 K, T_A = 1210 K, $N_{recycle}$ = 31018 mol/s, 38.6kg/s Hambach coal, the airflow into the air reactor is preheated to 1200K).

Figure 5.14 shows the exergy map of the whole system at point C (case 1) (T_F = 1153 K, T_A = 1165.3 K, $N_{recycle}$ = 31018 mol/s, 38.6kg/s Hambach coal). Initially, 100% of the fuel exergy comes into the fuel reactor. 13.7% exergy is used for heat exchange, and 21.7% exergy is lost due to irreversibility. For the air reactor, 52.1% exergy is used for heat exchange, and 5.7% exergy is lost due to irreversibility. The air reactor has larger heat exchange than the fuel reactor is because that the reactor

has larger heat content than the fuel reactor in Figure 5.11 (a). The fuel reactor has larger has larger irreversibility is due to the combustion of the fuel, which has huge exergy loss. The total exergy loss from heat exchanging can be calculated from the Figure 5.11 (a) by equation,

$$E_{HEL} = E_H - E_L = \int \left(1 - \frac{T_0}{T_H}\right) dQ - \int \left(1 - \frac{T_0}{T_L}\right) dQ = \int T_0 \left(\frac{1}{T_L} - \frac{1}{T_H}\right) dQ \qquad (5.12)$$

where E_{HEL} is the exergy loss from heat exchanging; E_H and E_L are the exergy of the hot and cold composite curves, respectively; T_0 is the reference environmental temperature; Q is the heat content. The total exergy loss from heat exchanging is 19.3%.

At the temperature below the pinch point 400K, there is also exergy loss since the temperature is too low to be usable. The corresponding $E_H = \int_{298.15}^{400} \left(1 - \frac{T_0}{T_H}\right) dQ$ is 1.8%.

In stream 7, water and CO_2 leave the chemical looping plant, which brings away 3.9% exergy; the stream 13 and stream 16 are flow- in and flow-out of air of the air reactor at reference environmental temperature, and the exergy of them are 0 and 0.12%, respectively. Similarly, stream 2 and stream 5 are flow-in and flow-out of O2 of the fuel reactor. The temperatures and contents of the two streams are same, so the exergy are same. Thus, they cancel out with each other.

For the steam cycle, 1% exergy is lost in the mixer; 2.6% exergy is lost in the condenser; 3.6% exergy is lost in three turbines.

Thus, the total exergy loss is E_{TL} = 21.7% + 5.7% + 19.3% + 1.8% + 3.9%+

0.12% + 1% + 2.5% + 3.3%=59.3%.

The rest part of exergy becomes the output work from the steam cycle system, which is 40.7% of the input fuel exergy, and the total exergy efficiency of the whole system is 40.7%. Operating conditions are changed to test if the exergy and thermal efficiency are independent of operating conditions: (case 2) Point B (T_F = 1153 K, T_A = 1165 K, $N_{recycle}$ = 31018 mol/s, 38.6kg/s Hambach coal, the airflow into the air reactor is preheated to 1155K).

Table 5.8 A comparison of exergy loss and thermal efficiency of two cases.

	Case 1	Case 2
Fuel reactor irreversibility	21.7%	21.6%
Air reactor irreversibility	5.7%	4.2%
Heat exchanging	19.3%	21.8%
Temperature lower than pinch point	1.8%	0.9%
Stream 7	3.9%	3.9%
Stream 16	0.12%	0.12%
Mixer	1%	1%
Condenser	2.5%	2.5%
Turbines	3.3%	3.3%
Thermal efficiency	40.7%	40.7%

Table 5.8 shows that, by altering the operating conditions, it just alters the balance of where the losses of exergy are. The changes of exergy losses are minor, and the thermal efficiency keeps the same.

There are two parts of main exergy losses: fuel reactor irreversibility and heat exchanging. For the fuel reactor, this is due to the combustion, which is unavoidable; for the heat exchanging, increasing the temperature of the air reactor can reduce it.

However, this reduction is partially cancelled by the increase of the air reactor irreversibility.

5.2.2 Significance of input parameters of chemical looping plant

There are four important input parameters of chemical looping plant: 1) flow rate of air into air reactor, 2) flow rate of CO_2 and water into the fuel reactor, 3) the temperature to which the gases entering the reactors are preheated in the chemical looping plant and 4) fuel type. In this section, the influences of these input parameters are discussed below.

5.2.2.1 Flow rate of air into air reactor (N_{air})

The minimum of the flow rate of air into air reactor is that which can ensure all oxygen carriers are fully oxidised. When the 1 kg/s of Hambach lignite coal is supplied, the minimum stoichiometric required airflow, N_{air}, is 255.7 mol/s. In Figure 5.3, the flow rate of air into air reactor was set to be twice this minimum, i.e. 511.4 mol/s. The choice of airflow is a balance of three factors: 1) Ensuring full oxidation and fluidisation of the air reactor; 2) Optimising the mechanical design of the air reactor; 3) maximising the steam flow rate in the power cycle. Factor 1 requires large flow rate; in contrast, factor 2 requires small flow rate since any additional air over and above the minimum more heat transfer in preheating and power to overcome frictional pressure losses. For factor 3, the relation between N_{air}

and steam flow in the power cycle is less obvious.

Figure 5.15 shows the composite curves and grand composite curves conditions as for point B ($N_{recycle}$ = 808.5 mol/s, N_{air} = 511 mol/s T_A = 1165.3 K, T_F = 1153 K), and when N_{air} is increased to 511×20 mol/s and decreased to 511.4/2 mol/s. The optimum steam flow decreases when N_{air} increases, 6.45 kg/s for 511/2 mol/s, 6.45 kg/s for 511 mol/s and 5.6 kg/s for 511×20 mol/s. This can be explained that: when N_{air} becomes larger, there is more heat taken from the air reactor. The extra heat taken from the air reactor is used to preheat the inlet airflow (stream 13), which leads to exergy loss since heat from the air reactor has higher temperature. Similar to factor 2, small flow rate is preferred. Thus, 511 mol/s, twice of the minimum flow rate, is chosen.

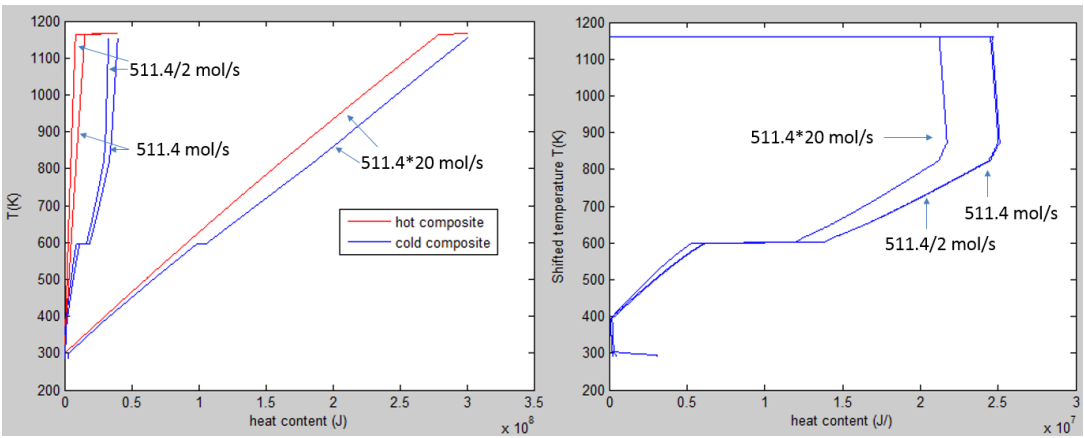

(a) (b)

Figure 5.15 The composite curves (a) and grand composite curves (b) at PointB ($N_{recycle}$ = 808.5 mol/s, T_A = 1165.3 K, T_F = 1153 K) for different N_{air} 1) 511/2 mol/s, 2) 511 mol/s and 3) 511×20 mol/s at optimum steam flow. The corresponding optimum steam flows are: 1) 6.5 kg/s for 511/2 mol/s, 2) 6.45 kg/s for 511 mol/s and

3) 5.6 kg/s for 511×20 mol/s.

5.2.2.2 Flow rate of CO_2 and water into the fuel reactor ($N_{CO_2,water}$)

As discussed above, this stream is a part of stream 6, and it has to be cooled down first to 773K to make sure it can go through a fan. It is then preheated to T_F-10K and goes into the fuel reactor. This process leads to exergy penalty; so small flow rate is preferred. In addition, larger flow rate of stream 4 means larger reactor, so the current flow rate, that is, the minimum one, is the suitable one.

5.2.2.3 Effect of pre-heating of flow-in air in chemical looping combustion plant

In previous sections, the inlet gas flow into the air reactor is pre-heated to 10 K below the temperature of the reactor. This process makes the system more complex and would require a large heat exchanger. Thus, whether the pre-heating temperature can be lowered without influence on the efficiency of the whole system is investigated in Figure 5.16.

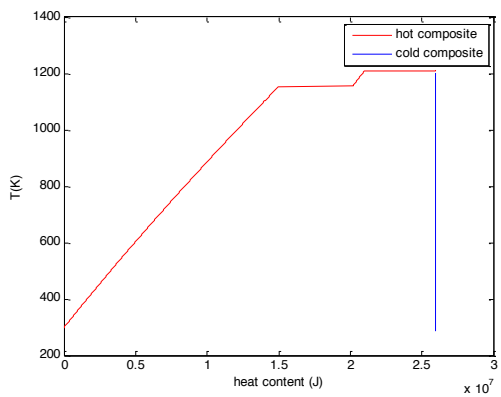

(a1)

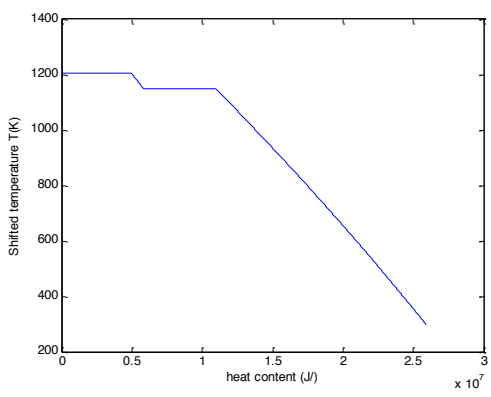

(b1)

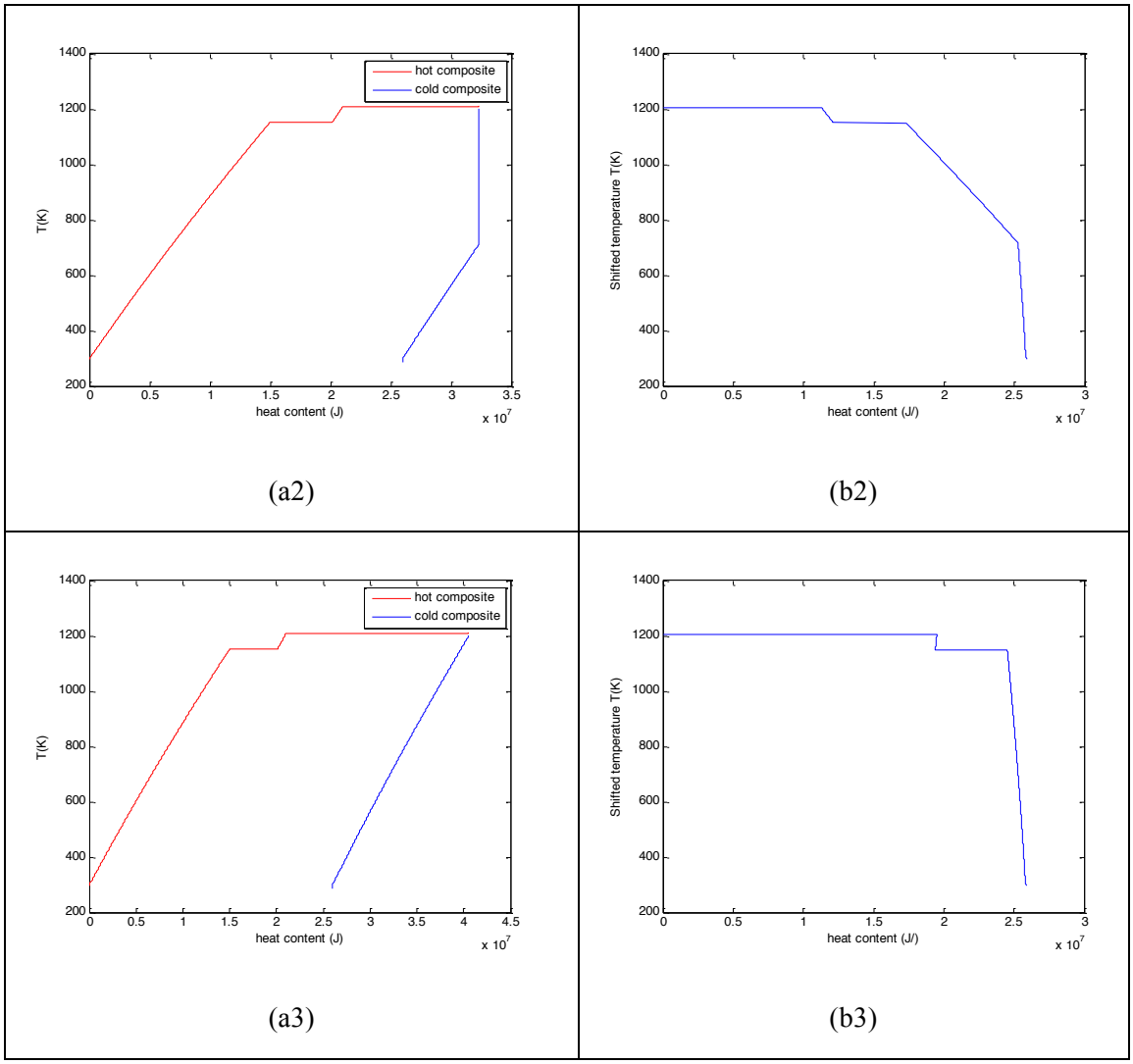

Figure 5.16 (a1-a3) the tests of different preheating plans: the preheat temperature T_{pre}, that is, the temperature of stream 14, is: (a1) 298.15K; (a2) 710K; (a3) 1200K. (T_F = 1153 K, T_A = 1210 K, $N_{recycle}$ = 808.5 mol/s); (b1-b3) the grand composite curves: (b1) 298.15K; (b2) 710K; (b3) 1200K.

In Figure 5.16, the composite curves obtained for three different preheating temperatures are shown: the preheat temperature T_{pre}, that is, the temperature of stream 14, is: (a1) 298.15K; (a2) 710K; (a3) 1200K. From the grand composite curves, the overall amount of heat available is the same in each of the three cases. For the base case (a3), which was previously discussed, the hot and cold composite curves

show there is significant heat exchange between the gases leaving and entering the reactor (i.e. the sloping sections), but that these heat exchanges can largely be met within the system without a pinch. The grand composite curve in this case is dominated by the horizontal sections, which represent the reactors. For cases in which the air stream is preheated to a lower temperature, the grand composite curves show that a larger proportion of heat is available at a lower temperature. For example in (b2), the section with the largest gradient, between 700 K and 300 K; arises from the need of heat the air stream using heat from the reactors, rather than recovering it form the exhaust. The preheating therefore maximises the amount of high temperature heat, which is available to the steam cycle. However, it was shown above that the pinch point when integrating the steam cycle is likely to be at the boiler feed water temperature. This means that providing the gas streams are preheated to via internal heat exchange with other gas streams to at least the temperature of boiler feed water, and further preheating will have no effect on the pinch point, or the amount of steam that can be produced in the boiler. Thus, a test is run about this issue. In the test, T_{BFW} is set between 393K and 413K. Since at 413K, the saturated vapour pressure has already reached 3.6 atm, which is quite high for the steam drum. In addition, with the change of T_{BFW}, many other parameters in Table 5.5, for instance, pressure of stream s1 and mass flow rate of stream s9, change as well. Taking all these changes into account, the maximum steam flow rate at different T_{pre} and T_{BFW} is shown below in Table 5.9.

Table 5.9 The maximum steam flow rate (kg/s) at different preheat temperature T_{pre} (298.15K – 1200K) and the temperature of the boiler feed water T_{BFW} (393K – 413K) (T_F = 1153 K, T_A = 1210 K, $N_{recycle}$ = 808.5 mol/s).

		Preheat temperature (T_{pre})				
		298.15K	398.15K	498.15K	598.15K	1200K
Temperature of boiler feed water (T_{BFW})	393K	234.9	248.3	248.3	248.3	248.3
	403K	236.1	250	250	250	250
	413K	237.3	251.9	253	253	253

In Table 5.9, there are two features: 1) when the temperature of the boiler feed water is fixed, the increase of the preheat temperature can increase the maximum steam flow rate, but when the preheat temperature reaches a certain value, the maximum flow rate stops increasing. This can be explained that if the airflow into the air reactor is not preheated, the mixing in the air reactor will lead to huge exergy loss. But when the preheat temperature is high enough, most of heat after mixing is still usable for the steam cycle. Thus, as long as the preheat temperature is too low, there is enough exergy to heat up the steam cycle. The lowest preheat temperature for the steam flow rate to reach its maximum is: for T_{BFW} = 393K or 403K, it is between 298.15K and 398.15K; for T_{BFW} = 413K, it is between 398.15K and 498.15K. Thus, the lowest preheat temperature for the maximum steam flow rate increases with the increase of T_{BFW}. This can be explained by the fact that since T_{BFW} increases, the temperature difference between T_A and T_{BFW} decreases, which means to heat up the steam cycle the chemical looping plant must has more exergy. Thus, more preheating is required to compensate for this; 2) with the increase of T_{BFW}, the maximum steam

flow rate increases as well. The increase of T_{BFW} means the pinch point of the hot and cold composite curves moving to a higher temperature, which leads to the total heat absorbed by the cold composite curve decrease. However, the cold composite curve is composed of two parts: chemical looping plant (air flow into the air reactor) and steam cycle. The ratio of steam cycle in cold composite curve increases when T_{BFW} increases since steam cycle can get more exergy in this mode.

The optimum preheating temperature is therefore chosen at the temperature between 298.15K and 398.15K, which depends on T_{BFW}. T_{BFW} is chosen between 393K and 403K. If T_{BFW} is higher than 403K, the operating pressure of the boiler will be higher than 2.7 atm, which is not economically reasonable.

5.2.2.4 Effect of fuel type

Different types of fuel have different heat of combustion, and this difference can influence many parameters in the whole system, for instance, the maximum flow rate of the steam cycle.

Table 5.10 shows the comparison of key parameters when Hambach lignite coal, Polish bituminous coal (#1286) and natural gas are used. To enable a fair comparison, a basis of 1GJ /s of fuel is used.

Table 5.10 Comparison of key parameters when different fuels are used: Hambach lignite coal, Polish bituminous coal (#1286) and natural gas.

		Hambach lignite Coal	Polish bituminous coal (#1286)	Natural gas
Parameters	Unit	Base case/ range	Base case/ range	Base case/ range
Flow rate of air into the air reactor (N_{air})	mol/s	19668	11392	25239
Flow rate of fluidising gas into the fuel reactor (N_f)	mol/s	1687	1883	0
Mass of fuel supply	kg/s	38.5	34.4	21.2
Energy of fuel supply	GJ/s	1	1	1
Heating value per mole of carbon	kJ/(mol carbon)	568	475	755
Recycle rate of metal oxide ($N_{recycle}$)	mol/s of Fe_2O_3	12423 to 49690	14364 to 121152	15942 to 211472
Temperature of the Air Reactor (T_A)	K	1093-1573	1093-1573	1093-1573
Temperature of the Fuel reactor (T_F)	K	1073-1273	1073-1273	1073-1273
Amount of oxygen required per GJ released	mol/s	2068	2395	2650

The amount of oxygen required per GJ released is: natural gas > Polish bituminous coal > Hambach lignite coal, which means $N_{recycle}$ are different. The larger the $N_{recycle}$ is, the more exergy Fe_2O_3 takes away from the air reactor to the fuel reactor. At Point B, the $N_{recycle}$ of CH_4 is about 1.25 times of Hambach lignite coal; at point D, $N_{recycle}$ of CH_4 is 4 times of Hambach lignite coal. This reduces the

temperature difference of the air reactor and the fuel reactor. The influence of preheating of Polish bituminous coal (#1286) and CH_4 is similar to Hambach lignite coal, which has minor influence on the grand composite curve. In Figure 5.17, comparison of grand composite curves for three kinds of fuel (1 GJ) is made. For Hambach Lignite coal, point B is chosen, which means the fuel reactor is adiabatic. For all three kinds of fuel, T_F = 1153 K and T_A = 1210 K; For Hambach lignite coal, $N_{recycle}$ = 31018 mol/s; For Polish bituminous coal (#1284), $N_{recycle}$ =121150 mol/s; For CH_4, $N_{recycle}$ =211472 mol/s. The preheating temperature of the airflow into the air reactor is 1200K. The results show that the maximum flow rate of steam cycle (248 kg/s) is same for all three kinds of fuel, which means the power output are same for three cases.

The heating value per mole of carbon is: natural gas > Hambach lignite coal > Polish bituminous coal, but the total energy fuel supply are same, so this factor has no influence.

Another difference is, since natural gas itself is gas, no extra fluidising gas into the fuel reactor, this can simplify one step in the flowsheet of chemical looping plant.

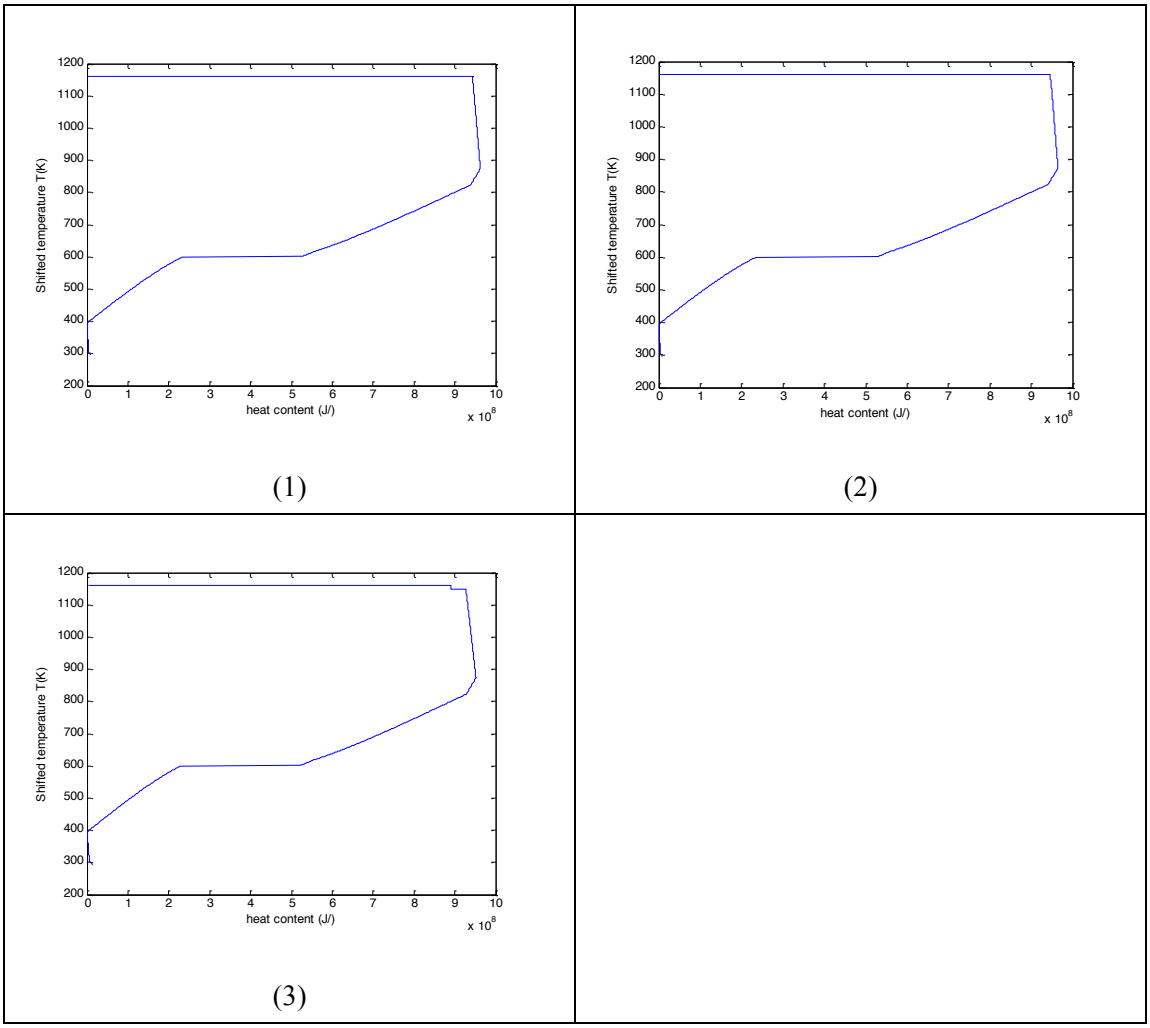

Figure 5.17 Comparison of grand composite curves of three kinds of fuel: (1) Hambach lignite coal; (2) Polish bituminous coal (#1284); (3) CH_4. (For all three kinds of fuel, T_F = 1153 K and T_A = 1210 K; For Hambach lignite coal, $N_{recycle}$ = 31018 mol/s; For Polish bituminous coal (#1284), $N_{recycle}$ =121150 mol/s; For CH_4, $N_{recycle}$ =211472 mol/s). The preheating temperature of the airflow into the air reactor is 1200K. Maximum flow rate of steam cycle (248 kg/s) is same for all three kinds of fuel.

5.2.3 The interaction between chemical looping plant and steam cycle

The optimum conditions for the chemical looping plant simply maximise the

amount of high temperature heat available for the steam cycle, and the majority of the heat is available at temperatures well above the steam cycle temperatures. When the steam flow rate increase, the part of steam cycle in the cold composite curve is scaled up to absorb the heat. The only case in which the design of the steam cycle and chemical looping plant would have a synergistic effect (i.e. couldn't be optimised separately) would be if, the pinch point could be changed. E.g. if the preheating is set to be 383K for the air flow into the air reactor, and the steam cycle has a T_{BFW} below 383K, but another design has a T_{BFW} above 383K, the chemical looping combustion plant could be further optimised for the latter by moving the pinch. That said, the amount of heat available below the T_{BFW} is relatively small, so as long as T_{pre} is above T_{BFW}, they can be optimised separately, which has been discussed in *Section 5.2.2.3*.

5.2.4 Comparison of different steam cycle schemes

In this chapter, steam cycle parameters are taken from Mukherjee (Mukherjee et al. 2014). However, the schemes are not the same. In addition, boiler feed water is set as a variable in this chapter. A comparison of different researchers, Peltola (Peltola 2014) and Mukherjee (Mukherjee et al. 2014), are shown in Table 5.11.

In Table 5.11, it shows that Peltola's steam cycle scheme has higher efficiency. This can be explained that in his scheme, both temperatures and pressures of turbines are generally higher than ones in Mukherjee's scheme. Thus, higher temperatures and pressures of turbines in the steam cycle can increase the efficiency and exergy

efficiency of the whole system.

Table 5.11 Temperature and pressure of turbines in different steam cycle schemes.

	Peltola (Peltola 2014)	Mukherjee (Mukherjee et al. 2014)
HP turbine temperature (K)	813	823
HP turbine pressure (bar)	170.5	124
IP turbine temperature (K)	883	823
IP turbine pressure (bar)	83.3	30
LP turbine temperature (K)	883	873
LP turbine pressure (bar)	17.7	6.5
Efficiency	45.7%	43.9%
Exergy efficiency	42.3%	40.7%

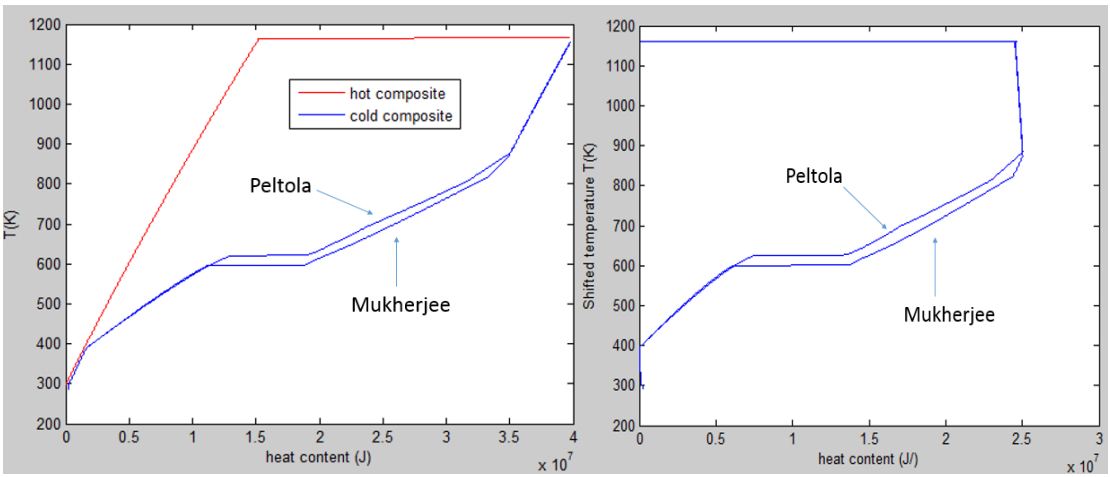

(a) (b)

Figure 5.18 Comparison of composite curves (a) and grand composite curves of scheme of Peltola and scheme of Mukherjee for Hambach lignite coal (1kg/s) at Point B (T_F = 1153 K and T_A = 1210 K, $N_{recycle}$ = 808.5 mol/s).

Figure 5.18 shows the Comparison of composite curves (a) and grand composite curves of scheme of Peltola and scheme of Mukherjee for Hambach lignite coal (1kg/s) at Point B (T_F = 1153 K and T_A = 1210 K, $N_{recycle}$ = 808.5 mol/s). In Figure 5.18 (a), the hot composite curves are the same since the parameters of chemical looping plant are the same. For the cold composite curves, the parts at low and high temperatures are same, but the parts at the medium temperature are different. Similar thing happens in the grand composite curves. This is because that at high temperature, the cold composite curve is just composed of preheating flow-in air; at low temperature, the cold composite curve is composed of preheating flow-in air and a part of stream s2 in the steam cycle. The middle part starts from the temperature of stream s6 of the steam cycle, and ends from stream s7 of the steam cycle, which is influenced by the temperature of turbines. In Peltola's scheme, the highest temperature of turbines is higher, so its middle part of cold composite curve is above the one of Mukherjee's scheme. The meaning of this difference is: the pinch point of two schemes are same, which means the total heat absorbed by the cold composite curves are the same. However, the total heat absorbed is composed of two parts: the chemical looping plant and the steam cycle. In the high temperature part, the cold composite curves of two schemes overlap with each other, which means the preheated air absorb same amount heat in this part; in the middle part, at the same temperature, the cold composite curve of Peltola's scheme is on the left of the one of Mukherjee's scheme, which means the steam cycle of Peltola's scheme absorbs more heat than Mukherjee's scheme. In the low part, two cold composite curves overlap each other

again. Thus, by using turbines at higher temperatures and pressures, Peltola's scheme has higher efficiency than Mukherjee's scheme. However, economic factors should also be considered since higher temperature and pressure means more costs on the turbines and relevant facilities. So the temperatures and pressures of turbines should be balanced after a full consideration.

5.2.5 Discussion

The results show that for different kinds of fuel, there is no difference on energy efficiency. However, for CH_4, it requires more amount of oxygen per GJ released, which means larger $N_{recycle}$. This leads to larger reactors and transport facility, which increases the cost of chemical looping plant. Thus, considering of economic factors, fuel requiring small amount of oxygen per GJ released is preferred.

Preheating of the flow-in air into the air reactor is important, since it reduce the exergy loss in the air reactor. However, this process also leads to more costs of preheating facilities. Thus, the preheating temperature should be balanced between the exergy loss and the costs of heat exchangers. In other researchers' work, for instance, Peltola (Peltola 2014), the temperature of the air reactor is 1189 K, and the preheating temperature of the flow-in air is 338 K, which is just 40K higher than the room temperature. This is same as the results from this chapter that since the temperatures of the air and fuel reactors are much higher than the temperatures of steam cycle (temperatures of turbines and boil feed water), so even there is some exergy loss in the air reactor, there is still enough exergy for the steam cycle. Thus,

the preheating temperature is chosen at 498.15K, which balances the exergy loss and economic factor.

As mentioned above, since in this chapter, the temperatures of the air and fuel reactors are much higher than the temperatures of the steam cycle, so the change of variable has no influence on the output of the steam cycle. The focus on choosing variables can be shifted from technology to economic factors: for instance, 1) the cost of maintaining the air and fuel reactors at higher temperatures; 2) the cost of building larger air and fuel reactors; 3) the cost of transporting Fe_2O_3 between reactors; 4) the cost of Fe_2O_3. In the suitable region, these economic factors are optimised and the operating parameters would be based on those results.

The efficiency of this Chemical Looping Combustion based method is 40.7%. Comparing with other CO_2 capture methods, it is higher than the net electrical efficiencies of pulverized coal (PC) (30%-35%) and Integrated Gasification Combined Cycle (IGCC) (32−40%), but lower than natural gas combined combustion (NGCC) (43%-50%).

5.3 CONCLUSIONS

In this chapter, a steady-state model of chemical looping plant and steam cycle is tested, and some important conclusions are drawn:

1) The effect of the fuel is largely due to the amount of oxygen required per GJ released.

2) Preheating is important, but seems to have a minor effect since the most of the heat is released at temperatures well above the pinch point.

3) In this chapter, since the temperatures of heat source --- the air reactor and the fuel reactor is well above the pinch point, the temperature of the boiler feed water, so all heat are usable for the steam cycle. In this case, the steam cycle and the chemical looping plant can be optimised separately.

4) As long as the preheat temperature of the air flow into the air reactor is higher than the temperature of turbines, in most of cases the power output is unaffected by the choice of variables, leaving the designer free to choose the most convenient.

5) The efficiency of this Chemical Looping Combustion based method is 40.7%, which is higher than the net electrical efficiencies of pulverized coal (PC) (30%-35%) and Integrated Gasification Combined Cycle (IGCC) (32−40%), but lower than natural gas combined combustion (NGCC) (43%-50%).

CHAPTER 6 DYNAMIC MODEL OF CHEMICAL LOOPING POWER PLANT USING HAMBACH LIGNITE CHAR WITH IRON OXIDE OXYGEN CARRIERS

6.1 INTRODUCTION

6.1.1 Models of chemical looping combustion system

A model of a chemical looping combustion (CLC) system consists of a model of the fuel reactor linked to that of the air reactor. The main inputs to such a model are the sizes of the reactors, operational parameters, the gases and solids properties, and the rates at which particles and gases convert; the main outputs of the models are the temperature profiles, the distribution of solids, the conversion of oxygen carrier and the gas concentrations in the exit gases (Juan Adanez et al. 2012).

For the fuel reactor, there two kinds of fuels could be used, solid and gaseous. Solid fuels mainly include char (Hayhurst and Parmar 2002) and coal (Ströhle, Orth, and Epple, 2010); gaseous fuels mainly include methane (Kolbitsch, Pröll, and Hofbauer 2009), H_2 (Xu et al. 2007), or syngas (Mattisson et al. 2007). Most of models in the literature consider the use of gaseous fuels rather than solid fuels (e.g. Kolbitsch (Kolbitsch, Pröll, and Hofbauer 2009), Xu (Xu et al. 2007)). Solid fuels pose more difficulties in chemical looping because unreacted fuel leaving the fuel reactor must be separated from the metallic oxygen carrier. Solid fuels are also more difficult to model because: 1) the conversion of the fuel must be modelled with a population balance; 2) solid fuels could produce gaseous products. For example, if

coal were used, the model must include both solid and gas phase reactions, and the reaction of the complex mix of volatiles produced by the coal.

Both the air reactor and the fuel reactor influence each other. For instance, the recycle rate of oxygen carriers influences the temperatures of the reactors and the conversion of oxygen carriers in both reactors. Thus, it is necessary to consider the CLC system as a whole. For the air reactor, there must be enough airflow for solid circulation, and in some designs the air reactor is a riser (Cloete, Johanse, and Amini, 2010) (Kruggel-Emden et al. 2010). However, if the airflow is too high, it will take away too much heat from the air reactor and influence the heat balance of the air reactor. Thus, a balanced airflow is important, which is discussed in detail in Chapter 5.

In this chapter, a phenomenological model of a fluidised bed, CLC system is constructed, using char as fuel. Using char as a fuel makes the system less complicated than using coal, since the only gas phase reactions are for those of the gasification products, there are no volatiles. Particle conversion distribution for solids in the bubbling fluidized bed in introduced, and the CLC system is tested by fitting Brown's gasification experimental data at both 1073K and 1223K. Then a dynamic CLC power plant using Hambach lignite char with iron oxide as oxygen carrier was modelled.

6.1.2 Fluidized bed model

There are three main factors, which must be considered in a model of a

fluidized bed: fluid dynamics, reactions and energy balances. They are tightly connected to each other and must be solved simultaneously. Fluid dynamics is more sensitive to external parameters, rather than temperature profile or internal gas generation; for energy balances and reactions, external parameters, fluid dynamical parameters are generally equally important (Pallarès and Johnsson 2006). Their relationship is shown in Figure 6.1, where the thickness of the arrows corresponds to the sensitivity of the modeling field to the input represented by the arrow.

Figure 6.1 Relationship between fluidised bed-modelling fields. (Adapted from Pallares (Pallarès and Johnsson 2006))

6.1.2.1 Fluid dynamics

Fluid dynamics deals with the flow and distribution of gases and solids in the fluidized bed reactor. There are two kinds of fluid dynamics models for the fluidized bed reactor: macroscopic fluid dynamics models, and computational fluid dynamics models (CFD).

Macroscopic fluid dynamics models, based on empirical and semi-empirical equations, describe the distribution of gases and solids in the emulsion phase and bubbling phase. It can also be applied to circulating fluidized beds (Kolbitsch, Pröll, and Hofbauer 2009), with different closure relationships. This method is mature, and can give good agreement within reasonable solution time. For instance, Pallarés and Johnsson (Pallarès and Johnsson 2006) showed that this method could simulate as large as 226 MW circulating fluidized bed (CFB) combustors and has good agreement with measurements. The main disadvantage for this method is that since empirical or semi-empirical models are used, it can just be applied to the conditions for which the models were developed. Some models just consider solid distribution in the dense bed, and some models consider both dense bed and free board (Kronberger, Löffler, and Hofbauer, 2005). In the dense bed, single-phase (Kolbitsch, Pröll, and Hofbauer 2009), two-phase (Xu et al. 2007) and three-phase (Iliuta et al. 2010) theories are all used, but most models use a two-phase approach (Abad et al. 2010) (Adánez et al. 2003).

The computational fluid dynamic codes (CFD) models are based on the first principles, to varying degrees, however there is still uncertainty in how details of the two-phase flow should be handled. CFD methods for two phase flows are still under development and calculations are computationally expensive (Pallarès and Johnsson 2006). So far, CFD models have mostly focussed on batch experiments with no circulation, and small-scale CLC systems (300–1000 Wth) (Juan Adanez et al. 2012).

6.1.2.2 Modelling gas solid reactions

6.1.2.2.1 General equations

To model a fluidized bed of reacting particles requires some knowledge of the rate at which the particles are reacting. The rate of reaction of a single porous particle is governed by several factors: external mass, internal mass transfer and chemical kinetics. A complete and exact description of the conversion of the particle requires the partial differential equations governing mass transport to be solved alongside that for solid conversion, and in the case where the temperature is varying, the energy equation. Within a spherical particle, the concentration of a gas phase species, i, is described by,

$$\frac{\partial c_i}{\partial t} = \frac{1}{r}\frac{\partial}{\partial r}\left(r^2(N_i)\right) - R_i\left(x_j, P_i, T\right) \tag{6.1}$$

where R_i is the rate of production of species i per unit volume, N_i is the molar flux in the radial direction, and r is the radial co-ordinate, such that $r = 0$ corresponds to the centre of the particle, and $r = a$ is the outer surface; P_i is the partial pressure of species i, and T is the temperature of surrounding atmosphere. For a solid species, j, the molar flux is zero, leading to,

$$\frac{\partial x_j}{\partial t} = R_j' \tag{6.2}$$

where x_j is the local conversion, and R_j' is the rate of conversion of solid. The gaseous species reacts with the solid species, so the rates of consumption of gas and solid are linked by the stoichiometry of the corresponding reactions.

A similar equation to Equation (6.1) applies outside the particle, extending from

the surface to the edge of the boundary layer (Saucedo-Martínez 2013). However, the problem is often simplified by using an analytical solution for the region outside the particle, or a semi-empirical relation (Saucedo-Martínez 2013). For example, the flux of a species leaving the particle can be described by,

$$N_i|_{r=a} = k_g\left(C_i^s - C_i^b\right) \tag{6.3}$$

where k_g is the mass transfer coefficient (m/s); C_i^s and C_i^{b} are the concentration of the gaseous species i at the surface of the particle and in the bulk gas phase, respectively. Note, that Equation (6.3) is often used in cases where it strictly does not apply, for example where there is non-equimolar counter diffusion, or where the fluxes cannot be described by Fick's law, *i.e.* in multicomponent diffusion where the Stefan-Maxwell relation should be used (Saucedo et al. 2014). In these latter cases the fluxes at the boundary should be calculated by solving the appropriate models either analytically, with suitable approximations (Hayhurst 1991), or numerically (Saucedo et al. 2014), which requires a detailed knowledge of the kinetics of reaction, the fluxes of species within the particles, and how they change with solid conversion, as discussed below (Saucedo-Martínez 2013).

Such models have been used to describe gas solid reactions, such as char combustion (Gavalas 1980) and gasification (Saucedo-Martínez 2013), but there are differences depending on the type of reactions. In the case of combustion (Gavalas 1980), the solid is consumed, leading to either changes in density, or changes in particle size; whilst for the reduction or oxidation of metal oxide (Hu et al. 2016), the particles would not change in size to a first approximation. The big difference

between these two methods cases is the moving boundary, which leads to different solution methods.

If the solid is consumed or the pore structure changes with reaction, the rate of reaction per unit volume, and the fluxes could vary in a complicated way with conversion of the solid (Gavalas 1980). For example, in a combustion reaction, both the porosity and the internal surface can influence the reaction rate. As the reaction precedes, the internal surface area increases initially, as the pores expand; as pores begin to overlap, the internal surface area starts to decrease. The rate of reaction is proportional to surface area, so the change of internal surface area influences the rates of reactions taking place in the particle; on the other hand, the porosity of the particle increases continuously, so the gaseous transport inside the particle is improved. The influence from the porosity can be described by effective diffusivity (Saucedo, Dennis, and Scott 2015),

$$D^{eff,X} = \frac{D^{eff,o} * (\varepsilon_o + (1-\varepsilon_o)X)}{\varepsilon_o} \tag{6.4}$$

where $D^{eff,X}$ is the effective diffusivity at conversion X; $D^{eff,o}$ is the effective diffusivity before the reaction; $(\varepsilon_o + (1-\varepsilon_o)X)$ is the porosity at conversion X; ε_o is the initial porosity at the start of the reaction.

Thus, some model is needed for the evolution of the porous structure of the solid. Two commonly used models, which deal with how the reaction rate changes during conversion, are the random pore model and the grain model (A. Calvelo 1971) (J. Szekely 1971) (Szekely and Evans 1971)**.** Alternatively, an empirical relationship

can be used, e.g. Saucedo (Saucedo-Martínez 2013).

Bhatia and Perlmutter (Bhatia and Perlmutter 1980) (Bhatia and Perlmutter 1981) proposed the random pore model, which considers the effect of the intersection of the pores caused by reactions. The model assumes that there are cylindrical pores in the particle initially. The product layer would grow around the pores and overlap each other as reaction processes.

In the grain model, Calvelo and Smith (A. Calvelo 1971) and Szekely and Evans (J. Szekely 1971) (Szekely and Evans 1971), the solid pellet consists of numerous tiny grains. There are many pores surrounding the grains, through which the gas can diffuse. The reaction takes place on the surface of grains. A product layer will gradually form on the outer surface of each grain and will resist further diffusion.

Galavas (Gavals 1980) employed a random capillary model to describe the evolution of pore volume and surface area and the frequency of pore intersections of a porous char particle during gasification at chemically controlled rates.

6.1.2.2.2 Difficulty in solving the full model

Solving the full model is possible, with any given set of assumed kinetics, flux model and structural model. However, incorporating such a detailed model within a full-scale reactor model is usually infeasible owing to the computational load, and approximate analytical expressions are required. For example, Noorman et al. (Noorman et al. 2011) modeled a packed bed of particles undergoing chemical looping reactions; the effect of mass and heat transfer limitations inside the oxygen

carrier particles on the axial concentration and temperature profiles in packed bed CLC was correctly accounted for; in this case, solving the full set of equations over a week to produce a solution, compared to minutes using an approximate expressions for conversion of the particles. (Noorman et al. 2011)

6.1.2.2.3 Approximate analytical expressions for particle conversion

A number of approximations can be made which lead to either analytical expressions, or simpler numerical models for the conversion of the particle. One common solution is to assume that the gas concentration is a pseudo steady state, i.e. the time differential in Equation (6.1) is zero**,** e.g. Williams et al. (Williams, Calvelo, and Cunningham 1972). Given the relative rates of solid and gas conversion this approximation does not lead to any appreciable error, and allows the analytical expressions for the gas concentration within a part to be found in some cases, e.g. where fluxes are described by Fick's law and the reaction is first order in gas concentration. This is typically the approach taken in modeling the reaction of a gas within a solid catalyst particle, leading to expression for the effectiveness factor, i.e. the rate of reaction observed over the rate if there were no concentration gradient within the particle. For cases where reaction is not first order or the fluxes are no longer described by Fick's law suitable approximations for the effectiveness factor exist, e.g. Bischoff (Bischoff 1965). When dealing with non-catalytic reactions in which the solid is consumed (for instance, Equation (3.2) in Chapter 3), the pseudo-steady approximation partially decouples the equations describing solid and

gas phase species, allowing the gas concentration within the particle to be calculated for a given snapshot of the state of the solid, and effectively allowing the particle to be modelled as a catalytic particle at each snap shot in time.

6.1.2.2.4 Approximation of the particle reaction by considering limiting cases

Some simplifications can also be made by considering limiting cases. In combustion systems, the solution to the above system of equation often falls into one of three distinct categories --- regime 1, regime 2 and regime 3 (Turnbull 1984). In regime 1 the reaction rate is governed solely by the kinetics of reaction and the reactions take place in the whole particle uniformly, i.e. an effectiveness factor of unity by analogy with catalytic systems. Regime 2 is an intermediate regime in which reaction is fast enough to prevent the reactant penetrating far into the unreacted material and reaction occurs within a thin front. In regime 3 the reaction rate is controlled by the rate of diffusion of reactant to the outer surface of the particle. Actually whether or not the reaction takes place on the outer surface or uniformly in this regime can be worked out with the equivalent of a Biot number. Turnbull (Turnbull 1984) and Gavalas (Gavalas 1980) wrote expressions for coal char combusting in each of these regimes. Since coal is consumed, in regime 1 this leads to a fall in density, while in regime 2 the reaction only happens near the surface and the particle shrinks.

Modelling (Gavalas 1980) of regime 2 properly requires a full solution to the above system since both kinetics and mass transfer are important. However, once the

particle is fully in regime 2, the reaction occurs at thin front, and there is effectively a shrinking core of unreacted material.

This has allowed some authors (Bhatia and Perlmutter 1980) (Bhatia and Perlmutter 1981) to treat the problem as the reaction of a shrinking sphere of unreacted material, with an effective rate constant giving the rate at which material is consumed at the front. For this approach to be valid, there must be a significant concentration gradient in the particle, which arise then the appropriate modulus is large, i.e. (Turnbull 1984) for first order kinetics in the gas phase when,

$$\boldsymbol{\Phi} = \frac{\boldsymbol{V_p}}{\boldsymbol{A_p}}\left(\frac{\boldsymbol{k_i S_E}}{\boldsymbol{D_E}}\right)^{\mathbf{0.5}} > \mathbf{3} \tag{6.5}$$

where Φ is the Thiele modulus; V_p is the particle volume and A_p is the external area; k_i is the intrinsic rate constant, which is defined as "the reaction rate per unit of pore surface (area) in the absence of any mass transfer limitations"; S_E is the effective pore area for combustion per unit volume; D_E is the diffusion coefficient the gaseous reactant in the particle. Bischoff (Bischoff 1965) suggested a general Thiele modulus for arbitrary reaction types in steady state,

$$\boldsymbol{\Phi} = \frac{\boldsymbol{LR'(C^s)}}{\sqrt{\mathbf{2}}}\left[\int_{\mathbf{0}}^{\boldsymbol{C^s}} \boldsymbol{D^{eff}(\alpha)R'(\alpha)d\alpha}\right]^{-\frac{\mathbf{1}}{\mathbf{2}}} \tag{6.6}$$

where L is the characteristic length of the particle, that is, the volume of the particle/external surface of the particle: here, it equals to one third of the initial radius of the particle; R' is the intrinsic reaction rate per particle volume in any form, which equals to R_i/V_i; C^s is the gaseous concentration on the surface of the particle; α is a dummy variable; D^{eff} is the effective diffusivity for the particle, which is often a

function of concentration, but is a constant here for simplicity. This general modulus in Cartesian coordinates brings all types of reactions forms into a relatively narrow region, and enables effectiveness factors of arbitrary reactions to be calculated.

6.1.2.2.5 The approximate methods for describing the reaction in regime 2

In his model of chemical looping, for the high Thiele modulus case, Harper (Harper 2013) assumed the reaction rate to be independent of conversion and first order in gas concentration. He then divided the calculation into two stages: (1) by assuming the reactions in solid are zero order, and the gas concentration is in pseudo steady state, the equation for gas concentration can be decoupled from the state of the solid and the PDE equation is converted into an ODE. This reaction diffusion equation could be solved to give an analytical expression for the effectiveness factor; (2) the effective rate was then calculated, with reaction assumed to occur on the outer surface of a sphere, allowing the rate at which this sphere shrank to be determined by material balance. Many authors (Bischoff 1965) (Turnbull 1984) have used this same approximation. For instance, Turnbull (Turnbull 1984) made the same assumption to derive an expression for the rate of char combustion.

For particular forms of rate expression at high Thiele modulus, an analytical form of the time-conversion relationship exists. William et al. (Williams, Calvelo, and Cunningham 1972) suggested the following model to describe the conversion-time relationship, allowing the local rate of reaction to be a function of both the solid conversion and the local gas concentration. The assumptions they introduced are: the

reaction rate in William's work (Williams, Calvelo, and Cunningham 1972) is expressed as,

$$\boldsymbol{r_A = k a_i C_A^{\gamma} (\gamma > 0)} \tag{6.7}$$

where r_A is the reaction rate per unit volume; a_i is the internal surface area of solid reactant B per unit volume; and C_A is the molar concentration of species A. Williams (Williams, Calvelo, and Cunningham 1972) divided the reaction into two stages: 1) the radius of char particle keeps constant and the density of char particle near the surface falls; 2) the char particle shrinks. He introduced a correction modulus of the effectiveness factor, which extends the results to non-equimolar counter-diffusion and a non-isothermal situation with external heat and mass transfer resistances.

One difficulty in applying the high Thiele modulus approximation in a simulation, is that as the unreacted core shrinks, the Thiele modulus falls from regime 3 to regime 1 and the corresponding effectiveness factor should change from $3/\Phi$ to unity, as shown in Figure 6.2. Modelling this transition would require a full solution numerical solution. To solve this problem, Harper (Harper 2013) took a more pragmatic approach and allowed regime 1 and 2 to be mixed up, and then transfer to regime 3, at the intersection of asymptotes form regime 1&2 and 3 behaviour, when $\Phi = \sqrt{3}$.

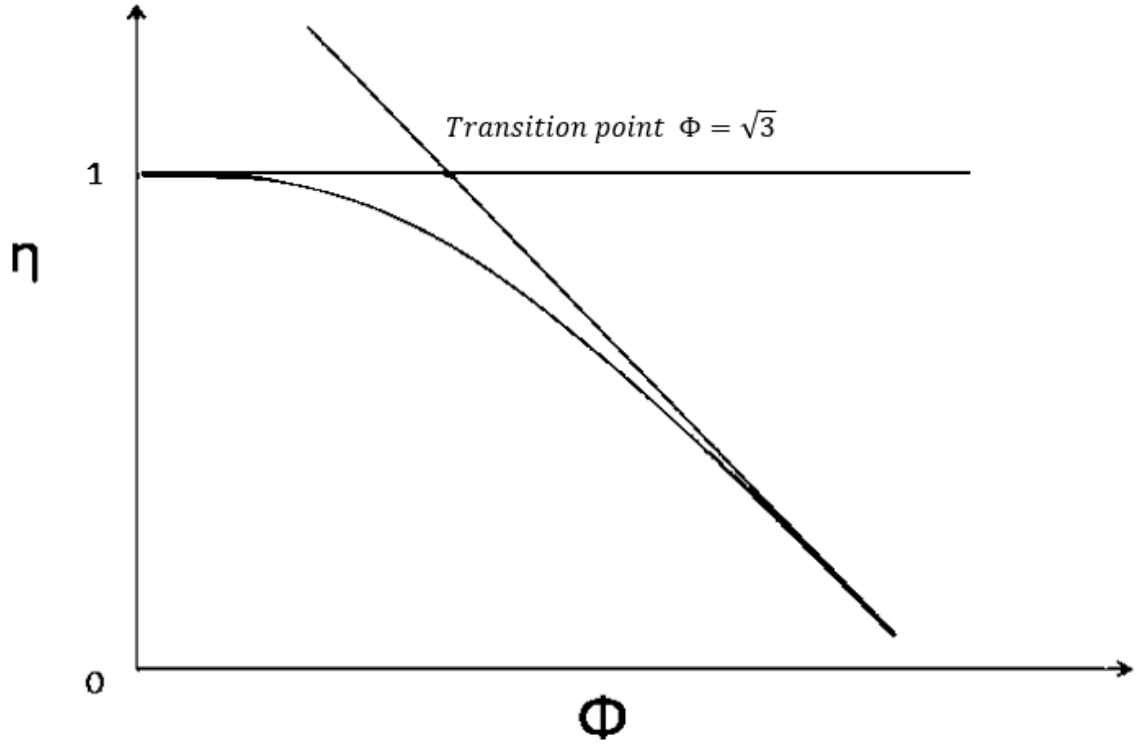

Figure 6.2 Effectiveness factor (η) versus Thiele modulus (Φ). The asymptotes at $\eta = 1$ and $\eta = \Phi/3$ show regime 1 and regime 3, respectively.

Here, it should be noticed that the shrinking core model for carbon particles (the fuel) and Fe_2O_3 particles (the oxygen carrier) are different. For the carbon combustion, the outer layer is ash and the particle shrinks during the reaction. Thus, there should be a moving boundary for the shrinking core regime. However, for the Fe_2O_3 reduction, an outer layer of Fe_3O_4 is formed and the outer boundary does not move. This difference will be discussed in later sections.

6.1.2.2.6 Comparison of different methods

The steady state assumption leads to a considerable simplification of the equations governing the conversion of the particle and leads to negligible errors. The

assumption that the reaction rate is not a function of conversion (as used by Turnbull (Turnbull 1984), Harper (Harper 2013), Bischoff (Bischoff 1965)) is incorrect but enables the gas equation and the solid equation to be solved independently, to give straight forward analytical expressions for conversion. However, the comparison between analytical solution (Williams, Calvelo, and Cunningham 1972) from Turnbull's assumptions (Turnbull 1984) and numerical solution (A. Calvelo 1971) shows that the difference is quite small. William's assumptions (Williams, Calvelo, and Cunningham 1972) allow the solid to affect the reaction rate and the results are in good agreement with the numerical solution. However, it would be complicated to use William's (Williams, Calvelo, and Cunningham 1972) solutions in a simulation: the corresponding numerical method would take much longer, for only a small gain in accuracy. Turnbull's (Turnbull 1984) assumptions will be used in the simulation described below.

6.2 MODEL DEVELOPMENT

This model is intended to simulate a chemical looping system, consisting of two interconnected, bubbling bed reactors. The assumptions made for the model are as follows:

- The bubbling phase just consists of gas, while the particulate phase contains both solids and gas;

- The two-phase model of Davidson (J. Davidson and Harrison 1971) is valid. I.e. the particles are always in the state of the minimum fluidization, and with any additional gas forming bubbles;
- The particulate phase is well-mixed, with gas also assumed to be well mixed, while the gas in the bubble phase assumed to be in plug flow;
- Reaction of the carbon, and the solid metal oxide are assumed to only take place in the particulate phase;
- Solids from the fuel reactor circulate into air reactor with no carry over of gas. All char and iron particles are fully oxidized in the air reactor. Oxygen carriers from air reactor circulate into fuel reactor, but off gases leave the system;
- In industry, Fe_2O_3 is only reduced to Fe_3O_4 in fuel reactor. In a chemical looping fuel reactor, which is well mixed, the high concentration of CO_2 would prevent any reduction to wustite or metallic iron. The only exception is in Brown's experiments (Brown 2010) at 1223K, where Fe_3O_4 is further reduced to $Fe_{.947}O$.
- All Fe_3O_4 and carbon particles in the air reactor are completely oxidized, which means the kinetics in the air reactor can be omitted;
- Temperature inside a reactor is uniform.

6.2.1 Equations governing the fluidized beds

Following the approach of (Brown et al. 2010) the concentration of species *i* (*i* = CO, N_2, CO_2, O_2) in the bubble phase is given by,

$$\frac{\partial C_i^b}{\partial t} = -\frac{\partial\left[(U-U_{mf})C_i^b\right]}{\varepsilon_b \partial h} + y_i^P \frac{F_p}{\varepsilon_b AH} + \frac{Q}{V_b}\left(C_i^p - C_i^b\right) \quad (6.8)$$

and in the particulate phase by,

$$H(1-\varepsilon_b)\varepsilon_{mf}\frac{dC_i^p}{dt} = -U_{mf}\left(C_i^{in} - C_i^p\right) + \frac{1}{A}\left(\beta_i R_g + \theta_i R_{Fe} + y_i^P F_p\right) + \int \frac{Q\varepsilon_b\left(C_i^p - C_i^b\right)}{V_b} dh$$

(i = CO, N_2, CO_2, O_2) (6.9)

Here, C_i^b and C_i^p are concentrations of species (mol/m^3) in bubbling phase and particulate phase, respectively. C_i^{in} is the concentration of species i at the inlet. U is the superficial gas velocity, and its increase with height is given as $\left.\frac{\partial U}{\partial h}\right|_t = \frac{F_p}{C^T AH}$, where C^T is the total concentration in the fluidized bed (mol/m^3). A well-known correlation is given by Wen and Yu (Wen and Yu 1966) to calculate Reynolds number Re_{mf}, and U_{mf}, the minimum fluidizing velocity for the solids in the bed can be calculated from Re_{mf}, and the simplified form is given as,

$$U_{mf} = \frac{(\rho_p - \rho_g) g d_p^2}{1650\mu_g} \quad (6.10)$$

H is overall depth of the fluidized bed, and h is the height above the distributor, which is given by Davison (J. F. Davidson and Harrison 1963),

$$\frac{\boldsymbol{H-H_{mf}}}{\boldsymbol{H_{mf}}} = \frac{\boldsymbol{U-U_{mf}}}{\boldsymbol{U_b}} \quad (6.11)$$

where U_b is the bubble rise velocity, given as (J. F. Davidson and Harrison 1963),

$$\boldsymbol{U_b = \left(U - U_{mf}\right) + 0.711\sqrt{g d_b}} \quad (6.12)$$

where d_b is the mean diameter of a bubble, which is calculated by correlation of Darton (Darton 1977).

$$d_b = \frac{0.54(U-U_{mf})^{0.4}}{g^{0.2}H}\int_0^H \left(h + 4\sqrt{A_0}\right)^{0.8} dh \quad (6.13)$$

where A_0 is the distributor area per orifice (m^2).

$\varepsilon_b = (H - H_{mf})/H$ is the volume fraction of the bed taken up by bubbles, and ε_{mf} is the voidage of bubble phase at minimum fluidization, which are both assumed to be independent of h. y_i^p is the mole fraction for species i in the particulate phase. F_p (mol/s) is the net flow of gas caused by chemical reaction, i.e. either gasification of carbon in the fuel reactor, or the oxidation of Fe_3O_4 in the air reactor. For gasification of carbon, F_p is equal to the rate of the consumption of carbon, because each mole carbon gasified results in on additional mole of gas being produced by the reaction $C+CO_2 = 2CO$. A is the cross section area of the fluidized bed reactor. Reaction is assumed to occur uniformly throughout the particulate phase, meaning that extra gas flow is generated uniformly over the entire height of the bed; thus the net flow term $y_i^P \frac{F_p}{\varepsilon_b AH}$ is taken to be constant with height h. $Q = 3U_{mf}\pi d_b^2/4$ is the volumetric rate of inter-phase transfer (m^3/s) and $V_b = 1/6\pi d_b^3$ is the mean bubble volume. $\beta_i R_g$ is the reaction rate of gasification of carbon in fuel reactor, or the oxidation of carbon in the air reactor. $\theta_i R_{Fe}$ is the reaction rate of the reduction of Fe_2O_3 in fuel reactor, or the oxidation of Fe_3O_4 in air reactor. β_i and θ_i are stoichiometric coefficients of species *i* for corresponding reactions.

6.2.2 Population balance for particles in the bubbling fluidized bed

The particles in the bubbling fluidized bed are not uniformly converted, and at

any given time a distribution of conversions exist, as illustrated in Figure 6.3. All particles are assumed to follow a residence time distribution, so the conversion of a particle depends on: 1) the length of time spent in the reactor and 2) the conditions in the reactor, i.e. temperature and gas concentrations.

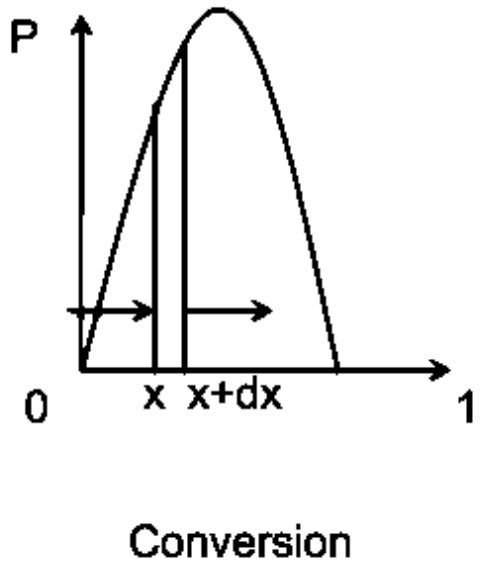

Figure 6.3 Diagram of the particle conversion distribution for solids in the bubbling fluidized bed. $\boldsymbol{X}$ is the conversion of the species and $\boldsymbol{P}$ is the distribution of the species at conversion $\boldsymbol{X}$.

Figure 6.3 illustrates the particle conversion distribution for oxygen carriers and char in the bubbling bed. A material balance on particles with conversion between X and $X + dX$ gives, as follows,

$$\frac{\partial(P_i(t,X)N_i)}{dt} = -\frac{\partial\left(N_i P_i(t,X) R_i(X)\right)}{\partial X} + \left(N_i^{IN} P_i^{IN}(t,X) - N_i^{OUT} P_i^{OUT}(t,X)\right)$$

(i = carbon, Fe_2O_3) (6.14)

where $P_i(t,X)dX$ is the fraction of the solid i particle with conversion between X

and $X + dX$ at time t. For iron oxide, in air and fuel reactors, $X = 0$ corresponds to particles which are entirely Fe_2O_3, whilst $X = 1$ corresponds to the particle consisting entirely of Fe_3O_4. The change in $P_i(t, X)$ is caused by 1) the inlet and outlet flow of particles, i.e. $N_i^{IN} P_i^{IN}(t, X) - N_i^{OUT} P_i^{OUT}(t, X)$ and 2) the consumption or production of species i by reactions, that is, the term $-\frac{\partial(N_i P_i(t,X) R_i(t,X))}{\partial X}$. N_i is the number of particles of species i in a reactor. N_i^{IN} and N_i^{OUT} are the flow-in and flow-out rates of particles of species i of the reactor (particle/s). $R_i(x)$ is the conversion rate of a particle of species i at conversion X.

The char particles could be completely consumed ($X = 1$), and completely consumed particles must be deduced from N_c, which is different from Fe particles. Thus, for char particle, $NP_c(t, X) = P_c(t, X) N_c$ is used to replace $P_c(t, X) N_c$ in Equation (6.14).

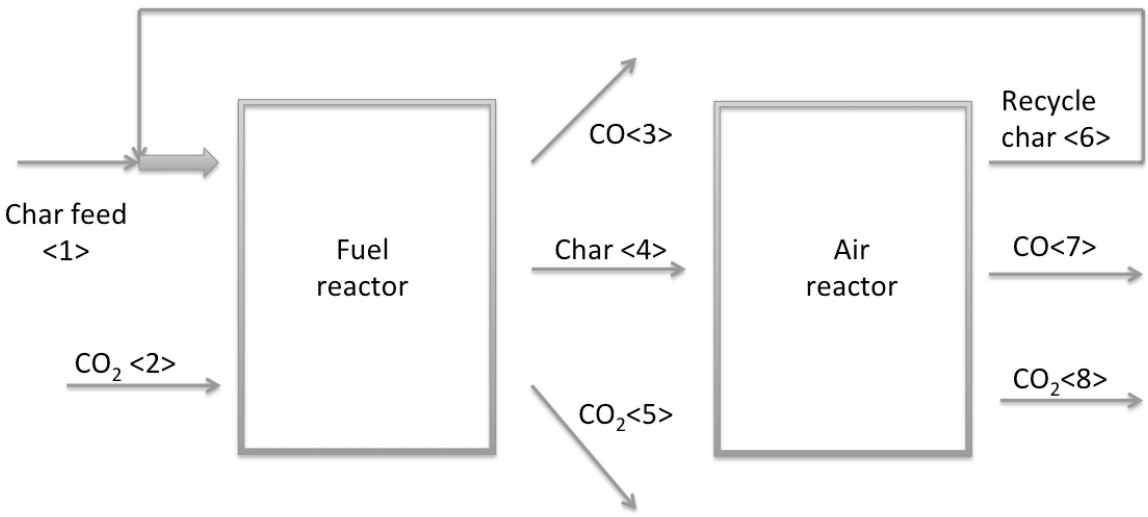

Figure 6.4 Diagram showing the carbon balance of the fuel reactor and the air reactor.

Figure 6.4 shows the carbon balance of the fuel reactor and the air reactor. The

carbon balance of fuel reactor is,

Feed-in rate of char <1> + Recycle rate of char <7> + Inflow rate of CO_2 <2> =

Outflow rate of char <4> + Outflow rate of CO <3> + Outflow rate of CO_2 <5> +

Char accumulation rate in the fuel reactor

Here, the total in flow of char particles into the fuel reactor is composed of the feed of unreacted char particles <1> and the recycled char particles <6> from the air reactor.

The off gases from the fuel reactor, CO <3> and CO_2 <5>, leave the system. The residual char particles <4> then enter the air reactor. The carbon balance of air reactor is:

Inflow rate of char <4> = Outflow rate of char <6> + Outflow rate of CO <7>

+ Outflow rate of CO_2 <8> + Char accumulation rate in the air reactor

All off gases (<7> and <8>) from the air reactor leave the system and residual char particles <6> are recycled to the fuel reactor.

The expression for molar char flow rate NP_c (<1>, <4>, <6>) is given as

$$\boldsymbol{NP_c = \int_0^1 n_c(1-X)N_cP_c(X)dX} \tag{6.15}$$

where n_c is mole number of carbon in each char particle at a conversion of zero; N_c is the flow rate of char particles (particle number/s). For the char feed <1>, the fuel enters the fuel reactor with a conversion of $X = 0$, so $P_c(X)$ is a delta function. The reactors are assumed to be well mixed, so all char particles in the reactors are at the same conversion. Thus, $P_c(X)$ in char flow <4> and <6> are equal to $P_c(X)$ in the fuel and air reactors, respectively.

6.2.3 Energy balance on the fluidised reactors

The temperature of a reactor is influenced by three factors: 1) inlet and outlet flow of gases and solids; 2) external heating; 3) the heat generation or absorption from reactions. In addition, based on the well-mixed assumption, the temperature inside a reactor is uniform. The temperature of circulating particles, which enter into another reactor, should be equal to the temperature of the previous reactor.

An energy balance on a reactor gives:

$$\frac{d\sum n_i u_i}{dt} = \left(\sum n_i^{IN} h_i^{IN}\right)_{in} - \left(\sum n_i^{OUT} h_i^{OUT}\right)_{out} + Q$$

(i = CO, CO_2, O_2, N_2, Fe_2O_3, Fe_3O_4, carbon, etc.) (6.16)

where u_i is the molar internal energy of species i, and n_i is the mole number of species i in the reactor. n_i^{IN} and n_i^{OUT} are inlet and outlet mole flow rate (mol/s) of species i. h_i^{IN} and h_i^{OUT} are inlet and outlet molar enthalpy (kJ/mol). Q is the external heating supplied (kJ/s). If $\frac{d(PV)}{dt}$ is neglected or the system has a fixed volume and pressure (as assumed here),

$$\frac{d\sum n_i u_i}{dt} \approx \frac{dH}{dt} = \frac{d\sum n_i h_i}{dt} \quad (6.17)$$

With $h_i(T) = h_i(T_{ref}) + \Delta h_i(T)$, the left hand side the energy balance can be rearranged to give,

$$\left(\sum Cp_i n_i\right)\frac{dT}{dt} = \sum\left(n_i^{IN}[h_i(T_{ref}) + \Delta h_i(T_{in})] - n_i^{OUT}[h_i(T_{ref}) + \Delta h(T)] - \frac{dn_i}{dt}(h_i(T_{ref} + \Delta h_i(T))\right) + Q$$

(6.18)

For mass balance, $\frac{dn_i}{dt} = n_i^{IN} - n_i^{OUT} + \sum_k \nu_{ki} R_k$. Here, R_k is the rate of reaction k. So,

$$\sum \left(\boldsymbol{n_i^{IN} - n_i^{OUT} - \frac{dn_i}{dt}} \right) \boldsymbol{h(T_{ref})} = \sum \boldsymbol{R_k \Delta H_k^{rxn}(T_{ref})} \tag{6.19}$$

where $\Delta H_k^{rxn}(T_{ref})$ is the reaction enthalpy of reaction k. Therefore, the energy balance can be written as,

$$\left(\sum n_i Cp_i \right) \frac{dT}{dt} = \sum_k \left(R_k \Delta H_k^{rxn}(T_{ref}) \right) + Q +$$

$$\sum_i \left(\boldsymbol{n_i^{IN} \Delta h_i(T_{in}) - n_i^{OUT} \Delta h_i(T) - \frac{dn_i}{dt} \Delta h_i(T)} \right) \tag{6.20}$$

The energy balance equation can be simplified further by setting $T_{ref} = T$ (i.e. using the temperature of the reactor itself as the reference temperature). Then $\Delta h_i(T) = \Delta h_i(T_{ref}) = 0$, and the terms $n_i^{OUT} \Delta h_i(T)$ and $\frac{dn_i}{dt} \Delta h_i(T)$ are zero, giving,

$$\left(\sum \boldsymbol{n_i Cp_i} \right) \boldsymbol{\frac{dT}{dt}} = \sum_k \boldsymbol{(R_k \Delta H_k^{rxn}(T))} + \boldsymbol{Q} + \sum_i \left(\boldsymbol{n_i^{IN} \Delta h_i(T_{in})} \right) \tag{6.21}$$

where it should be noted, that heat of reaction should be evaluated at the reactor temperature.

6.2.4 The reactions in the bubbling fluidized bed reactors

Four kinds of reactions take place in the bubbling fluidized bed reactors: 1) the gasification of carbon particles in the fuel; 2) reactor the oxidation of the carbon particles in the air reactor; 3) the reduction of Fe_2O_3 particles in the fuel reactor; 4)

the oxidation of the Fe_2O_3 particles in the air reactor.

The kinetic expressions used here are simplified to allow a solution to be obtained within a reasonable time. However, using simplified kinetic models, rather than solving the time dependent equation for each particle in the system, means that any history dependence cannot be captured accurately. For example if there is a change in regime between regime 1 and regime 2, the conversion does not uniquely specify the state of the particle since the same carbon conversion can be obtained with a less dense particle as with a higher density but smaller particle. To solve this problem, it is assumed that all char particles and iron particles are fully oxidized in the air reactor. In this way, only the history of particles in the fuel can be passed to the air reactor. Fully oxidized Fe_2O_3 particles and no char particle circulate from the air reactor to the fuel reactor.

6.2.4.1 Kinetics of gasification reactions in the bubbling fluidized bed reactors

The oxygen-exchange scheme (Ergun 1956) is employed to explain the carbon gasification reaction: CO_2 is first adsorbed on an active site, C^*, on the carbon; then, the product CO desorbs from the carbon, which are shown in Equations (6.22) and Equation (6.23),

$$C^* + CO_2(g) \underset{k_{-1}}{\overset{k_1}{\longleftrightarrow}} C(O) + CO(g) \tag{6.22}$$

$$\boldsymbol{C(O) \overset{k_2}{\rightarrow} C^* + CO(g)} \tag{6.23}$$

The rate of gasification is given as，

$$\boldsymbol{R_g(X, P_i, T) = f(X) R_{g,0}(p_i, T)} \tag{6.24}$$

Here, $R_{g,0}$ is the initial rate of reaction per unit mass of carbon when $X = 0$. The Ergun mechanism given above then gives $R_{g,0}$ as

$$\boldsymbol{R_{g,0} = \frac{2ck_2 P_{CO_2}}{P_{CO_2} + \left(\frac{k_2}{k_1}\right) + \left(\frac{k_{-1}}{k_1}\right) P_{CO}}} \tag{6.25}$$

where k_1, k_{-1} and k_2 are rate constants per active site; c is the concentration of active sites per unit mass of sample; p_{CO} and p_{CO_2} are partial pressure of CO and CO_2, respectively. The conversion dependence, $f(X)$, then accounts for the variation in the number of active sites, C^*, as the particle converts and the structure of the particle evolves.

Brown (Brown et al. 2010) tested the expression at 1073K using Hambach lignite char and found that,

$$\boldsymbol{R'_{g,0} = \frac{dX_0}{dt} = \frac{0.0157 P_{CO_2}}{1 + 13.1 P_{CO_2} + 52.4 P_{CO}}} \tag{6.26}$$

where $R'_{g,0}$ is intrinsic rate of gasification at zero conversion.

Saucedo (Saucedo-Martínez 2013) also tested the expression using Hambach lignite char by experiments and found that it is valid between 1048K and 1248 K. Other parameters are given below in Table 6.1.

As the gasification reaction takes place, pores in the char particle gradually evolves, which changes the gasification reaction rate by changing the reaction surface area of the char particle. $f(X) = R_g(X, T, P_i)/R_{g,0}(T, P_i)$ is used to represent the

change of reaction surface area from char particle conversion.

Table 6.1 Parameters for carbon gasification reaction from Saucedo (Saucedo-Martínez 2013).

	Value
Temperature (K)	1048-1248
Diameter of the char particle (μm)	600-1000
E_{k_{-1}/k_1} (kJ mol^{-1})	-91.0
k_{-1}/k_1 (bar)	$2.4\times10^{-4}\exp[-E_{k_{-1}/k_1}/RT]$
k_2/k_1 (bar)	$4.92\times10^{4}\exp[-10830/T]$
$2ck_1$ (mmol s^{-1} g^{-1} bar^{-1})	$2.56\times10^{9}\exp[-24050/T]$
$2ck_2$ (mmol s^{-1} g^{-1})	$1.26\times10^{14}\exp[-34880/T]$

The random pore model of Bhatia and Perlmutter, which gives a maximum in the rate of reaction as a function of conversion, is employed here,

$$\boldsymbol{X = 1 - \left(1 - \frac{\tau}{\sigma}\right)^3 exp\left[-\tau\left(1 + \frac{\psi\tau}{4}\right)\right]} \tag{6.27}$$

where, $\sigma = r_0 S_0/(1-\varepsilon_0)$, and $\psi = 4\pi L_0 - (1-\varepsilon_0)/S_0^2$. r_0 is the initial radius of the carbon particle; S_0 is the initial internal surface area per unit volume; ε_0 is the initial porosity; L_0 is the initial length of overlapped cylindrical pores. For porous particles, the internal surface area is much larger than the external surface area, which means that $\frac{\tau}{\sigma} \to 0$. Thus, Equation (6.27) becomes,

$$\boldsymbol{X = 1 - exp\left[-\tau\left(1 + \frac{\psi\,\tau}{4}\right)\right]} \tag{6.28}$$

Differentiating Equation (6.28) with respect to τ and rearranging the equation

gives,

$$\boldsymbol{f(X) = (1 - X)\sqrt{1 - \psi\, ln(1 - X)}} \tag{6.29}$$

6.2.4.2 Correction to the gasification rate at high temperatures

In the previous section the particle was assumed to be reacting under fully kinetic control with no gradient of concentration within it. At high temperatures, mass transfer effects can be significant with these chars (Saucedo, Dennis, and Scott 2015). As noted previously it is difficult to exactly account for the transition between regimes 1 and 2. Here an approximate method is used, following Turnbull's (Turnbull 1984) and Harper's (Harper 2013) approach. For each conversion bin (a conversion bin is defined as a conversion region from conversion X_n to X_{n+1} for a reacting particle) the rate is calculated as follows,

1. Calculate intrinsic rate of gasification at zero conversion. In Brown's (Brown et al. 2010) work, the parameters for $R'_{g,0}$ is experimentally tested only at 1073K, so can not be used at 1223K. Thus, Saucedo's (Saucedo, Dennis, and Scott 2015) expression of $R_{g,0}$ is used instead. Although Brown and Saucedo both used Hambach lignite char, differences in char preparation could still influence the char activities. At 1073K, the intrinsic rate of gasification at zero conversion for Brown's char is about 2.2 times to Saucedo's char. For the sake of simplicity, it is assumed that the ratio in relativities remains the same at 1223K.

2. Calculate the effectiveness factor η using the approach given by Saucedo (Saucedo, Dennis, and Scott 2015)，which is given as,

$$\boldsymbol{\eta = tanh(\lambda\phi^*)\,/\phi^*} \tag{6.30}$$

where $\lambda = 1 - 0.4457\alpha^2\phi^* \exp\left(-0.1153\phi^{*2}\right)$, and $\phi^* = \phi_M/\phi_C$.

$\alpha = Kp_{CO_2}^s$, where p_i^s is the partial pressure of species at the surface of the char particle, and

$$\boldsymbol{K = \frac{K_{CO_2} - \frac{D_{CO_2}^{eff}}{D_{CO}^{eff}} K_{CO}\nu_{CO}}{\omega}} \tag{6.31}$$

where $K_{CO_2} = k_1/k_2$and $K_{CO} = k_{-1}/k_2$; $\nu_{CO} = 2$ is the stoichiometric value of CO in the gasification reaction; $D_i^{eff} = D_{CO_2}(\varepsilon_0 + (1-\varepsilon_0)X)/\tau_{in}^2$ is the effective diffusivity of species i, where ε_0 is the initial porosity of the char particle and τ_{in}^2 is the tortuosity factor of the particle; ω is given as,

$$\boldsymbol{\omega = 1 + \left(\frac{D_{CO_2}^{eff}}{D_{CO}^{eff}}\right) p_{CO_2}^s K_{CO}\nu_{CO} + K_{CO}p_{CO}^s} \tag{6.32}$$

$\phi_C = \sqrt{2}(1+\alpha)\left[\frac{1}{\alpha^2}(\alpha - \ln(1+\alpha))\right]^{0.5}$. ϕ_M is the modified Thiele modulus, given as,

$$\boldsymbol{\phi_M = L\left[\frac{k'RT}{D_{CO_2}^{eff}}\right]^{0.5}} \tag{6.33}$$

where $L = d_c/6$ is the ratio of char particle volume to char surface area, $k = ck_1\rho_c f(X)$, and $k' = k/\omega$.

3. If $\eta > \eta_{crit}$, the reaction is in regime 2, and it is assumed that the reaction occurs on the outer surface of the char particle, that is, the shrinking core

model. In this case, the shrinking rate of the particle is equal to the rate of carbon consumption, and the conversion of inner core keeps X_0 unchanged. The reaction rate expression $R_{c,shr}$ (CO molar production rate per second per char particle) is given as,

$$\boldsymbol{R_{c,shr} = R_{g,0} \times m_{X,c} \times \frac{m_{X,c}}{m_{0,c}}} \quad (6.34)$$

where $m_{0,c}$ is the initial mass of the char particle, and $m_{X,c} = m_{0,c}(1 - X)$ is the residual mass of the char particle at conversion X.

4. As the gasification reaction proceeds, the char particle becomes smaller. When $\eta < \eta_{crit}$, it is assumed that the reaction is uniform throughout and the pore evolution in the char particle must be considered. The reaction rate is $R_g(X, T, P_i) = R_{g,0}(T, P_i) f(X)$

This approach would only work when the transition between regimes is caused only by the shrinkage of particles, so that at a critical conversion, the particle moves to kinetic control. Also valid is the case where the particle remains in kinetic control throughout. This model also effectively takes the reaction in regime 2 to be zeroth order in solid at a fixed conversion X_0, which is an approximation. In reality there would be a continuum of conversions across the reaction front.

6.2.4.3 Kinetics of iron oxide reactions in the bubbling fluidized bed reactors

At 1073K, Fe_2O_3 is reduced to Fe_3O_4. The rate of the reduction of Fe_2O_3 in the fuel reactor is a function of both P_{CO}, the partial pressure of CO, and the

conversion X of Fe particle. The reaction rate $R_{Fe_2O_3}$ (mol/(s g)), based on unit mass of oxygen carrier particles was given by Bohn (C. Bohn 2010) as

$$R_{Fe_2O_3} = \frac{k^{Fe_2O_3}}{\rho_{Fe_2O_3}}\left(C_{CO} - \frac{C_{CO_2}}{K_p^{Fe_2O_3}}\right)\left(1 - \frac{X_{Fe_2O_3}}{0.8}\right)^{0.4} \quad (6.35(a))$$

$$\boldsymbol{k^{Fe_2O_3} = 2.4\times10^7\, exp\left(-\frac{75000}{RT}\right)} \quad (6.35(b))$$

where the unit of pre-exponential factor $k^{Fe_2O_3}$ is (1/s); R is the universal gas constant, 8.31 J/(mol K); T is the reactor temperature (K); C_{CO} and C_{CO_2} are concentrations of CO and CO_2 in particulate phase (mol/m^3); K_{p,Fe_2O_3} is the equilibrium constant for the Fe_2O_3 to Fe_3O_4 transition, and $X_{Fe_2O_3}$ is the conversion of Fe_2O_3 to Fe_3O_4. In Equation (6.35(a)), it should be noticed that: first, the equilibrium constant K_{p,Fe_2O_3} is very large so the back reaction term can be neglected; second, this expression is used at 1073K, and at 1223K, and modifications must be made, to account for mass transfer limitations when the temperature is higher than 973K; third, in Bohn's results, some of the Fe_2O_3 never reacts, which is due to agglomeration or other reasons, so his rate constant reaches zero when conversion $X_{Fe_2O_3}$ equals to 0.8. In Brown's work (Brown et al. 2010), the Fe_2O_3 particles are about 87% active, and her the last term was changed into $\left(1 - X_{Fe_2O_3}\right)^{0.4}$. In this thesis, when the last term was kept as $\left(1 - \frac{X_{Fe_2O_3}}{0.8}\right)^{0.4}$, since that 1) it is impossible that all Fe_2O_3 is active and using 80% conversion is more realistic; 2) the reaction rate expression should be considered as a whole, and the modification on one term could make it inaccurate.

At 1223K in Brown's experiments (Brown 2010), Fe_3O_4 can be further reduced to $Fe_{.947}O$, and the kinetics are given by Bohn (C. Bohn 2010) at 923K to 1173K,

$$\boldsymbol{R_{Fe_3O_4} = \frac{k^{Fe_3O_4}}{\rho_{Fe_2O_3}}\left(C_{CO} - \frac{C_{CO_2}}{K_p^{Fe_3O_4}}\right)\left(1 - \frac{X_{Fe_3O_4}}{0.8}\right)^{1.2}} \quad (6.36(a))$$

$$\boldsymbol{k^{Fe_3O_4} = 4.3\times10^7\, exp\left(-\frac{94000}{RT}\right)} \quad (6.36(b))$$

where $k^{Fe_3O_4}$, $K_p^{Fe_3O_4}$ and $X_{Fe_3O_4}$ are the rate constant (1/s), equilibrium constant and conversion for the Fe_3O_4 transition to $Fe_{.947}O$, respectively.

6.2.4.4 Shrinking core model for Fe_2O_3 particles

At high temperatures, the Fe_2O_3 transition to Fe_3O_4 reaction is in regime 2 (Fe_3O_4 transition to $Fe_{.947}O$ reaction is much slower, so it is still in regime 1), and could be described by the shrinking core model.

The main difference in shrinking core models between char gasification reactions and Fe_2O_3 reduction reactions is: there is an outer layer of Fe_3O_4 product formed around the shrinking Fe_2O_3 core as shown in Figure 6.5.

Since the reactions for Fe_2O_3 particles are multi-steps (Fe_2O_3-Fe_3O_4-$Fe_{.947}O$), the product layer may still be able to react, but the analysis would be the same. For the sake of simplicity, it is assumed that the product layer would not react until the inner core is fully consumed.

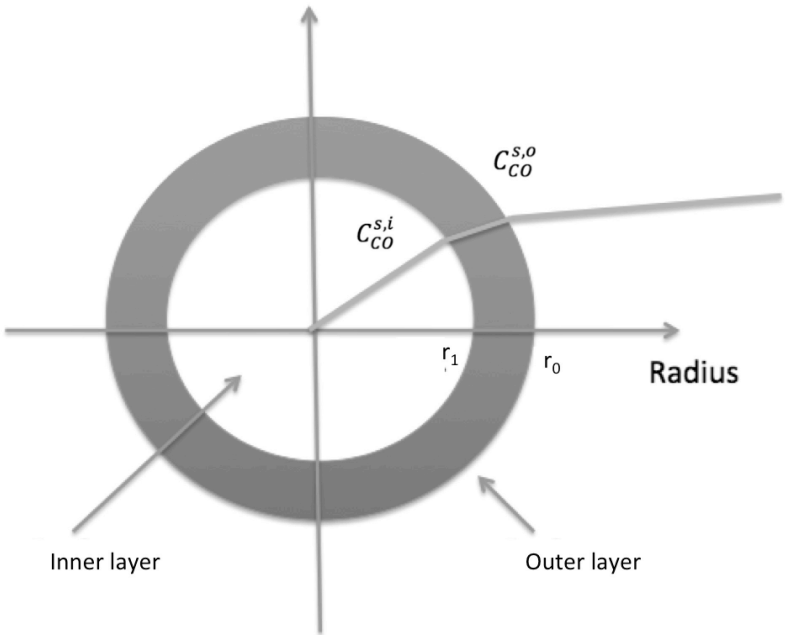

Figure 6.5 Schematic of the CO concentration around and within an iron oxide particle. $\boldsymbol{C_{CO}^{s,i}}$ and $\boldsymbol{C_{CO}^{s,o}}$ are the CO concentration on the surface of the inner layer and the outer layer of the particle, respectively.

The total gaseous reactant molar flow of CO from the particulate phase to the outer surface of the Fe particle Q_M is given as,

$$\boldsymbol{Q_M = k_g 4\pi r_0^2 \left(C_{CO}^{p} - C_{CO}^{s,o}\right)} \tag{6.37}$$

where r_0 is the radius of the Fe particle. C_{CO}^{p} and $C_{CO}^{s,o}$ are the concentrations of species i in the particulate phase and on the outer layer of the Fe particle (mol/m^3), respectively.

The total gaseous reactant molar flow of CO from the outer layer to the inner layer is still Q_M, and is given as,

$$\boldsymbol{Q_M = -J_{CO} 4\pi r^2 = D_{CO}^{eff} 4\pi r^2 \frac{dC_{CO}}{dr}} \tag{6.38}$$

where J_{CO} is the flux (mol/(m^2 s) of CO from the inner surface to the outer surface of

the product layer. Integrating from r_0 to r_1, it gives,

$$\boldsymbol{Q_M = 4\pi D_{CO}^{eff} \frac{C_{CO}^{s,o} - C_{CO}^{s,i}}{\frac{1}{r_1} - \frac{1}{r_0}}} \tag{6.39}$$

where $r_1 = \mathrm{r}_0 \sqrt[3]{1 - X}$, and D_{CO}^{eff} is calculated by,

$$\boldsymbol{D_{CO}^{eff} = \frac{\varepsilon_{Fe_2O_3}}{\tau_{Fe_2O_3}} \frac{1}{\frac{1}{D_{CO}^{k}} + \frac{1}{D_{CO}}}} \tag{6.40}$$

where $\varepsilon_{Fe_2O_3}$ is the porosity for Fe_2O_3, $\tau_{Fe_2O_3}$ is the tortuosity for Fe_2O_3, D_{CO}^{k} is the Knudsen diffusivity given by Lovell (Lovell 1981),

$$\boldsymbol{D_{CO}^{k} = \frac{d_p}{3} \sqrt{\frac{8RT}{\pi M_{CO}}} = \frac{2.13\, \varepsilon_{Fe_2O_3}}{S_g \rho_{Fe_2O_3}} \sqrt{\frac{RT}{M_{CO}}}} \tag{6.41}$$

where d_p is the effective diameter of a cylindrical pore; S_g is the specific surface area for Fe_2O_3.

On the surface of the inner layer, where the reaction takes place, and the consumption rate of CO is equal to the mass transfer rate of CO through the outer layer, Q_M. Thus, the consumption rate of CO is given as,

$$\boldsymbol{Q_M = k_{eff} 4\pi r_1^2 C_{CO}^{s,i}} \tag{6.42}$$

where $k_{eff} = k_s \eta$ is the effective rate constant for the reaction taking place on the inner surface; k_s is the area intrinsic rate constant for the reaction (mol/(m^2s)). Here, the effectiveness factor $\eta = 3/\phi$, and the Thiele modulus $\phi = r_1 \sqrt{\frac{k_s \lambda}{D_i^{eff}}}$. $\lambda = 3/r_1$ is a correction factor, and for the Fe_2O_3 transition to Fe_3O_4, it is given as,

$$\boldsymbol{k_s^{Fe_2O_3} \lambda = 2.4 \times 10^7 \, exp\left(-\frac{75000}{RT}\right)} \tag{6.43(a)}$$

And for the Fe_3O_4 transition to $Fe_{.947}O$, it is given as,

$$k_s^{Fe_3O_4}\,\lambda = \mathbf{4.3\times10^7}\,\boldsymbol{exp}\left(-\frac{\mathbf{94000}}{\boldsymbol{RT}}\right) \tag{6.43(b))}$$

Thus,

$$\boldsymbol{k_{eff} = k_s\eta = \sqrt{k_s\,\lambda D_{CO}^{eff}}} \tag{6.44}$$

Solving the equations above, it gives that,

$$\boldsymbol{Q_M = \frac{C_{CO}^{p}}{\frac{1}{kg4\pi r_0^2}+\frac{\frac{1}{r_1}-\frac{1}{r_0}}{4\pi D_{CO}^{eff}}+\frac{1}{k_{eff}4\pi r_1^2}}} \tag{6.45}$$

6.2.5 Modelling the air reactor

A simplified model of the air reactor is used, since oxidation reaction are usually fast and not limiting. For the air reactor, the unsteady energy equation is used, i.e. Equation (6.21), which accounts for the change in heat produced, but the material balance is assumed to be in steady state. The rate of conversion of Fe_3O_4 to Fe_2O_3 is equal to the rate at which Fe_3O_4 enters the system.

6.3 NUMERICAL SOLUTION FOR THE PDE EQUATIONS

The population balances are partial differential equations, and they can be discretised into ODE equations, which can then be solved using the MATLAB stiff solver ode15s. The convective terms in the fluidised bed equations were discretised using a first order upwind scheme to prevent instabilities.

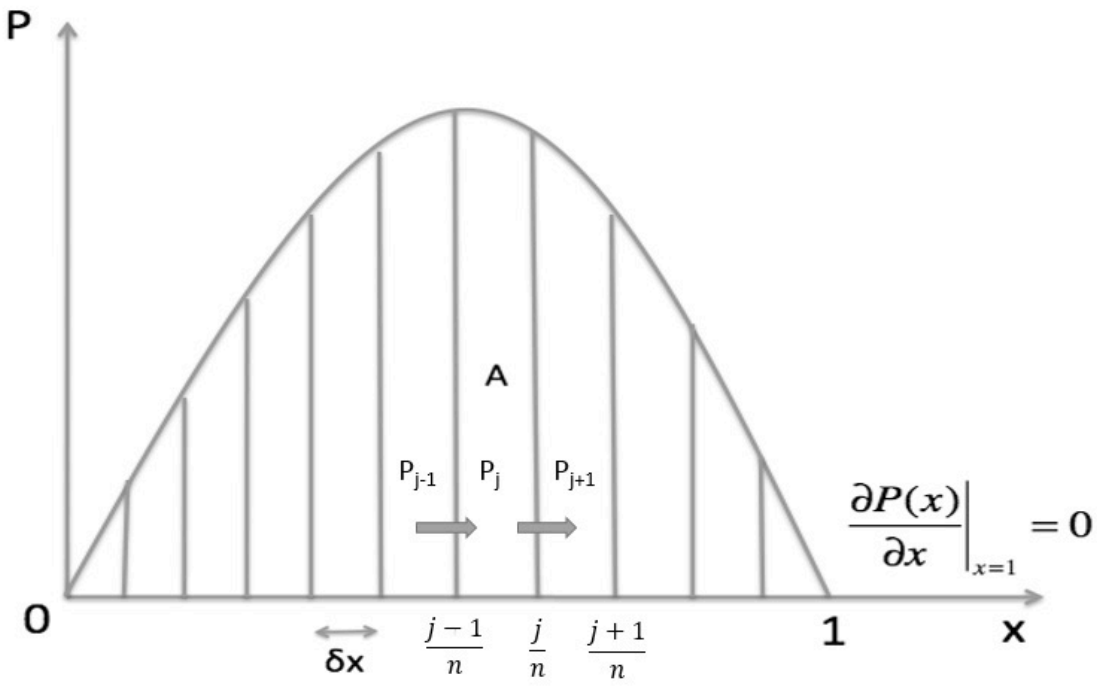

Figure 6.6 The domain of the PDE (Figure 6.2) divided up into finite volumes. From region A is shown. $\boldsymbol{P_j}$ is the conversion distribution of the Fe_2O_3 or the carbon particle at conversion $\boldsymbol{x = j/n}$.

As Figure 6.6 shows, to discretise Equation (6.14), a vector $(0, 1/n, 2/n, \dots, 1)$ is set, which discretises the conversion distribution of the Fe_2O_3 or the carbon particle into n bins. For the Fe_2O_3 particles, the discretised population balance is given as,

$$\frac{d(P_{Fe}(t,j)N_{Fe}^T)}{dt} = -\frac{P_{Fe}(t,j)N_{Fe}^T R_{Fe}(j) - P_{Fe}(t,j-1)N_{Fe}^T R_{Fe}(j-1)}{\Delta\left(\frac{1}{n}\right)}$$

$$+\left(N_{Fe}^{IN}P_{Fe}^{IN}(t,j) - N_{Fe}^{OUT}P_{Fe}^{OUT}(t,j)\right) \qquad (j = 0, 1, 2, \dots, n) \qquad (6.46)$$

The boundary condition for Equation (6.46) is, when $j = 0$ (the Fe particle is full of Fe_2O_3),

$$\frac{d(P_{Fe}(t,0)N_{Fe}^T)}{dt} = -\frac{P_{Fe}(t,0)N_{Fe}^T R_{Fe}(0)}{\Delta\left(\frac{1}{n}\right)} + (N_{Fe}^{IN}P_{Fe}^{IN}(t,0) - N_{Fe}^{OUT}P_{Fe}^{OUT}(t,0)) \qquad (6.47)$$

The expressions for R_{Fe} in Equation (6.46) for the fuel reactor is given as,

$$R_{Fe,fuel}(j) = Q(j)\times 3/mol_{Fe} \qquad (j = 0,1,2,\dots,n) \qquad (6.48)$$

where 3 is the stoichiometry of reaction $CO + 3Fe_2O_3 = 2Fe_3O_4 + CO_2$; mol_{Fe} is the initial mole number of Fe_2O_3 in each Fe particle. And Q is given as,

$$Q(j) = \frac{C_{CO}^{p}}{\frac{1}{kg4\pi r_0^2} + \frac{\frac{1}{\sqrt[3]{1-\frac{j}{n}}r_0} - \frac{1}{r_0}}{4\pi D_{CO}^{eff}} + \frac{1}{k_{eff}4\pi\left(\sqrt[3]{1-\frac{j}{n}}r_0\right)^2}} \qquad (6.49)$$

The initial condition is, when t=0,

$$P_{Fe}(0,0) = 1 \qquad (6.50(a))$$

$$P_{Fe}^{IN}(0,0) = 1 \qquad (6.50(b))$$

$$P_{Fe}^{OUT}(0,0) = 1 \qquad (6.50(c))$$

For the carbon particle, the discretised Equation (6.14), the expression of total mole number of carbon in each char particle is given as,

$$\frac{d\left(NP_c(t,j)\right)}{dt} = -\frac{NP_c(t,j)R_c(j) - NP_c(t,j-1)R_c(j-1)}{\Delta\left(\frac{1}{n}\right)}$$

$$+\left(N_c^{IN}P_c^{IN}(t,j) - N_c^{OUT}P_c^{OUT}(t,j)\right) \qquad (j = 0,1,2,\dots,n) \qquad (6.51)$$

The boundary condition for Equation (6.51) is: when j=0,

$$\frac{\boldsymbol{d\left(NP_c(t,0)\right)}}{\boldsymbol{dt}} = -\frac{\boldsymbol{NP_c(t,0)R_c(0)}}{\boldsymbol{dx}} + \left(\boldsymbol{N_c^{IN}P_c^{IN}(t,0) - N_c^{OUT}P_c^{OUT}(t,0)}\right) \qquad (6.52)$$

When $j = n$,

$$\frac{d\left(NP_c(t,1)\right)}{dt} = 0 \qquad (6.53)$$

Because this carbon has a conversion of 100%, so it does not contribute to the carbon balance.

The expressions for R_c in Equation (6.51) for the fuel reactor is given as,

$$R_c(j) = \frac{2ck_2P_{CO_2}}{P_{CO_2}+\left(\frac{k_2}{k_1}\right)+\left(\frac{k-1}{k_1}\right)P_{CO}}\left(1-\frac{j}{n}\right)\sqrt{1-\psi\, ln\left(1-\frac{j}{n}\right)} \quad (j = 0,1,2,\dots,n) \quad (6.54)$$

The boundary condition for Equation (6.54) is given as: when $i = n$,

$$\boldsymbol{R_c(1) = 0} \quad (6.55)$$

The initial condition for equation is: for the fuel reactor, when $t = 0$,

$$P_c(0,0) = 1 \quad (6.56(a))$$

$$P_c^{IN}(0,0) = 1 \quad (6.56(b))$$

$$P_c^{OUT}(0,1) = 1 \quad (6.56(c))$$

$$N_cP_c(0,0) = N_c^{IN} \quad (6.56(d))$$

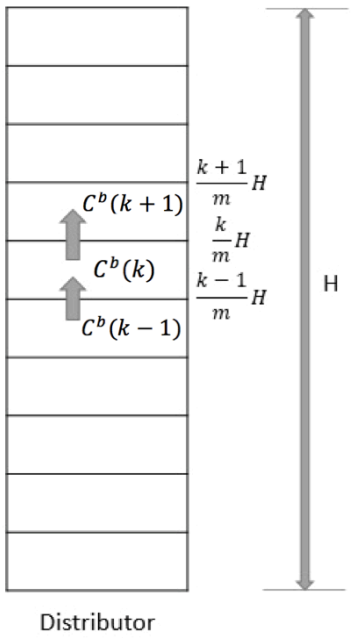

Figure 6.7 The bubbling fluidized bed is (Equation (6.8) and Equation (6.9)) divided up into finite volumes. $\boldsymbol{C^b(k)}$ is the molar concentrations of gaseous species in bubbling phase at height $\boldsymbol{\frac{k}{m}H}$ from the distributor.

Figure 6.7 shows that, to discretise Equation (6.8) and Equation (6.9), a vector $(0, H/m, 2H/m, \dots, H)$ is set, which discretises the height of the bubbling fluidised

bed H into m parts. Thus, Equation (6.8), the molar concentrations of gaseous species in bubbling phase, is given as,

$$\frac{\partial C_i^b(t,k)}{\partial t} = \frac{U - U_{mf}}{\varepsilon_b \Delta\left(\frac{H}{m}\right)}\left(C_i^b(t,k-1) - C_i^b(t,k)\right) + \frac{Q}{V_b}\left(C_i^p(t) - C_i^b(t,k)\right) + y_i^P \frac{F_p}{\varepsilon_b AH}$$

$$(i = \text{CO},\ \text{CO}_2,\ \text{N}_2,\ \text{O}_2;\ k = 1,\ 2,\ 3,\ \ldots,\ m) \qquad (6.57)$$

The boundary condition for Equation (6.57) is given as: when $k = 1$,

$$\frac{\partial C_i^b(t,1)}{\partial t} = \frac{U - U_{mf}}{\varepsilon_b dh}\left(C_i^{in}(t) - C_i^b(t,1)\right) + \frac{Q}{V_b}\left(C_i^p(t) - C_i^b(t,1)\right) + y_i^P \frac{F_p}{\varepsilon_b AH}$$

$$(i = \text{CO},\ \text{CO}_2,\ \text{N}_2,\ \text{O}_2) \qquad (6.58)$$

The initial condition for Equation (6.57) is given as: when $t = 0$,

1) For the fuel reactor,

$$\left(C_{O_2}^b(0,h), C_{N_2}^b(0,h), C_{CO_2}^b(0,h), C_{CO}^b(0,h)\right) = \left(C_{O_2}^p(0), C_{N_2}^p(0), C_{CO_2}^p(0), C_{CO}^p(0)\right)$$

$$= \left(C_{O_2}^{in}(0), C_{N_2}^{in}(0), C_{CO_2}^{in}(0), C_{CO}^{in}(0)\right) = (0, 0, 6.3, 0) \qquad (6.59(a))$$

This means, CO_2 is initially used to fluidise the fuel reactor and the bubbling phase and the particulate phase in the fuel reactor are full of CO_2.

2) For the air reactor,

$$\left(C_{O_2}^b(0,h), C_{N_2}^b(0,h), C_{CO_2}^b(0,h), C_{CO}^b(0,h)\right) = \left(C_{O_2}^p(0), C_{N_2}^p(0), C_{CO_2}^p(0), C_{CO}^p(0)\right)$$

$$= \left(C_{O_2}^{in}(0), C_{N_2}^{in}(0), C_{CO_2}^{in}(0), C_{CO}^{in}(0)\right) = (2.1, 7.9, 0, 0) \qquad (6.59(b))$$

This means, airflow is used to fluidise the air reactor. In addition, initially the gaseous phase of the bubbling phase and the particulate phase in the air reactor is full of air.

The discretised Equation (6.9), the concentrations of gaseous species in

particulate phase, is given as，

$$H(1-\varepsilon_b)\varepsilon_{mf}\frac{dC_i^p(t)}{dt} = -U_{mf}\left(C_i^{in}(t) - C_i^p(t)\right) + \sum_m \frac{Q\varepsilon_b\left(C_i^p(t) - C_i^b(t,k)\right)}{V_b}\Delta\left(\frac{H}{m}\right)$$

$$+\frac{\mathbf{1}}{\boldsymbol{A_r}}\left(\sum_{\boldsymbol{n}}\left(\boldsymbol{\beta_i R_c(j) N P_c(t,j)}\right) + \sum_{\boldsymbol{n}}\left(\boldsymbol{\theta_i R_{Fe}(j) N_t P_{Fe}(t,j)}\right) + \boldsymbol{y_i^P F_p}\right)$$

(i = CO, CO_2, N_2, O_2; j = 0, 1, 2, …, n; k = 1, 2, 3, …, m) (6.60)

The boundary conditions for Equation (6.60), is given as: when $j = n, k = 1$,

$$H(1-\varepsilon_b)\varepsilon_{mf}\frac{dC_i^p(t)}{dt} = -U_{mf}\left(C_i^{in}(t) - C_i^p(t)\right) + \sum_m \frac{Q\varepsilon_b\left(C_i^p(t) - C_i^b\left(t,\frac{1}{m}\right)\right)}{V_b}\Delta\left(\frac{H}{m}\right)$$

$$+\frac{\mathbf{1}}{\boldsymbol{A_r}}\left(\sum_{\boldsymbol{n}}\left(\boldsymbol{\beta_i R_c(1) N P_c(t,1)}\right) + \sum_{\boldsymbol{n}}\left(\boldsymbol{\theta_i R_{Fe}(1) N_t P_{Fe}(t,1)}\right) + \boldsymbol{y_i^P F_p}\right)$$

(i = CO, CO_2, N_2, O_2; j = 0, 1, 2, …, n; k = 1, 2, 3, …, m) (6.61)

The initial condition for Equation (6.60) is same as Equation (6.57).

All terms in Equation (6.57) have the same meaning for both the fuel reactor and the air reactor, except for R_c and R_{Fe}, which has been discussed above.

6.4 RESULTS AND DISCUSSION

6.4.1 Modelling continuous feeding of char to a batch chemical looping system

6.4.1.1 Modelling gasification reactions at 1073K

The gasification simulations of Brown (Brown et al. 2010) and this thesis are compared first. Figure 8 shows the measured and predicted rates of gasification when there is a continuous feed of lignite char to an inert fluidised bed. Brown's simulation gasification rate is slower than the experimental data, and this thesis' simulation

gasification rate (using the same kinetic expression for gasification) is marginally faster than the experimental data. This could be due to different methods used to solve the population balance here compared with that of Brown (Brown et al. 2010). Despite the differences there is a good agreement between the model in this thesis and the experimental data.

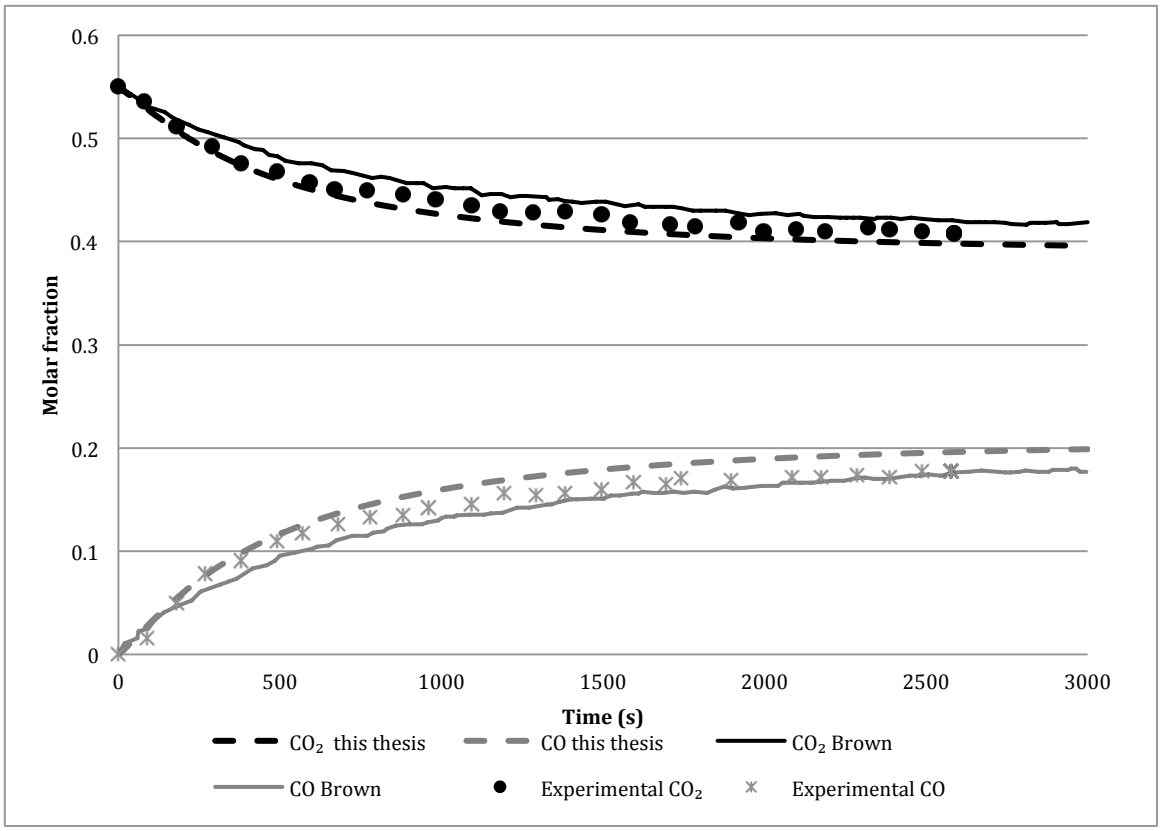

Figure 6.8 A comparison of Brown's gasification experimental data (Brown et al. 2010), simulation (Brown et al. 2010), and the simulation in this thesis at 1073K. The inlet flow is 55% CO_2 in N_2 at the flow rate of 45 ml/s (298K, 1 bar). The char feeding rate is 0.18g/min, and the initial mass of Fe_2O_3 in the reactor is 40g. Other parameters are in the Appendix C.

Brown (Brown et al. 2010) modelled the gasification of a continuous feed of char in a bed of iron oxide (at 1073 K) using Bohn's (C. Bohn 2010) Fe_2O_3 reduction

kinetics expression, with the assumption that Fe_2O_3 is just reduced to Fe_3O_4. In this thesis, much slower Fe_2O_3 reduction kinetics expressions are used for simulation, given as,

$$k^{Fe_2O_3} = 2.4\times10^7\, exp\left(-\frac{75000}{RT}\right) \tag{6.62}$$

$$\boldsymbol{R_{Fe_2O_3}} = \frac{\boldsymbol{k^{Fe_2O_3}}}{\boldsymbol{\rho_{Fe_2O_3}}}\left(\boldsymbol{C_{CO}} - \frac{\boldsymbol{C_{CO_2}}}{\boldsymbol{K_p^{Fe_2O_3}}}\right)\times\frac{\mathbf{1}}{\mathbf{60}} \tag{6.63}$$

i.e., Bohn's expression with the conversion dependence removed and multiplied by a factor of 1/60. The rational for the factor of 1/60 discussed further below, and as will be seen has little impact on the results. For the char gasification, Brown's kinetics expression and parameters are used. The results from the model are compared with Brown's model in Figure 6.9. The completion of Fe_2O_3 transition to Fe_3O_4 for this thesis and Brown's work are at is at 450s and 515s, respectively. As mentioned above, in the simulation, Brown (Brown et al. 2010) removed 0.8 from the term $\left(1-\frac{X_{Fe_2O_3}}{0.8}\right)^{0.4}$, so her Fe_2O_3 takes a longer to be used up. The oxygen balance from the start of the simulation to the completion of Fe_2O_3 transition to Fe_3O_4 shows that 0.083 mol of oxygen removed from Fe_2O_3, which is equal to the oxygen release when 40g Fe_2O_3 is totally reduced to Fe_3O_4.

In Figure 6.9, both simulations from Brown (Brown et al. 2010) and this thesis can fit well the experimental data from 0 to 6 minutes, which indicates that, even divided by a factor 60, Bohn's reaction rate at 1073K is still fast enough to oxidize the products of gasification, and in fact was iron oxide reduction was not

limiting. Thus, removing the conversion dependence on the rate, or reducing the reaction rate had little effect. At 1073K, the results are insensitive to the Fe_2O_3 reduction kinetics.

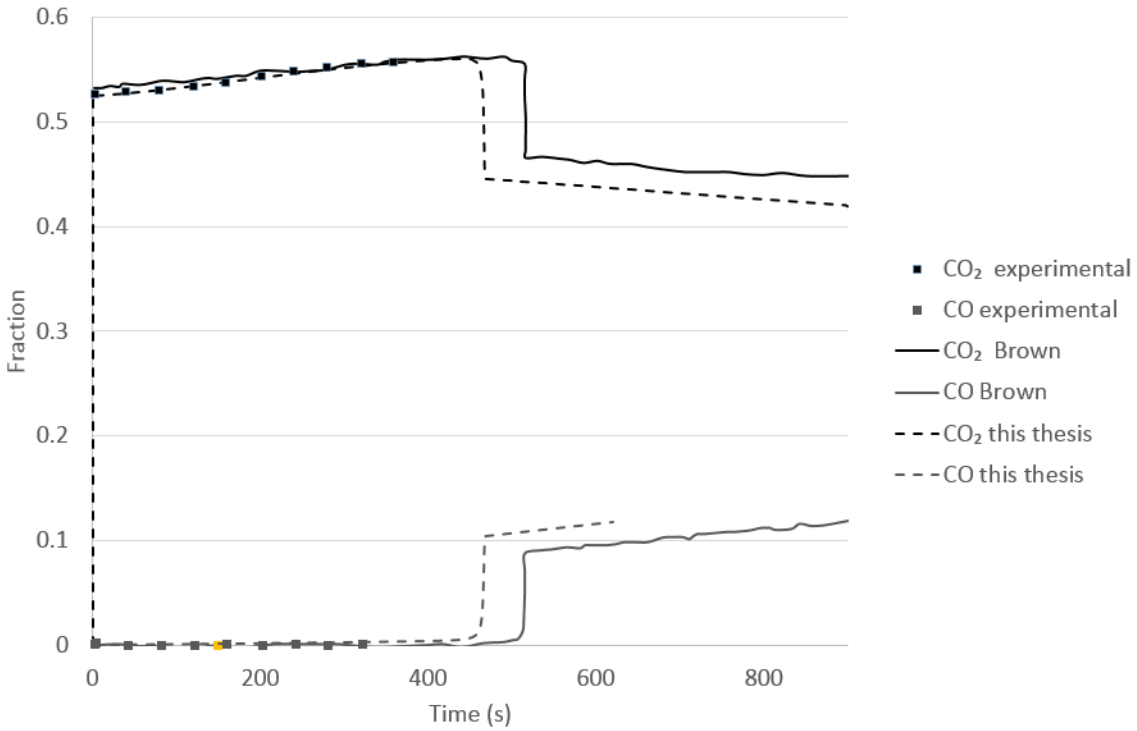

Figure 6.9 Simulations versus experimental data of char gasification at 1073K. The conditions for the simulation are: 52.7% CO_2 in N_2 inlet gas flows into the reactor at 45 ml/s (298K, 1 bar). The char feeding rate is 0.18g/min, and the initial mass of Fe_2O_3 in the reactor is 40g. All other parameters used and the ultimate analysis of Hambach lignite char is given in the Appendix C.

6.4.1.2 Modelling gasification reactions at 1223K

Brown (Brown 2010) ran char gasification experiments with continuous feeding of Hambach lignite char into a bed at 1223K, but was unable to get her model to fit

these experiments. Her model did not take into account mass transfer effects, which were likely to be important at the higher temperatures, nor was any data given for the gasification kinetics at higher temperatures. At 1073K, the initial char gasification rate from Brown (Brown et al. 2010) is 2.2 times to the rate from Saucedo (Saucedo et al. 2014) for a char which is nominally the same. Saucedo (Saucedo et al. 2014), however, gives a more comprehensive rate expression which includes the effect of temperature. For the sake of simplicity, the gasification rate expression at 1223K is the rate expression from Saucedo multiplied by 2.2, given as,

$$\boldsymbol{R_{g,0}} = \frac{\boldsymbol{2ck_2P_{CO_2}}}{\boldsymbol{P_{CO_2}+\left(\frac{k_2}{k_1}\right)+\left(\frac{k_{-1}}{k_1}\right)P_{CO}}} \times \mathbf{2.2} \qquad (6.64)$$

The effectiveness factor η for char gasification at 1223K versus conversion X when $P_{CO_2} = 0.5\ bar$ and $P_{CO} = 0\ bar$ is given in Figure 6.10.

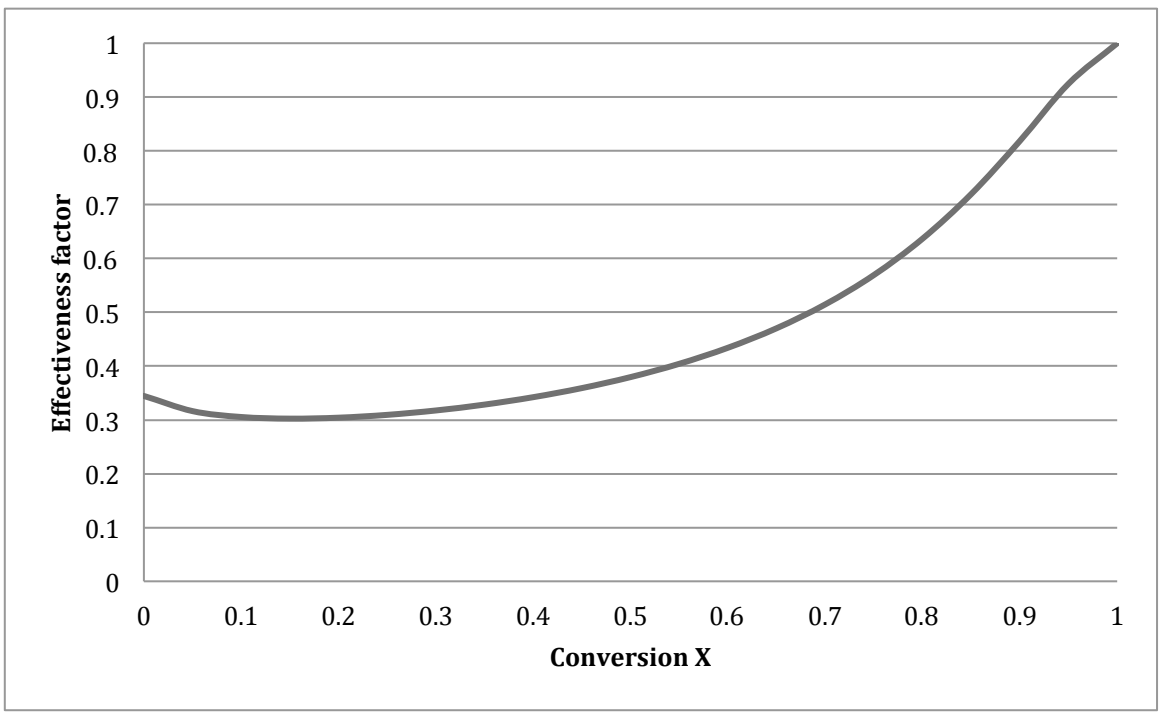

Figure 6.10 The effectiveness factor $\boldsymbol{\eta}$ for char gasification at 1223K versus conversion $\boldsymbol{X}$ when $\boldsymbol{P_{CO_2} = 0.5\ bar}$ and $\boldsymbol{P_{CO} = 0\ bar}$.

Figure 6.10 shows that the effectiveness factor is 0.35 when $X = 0$, and it increases to 0.95 when $X = 0.96$. Thus, it is assumed that when $X = 0.96$, the gasification reaction switches from a shrinking core whose effective rate of shrinkage is influenced by mass transfer, to being governed only by kinetics.

The effectiveness factor of Fe_2O_3 is around 0.34, which indicates that the Fe_2O_3 reduction is in regime 2, i.e. can be modeled as a shrinking core. For the Fe_2O_3 reduction kinetics expression, the fitting gives that,

$$\boldsymbol{R_{Fe_2O_3}} = \frac{\boldsymbol{k^{Fe_2O_3}}}{\boldsymbol{\rho_{Fe_2O_3}}} \boldsymbol{C_{CO}} \boldsymbol{\eta_{Fe_2O_3}} \times \frac{\mathbf{1}}{\mathbf{60}} \tag{6.65}$$

At 1223K, $\eta_{Fe_2O_3}$=0.33 at the start of the Fe_2O_3 reduction. Thus, it is 1/(1/0.33 × 60)=1/190 of Bohn's kinetics expression ignoring the conversion dependence. As discussed in *Section 6.4.1.1*, this modified reaction rate expression is still valid at 1073K, but it is impossible to know the exact reaction rate expression with only data from Figure 6.9. In fact, Brown used similar but not identical particles to those of Bohn, so it is not unreasonable that they had a different activity. The results of the simulation are compared with the experimental data from Brown (Brown 2010) in Figure 6.11. One difference between Figure 6.9 and Figure 6.10 is that in Figure 6.10, the CO leaves the reactor, indicating that at 1223 K, CO is produced by gasification faster than the iron oxide oxidise it to CO_2. In fact, using Bohn's kinetics without modification leads to too high a rate of CO conversion, and very little CO escapes the bed. Dividing the reaction rate of Bohn by a value of 60 (as in Equation (6.63)) reproduces the correct behavior, and is the reason for its inclusion.

At these temperatures, the iron oxide particles are much less active than would be predicted by extrapolating Bohn's kinetics.

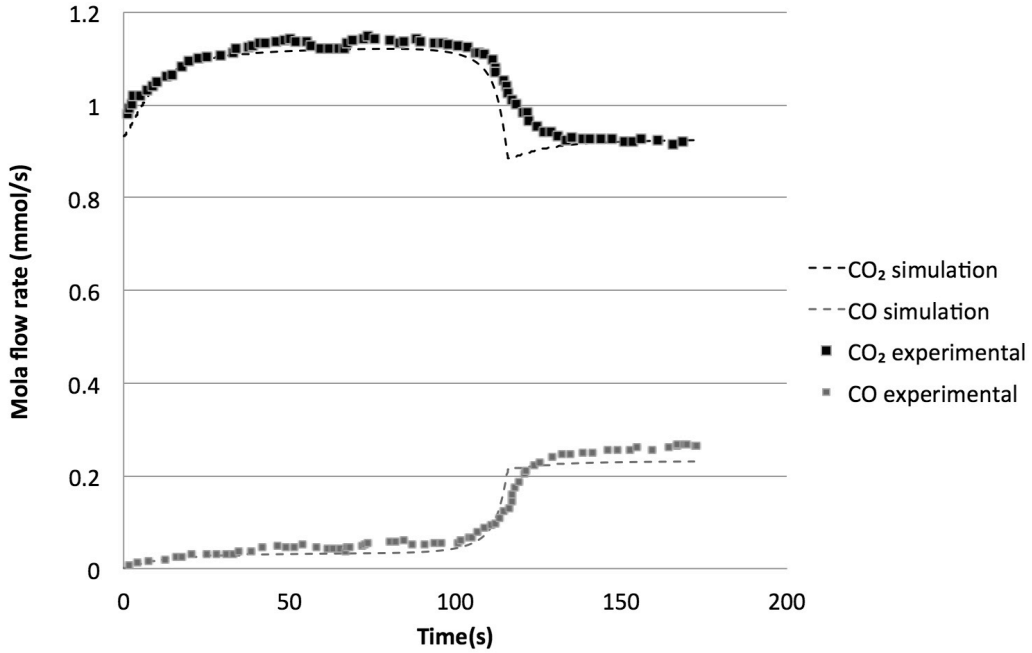

Figure 6.11 Molar flow rate of gases of Brown's (Brown et al. 2010) char gasification experiments with continuous feeding of Hambach lignite char at 1223K. The feeding rate of carbon is 3.2 ± 0.36 mg/s, and the initial mass of Fe_2O_3 is 20g. The content of flow-in gas is 50% CO_2 in N_2. All other parameters are given in the Appendix C.

Another difference between Figure 6.9 and Figure 6.11 is that, at 1073K, Fe_3O_4 is the only product from Fe_2O_3 reduction; however, at 1223K, $Fe_{.947}O$ is produced as well, which is shown in Figure 6.12.

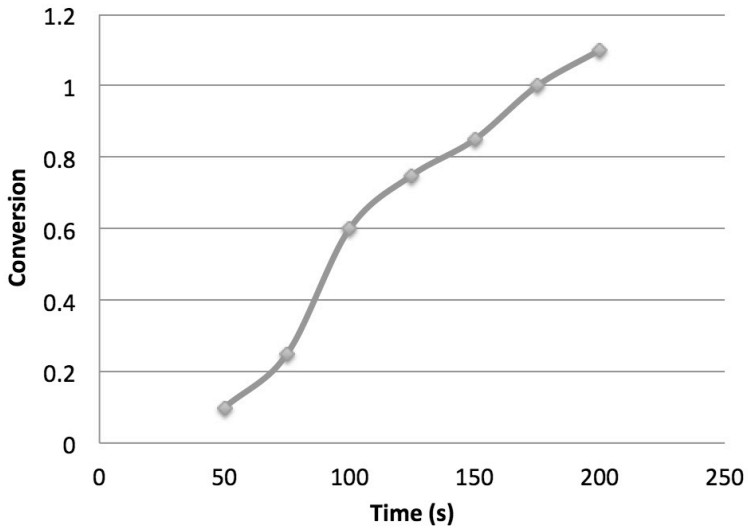

Figure 6.12 Fe_2O_3 conversion to Fe_3O_4 ($Fe_{.947}O$) in Figure 6.11 versus time (s).

In Figure 6.12, the Fe_2O_3 conversion to Fe_3O_4 is higher than 1 after 160s, which suggests that some Fe_3O_4 is further reduced to $Fe_{.0947}O$. Assuming that Fe_2O_3 is 100% active, $Fe_{.0947}O$ is produced at around 175s, which is the 'turning point' in Figure 6.11. In Figure 6.11, CO_2 flow rate starts to increase since the char feeding, and it reaches a plateau from 80s to 140s. Then it drops after the 'turning point' at 140s, and becomes steady at 170s. From the start of the char feeding to the turning point Fe_2O_3 is converting to Fe_3O_4; from the turning point to the end of the gasification, Fe_3O_4 is converting to $Fe_{.0947}O$.

The 'L' shape curve in Figure 6.11 between 100s and 120s is because in the simulation, Fe_2O_3 reduction to Fe_3O_4 and Fe_3O_4 reduction to $Fe_{.947}O$ are assumed to take place one by one for the sake of simplicity. However, it is possible that the two reactions take place simultaneously, which makes the curve between 100s and 120s smoother.

6.4.2 Modelling a continuous looping system

The aim of this section is to model a continuous looping system for a power station.

6.4.2.1 The modeled system

The parameters of reactors are taken from Lyngfelt's (Lyngfelt and Leckner 2015) 1000 MW_{th} theoretical boiler designed for solid fuels, and are given in Table 6.2.

Table 6.2 The parameters of reactors taken from Lyngfelt (Lyngfelt and Leckner 2015).

	Fuel reactor	Air reactor
The initial inventory of Fe_2O_3 particles (tonnes)	500	250
Cross section area (m^2)	77(11×7)	198(11×18)
H_{mf} (m)	3.1	0.8

The bubbling bed model and kinetic models in section 2 are used in the circulation simulation. The flow rate of fluidising gas into the fuel reactor in the dynamic simulation is 84.35 mol/s, which makes $U/U_{mf} \approx 8.5$, to ensure the fuel reactor is a bubbling bed. The diameter of the Fe_2O_3 particles is set as 150-300 μm.

In Chapter 5, the steady state model of a chemical looping power plant is discussed, and the ranges of operation parameters are given. The fuel used in Chapter 5 was Hambach lignite coal, and the fuel used in this chapter is Hambach lignite coal char, and the differences are shown in Table 6.3. It should be noted that Chapter 5

used thermodynamic models of the chemical looping reactors, so did not account for differences such as the high volatile content of the coal compared to the char.

Table 6.3 The comparison of Hambach lignite coal and Hambach lignite char.

Ultimate analysis (wt%)	Hambach lignite coal (dried)	Hambach lignite char
C	54.91	84.21
H	5.47	1.07
O	18.33	4.64
N	0.93	1.10
S	0	Unknown
Other (ash)	5.83	8.94
Lower heating value (kJ/kg)	26003	27628

The operation parameters given in Chapter 5 are for Hambach lignite coal, and they are converted for Hambach lignite char based on Table 6.3, which are shown in Table 6.4.

Table 6.4 The operation parameters for the Hambach lignite char.

Parameters	Unit	Base case/ range
Flow rate of air into the air reactor (N_{air})	mol/s	19668
Flow rate of fluidising gas into the fuel reactor (N_f)	mol/s	84.35
Mass of fuel supply	kg/s	38.5
Energy of fuel supply	GJ/s	1
Amount of oxygen required per GJ released	mol/s	2068
Heating value per mole of carbon	kJ/(mol carbon)	568
Recycle rate of metal oxide (Nrecycle)	mol/s of Fe_2O_3	12423 to 49690
Temperature of the Air Reactor (T_A)	K	1093-1573
Temperature of the Fuel reactor (T_F)	K	1073-1273

In Chapter 5, the temperatures of gases flowing into the air and fuel reactors are

$T_A - 10K$ and $T_F - 10K$, respectively, and the same assumption is made here.

For the air reactor, since the char combustion and Fe_3O_4 oxidation are both fast, it is assumed that all char particles in the air reactor are totally combusted and all Fe_3O_4 in the air reactor are totally oxidized into Fe_2O_3 when the airflow is sufficient. In the outlet gas, the molar ratio of O_2/N_2 is set to be 5/95, and the inlet airflow rate is controlled to ensure the ratio. This greatly simplifies the simulation of the system since the air reactor can be modeled as being as a simple unit, which converts all of the incoming iron oxide to Fe_2O_3. As discussed in the Appendix C, the wall thickness of the reactors is assumed to be 20 mm, and the height of the reactors is assumed to be 48 m. Thus, the heat capacities of the fuel and air reactors are 2.22×10^8 and 3.75×10^8 J/K, respectively. The load of Fe_2O_3 in the air reactor is 50 - 500 tons, so the total heat capacity of Fe_2O_3 in the air reactor is 0.44×10^8 - 4.41×10^8 J/K. Both the reactor and Fe_2O_3 particles have influence on the total heat capacity of the air reactor. Similar results can be obtained from the fuel reactor.

There are two cases discussed for the fuel reactor: with or without a char stripper (Kramp et al. 2012). With a char stripper, char particles are separated from the Fe_2O_3 particles leaving the fuel reactor, and are put back into the fuel reactor. Without a char stripper, char particles have the same probability as the Fe_2O_3 particles to leave the fuel reactor and flow into the air reactor.

6.4.2.2 The control system and operation

The heat demand of the fuel reactor is set to be zero, with all heat being

removed from the air reactor. Two PID controllers are used to control the temperatures of the fuel and air reactors: 1) one PID controller using recycle rates of Fe_2O_3 particles in the air and fuel reactors to control the temperature of the fuel reactor. Here, the ratio of recycle rates of Fe_2O_3 particles in the air and fuel reactors is set to be a certain value. For instance, if the value is one, the inventories of particles in each reactor do not change; if the value is less than one, the Fe_2O_3 particles accumulate in the fuel reactor; 2) a PID controller which sets the heat removal rate from the air reactor to control the air reactor temperature. The controllers are shown in Figure 6.13.

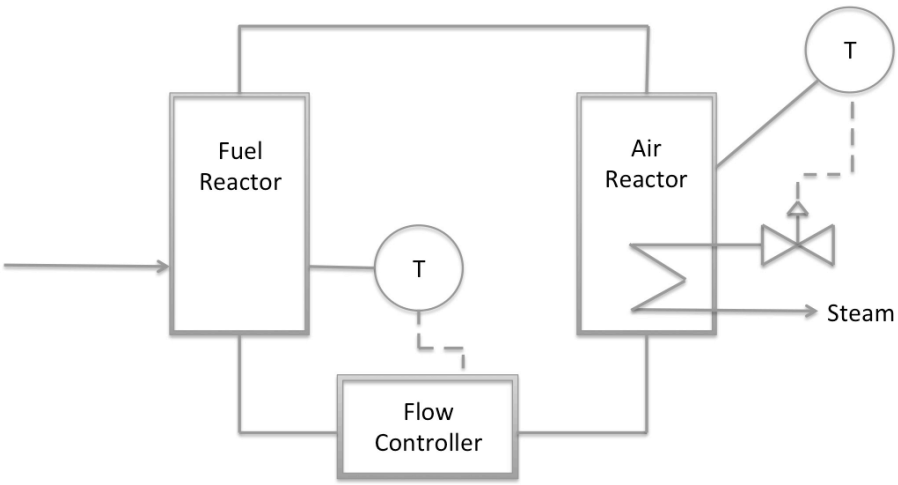

Figure 6.13 The diagram of PID controllers in the system.

6.4.2.3 Implementation

The air and fuel reactors were implemented as custom S-function blocks in Matlab Simulink. This allows the recycle and relationships between the reactors to be modeled by connecting the reactors. The use of a pseudo steady state for the air

reactor greatly simplifies the convergence of the simulation to a solution. Furthermore, assuming the iron oxide is fully oxidized before being returned to the fuel reactor breaks the algebraic loops in the simulation, which Simulink would otherwise have to iterate to convergence. Full reoxidisation of the iron oxide also means that there is no need to model the full history dependence of the iron oxide particles; if this were not the case, iron oxide would not be characterized only by its conversion, as assumed here.

6.4.2.4 The discussion of parameters

The parameters in the system interact with each other and can be controlled to influence the system. These parameters are discussed below.

6.4.2.4.1 Recycle rate of metal oxide particles

This is the most important parameter in the system. The recycle has two functions: 1) transporting heat between fuel and air reactors; 2) transporting reduced metal oxide to the air reactor where it is oxidized to release heat. Function 1 means that there are two ways to increase the heat transport between the reactors, that is, either increases the temperature difference between the reactors or the recycle rate of Fe_2O_3 particles. For function 2, there are two ways to increase the heat release in the air reactor. Firstly increasing the recycle rate of Fe_2O_3 particles and secondly increasing the average conversion of the Fe_2O_3 particles flowing into the air reactor,

since the heat release is proportional to the change in conversion as the material flows through the air reactor. This is circular argument, since the recycle means that that the average conversion of Fe_2O_3 particles leaving the fuel reactor is controlled by the airflow rate in the air reactor and the recycle rate of Fe_2O_3 particles. If the airflow is insufficient to oxidize all Fe_3O_4 flowing into the air reactor, some Fe_3O_4 flows back to the fuel reactor, and the average conversion of Fe_2O_3 in the fuel reactor can be partially controlled by the airflow rate of the air reactor (though not here, since the air flow is controlled to ensure excess air is available). If the airflow is sufficient (as assumed here), the lower the recycle rate of Fe_2O_3 particles is, the higher the average conversion of Fe_2O_3 particles in the fuel reactor, to maintain a fixed heat output. There is of course a limit where the conversion increases to 1 when the recycle rate of Fe_2O_3 particles is not large enough to oxidize all char particles fed as fuel.

6.4.2.4.2 The temperatures of the fuel and air reactors

The temperatures of the reactors influence the reaction rates in the fuel reactor (in the air reactor, the oxidation rate is assumed to be infinitely fast). The temperature difference influences the required recycle rate of Fe_2O_3, since to maintain the fuel reactor as adiabatic, if the temperature difference were too high, the recycle rate would too small. Otherwise Fe_2O_3 could take too much heat from the air reactor to the fuel reactor. At steady state, to ensure all inflow of char is oxidized into CO_2, the molar ratio of char in rate over Fe_2O_3 recycle rate should be no more than 1:6. If the ratio were higher than 1:6, CO would appear in the outlet gas of the fuel reactor take

away energy. The energy output of the system at steady state would be less than 1 GJ/s. Thus, in this simulation, the temperature difference of the reactors is controlled within 70K to 80K.

6.4.2.4.3 Fluidising gas of the reactors

In Brown's experiments (Brown 2010), the fluidising gas of the fuel reactor is CO_2(50%)/N_2(50%) (Brown et al. 2010), so as the CO_2 sensor could detect the CO_2 signal. In the dynamic simulation of this chapter, the fluidising gas of the fuel reactor is pure CO_2. To ensure the fuel reactor is a bubbling bed, the fluidising gas flow rate per unit area is low. This however, does not detrimentally influence the reactions in the fuel reactor, since all CO_2 consumed in the gasification can be regenerated by the Fe_2O_3 reduction, when Fe_2O_3 is sufficient and the reduction is fast enough. The fluidising gas of the air reactor is preheated to 10 K below the temperature of the air reactor. The airflow has heat capacity, and but doesn't influence the air reactor temperature because its temperature is controlled. For a given rate of oxidation, the airflow rate will change the amount of heat, which needs to be removed from the fuel reactor. When the flow rate of the air is sufficient to oxidize the flow-in char and Fe_2O_3 particles at steady state, the energy produced by the system is equal to the energy of the flowing in with the fuel. When the rate of air is insufficient, char accumulates in the air reactor and the average conversion of Fe_2O_3 in the fuel reactor increases. This is one way of using the system to store energy.

6.4.2.4.4 Heat demand of the reactors

The heat output of the fuel reactor is set to be zero. Thus, at steady, when the system is not in an energy storage mode, the heat output of the air reactor is always equal to the energy of the flow-in fuel. When the temperature difference of reactors changes, the system changes the recycle rate of Fe_2O_3 and the average conversion, and the heat output of the air reactor remains the same.

6.4.2.4.5 Inventory of Fe_2O_3 in the reactors

The inventory has three influences on the system: first, it is a factor of the heat capacity of the reactor. In this system, at 1143K, the heat capacities of the fuel reactor and 500 tons Fe_2O_3 particles are about $2.14\times10^8 J/K$ and $4.6\times10^8 J/K$, respectively (See Appendix C). The heat capacity of the reactor is similar to the Fe_2O_3 particles, which means that in this system, the change of inventory has influence on the overall reactor heat capacity; second, reduced Fe_2O_3 stores energy in the system, and the larger the inventory is, the more energy could be stored in the system; third, it influences the time for the system to reach steady state. The larger the inventory is, the longer for the system to reach steady state.

6.4.2.5 The response time of the system

11111 For a power plant, the heat demand could be changed due to different reasons. Thus, it is important for a power plant to be able to offer extra energy quickly.

According to the UK grid code, the time of switching operation, that is, the response time, should be within two hours (National Grid Electricity Transmission plc 2016). To measure the response time of the system with a char stripper, the system is first set to reach the steady state. The steady state conditions are shown in Table 6.5.

Table 6.5 The steady state conditions of the system with a char stripper.

Parameters	Unit	Value at steady state
Flow rate of air into the air reactor (N_{air})	mol/s	19668
Flow rate of fluidising gas into the fuel reactor (N_f)	mol/s	84.35
Mass of fuel supply	kg/s	38.5
Energy of fuel supply	GJ/s	1
Recycle rate of metal oxide ($N_{recycle}$)	mol/s (Fe_2O_3)	30650
Temperature of the Air Reactor (T_A)	K	1210
Temperature of the Fuel reactor (T_F)	K	1143
The inventory of Fe_2O_3 particles	Tonne	500(fuel reactor)/ 250(air reactor)
Heat demand of the fuel reactor	J/s	0

After reaching the steady state, the energy of fuel supply is then doubled to simulate the switching operations of a power plant, and the heat demand of air reactor versus time is shown in Figure 6.14.

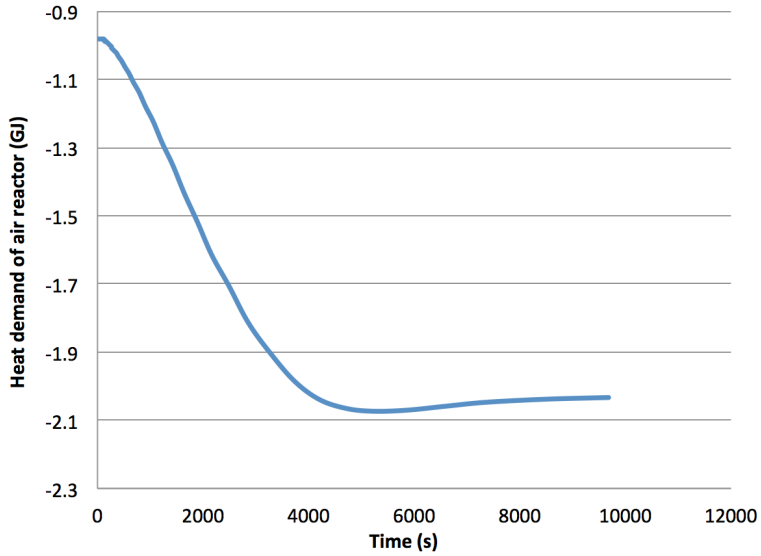

Figure 6.14 The heat demand of air reactor (GJ) versus time (s) after the step change of energy of fuel supply (from 1GJ/s to 2 GJ/s). The negative number means that heat is taken out from the system.

Figure 6.14 shows that the time for the system to reach steady state is about 5000s, i.e., about one hour and a half, which is less than two hours. A power station on using chemical looping would therefore be capable of meeting this aspect of the grid code.

6.4.2.6 The use of the char stripper

In the outlet recycles of the fuel reactor, the char particles flow out from the fuel reactor with the same probability as Fe_2O_3 particles, and then flow into the air reactor. A char stripper separates Fe_2O_3 and char particles, and puts char particles back into the fuel reactor.

Binary particles mixture flow, which consists of oxygen carriers (heavy particles) and char particles (light particles), first enters into a center riser. The gas

velocity u_1 in the riser is higher than the terminal velocities of char particle ($u_{t,L}$) and heavy particle oxygen carrier ($u_{t,H}$). Terminal velocity is defined as the highest velocity attainable by an object as it falls through a fluid, so the binary particles mixture flow rises up into the cylindrical zone. The gas velocities in the cylindrical zone (u_2) and annular fluidised bed (u_3) are set to be higher than $u_{t,L}$ but close to t $u_{t,H}$ ($0.8u_{t,H} \sim u_{t,H}$), so the maximum separation of binary particles mixture flow could be achieved: char particles flows up and leave the char stripper through the upper exit; oxygen carriers falls down and leaves the char stripper through the exit in the annular zone. (Cheng et al. 2017)

The steady state conditions of the system with a char stripper were shown previously in Table 6.5, and the ones without a char stripper are shown in Table 6.6.

Table 6.6 The steady state conditions of the system without a char stripper.

Parameters	Unit	Value at steady state
Flow rate of air into the air reactor (N_{air})	mol/s	19668
Flow rate of fluidising gas into the fuel reactor (N_f)	mol/s	84.35
Mass of fuel supply	kg/s	38.5
Energy of fuel supply	GJ/s	1
Recycle rate of metal oxide ($N_{recycle}$)	mol/s (Fe_2O_3)	18390
Temperature of the Air Reactor (T_A)	K	1210
Temperature of the Fuel reactor (T_F)	K	1143
The inventory of Fe_2O_3 particles	Tonne	500(fuel reactor)/ 250(air reactor)
Heat demand of the fuel reactor	J/s	0

Comparing Table 6.5 and Table 6.6, it can be seen that the ratio of recycle rate

of metal oxide of the system with and without the char stripper is 0.6:1. This is because without a char splitter, part of the char is oxidized in the air reactor, so less Fe_2O_3 is required in the fuel reactor. The portion of char particles flowing into the air reactor is calculated by the conversion distributions of char particles accumulated in the fuel reactor, which are shown in Figure 6.15.

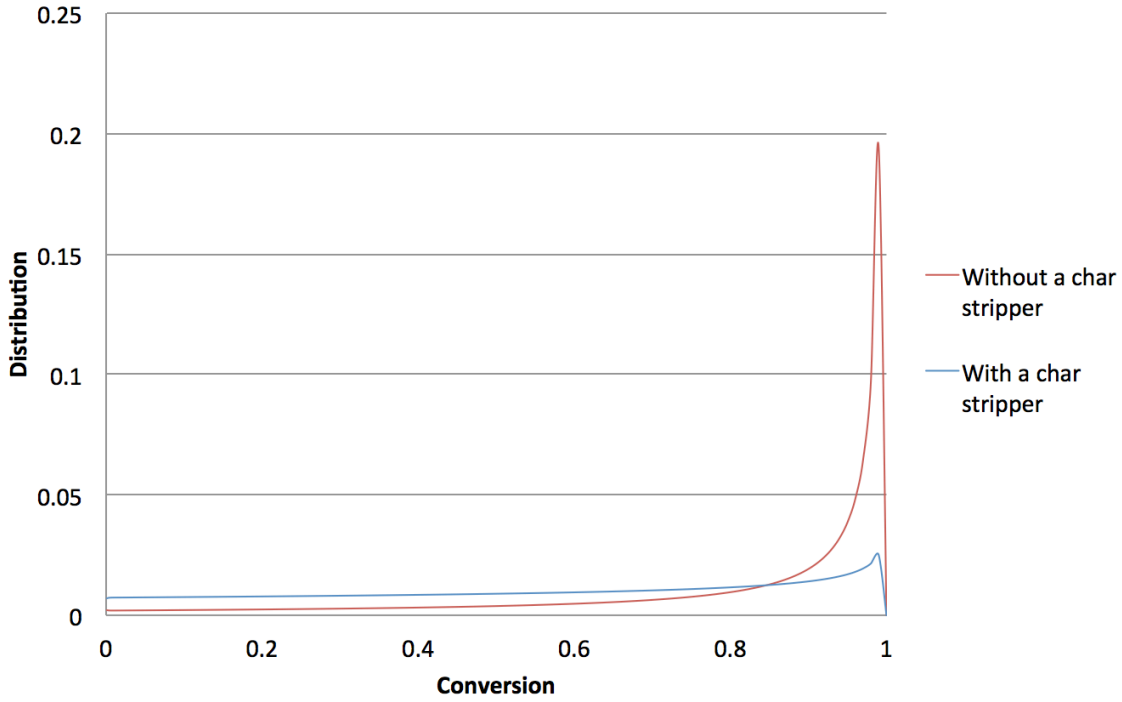

Figure 6.15 The char accumulation conversion distribution (the number of char particles) at steady state in the fuel reactor with and without a char stripper.

In Figure 6.15, with a char stripper, the average char conversion is 81%, and the total number of char particles is 6×10^{10}; without a char stripper, the average char conversion is 57%, and the total number of char particles is 1.56×10^{10}. The residence time of char particles in the case of without a char stripper is infinite, so its average conversion is much larger than the one in the case of with a char stripper. Thus, for the char particles flowing out from the fuel reactor in the case of with a char

stripper, the average conversion is only 57% conversion, and the mass of char flow out is 15 kg/s, which is about 40% of char fed into the system. Therefore, it is important to have a char stripper, otherwise 40% char particles would be oxidized in the air reactor, and the CO_2 would be hard to capture.

6.4.2.7 Energy storage mode

The energy requirement for a power plant is variable, so it is important to store energy to deal with the sudden increase of energy requirement. There are two ways to store energy: 1) make the inflow rate of Fe_2O_3 particles of the air reactor faster than the rate of outflow, so reduced Fe_2O_3 particles accumulate in the air reactor; 2) make the airflow of the air reactor insufficient for complete conversion, so the energy is stored by increasing the average conversion of Fe_2O_3 in the fuel reactor. The stored energy can be released by increasing the airflow to the air reactor.

Table 6.7 The conditions of method 1 for the system with a carbon stripper.

Parameters	Unit	Value
Flow rate of air into the air reactor (N_{air})	mol/s	19668
Flow rate of fluidising gas into the fuel reactor (N_f)	mol/s	84.35
Mass of fuel supply	kg/s	38.5
Energy of fuel supply	GJ/s	1
Recycle rate of metal oxide ($N_{recycle}$)	mol/s (Fe_2O_3)	Steady state phase: 30650 Energy release phase: ~32489 (fuel reactor in, air reactor out) ~29424 (fuel reactor out, air reactor in)
Temperature of the air reactor (T_A)	K	1210
Temperature of the fuel reactor (T_F)	K	1143

The initial inventory of Fe_2O_3 particles	ton	800(fuel reactor)/ 100(air reactor)
Average Fe_2O_3 conversion in the fuel reactor	-	53%

For the first method, the system first reaches steady state, and the average conversion of Fe_2O_3 in the fuel reactor is 55%. Then the recycle rate of Fe_2O_3 is suddenly changed, the inflow rate of the iron oxide in the fuel reactor (and out flow from air reactor) is kept constant, whilst the flow rate leaving the fuel reactor (and inflow to the air reactor) is decreased by 10%. The system has a carbon stripper. All initial conditions are shown in Table 6.7.

The Fe_2O_3 accumulation rate in the air reactor is about 0.5 ton/s. The heat capacity of the air reactor is large, so after 1400 s the procedure is stopped and steady state flow resumed. This method is making use of the stored energy within the inventory of the reduced material that has built up in the approach to steady state.

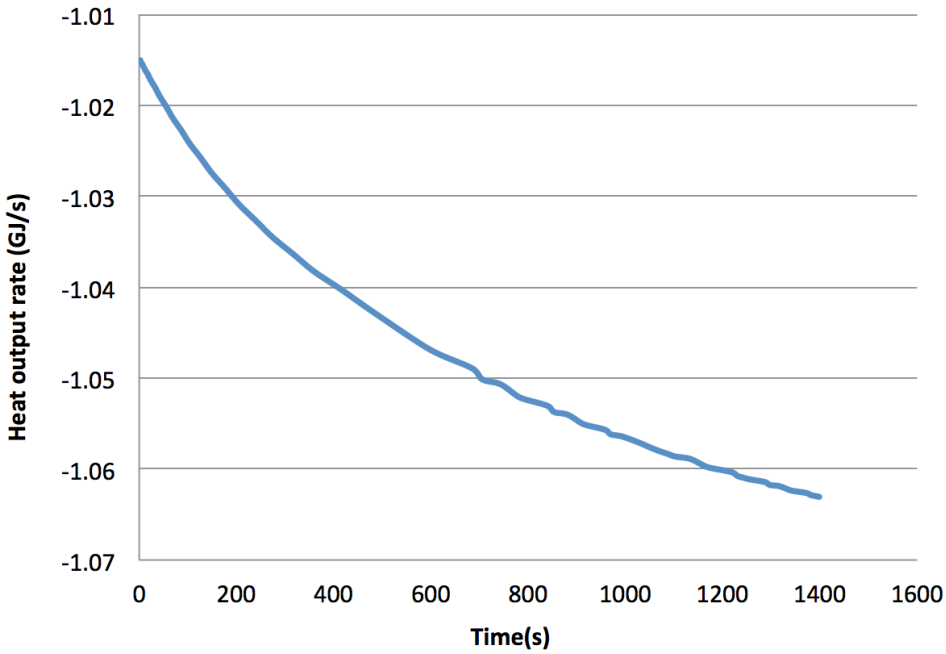

Figure 6.16 The heat output of the air reactor for method 1 when the stored energy is released.

Figure 6.16 shows the heat output of the air reactor from the simulation. As can be seen, when the stored energy is released, the rate of release of energy gradually increases from 1.015 GJ/s to 1.064GJ/s. When steady the flows of metal oxide are re-adjusted to return the reactors back to their initial inventory's, the heat output from the air reactor has to reduce, as energy is once again being stored in the reduced material. The total amount of energy stored, that is, the inventory stored and then discharged over this period can be estimated by considering the change in inventory of Fe_2O_3, the total energy released is $(800-100)\times10^6/160\times0.53\times\frac{2}{3}\times\left(-\Delta H_{rxn}^{Fe_3O_4}\right)=94.3\ GJ$, where $\Delta H_{rxn}^{Fe_3O_4}=-61kJ/mol$ is the enthalpy for the reaction $Fe_3O_4+\frac{1}{4}O_2=\frac{3}{2}Fe_2O_3$, and 0.53 is the average Fe_2O_3 conversion in the fuel reactor during the energy release phase. The total energy released consists of two parts: first is the heat output from the air reactor, which is about 60GJ in Figure 6.16; second is the heat required to heat up around 700 ton mixture of Fe_2O_3 and Fe_3O_4 from 1143K to 1210K, which is about 35GJ. The first part of energy can be gained from the heat output of the air reactor; the second part of energy can be gained by putting the 700 tons Fe_2O_3 in the air reactor back to the fuel reactor. The total energy released (94.3GJ) is only equivalent to the heat release from 94.3s of fuel feeding, demonstrating that if this method were to be used, there would not be much usable stored energy.

For the second method, the previous assumption that all Fe_3O_4 is oxidized into Fe_2O_3 in the air reactor is invalid. Recycling Fe_3O_4 back to the fuel reactor means that history dependence of Fe_2O_3 particles is introduced. After several recycles, the inner

structure of a Fe_2O_3 particle with history dependence is shown in Figure 6.17.

In the fuel reactor, for a Fe_2O_3 particle with no history dependence, its outer layer is made of Fe_3O_4, and CO diffuses through the outer layer and reduce its inner layer of Fe_2O_3; for a Fe_2O_3 particle with history dependence, CO first reduces the outer layer of Fe_2O_3, then diffuses through the medium layer of Fe_3O_4, then reduces the inner layer of Fe_2O_3. The reaction rate for the second case is a little faster than the first case since for the reduction of the outer layer of Fe_2O_3, CO does not have to diffuse through the thick Fe_3O_4 layer. The longer the system runs, the more layers the particles have. For the sake of simplicity, the differences of two cases in the fuel reactor are ignored. Similar thing happens in the air reactor, but it is assumed that the Fe_3O_4 oxidation is very fast, so the influence on the reaction rate can be ignored.

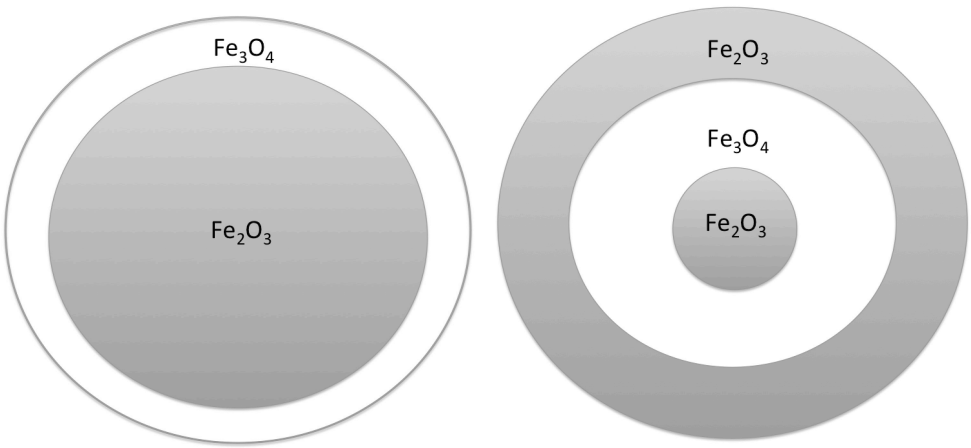

Figure 6.17 The diagram of Fe_2O_3 particles at the same conversion without (left) or with (right) history dependence in the fuel reactor.

For the second method, the airflow in the air reactor is first controlled to be insufficient, and gradually, the average conversions of Fe_2O_3 in the fuel reactor and the air reactor become the same, that is, close to 1 (i.e. almost completely magnetite).

However, if the average conversion of Fe_2O_3 is equal 1, it means that there is no airflow in the air reactor, which is unrealistic. Thus, the minimum airflow rate should be the flow rate, which could ensure the air reactor runs properly. To produce extra heat, the airflow in the air reactor is increased to be in excess. The rate of heat release is proportional to the air supply rate, so it is controllable and the damage of the reactor due to overheat can be avoided.

Since the history dependence of Fe_2O_3 particles makes the assumptions in the model invalid, and here only the principle of method 2 is discussed. Initially, the system is at steady state. Then the system is switched to the energy storage phase, that is, the airflow rate in air reactor becomes smaller and the fuel feed rate is kept constant. The heat output from the air reactor is lower; gradually the conversions of Fe_2O_3 in the air reactor decrease and in the fuel reactor increase, and they finally become the same. The stored heat consists of two parts: the stored heat in the fuel reactor and the air reactor, respectively.

Then the system is switched to the energy release phase, and the airflow in the air reactor is increased. As mentioned above, since it is assumed that the oxidation of Fe_3O_4 is very fast, so the heat release rate in the air reactor could be controlled by the rate of air supply. Thus, the airflow rate should be set to a proper value to meet the heat demand and ensure the safety of the air reactor. The average conversion of Fe_2O_3 in the air reactor gradually decreases to zero, and the one in the fuel reactor gradually decreases to the initial average conversion. Different to method 1, the flow-in and flow-out recycle rates of metal oxide are same for method 2, so the total heat released

is generally equal to the heat output from the air reactor.

6.4.2.8 The discussion of ideal operation conditions

In this system, the fuel feed is 1GJ/s. To oxidize the fuel into CO_2, the minimum recycle rate of Fe_2O_3 is about 2.6 ton/s. The minimum temperature difference of the fuel reactor and the air reactor is set to be 10K, and the corresponding recycle rate of Fe_2O_3 is about 5.5 ton/s. Thus, the recycle rate of Fe_2O_3 is between 2.6 and 5.5 ton/s. The inventory of Fe_2O_3 is 500 tons, so the ratio of recycle rate over inventory is around 1/200-1/90, which is very large. The recycle rate is quite large and will impose an energy penalty. In their work on the 1000 MWth design (Lyngfelt and Leckner 2015), Lyngfelt and Leckner estimated this penalty to be 3.9%. Ideally, the energy penalty for the chemical looping combustion of solid fuels should be around 2.5% (Lyngfelt and Linderholm 2014), so the penalty here is about 56% higher than the ideal standard.

The char stripper is necessary to avoid too much char burning in the air reactor, rather than the fuel reactor. However, the efficiency of char stripper cannot be 100%. If the efficiency is 60%, there are about 25% char particles burns in the air reactor, which means the carbon capture efficiency is only 75%.

The inventory of the fuel reactor and the air reactor are 500 tons and 250 tons, respectively. Whilst this seems quite large, it doesn't provide much capacity for energy storage.

6.5 CONCLUSIONS

In this chapter, models are made to simulate Brown's (Brown et al. 2010) char gasification experiments at 1073K and 1223K. The results indicate that: 1) Bohn's Fe_2O_3 reduction rate expression is too fast at 1073K and 1223K, and modification should be made; 2) At 1223K, for both the char gasification and Fe_2O_3 reduction, the shrinking core model could be applied. The model was calibrated to match the date from Brown's (Brown et al. 2010), then this model scaled to represent a 1 GWth power plant consisting of a fuel reactor connected with an air reactor.

The dynamic model for a 1 GWth power plant shows that: 1) the response time of the system is about one hour and a half; 2) a char stripper is necessary for carbon capture; 3) the system could store around 100 GJ energy, and release the energy in 20 to 30 minutes; 4) the recycle rate of the system is between 2.6 and 5.5 ton/s. The capacity for energy storage is limited compared to the power output of the system; 5) Two methods of energy storage are discussed, and the energy stored in the system is about the energy of 90s inflow fuel, meaning that using the chemical looping material as a transient store of energy for load balance is not likely to be of value.

CHAPTER 7 CONCLUSIONS

In this thesis, chemical looping combustion process in the fluidised bed using Fe_2O_3 and CuO as oxygen carriers is discussed, and a steady state model and a dynamic model of a power plant are tested in Chapter 5 and Chapter 6, respectively. To model the CLC process in the fluidised bed, the kinetics of oxygen carriers (Fe_2O_3 and CuO) must be known, which are discussed in Chapter 3 and Chapter 4. In addition, the Sherwood number in the fluidised bed, which represents the mass transfer rate, must be known as well. There are several ways to measure the Sherwood number, and one way is to use the CO/CO_2 ratio of carbon combustion, which is discussed in Chapter 2.

Chapter 2 was inspired by Hayhurst and Parmar's (Hayhurst and Parmar 2002) work, which used the CO/CO_2 ratio of carbon combustion to measure Sherwood number in the fluidised bed: in the carbon combustion experiments, the Sherwood number can be calculated by the mass transfer rate of O_2 from the bulk phase to the surface of carbon particle. However, the mass transfer rate of O_2 could be overestimated since CO produced on the surface of char particle could be oxidized in the boundary layer or in the free board. Thus, the CO/CO_2 ratio must be known so as to cancel out this error. Hayhurst and Parmar (Hayhurst and Parmar 1998) calculated the CO/CO_2 ratio by measuring the temperature difference between the carbon particle and the bulk phase, which could be flawed since he assumed that the heat from oxidation of CO into CO_2 around the particle could heat up the particle. In fact,

the oxidation of CO could be far away from the particle and the temperature of the particle was overestimated, which leads to the underestimate of CO/CO_2 ratio. In this thesis, a fast O_2 analyser, UEGO was employed, which could automatically oxidize all CO in the sample gas into CO_2. With this characteristic, the O_2 consumption rate of char combustion measured by UEGO is actually the carbon consumption rate in the fluidised bed. To know the real O_2 consumption rate, Fe particle at the same size of the char particle is used as well. Using both carbon consumption rate and O_2 consumption rate, the CO/CO_2 ratio could be calculated, and the results were compared with previous researchers, indicating that the major product of carbon combustion is CO. In contrast to Hayhurst and Parmar (Hayhurst and Parmar 2002) who assumed CO_2 was the main product, for this char the actual ratio of CO/CO_2 was almost zero. The measurement here is in agreement with Arthur. This more accurate determination of CO/CO_2 allows a better estimate of the mass transfer coefficient and leads to a correction of the Hayhurst and Parmar's (Hayhurst and Parmar 2002) correlation by a factor of ½. Interestingly, very small fluidised beds have mass transfer coefficients which are about twice that expected in a large bed (owing to the very different flow and indeterminate flow pattern). This means the correlation of Hayhurst and Parmar (Hayhurst and Parmar 2002), by fortuitous coincidence works wells for beds with diameters < 30 mm., without the correction factor, should be ignored.

In the fluidised bed of CLC process, different fluidising material could have different influence on the reactions. Thus, it is worth discussing different kinds of

fluidising materials. In Chapter 3, the char combustion in the fluidised bed is simulated by using inert (sand) and active (Fe_2O_3 or CuO) fluidising materials. It is assumed that 1) sand could not react with the gaseous products CO and CO_2 (although sand could inhabit the oxidation of CO into CO_2 in the boundary layer (Hayhurst and Parmar 1998)); 2) Fe_2O_3 could reduce CO_2 into CO in the boundary layer; 3) CuO could decompose and produce O_2 in the boundary layer. The boundary layer thickness is calculated by the EMCD assumption and the fluxes in the boundary layer are modeled by the full Stefan-Maxwell equations. The issue that if CO could be oxidized in the boundary is also tested. The results indicate that: 1) CO combustion in the boundary layer leads to smaller carbon consumption rate and larger oxygen consumption rate; 2) Using Fe_2O_3 particles as fluidising materials slows down the carbon consumption rate, since the diffusivity of CO_2 is smaller than CO; 3) Using CuO particles as fluidising materials at small Sherwood number ($Sh = 1.5$) makes the carbon consumption rate faster, since CuO decomposition produces O_2 near the surface of char particle; at large Sherwood number (Sh =2 or 2.5), the rate of CO combustion in the boundary layer becomes larger and partly compensates for the oxygen produced by CuO decomposition, so the net effect is that CuO particles slow down the carbon consumption rate at large Sherwood number (Sh =2 or 2.5).

In Chapter 4, the influence of using CuO as fluidising material is further discussed experimentally. In Chapter 3, the fluidising gas is air, so in most parts of the fluidised bed, the oxygen concentration is relatively high, and only in a thin layer around the char particle, the oxygen concentration is close to zero. CuO could only

decompose when the oxygen concentration is close to zero, so the conditions in Chapter 3 could not ensure that the influence of CuO decomposition is fully tested. Thus, in Chapter 4, the compositions of fluidising gas are 5% O_2 + 95% N_2, 1% O_2 + 99% N_2 and pure N_2. The results indicate that since the amount of CuO used in the experiment is small, when the O_2 concentration in the bulk phase is lower than the equilibrium concentration, the O_2 concentration in the bulk phase gradually decreases, and the O_2 concentration in the bulk phase has large influence on the char particle combustion.

In Chapter 5, a chemical looping power plant at steady state is modeled, which consists of two systems: 1) the combustor of coal via chemical looping combustion; 2) a steam cycle, which uses the heat generated by the chemical looping combustor. These two systems interact with each other by heat exchange. Different kinds of fuels are tested, including Hambach lignite coal, Polish bituminous coal and natural gas. The results indicate that: (1) The effect of the fuel is largely due to the amount of oxygen required per GJ released; (2) Preheating is important, but seems to have a minor effect since the most of the heat is released at temperatures well above the pinch point; (3) In this chapter, since the temperatures of heat source --- the air reactor and the fuel reactor is well above the pinch point, the temperature of the boiler feed water, so all heat are usable for the steam cycle. In this case, the steam cycle and the chemical looping plant can be optimised separately; (4) As long as the preheat temperature of the air flow into the air reactor is higher than the temperature of turbines, the results are not sensitive, and in many cases the power output is

unaffected by the choice of variables, leaving the designer free to choose the most convenient.

In Chapter 6, a dynamic model of a chemical looping power plant using Hambach lignite char is tested. In Chapter 5, since the system is at steady state, the chemical looping combustion system is just considered as a steady-state heat source. In this chapter, the parameters of the chemical looping combustion system are adjusted so as to simulate the operations of a real chemical looping power plant. The two-phase model is employed for the fluidised bed reactors. Experimental data from Brown (Brown 2010) was simulated using this model first to test its validity. Then the model is scaled up to simulate a 1GWth dynamic power plant. The ideal operation conditions are found, and a char stripper is found helpful for carbon capture. The response time of the system is about one hour and a half. Two methods of energy storage are discussed, and the energy stored in the system is about the energy of 90s flow-in fuel. The method of insufficient airflow in the air reactor is found better, since it is easier to control the airflow rate rather than the recycle rate of metal oxide.

APPENDICES

A. The deviation of the reaction rate expression for Fe_2O_3 reduction with CO

In Section 2.2.2.1, the reaction of Fe_2O_3 reduction with CO is assumed to be pseudo steady state, which means that the CO consumption must equal to the amount of CO transported to the Fe_2O_3 particle. The CO consumption rate is given as,

$$(1-\varepsilon_{mf})(1-\varepsilon_{Fe_2O_3})\xi_{CO} = \left(1-\varepsilon_{mf}\right)\left(1-\varepsilon_{Fe_2O_3}\right)k_{Fe_2O_3}c_{CO} \quad \text{(A.1)}$$

And the CO transportation rate is given as,

$$(1-\varepsilon_{mf})(1-\varepsilon_{Fe_2O_3})\xi_{CO} = \frac{A_{Fe_2O_3}k_c(c_{CO}-c_{CO,s})}{V_{Fe_2O_3}} \quad \text{(A.2)}$$

The molar concentration of CO on the surface of the Fe_2O_3 particle, $c_{CO,s}$ is assumed to be zero, so Equation (A.2) becomes,

$$(1-\varepsilon_{mf})(1-\varepsilon_{Fe_2O_3})\xi_{CO} = \frac{A_{Fe_2O_3}k_c c_{CO}}{V_{Fe_2O_3}} \quad \text{(A.3)}$$

Multiplying Equation (A.3) by $k_{Fe_2O_3}V_{Fe_2O_3}/A_{Fe_2O_3}k_c$, and adding it to equation (A.3),

$$\left(1+\frac{k_{Fe_2O_3}V_{Fe_2O_3}}{A_{Fe_2O_3}k_c}\right)(1-\varepsilon_{mf})(1-\varepsilon_{Fe_2O_3})\xi_{CO} = k_{Fe_2O_3}c_{CO}\left(\left(1-\varepsilon_{mf}\right)\left(1-\varepsilon_{Fe_2O_3}\right)+1\right) \quad \text{(A.4)}$$

Rearranging equation (A.4), it gives that,

$$(1-\varepsilon_{mf})(1-\varepsilon_{Fe_2O_3})\xi_{CO} = \frac{\left((1-\varepsilon_{mf})(1-\varepsilon_{Fe_2O_3})+1\right)c_{CO}}{\left(\frac{1}{k_{Fe_2O_3}}+\frac{V_{Fe_2O_3}}{A_{Fe_2O_3}k_c}\right)} \quad \text{(A.5)}$$

Equation (A.6) can be used in other reactions, such as copper oxide reduction with CO or copper oxide decomposition, with only the changes of relevant parameters.

B. The deconvolution of reactor and measuring system

The reactor and the measuring system can be simplified into a CSTR (continuous stirred tank reactor) and a PFR (plug flow reactor), which is shown in Figure B.1.

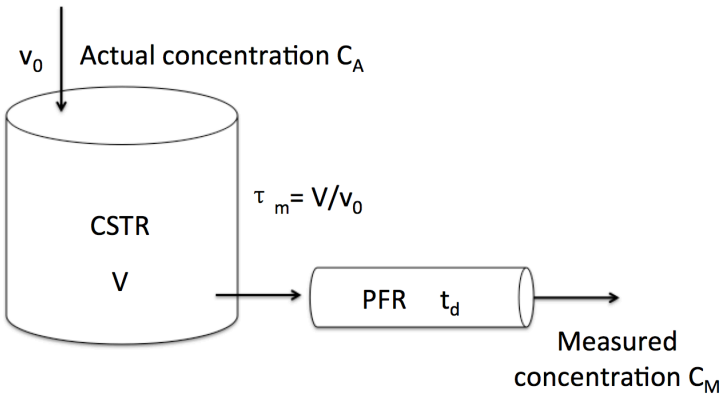

Figure B.1 The diagram of the deconvolution in the reactor and the measuring system.

In Figure B.1, v_0 is the inlet flow rate, V is the volume of the CSTR, and $\tau_m = V/v_0$ is the time constant of the CSTR. C_A is the actual concentration, and C_M is the measured concentration. t_d is the delay time. The mass balance of the whole system is given as,

$$V\frac{dC_M|_t}{dt} = v_0\left(C_A|_{t-t_d} - C_M|_t\right) \tag{B.1}$$

Solving and rearranging the Equation (B.1),

$$C_A|_{t-t_d} = C_M|_t + e^{-\frac{t-t_d}{\tau_m}+m} \tag{B.2}$$

When $t = t_d$, $C_M|_{t_d} = 0$, so $m = lnC_A|_0$. And $C_M|_t$ is given as,

$$C_M|_t = C_A|_{t-t_d} - C_A|_0 e^{-\frac{t-t_d}{\tau_m}} \tag{B.3}$$

The time constant τ_M is fitted by experiments and the experimental conditions are: the reactor bed is first fluidised by pure N_2 using sand as fluidizing material at U/U_{mf} =7, and then quickly switched the target gas at U/U_{mf} =7 (for instance, 20% CO_2 in N_2) by a solenoid valve. The fitting is shown in Figure A.1 ($\tau_M = 9s$, $t_d = 15s$).

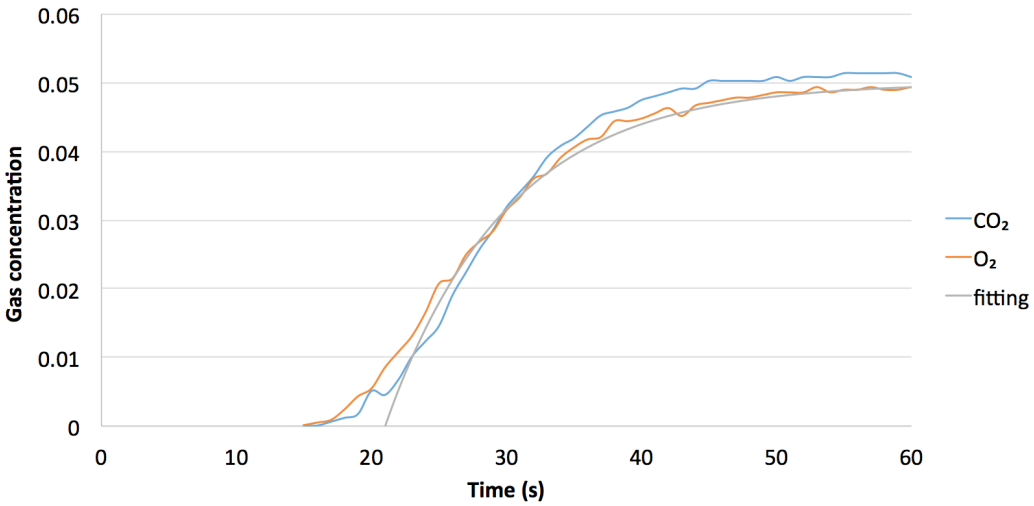

Figure B.2 The fitting of τ_M. In the inlet gas, O_2 and CO_2 were suddenly changed from 0 to 5%. $U/U_{mf} = 7$, and the temperature is at 973K.

$C_A|_{t-t_d}$ is given as,

$$C_A|_{t-t_d} = C_M|_t + \tau_M \frac{dC_M|_t}{dt} \tag{B.4}$$

Here, the measured data is first smoothed by taking average of 20 consecutive data points, and then be fitted by $C_M|_t = at^3 + bt^2 + ct + d$. Figure B.3 shows the comparison of actual and measured gas concentrations at 1223K.

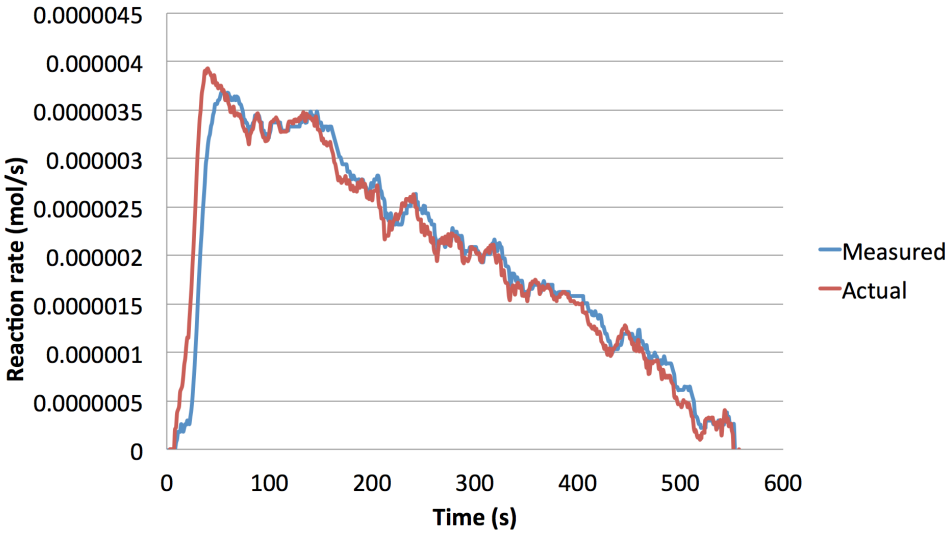

Figure B.3 The comparison of actual and measured gas concentrations at 1223K.

It shows that the actual gas concentration is sharper than the measured one.

C. Parameters, database and the equations of air reactor for the dynamic model in Chapter 6

Parameters for the dynamic model in Chapter 6 are from different literatures and Chapter 3, the pseudo-steady state model of chemical looping plant.

Table C.1 Parameters for simulations of Brown and this thesis at 1073K and 1223K.

Parameters	Units	Value (1073K)	Value (1223K)
A_r	m^2	4.9×10^{-4}	4.9×10^{-4}
d_c	μm	600-1400	600-1400
d_{Fe}	μm	300-425	300-425
$D_{CO_2}^{eff,Fe}$	m^2/s	2.08×10^{-5}	2.45×10^{-5}
$D_{CO_2}^{eff,p}$	m^2/s	5.56×10^{-5}	6.92×10^{-5}
H	mm	88	53
H_{mf}	mm	41	33
K_{p,Fe_3O_4}		1.9	3.2
F_c	mg/s	3	3.8
Q	m^3/s	3.1×10^{-5}	1.22×10^{-5}
Sh	—	—	1.16
U_0	m/s	0.32	0.342
U_{mf}	m/s	0.05	0.036
U_b	m/s	0.56	0.604
d_b	mm	16.2	12

V_b	m	2.2×10^{-6}	9.03×10^{-7}
ε_b	—	0.539	0.374
ε_{mf}	—	0.4	0.4
ν	m^2/s	1.02×10^{-4}	1.26×10^{-4}
ρ_c	kg/m^3	850	850
$\rho_{Fe_2O_3}$	kg/m^3	2060	2060
$m_{Fe_2O_3}$	g	40	20
P	bar	1	1
$\varepsilon_{Fe_2O_3}$	-	0.6	0.6
$\tau_{Fe_2O_3}$	-	2.5	2.5
S_g	m^2/g	1	1
ψ		15.9	15.9

Table C.2 Parameters adapted from Lyngfelt (Lyngfelt and Leckner 2015) for circulating simulations

Parameters	Units	Value (fuel reactor, 1143K)	Value (air reactor, 1210K)
A_0	m^2	0	0
d_c	μm	600-1400	600-1400
d_{Fe}	μm	150-300	150-300
$D_{CO_2}^{eff,Fe}$	m^2/s	2.08×10^{-5}	2.45×10^{-5}
$D_{CO_2}^{eff,p}$	m^2/s	5.56×10^{-5}	6.92×10^{-5}

H	mm	88	53
H_{mf}	mm	41	33
K_{p,Fe_3O_4}		1.9	3.2
F_c	mg/s	3	3.8
Q	m^3/s	3.1×10^{-5}	1.22×10^{-5}
Sh	—	—	1.16
U_{mf}	m/s	0.126	0.126
U_b	m/s	0.56	0.604
d_b	mm	16.2	12
V_b	m	2.2×10^{-6}	9.03×10^{-7}
ε_b	—	0.539	0.374
ε_{mf}	—	0.4	0.4
ν	m^2/s	4.79×10^{-5}	4.36×10^{-5}
ρ_c	kg/m^3	850	850
$\rho_{Fe_2O_3}$	kg/m^3	2060	2060
$m_{Fe_2O_3}$	g	40	20
P	bar	1	1
$\varepsilon_{Fe_2O_3}$	-	0.6	0.6
$\tau_{Fe_2O_3}$	-	2.5	2.5
S_g	m^2/g	1	1
ψ		15.9	15.9

*The calculation of heat capacities of the reactors: the sizes ($L \times W \times H$) of the fuel reactor and the air reactor are $11m \times 7m \times 48m$ and $18m \times 11m \times 48m$, respectively. The wall thickness of the fuel reactor and the air reactor (including the bottom and the lid) is 20 mm, so the total volumes are 37.7 m^3 and 63.6 m^3, respectively. The reactors are made of stainless steel. The density of stainless steel is 7.86×10^3 kg/m^3, and the heat capacity of stainless steel at 1173K is 42 J/(mol K). The heat capacities of the fuel reactor and the air reactor are 2.22×10^8 and 3.75×10^8 J/K, respectively. The heat capacity of Fe_2O_3 at 1173K is 141 J/(mol K). If the load of Fe_2O_3 in the air reactor is 500 tons, the total heat capacity of Fe_2O_3 in the air reactor is 4.41×10^8 J/K, which is similar to the heat capacity of the air reactor; if the load of Fe_2O_3 in the air reactor is 50 tons, the total heat capacity of Fe_2O_3 in the air reactor is 0.44×10^8 J/K, 11.7% of the heat capacity of the air reactor. Thus, the air reactor has influence on the total heat capacity of the air reactor (the air reactor plus Fe_2O_3 inside), especially when the load of Fe_2O_3 is small (less than 50 tons). Similar results can be obtained for the fuel reactor.

NOMENCLATURE

A	Cross section area of the fluidized bed reactor	m^2
A_0	Distributor area per orifice	m^2
A_r	Archimedes number of inert particles $= (\rho_p - \rho_g)\,\rho_g g d_p^3/\mu_g^2$	
a	Radius of reacting particle	m
a_0	Initial radius of reacting particle	m
C_i	Concentration of species i	mol/m^3
C_i^b	Concentration of species i in bubbling phase	mol/m^3
C_i^c	Concentration of species i in the unreacted core	mol/m^3
C_i^{eq}	Equilibrium concentration of species i	mol/m^3
C_i^{in}	Inlet flow concentration of species i	mol/m^3
C_i^p	Concentration of species i in the particular phase	mol/m^3
C_i^s	Concentration of species i on the surface of reacting particle	mol/m^3
$C_i^{s,i}$	Concentration of species i on the inner layer of surface of reacting particle	mol/m^3
$C_{CO}^{s,o}$	Concentration of species i on the outer layer of surface of reacting particle	mol/m^3
C^t	Total concentration in the fluidized bed	mol/m^3
D	Diffusivity of the vapour in the gas flow	m^2/s

D_b	Inner diameter of the fluidised bed	m
D^{eff}	Effective diffusivity	m^2/s
$D^{eff,o}$	Effective diffusivity before the reaction	m^2/s
$D^{eff,X}$	Effective diffusivity at conversion X	m^2/s
D_i^k	Knudsen diffusivity for species i	m^2/s
D^{mol}	Molar diffusivity	m^2/s
D_{O_2,CO_2}	Diffusivity of O_2 and CO_2 in fluidising air	m^2/s
d	Diameter of reacting particle	m
d_c	Diameter of the coal particle	m
d_{Fe}	Diameter of the Fe_2O_3 particle	m
d_p	Diameter of mean diameter of inert bed particles	m
E	Activation energy of the reaction	kcal/mol
F_c	Char feed in rate	g/s
F_p	Net flow rate in the bubbling fluidized bed	mol/s
g	Acceleration because of gravity	$kg{\cdot}m/s^2$
H	Depth of fluidised sand	m
H_L	Limiting bed height where coalescence is complete and a stable slug spacing achieved	m
H_{mf}	Depth of unfluidised sand	m
h	Fluidized bed height above the distributor	m
h_i^{IN}	Inlet molar enthalpy	kJ/mol
h_i^{OUT}	Outlet molar enthalpy	kJ/mol

i	Species in the fluidised bed (CO, CO_2, O_2, N_2, carbon and Fe_2O_3)	
J_i	Molar flux of gaseous species i	mol/m^2/s
$K_p^{Fe_2O_3}$	Dimensionless equilibrium constant for the reaction $3Fe_2O_3 + CO = 2Fe_3O_4 + CO_2$	
k_0	Reaction rate constant of the oxidation of CO	ml/mol/s
k_1	Rate constants per active site for char gasification	
k_{-1}	Rate constants per active site for char gasification	
k_2	Rate constants per active site for char gasification	
$k^{Fe_2O_3}$	Rate constant of the Fe_2O_3 reduction reaction	s^{-1}
$k^{Fe_3O_4}$	Rate constant of the Fe_3O_4 reduction reaction	s^{-1}
k_g	Mass transfer coefficient	m/s
L	Characteristic length of the particle	m
L_0	Initial length of overlapped cylindrical pores	m
M_i	Molecular weight of species i	g
m_{steam}	Flow rate of steam cycle (water)	kg/s
N_{air}	Flow rate of air into the air reactor	mol/s
N_f	Flow rate of fluidising gas into the fuel reactor	mol/s
N_i^{IN}	Flow-in rate of species i into the bubbling fluidized bed	mol/s
N_i^{OUT}	Flow-out rate of species i from the bubbling fluidized bed	mol/s
N_i^T	Total mole number of species i in the bubbling fluidized bed	mol/s

$N_{recycle}$	Recycle rate of metal oxide (Fe_2O_3)	mol/s
NPc^{IN}	Molar flow-in rate of carbon into the bubbling fluidised bed from flow-in coal particles	mol/s
NPc^{OUT}	Molar flow-out rate of carbon into the bubbling fluidised bed from flow-in coal particles	mol/s
n_c^{IN}	Molar number in each flow-in coal particle	mol
n_c^{OUT}	Molar number in each flow-out coal particle	mol
P	Pressure	Pa
$P_c(t, X)$	Distribution of species i at conversion X at time t	
$P_i^{IN}(t, X)$	Distribution of flow-in species i at conversion X at time t	
$P_i^{OUT}(t, X)$	Distribution of flow-out species i at conversion X at time t	
P_i	Pressure of species i	Pa
Pe	Peclet number $= U\tau^2 d/D_\varepsilon$	
p	Constant $p = -\frac{RT}{P\frac{Sh_0}{2}D_{O_2,N_2}^{mol}}$	
Q	External heating supplied	kJ/s
Q_M	The total gaseous reactant molar flow from the particulate phase to the outer surface of the acting particle	mol/s
q	Constant $q = -\frac{\theta p}{a}$	
R	Universal gas constant = 8.314	J/K/mol

R_c	Reaction rate of carbon in the bubbling fluidized bed	mol/s
R_{Fe}	Reaction rate of iron oxide in the bubbling fluidized bed	mol/s
Re	Reynolds number based on superficial fluidized velocity $= Ud/\nu$	
Re_{mf}	Reynolds number at minimum fluidisation $= U_{mf}d/\nu$	
Re_p	Reynolds number in particulate phase $= U_p d/\nu$	
R_g	Gasification rate per unit mass of carbon	mol/s/g
$R_{g,0}$	Initial gasification rate per unit mass of carbon when $X = 0$	mol/s/g
r	Radius	m
r_C	Rate of carbon consumption	mol/s
r_d	Dimensionless radius $= r/a$	
r_{O_2}	Rate of oxygen consumption	mol/s
S_0	Initial internal surface area per unit volume	m^2/m^3
Sc	Schmidt number $= \nu/D$	
Sh	Sherwood number $= k_g d/D$	
Sh_0	Sherwood number for the stagnant case	
Sh_{EMCD}	Sherwood number for equimolar counter-diffusion of reactant and product	
T	Temperature	K
T_A	Temperature of the air reactor	K
T_{BFW}	Temperature of the boiler feed water	K

T_F	Temperature of the fuel reactor	K
T_{pre}	Preheating temperature of airflow into the air reactor	K
T_{ref}	Reference temperature	K
t	Time	s
U	Total superficial velocity of fluidising gas	m/s
U_b	Bubble velocity	m/s
U_{mf}	Minimum fluidising velocity	m/s
U_{opt}	Optimal gas velocity	m/s
U_p	Velocity of gas in particulate phase $= U_{mf}/\varepsilon$	m/s
u_i	Molar internal energy of species i	kJ/mol
V_b	Mean bubble volume in the bubbling fluidized bed	m
X_{CuO}	Conversion from CuO to Cu_2O	
$X_{Fe_2O_3}$	Conversion from Fe_2O_3 to Fe_3O_4	
x_j	Local conversion of the solid particle of species j (j=coal, Fe_2O_3)	
y_i^P	Mole fraction for species i in the particulate phase	
α_i	Constant $\alpha_i = \frac{C_i^p - C_i^s}{\frac{1}{a} - \frac{1}{a+\delta}}$	
β_i	Constant or Stoichiometric coefficients of species i for R_c	
$\Delta H_k^{rxn}(T_{ref})$	Reaction enthalpy of reaction k	kJ/mol
ΔT_{min}	Minimum temperature difference of the hot composite	K

	curve and the cold composite curve	
δ	Thickness of boundary layer	m
ε	Voidage fraction in the fluidised sand	
ε_b	Bubble fraction	
ε_{CuO}	Voidage of the CuO particle	
$\varepsilon_{Fe_2O_3}$	Voidage of the Fe_2O_3 particle	
ε_{mf}	Minimum voidage in the particulate phase	
η	Molar fraction of CO_2 in the primary product of carbon combustion or effectiveness factor	
η_{crit}	Critical effectiveness factor	
θ	Constant $\theta = \frac{\ln\left(1-x_{O_2}^{p}\right)}{p\left(\frac{1}{a+\delta}-\frac{1}{a}\right)}$	
θ_i	Stoichiometric coefficients of species i for R_{Fe}	
Λ	Effective factor	
λ	Correction factor	
μ_g	Dynamic viscosity of fluidising gas	N·s/m^2
ξ_i	Molar rate of production of species i per volume reactant in the boundary layer	mol/m^3/s
ν	Kinematic viscosity of fluidising gas $= \mu/\rho_g$	m^2/s
ρ_c	Density of reacting particles	kg/m^3
$\rho_{Fe_2O_3}$	Initial bulk density of the Fe_2O_3 particle	g/m^3
ρ_g	Density of gas	kg/m^3

τ^2	Tortuosity of a bed of fluidised particles
$\tau_{Fe_2O_3}$	Tortuosity for Fe_2O_3
Φ	Thiele modulus
ϕ_M	Modified Thiele modulus

REFERENCES

Abad, Alberto, Juan Adánez, Francisco García-Labiano, Luis F. de Diego, and Pilar Gayán. 2010. 'Modeling of the Chemical-Looping Combustion of Methane Using a Cu-Based Oxygen-Carrier'. *Combustion and Flame* 157 (3): 602–15. doi:10.1016/j.combustflame.2009.10.010.

A. Calvelo, J. M. Smith. 1971. 'Intrapellet Transport in Gas-Solid Non- Catalytic Reactions'. *Pp 3.1-24 of Chemeca '70. Sydney Butterworths (1971).*

Adanez, J., L. Diego, F. Garcia-Labiano, P. Gayan, and A. Abad. 2004. 'Screening of Oxygen Carriers for Chemical-Looping Combustion'. *Energy & Fuels* 18: 371–77.

Adanez, Juan, Alberto Abad, Francisco Garcia-Labiano, Pilar Gayan, and Luis F. de Diego. 2012. 'Progress in Chemical-Looping Combustion and Reforming Technologies'. *Progress in Energy and Combustion Science* 38 (2): 215–82. doi:10.1016/j.pecs.2011.09.001.

Adánez, Juan, Francisco García-Labiano, Luis F. de Diego, Ainhoa Plata, Javier Celaya, Pilar Gayán, and Alberto Abad. 2003. 'Optimizing the Fuel Reactor for Chemical Looping Combustion', January, 173–82. doi:10.1115/FBC2003-063.

Alberto Abad, Juan Adánez. 2010 'CLC Modeling: The Fuel-Reactor at Fast fluidization–Conversion of CH_4 Using a NiO-Based Oxygen-Carrier in a 120 kW Th Unit'.

Arthur, J. R. 1951. 'Reactions between Carbon and Oxygen'. *Transactions of the Faraday Society* 47 (0): 164–78. doi:10.1039/TF9514700164.

Avedesian, M.M., and J.F. Davidson. 1973. 'Combustion of Carbon Particles in a Fluidised Bed'. *Trans. Instn. Chem. Engrs.* 51: 121–31.

Baeyens, J., and D. Geldart. 1974. 'An Investigation into Slugging Fluidized Beds'. *Chemical Engineering Science* 29 (1): 255–65. doi:10.1016/0009-2509(74)85051-7.

Bhatia, S. K., and D. D. Perlmutter. 1980. 'A Random Pore Model for Fluid-Solid Reactions: I. Isothermal, Kinetic Control'. *AIChE Journal* 26 (3): 379–86. doi:10.1002/aic.690260308.

———. 1981. 'A Random Pore Model for Fluid-Solid Reactions: II. Diffusion and Transport Effects'. *AIChE Journal* 27 (2): 247–54. doi:10.1002/aic.690270211.

Bischoff, Kenneth B. 1965. 'Effectiveness Factors for General Reaction Rate Forms'. *AIChE Journal* 11 (2): 351–55. doi:10.1002/aic.690110229.

Bohn, C. D., J. P. Cleeton, C. R. Müller, J. F. Davidson, A. N. Hayhurst, S. A. Scott, and J. S. Dennis. 2010. 'The Kinetics of the Reduction of Iron Oxide by Carbon Monoxide Mixed with Carbon Dioxide'. *AIChE Journal* 56 (4): 1016–29. doi:10.1002/aic.12084.

Bohn, Christopher. 2010. 'The Production of Pure Hydrogen with Simultaneous Capture of Carbon Dioxide'. PhD thesis, Cambridge, UK: University of Cambridge.

'BP's 2011 Statistical Review of World Energy'. 2011.

Bradshaw, R. D., and J. E. Myers. 1963. 'Heat and Mass Transfer in Fixed and Fluidized Beds of Large Particles'. *AIChE Journal* 9 (5): 590–95. doi:10.1002/aic.690090505.

Brown, T.A. 2010. *Chemical Looping Combustion with Solid Fuels*. University of Cambridge.

Brown, T. A., J. S. Dennis, S. A. Scott, J. F. Davidson, and A. N. Hayhurst. 2010. 'Gasification and Chemical-Looping Combustion of a Lignite Char in a Fluidized Bed of Iron Oxide'. *Energy & Fuels* 24 (5): 3034–48. doi:10.1021/ef100068m.

'Carbon Dioxide Information Analysis Center (CDIAC)'. 2010, August.

Cheng M, Sun H, Li Z, Cai N. 2017. 'Annular Carbon Stripper for Chemical-looping Combustion of Coal'. Ind Eng Chem Res 56:1580–93.

Chiesa, Paolo, Giovanni Lozza, Alberto Malandrino, Matteo Romano, and Vincenzo Piccolo. 2008. 'Three-Reactors Chemical Looping Process for Hydrogen Production'. *International Journal of Hydrogen Energy* 33 (9): 2233–45. doi:10.1016/j.ijhydene.2008.02.032.

Cho, P., T. Mattisson, and A. Lyngfelt. 2000. 'Reactivity of iron oxide with methane in a laboratory fluidized bed-application of chemical looping combustion'. *Proceedings of the 7th International Conference on Fluidized Bed Combustion*, 599.

Chuang, S.Y. 2009. *Development and Performance of a Cu-Based Oxygen-Carrier for Chemical-Looping Combustion of Solid Fuels*. PhD Thesis. Cambridge, UK.

Chuang, S. Y., J. S. Dennis, A. N. Hayhurst, and S. A. Scott. 2008. 'Development and Performance of Cu-Based Oxygen Carriers for Chemical-Looping Combustion'. *Combustion and Flame* 154 (1–2): 109–21. doi:10.1016/j.combustflame.2007.10.005.

Cleeton, Jason. 2011. 'Chemical Looping Combustion with Simultaneous Power Generation and Hydrogen Production Using Iron Oxides'. PhD thesis, Cambridge, UK: University of Cambridge.

Cloete, S, ST Johanse, and S Amini. 2010 ‘Multiphase CFD–based Models for a Chemical Looping Combustion Process.’ *Proc 1st Int Conf on Chemical Looping. Lyon, France.*

Coelho, M. a. N., and J. R. F. Guedes De Carvalho. 1988. ‘Transverse Dispersion in Granular Beds. I: Mass Transfer from a Wall and the Dispersion Coefficient in Packed Beds’. *Chemical Engineering Research & Design* 66 (2): 165–77.

Constantineau, J. P., J. R. Grace, C. J. Lim, and G. G. Richards. 2007. ‘Generalized Bubbling–slugging Fluidized Bed Reactor Model’. *Chemical Engineering Science*, Fluidized Bed Applications, 62 (1–2): 70–81. doi:10.1016/j.ces.2006.08.011.

Copeland, Robert J., Gokhan Alptekin, Mike Cesario, and Yevgenia Gershanovich. 2002. ‘Sorbent Energy Transfer System (SETS) for CO_2 Separation With High Efficiency’. In *27th International Conference on Coal Utilization & Fuel Systems*, 4–7.

Corbella, Beatríz M., and José María Palacios. 2007. ‘Titania-Supported Iron Oxide as Oxygen Carrier for Chemical-Looping Combustion of Methane’. *Fuel* 86 (1–2): 113–22. doi:10.1016/j.fuel.2006.05.026.

Cormos, Calin-Cristian. 2012. ‘Evaluation of Syngas-Based Chemical Looping Applications for Hydrogen and Power Co-Generation with CCS’. *International Journal of Hydrogen Energy*, ICCE-2011, 37 (18): 13371–86. doi:10.1016/j.ijhydene.2012.06.090.

Darton, R. C. 1977. ‘Bubble Growth Due to Coalescence in Fluidized Bed’. *Trans. Inst. Chem. Eng.* 55: 274–80.

Davidson, J.F., and D. Harrison. 1963. *Fluidised Particles*. Cambridge: Cambridge University Press.

Davidson, J, and D Harrison. 1971. *Fluidisation*. Academic Press: New York.

Deng, Z. G., R. Xiao, B. S. Jin, Q. L. Song, and H. Huang. 2008. ‘Multiphase CFD Modeling for a Chemical Looping Combustion Process (Fuel Reactor)’. *Chemical Engineering & Technology* 31 (12): 1754–66. doi:10.1002/ceat.200800341.

Dennis, John S., Christoph R. Müller, and Stuart A. Scott. 2010. ‘In Situ Gasification and CO_2 Separation Using Chemical Looping with a Cu-Based Oxygen Carrier: Performance with Bituminous Coals’. *Fuel* 89 (9): 2353–64. doi:10.1016/j.fuel.2010.01.037.

Dennis, John S., and Stuart A. Scott. 2010. ‘In Situ Gasification of a Lignite Coal and

CO_2 Separation Using Chemical Looping with a Cu-Based Oxygen Carrier'. *Fuel*, 17th International Symposium on Alcohol Fuels, 89 (7): 1623–40. doi:10.1016/j.fuel.2009.08.019.

Dennis, J. S., A. N. Hayhurst, and I. G. Mackley. 1982. 'The Ignition and Combustion of Propane/air Mixtures in a Fluidised Bed'. *Symposium (International) on Combustion*, Nineteenth Symposium (International) on Combustion, 19 (1): 1205–12. doi:10.1016/S0082-0784(82)80297-X.

Donat, Felix, Wenting Hu, Stuart A. Scott, and John S. Dennis. 2015. 'Characteristics of Copper-Based Oxygen Carriers Supported on Calcium Aluminates for Chemical-Looping Combustion with Oxygen Uncoupling (CLOU)'. *Industrial & Engineering Chemistry Research* 54 (26): 6713–23. doi:10.1021/acs.iecr.5b01172.

Dryer, F. L., and I. Glassman. 1973. 'High-Temperature Oxidation of CO and CH_4'. *Symposium (International) on Combustion*, Fourteenth Symposium (International) on Combustion, 14 (1): 987–1003. doi:10.1016/S0082-0784(73)80090-6.

Du, Zhiyou, Adel F. Sarofim, John P. Longwell, and Charles A. Mims. 1991. 'Kinetic Measurement and Modeling of Carbon Oxidation'. *Energy & Fuels* 5 (1): 214–21. doi:10.1021/ef00025a035.

'ECN. Phyllis, Database for Biomass and Waste, Http://www.ecn.nl/phyllis, Energy Research Centre of the Netherlands'. 2004

Epstein, Norman. 1989. 'On Tortuosity and the Tortuosity Factor in Flow and Diffusion through Porous Media'. *Chemical Engineering Science* 44 (3): 777–79. doi:10.1016/0009-2509(89)85053-5.

Ergun, Sabri. 1956. 'Kinetics of the Reaction of Carbon with Carbon Dioxide'. *The Journal of Physical Chemistry* 60 (4): 480–85. doi:10.1021/j150538a022.

Fan, Liang-Shih, Liang Zeng, William Wang, and Siwei Luo. 2012. 'Chemical Looping Processes for CO_2 Capture and Carbonaceous Fuel Conversion – Prospect and Opportunity'. *Energy & Environmental Science* 5 (6): 7254–80. doi:10.1039/C2EE03198A.

Fennell, Pual, and Ben Anthony. 2015. *Calcium and Chemical Looping Technology for Power Generation and Carbon Dioxide (CO_2) Capture (p21-p30)*. Woodhead Publishing.

Friedman, S. P., and N. A. Seaton. 1995. 'A Corrected Tortuosity Factor for the Network Calculation of Diffusion Coefficients'. *Chemical Engineering Science* 50 (5):

897–900. doi:10.1016/0009-2509(94)00220-L.
Frössling, N. 1938. ‘The Evaporation of Falling Drops.’ *Gerlands Beiträge Zur Geophysik* 52: 170–216.
Gavalas, George R. 1980. ‘Analysis of Char Combustion Including the Effect of Pore Enlargement’. *Combustion Science and Technology* 24 (5-6): 197–210. doi:10.1080/00102208008952438.
Gavals, George R. 1980. ‘A Random Capillary Model with Application to Char Gasification at Chemically Controlled Rates’. *AIChE Journal* 26 (4): 577–85. doi:10.1002/aic.690260408.
Glicksman, L., W. Lord, J. Valenzuela, A. Bar-Cohen, and R. Hughes. 1981. ‘A Model of the Fluid Mechanics in Fluidized Bed Combustors’. *AIChE Symp. Ser.* 77: 139.
‘Greenhouse Gas’. 2016. *Wikipedia, the Free Encyclopedia*. https://en.wikipedia.org/w/index.php?title=Greenhouse_gas&oldid=733193411.
Harlick, P. J. E.; Tezel, F. H. 2003. ‘Adsorption of carbon dioxide, methane and nitrogen: pure and binary mixture adsorption for ZSM-5 with SiO_2/Al_2O_3 ratio of 280’. *Separation and Purification Technology*. 33: 199-210.
Harper, Ryan. 2013. ‘Chemical Looping Combustion with Copper-Based Oxygen Carriers’. PhD thesis, Cambridge, UK: University of Cambridge.
Hart, A.; Gnanendran, N. 2009. ‘Cryogenic CO_2 capture in natural gas’. Energy Procedia: 1: 697-706.
Hayhurst, A. N. 1991. ‘Does Carbon Monoxide Burn inside a Fluidized Bed? A New Model for the Combustion of Coal Char Particles in Fluidized Beds’. *Combustion and Flame* 85 (1–2): 155–68. doi:10.1016/0010-2180(91)90184-D.
———. 2000. ‘The Mass Transfer Coefficient for Oxygen Reacting with a Carbon Particle in a Fluidized or Packed Bed’. *Combustion and Flame* 121 (4): 679–88. doi:10.1016/S0010-2180(99)00178-9.
Hayhurst, A. N., and M. S. Parmar. 1998. ‘Does Solid Carbon Burn in Oxygen to Give the Gaseous Intermediate CO or Produce CO_2 Directly? Some Experiments in a Hot Bed of Sand Fluidized by Air’. *Chemical Engineering Science* 53 (3): 427–38. doi:10.1016/S0009-2509(97)00334-5.
Hayhurst, A. N., and M. S. Parmar. 2002. ‘Measurement of the Mass Transfer Coefficient and Sherwood Number for Carbon Spheres Burning in a Bubbling

Fluidized Bed'. *Combustion and Flame* 130 (4): 361–75. doi:10.1016/S0010-2180(02)00387-5.

Hayhurst, A. N., and R. F. Tucker. 1990. 'The Combustion of Carbon Monoxide in a Two-Zone Fluidized Bed'. *Combustion and Flame* 79 (2): 175–89. doi:10.1016/0010-2180(90)90042-P.

He, Fang, Hua Wang, and Yongnian Dai. 2007. 'Application of Fe_2O_3/Al_2O_3 Composite Particles as Oxygen Carrier of Chemical Looping Combustion'. *Journal of Natural Gas Chemistry* 16 (2): 155–61. doi:10.1016/S1003-9953(07)60041-3.

Herzog, H., and D. Golomb. 2004. 'Carbon Capture and Storage from Fossil Fuel Use'. *Encyclopedia of Energy*.

He, Wei, Rong He, Takamasa Ito, Toshiyuki Suda, and Jun 'ichi Sato. 2011. 'Numerical Investigations of CO/CO_2 Ratio in Char Combustion'. *Combustion Science and Technology* 183 (9): 868–82. doi:10.1080/00102202.2011.569803.

Howard, J. B., G. C. Williams, and D. H. Fine. 1973. 'Kinetics of Carbon Monoxide Oxidation in Postflame Gases'. *Symposium (International) on Combustion* 14 (1): 975–86. doi:10.1016/S0082-0784(73)80089-X.

Hsiung, Thomas H., and George Thodos. 1977. 'Mass Transfer in Gas-Fluidized Beds: Measurement of Actual Driving Forces'. *Chemical Engineering Science* 32 (6): 581–92. doi:10.1016/0009-2509(77)80223-6.

Hu, Wenting, Felix Donat, S. A. Scott, and J. S. Dennis. 2016. 'Kinetics of Oxygen Uncoupling of a Copper Based Oxygen Carrier'. *Applied Energy* 161 (January): 92–100. doi:10.1016/j.apenergy.2015.10.006.

Iliuta, Ion, Raul Tahoces, Gregory S. Patience, Sebastien Rifflart, and Francis Luck. 2010. 'Chemical-Looping Combustion Process: Kinetics and Mathematical Modeling'. *AIChE Journal* 56 (4): 1063–79. doi:10.1002/aic.11967.

Intergovernmental Panel on Climate Change. 2005. 'Special Report on Carbon Dioxide Capture and Storage'. *Cambridge University Press*.

Ishida, Masaru, and Hongguang Jin. 1994. 'A New Advanced Power-Generation System Using Chemical-Looping Combustion'. *Energy* 19 (4): 415–22. doi:10.1016/0360-5442(94)90120-1.

———. 1996. 'A Novel Chemical-Looping Combustor without NOx Formation'. *Industrial & Engineering Chemistry Research* 35 (7): 2469–72. doi:10.1021/ie950680s.

Ishida, Masaru, Kenji Takeshita, Kumi Suzuki, and Takeyasu Ohba. 2005. 'Application of Fe_2O_3−Al_2O_3 Composite Particles as Solid Looping Material of the Chemical-Loop Combustor'. *Energy & Fuels* 19 (6): 2514–18. doi:10.1021/ef0500944.

Johansson, Marcus, Tobias Mattisson, and Anders Lyngfelt. 2004. 'Investigation of Fe_2O_3 with $MgAl_2O_4$ for Chemical-Looping Combustion'. *Industrial & Engineering Chemistry Research* 43 (22): 6978–87. doi:10.1021/ie049813c.

Joulié, Régis, Mahfoud Barkat, and Gilbert M. Rios. 1997. 'Effect of Particle Density on Heat and Mass Transfer during Fluidized Bed Sublimation'. *Powder Technology* 90 (1): 79–88. doi:10.1016/S0032-5910(96)03203-2.

Joulié, R., and G.M. Rios. 1993. 'Theoretical Analysis of Heat and Mass Transfer Phenomena during Fluidized Bed Sublimation'. *Drying Technology* 11 (1): 157–82. doi:10.1080/07373939308916807.

Joulie, R., G.M. Rios, H. Gibert, and H. Gibert. 1986. 'Sublimation of Pure Substances in Gas Fluidized Beds at Atmoshperic Pressure.' *Drying Technology* 4 (1): 111–35. doi:10.1080/07373938608916314.

J. Szekely, J. W. Evans. 1971. 'Studies in Gas-Solid Reactions: Part I. A Structural Model for the Reaction of Porous Oxides with a Reducing Gas'. *Metallurgical Transactions* 2 (6): 1691–98. doi:10.1007/BF02913895.

Jung, Jonghwun, and Isaac K. Gamwo. 2008. 'Multiphase CFD-Based Models for Chemical Looping Combustion Process: Fuel Reactor Modeling'. *Powder Technology*, Festschrift Issue in Honor of Professor Robert Pfeffer - Articles Presented at the Honoring Session of the AIChE Annual Meeting in 2006, 183 (3): 401–9. doi:10.1016/j.powtec.2008.01.019.

Kidambi, Piran R., Jason P. E. Cleeton, Stuart A. Scott, John S. Dennis, and Christopher D. Bohn. 2012. 'Interaction of Iron Oxide with Alumina in a Composite Oxygen Carrier during the Production of Hydrogen by Chemical Looping'. *Energy & Fuels* 26 (1): 603–17. doi:10.1021/ef200859d.

Kierzkowska, A. M., C. D. Bohn, S. A. Scott, J. P. Cleeton, J. S. Dennis, and C. R. Müller. 2010. 'Development of Iron Oxide Carriers for Chemical Looping Combustion Using Sol−Gel'. *Industrial & Engineering Chemistry Research* 49 (11): 5383–91. doi:10.1021/ie100046f.

Kim, Albert S., and Huaiqun Chen. 2006. 'Diffusive Tortuosity Factor of Solid and

Soft Cake Layers: A Random Walk Simulation Approach'. *Journal of Membrane Science* 279 (1–2): 129–39. doi:10.1016/j.memsci.2005.11.042.
Kolbitsch, Philipp, Tobias Pröll, and Hermann Hofbauer. 2009. 'Modeling of a 120 kW Chemical Looping Combustion Reactor System Using a Ni-Based Oxygen Carrier'. *Chemical Engineering Science* 64 (1): 99–108. doi:10.1016/j.ces.2008.09.014.
Kotas TJ. 1995. *The Exergy Method of Thermal Plant Analysis*. Krieger Publishing Company.
Kramp, M., A. Thon, E.-U. Hartge, S. Heinrich, and J. Werther. 2012. 'Carbon Stripping – A Critical Process Step in Chemical Looping Combustion of Solid Fuels'. *Chemical Engineering & Technology* 35 (3): 497–507. doi:10.1002/ceat.201100438.
Kronberger, B, G Löffler, and H Hofbauer. 2005 'Chemical-Looping Combustion-Reactor Fluidization Studies and Scale-up Criteria.' *In: Thomas DC, Benson SM, Editors. Carbon Dioxide Capture for Storage in Deep Geologic Formations– Results from the CO_2 Capture Project, Oxford, UK: Elsevier; Vol. 1, Chapter 35.*
Kruggel-Emden, H., S. Rickelt, F. Stepanek, and A. Munjiza. 2010. 'Development and Testing of an Interconnected Multiphase CFD-Model for Chemical Looping Combustion'. *Chemical Engineering Science* 65 (16): 4732–45. doi:10.1016/j.ces.2010.05.022.
Kunii, Daizo, and Octave Levenspiel. 1968. 'Bubbling Bed Model. Model for Flow of Gas through a Fluidized Bed'. *Industrial & Engineering Chemistry Fundamentals* 7 (3): 446–52. doi:10.1021/i160027a016.
LaNauze, R. D., and K. Jung. 1982. 'The Kinetics of Combustion of Petroleum Coke Particles in a Fluidized-Bed Combustor'. *Symposium (International) on Combustion*, Nineteenth Symposium (International) on Combustion, 19 (1): 1087–92. doi:10.1016/S0082-0784(82)80284-1.
La Nauze, R. D., K. Jung, and J. Kastl. 1984. 'Mass Transfer to Large Particles in Fluidised Beds of Smaller Particles'. *Chemical Engineering Science* 39 (11): 1623–33. doi:10.1016/0009-2509(84)80089-5.
Lewis, W.K., and E.R. Gilliland. 1954. 'Production of Pure Carbon Dioxide'. *U.S. Patent No: 2665972*.
Li, Fanxing, Hyung Ray Kim, Deepak Sridhar, Fei Wang, Liang Zeng, Joseph Chen, and L.-S. Fan. 2009. 'Syngas Chemical Looping Gasification Process: Oxygen

Carrier Particle Selection and Performance'. *Energy & Fuels* 23 (8): 4182–89. doi:10.1021/ef900236x.

Linjewile, Temi M., and Pradeep K. Agarwal. 1995. 'The Product CO/CO_2 Ratio from Petroleum Coke Spheres in Fluidized Bed Combustion'. *Fuel* 74 (1): 5–11. doi:10.1016/0016-2361(94)P4322-S.

Liu, Wen, and Stuart A. Scott. 2014. 'A Steady-State Flowsheet Model for Power Generation by Chemical Looping and Oxygen Uncoupling'. Cambridge, UK: University of Cambridge.

Lovell, P. F. 1981. 'Heterogeneous Catalysis in Practice by Charles N. Satterfield, McGraw-Hill Company, May 1980; 416 Pages; $26.95'. *AIChE Journal* 27 (2): 86–94. doi:10.1002/aic.690270223.

Lyngfelt, Anders, and Bo Leckner. 2015. 'A 1000 MWth Boiler for Chemical-Looping Combustion of Solid Fuels – Discussion of Design and Costs'. *Applied Energy* 157 (November): 475–87. doi:10.1016/j.apenergy.2015.04.057.

Lyngfelt, Anders, and Carl Linderholm. 2014. 'Chemical-Looping Combustion of Solid Fuels – Technology Overview and Recent Operational Results in 100 kW Unit'. *Energy Procedia*, 12th International Conference on Greenhouse Gas Control Technologies, GHGT-12, 63: 98–112. doi:10.1016/j.egypro.2014.11.011.

Martínez, I., et al. 2016. 'Review and research needs of Ca-Looping systems modelling for post-combustion CO_2 capture applications'. *International Journal of Greenhouse Gas Control*: 50: 271-304

Mattisson, Tobias, Francisco García-Labiano, Bernhard Kronberger, Anders Lyngfelt, Juan Adánez, and Hermann Hofbauer. 2007. 'Chemical-Looping Combustion Using Syngas as Fuel'. *International Journal of Greenhouse Gas Control*, 8th International Conference on Greenhouse Gas Control TechnologiesGHGT-8, 1 (2): 158–69. doi:10.1016/S1750-5836(07)00023-0.

Mattisson, Tobias, Anders Järdnäs, and Anders Lyngfelt. 2003. 'Reactivity of Some Metal Oxides Supported on Alumina with Alternating Methane and OxygenApplication for Chemical-Looping Combustion'. *Energy & Fuels* 17 (3): 643–51. doi:10.1021/ef020151i.

Mattisson, Tobias, Marcus Johansson, and Anders Lyngfelt. 2004. 'Multicycle Reduction and Oxidation of Different Types of Iron Oxide ParticlesApplication to Chemical-Looping Combustion'. *Energy & Fuels* 18 (3): 628–37.

doi:10.1021/ef0301405.
McBride, B, M Zehe, and S Gordon. 2002. 'NASA Glenn Coefficients for Calculating Thermodynamic Properties of Individual Species.' *NASA*.
Mukherjee, Sanjay, Prashant Kumar, Ali Hosseini, Aidong Yang, and Paul Fennell. 2014. 'Comparative Assessment of Gasification Based Coal Power Plants with Various CO_2 Capture Technologies Producing Electricity and Hydrogen'. *Energy & Fuels* 28 (2): 1028–40. doi:10.1021/ef4024299.
National Grid Electricity Transmission plc. 2016. *The Grid Code*. Vol. Issue 5. Revision 17.
Neale, Graham H., and Walter K. Nader. 1973. 'Prediction of Transport Processes within Porous Media: Diffusive Flow Processes within an Homogeneous Swarm of Spherical Particles'. *AIChE Journal* 19 (1): 112–19. doi:10.1002/aic.690190116.
Noorman, S., F. Gallucci, M. van Sint Annaland, and J. A. M. Kuipers. 2011. 'A Theoretical Investigation of CLC in Packed Beds. Part 2: Reactor Model'. *Chemical Engineering Journal* 167 (1): 369–76. doi:10.1016/j.cej.2011.01.012.
Pallarès, David, and Filip Johnsson. 2006. 'Macroscopic Modelling of Fluid Dynamics in Large-Scale Circulating Fluidized Beds'. *Progress in Energy and Combustion Science* 32 (5–6): 539–69. doi:10.1016/j.pecs.2006.02.002.
Peltola, Petteri. 2014. 'Analysis and Modelling of Chemical Looping Combustion Process with and without Oxygen Uncoupling'. PhD thesis, Lappeenranta, Finland: Lappeenranta University of Technology.
Plewa, Julian, and Jerzy Skrzypek. 1989. 'Kinetics of the Reduction of Copper Oxide with Carbon Monoxide'. *Chemical Engineering Science* 44 (12): 2817–24. doi:10.1016/0009-2509(89)85091-2.
Prins, W. 1987. 'Ph.D. Thesis'. *Twente University*.
Prins, W., T. P. Casteleijn, W. Draijer, and W. P. M. van Swaaij. 1985. 'Mass Transfer from a Freely Moving Single Sphere to the Dense Phase of a Gas Fluidized Bed of Inert Particles'. *Chemical Engineering Science* 40 (3): 481–97. doi:10.1016/0009-2509(85)85109-5.
ProcessTrends.com, and globalissues.org. 2015. 'Goddard Institute for Space Studies (GISS) and Climate Research Unit (CRU)'.
Riccetti, Richard E., and George Thodos. 1961. 'Mass Transfer in the Flow of Gases through Fluidized Beds'. *AIChE Journal* 7 (3): 442–44. doi:10.1002/aic.690070319.

Richter, H.J., and K.F. Knoche. 1983. ‘Richter, H.J., Knoche, K.F. “Reversibility of Combustion Processes, Efficiency and Costing, Second Law Analysis of Processes,” ACS Symposium Series, Vol. 235, Pp. 71–85, 1983’.

Rochelle, G. T. 2009. ‘Amine Scrubbing for CO_2 Capture’. *Science*. 325: 1652-4.

Rossberg, M. 1956. ‘Experimental Investigation on the Primary Reactions in Coal Combustion’. *Z. Elektrochem.* 60: 952.

Salatino, Piero, Fabrizio Scala, and Riccardo Chirone. 1998. ‘Fluidized-Bed Combustion of a Biomass Char: The Influence of Carbon Attrition and Fines Postcombustion on Fixed Carbon Conversion’. *ResearchGate* 27 (2): 3103–10. doi:10.1016/S0082-0784(98)80172-0.

Saucedo, Marco A., John S. Dennis, and Stuart A. Scott. 2015. ‘Modelling Rates of Gasification of a Char Particle in Chemical Looping Combustion’. *Proceedings of the Combustion Institute* 35 (3): 2785–92. doi:10.1016/j.proci.2014.07.005.

Saucedo, Marco A., Jin Yang. Lim, John S. Dennis, and Stuart A. Scott. 2014. ‘CO_2-Gasification of a Lignite Coal in the Presence of an Iron-Based Oxygen Carrier for Chemical-Looping Combustion’. *Fuel*, Fluidized Bed Combustion and Gasification – CO_2 and SO_2 capture: Special Issue in Honor of Professor E.J. (Ben) Anthony, 127 (July): 186–201. doi:10.1016/j.fuel.2013.07.045.

Saucedo-Martínez, Marco. 2013. ‘The Gasification of Solid Fuels and Its Relation to Chemical-Looping and Oxy-Fuel Combustion’. PhD thesis, Cambridge, UK: University of Cambridge.

Scala, Fabrizio. 2007. ‘Mass Transfer around Freely Moving Active Particles in the Dense Phase of a Gas Fluidized Bed of Inert Particles’. *Chemical Engineering Science* 62 (16): 4159–76. doi:10.1016/j.ces.2007.04.040.

Stewart, P. S. B., and J. F. Davidson. 1967. ‘Slug Flow in Fluidised Beds’. *Powder Technology* 1 (2): 61–80. doi:10.1016/0032-5910(67)80014-7.

Ströhle, J, M Orth, and B Epple. 2010. ‘Simulation of the Fuel Reactor of a 1 MWth Chemical Looping Plant for Coal.’ *In: Proc. 1st Int Conf on Chemical Looping. Lyon, France.*

Szekely, J., and J. W. Evans. 1971. ‘Studies in Gas-Solid Reactions: Part II. An Experimental Study of Nickel Oxide Reduction with Hydrogen’. *Metallurgical Transactions* 2 (6): 1699–1710. doi:10.1007/BF02913896.

Theo WL, Lim JS, Hashim H, Mustaffa AA, Ho WS. 2016 ‘Review of

Pre-combustion Capture and Ionic Liquid in Carbon Capture and Storage'. *Appl Energy*.183:1633–63.

Tognotti, L., J. P. Longwell, and A. F. Sarofim. 1991. 'The Products of the High Temperature Oxidation of a Single Char Particle in an Electrodynamic Balance'. *Symposium (International) on Combustion*, Twenty-Third Symposium (International) on Combustion, 23 (1): 1207–13. doi:10.1016/S0082-0784(06)80382-6.

Tsotsas, E. 1994. 'Discrimination of Fluid Bed Models and Investigation of Particle-to-Gas Mass Transfer by Means of Drying Experiments'. *Chemical Engineering and Processing: Process Intensification* 33 (4): 237–45. doi:10.1016/0255-2701(94)01005-6.

Turnbull, E. 1984. 'Effect of Pressure on Combustion of Char in Fluidized Beds'. *AIChE J.* 30: 881–89.

Wakao, N., and T. Funazkri. 1978. 'Effect of Fluid Dispersion Coefficients on Particle-to-Fluid Mass Transfer Coefficients in Packed Beds'. *Chemical Engineering Science* 33 (10): 1375–84. doi:10.1016/0009-2509(78)85120-3.

Wang, Y.; Zhao, L.; Otto, A.; Robinius, M.; Stolten, D. 2017. 'A Review of Post-combustion CO_2 Capture Technologies from Coal-fired Power Plants'. *Energy Procedia*. 114, 650–665.

Wen, C. Y., and Y. H. Yu. 1966. 'A Generalized Method for Predicting the Minimum Fluidization Velocity'. *AIChE Journal* 12 (3): 610–12. doi:10.1002/aic.690120343.

Wilkins, George S., and George Thodos. 1969. 'Mass Transfer Driving Forces in Packed and Fluidized Beds'. *AIChE Journal* 15 (1): 47–50. doi:10.1002/aic.690150114.

Williams, R. J. J., A. Calvelo, and R. E. Cunningham. 1972. 'A General Asymptotic Analytical Solution for Non-Catalytic Gas-Solid Reactions'. *The Canadian Journal of Chemical Engineering* 50 (4): 486–90. doi:10.1002/cjce.5450500407.

Xu, Min, Naoko Ellis, Ho-Jung Ryu, and C. Jim Lim. 2007. 'Modeling of an Interconnected Fluidized Bed Reactor for Chemical Looping Combustion'. *The 12th International Conference on Fluidization - New Horizons in Fluidization Engineering*, May. http://dc.engconfintl.org/fluidization_xii/113.

Young, J. B., and B. Todd. 2005. 'Modelling of Multi-Component Gas Flows in Capillaries and Porous Solids'. *International Journal of Heat and Mass Transfer* 48 (25–26): 5338–53. doi:10.1016/j.ijheatmasstransfer.2005.07.034.

Zafar, Qamar, Tobias Mattisson, and Börje Gevert. 2005. ‘Integrated Hydrogen and Power Production with CO_2 Capture Using Chemical-Looping ReformingRedox Reactivity of Particles of CuO, Mn_2O_3, NiO, and Fe_2O_3 Using SiO_2 as a Support’. *Industrial & Engineering Chemistry Research* 44 (10): 3485–96. doi:10.1021/ie048978i.

Zhao, L., et al. 2008. ‘A parametric study of CO_2/N_2 gas separation membrane processes for post-combustion capture’. *Journal of Membrane Science*. 325: 284-94.